



**HAL**  
open science

# Comprehensive study of the MoS<sub>2</sub>-Ketjenblack structure – electrochemical performance relationships in lithium sulfur batteries

Célestine Desoeurbrun

► **To cite this version:**

Célestine Desoeurbrun. Comprehensive study of the MoS<sub>2</sub>-Ketjenblack structure – electrochemical performance relationships in lithium sulfur batteries. Chemical engineering. Université Grenoble Alpes [2020-..], 2023. English. NNT : 2023GRALI100 . tel-04531769

**HAL Id: tel-04531769**

**<https://theses.hal.science/tel-04531769>**

Submitted on 4 Apr 2024

**HAL** is a multi-disciplinary open access archive for the deposit and dissemination of scientific research documents, whether they are published or not. The documents may come from teaching and research institutions in France or abroad, or from public or private research centers.

L'archive ouverte pluridisciplinaire **HAL**, est destinée au dépôt et à la diffusion de documents scientifiques de niveau recherche, publiés ou non, émanant des établissements d'enseignement et de recherche français ou étrangers, des laboratoires publics ou privés.

## THÈSE

Pour obtenir le grade de

### DOCTEUR DE L'UNIVERSITÉ GRENOBLE ALPES

École doctorale : I-MEP2 - Ingénierie - Matériaux, Mécanique, Environnement, Energétique, Procédés, Production

Spécialité : 2MGE - Matériaux, Mécanique, Génie civil, Electrochimie

Unité de recherche : Laboratoire d'Electrochimie et de Physico-Chimie des Matériaux et des Interfaces.

**Etude des relations entre la structure et les performances électrochimiques de matériaux MoS<sub>2</sub>-Ketjenblack pour les batteries lithium-soufre.**

**Comprehensive study of the MoS<sub>2</sub>-Ketjenblack structure – electrochemical performance relationships in lithium sulfur batteries.**

Présentée par :

**Célestine DESOEURBRUN**

#### Direction de thèse :

<b>Renaud BOUCHET</b> PROFESSEUR DES UNIVERSITES, Université Grenoble Alpes	Directeur de thèse
<b>Didier DEVAUX</b> CHARGE DE RECHERCHE, Université Grenoble Alpes	Co-encadrant de thèse
<b>Denis UZIO</b> IFPEN	Co-encadrant de thèse

#### Rapporteurs :

<b>Philippe BARBOUX</b> PROFESSEUR EMERITE, Chimie ParisTech
<b>Claude GUERY</b> PROFESSEURE DES UNIVERSITES, Université de Picardie Jules Verne

#### Thèse soutenue publiquement le **19 décembre 2023**, devant le jury composé de :

<b>Renaud BOUCHET</b> PROFESSEUR DES UNIVERSITES, Université Grenoble Alpes	Directeur de thèse
<b>Philippe BARBOUX</b> PROFESSEUR EMERITE, Chimie ParisTech	Rapporteur
<b>Claude GUERY</b> PROFESSEURE DES UNIVERSITES, Université de Picardie Jules Verne	Rapporteuse
<b>Jean-Claude LEPRETRE</b> PROFESSEUR DES UNIVERSITES, Grenoble INP	Examineur
	Président

#### Invités :

<b>Christian JORDY</b> INGENIEUR DOCTEUR, SAFT
<b>Denis UZIO</b> INGENIEUR HDR, IFPEN Solaize





*« La glace fond et le plastique reste.  
J'traverse les saisons 'vec la même 'tite veste »*

- Biga Ranx

*« L'utopie est simplement ce qui n'a pas encore été essayé ! »*

- Théodore Monod



*To : P-J-R-S-J-H-B-B-R*



## Acknowledgements

It is with great emotion that I wrote these few lines to thank the people who contributed, alongside me, to the success of this beautiful project. These acknowledgments also extended to the people who helped me, over the years, to refine my studies, my thesis project, my professional projects and who were involved in my personal growth. I realized that this thanks were as challenging as the PhD synthesis, with the apprehension of forgetting key members who nevertheless color my career and the DNA of my thought. To those I forgot to mention, I apologize in advance. You will certainly find yourself in my memoirs, published by "La grande traversée" in 2195, in our orchestrated world. Is being synthetic what is required of a researcher? I'll let you appreciate my mastery of the exercise.

I would like to begin by thanking each of the members of the jury, who accepted to evaluate my research work, in a particular order, whose subtlety will be expressed later in this statement. First of all, I would like to thank Claude Guéry of the LRCS and Philippe Barboux of the IRCP who took the time to report on my work, who were able to highlight the key points and guide me on some improvements. My thanks also go to Christian Jordy, engineer of the « Prospective » team at SAFT and to Jean-Claude Leprêtre, member of the UGA and president of the jury. The thesis defense was, for me, a real moment of pleasure, a rich and constructive exchange reflecting everyone's enthusiasm for the scientific knowledge and understanding of complex systems from both an academic and industrial point of view. This defense was also an opportunity for me to gather the actors who have allowed me, education after education, from the chemistry bachelor's degree at UPJV, through Chimie Paris Tech engineering school, internships, to the education of the doctoral school at UGA, to carry out my higher education course with great satisfaction. I have always met motivated people, who know how to pass on their knowledge and their passion and who have thus given me the desire to constantly learn at every levels, and with a smile. I would like to particularly emphasize the chemistry program at UPJV, which was the first step of my graduate studies. It was during those three years of undergraduate study that I developed a passion for materials and their applications, with a penchant for solid-state chemistry, which was made pleasantly fun and electrochemistry, which was taught with great rigor, a field that does not make everyone dream. From this solid academic background, my studies have been a real learning pleasure, which I insist on because there is nothing more important than doing something that makes sense to you, something that is pursued with joy.

More generally, due to a limited members of PhD jury, I would like to express, chronologically, my gratitude to all the teaching staff of the trainings I attended, the trust of the teams and structures in which I did my six internships from France to the Netherlands, the members of the CSI (Mathieu Morcrette and Lorenzo Stievano), without whom I would not have reached the choice of the PhD and its achievement. The idea for the PhD took root in me at the end of my final year of my bachelor's degree (thanks to Thibaut Chartrel and Franck Dolhem) and was confirmed during my further studies. This is how I carefully chose my PhD topic on the Li-Sulfur subject.



The PhD was a fresh collaboration (with 5 active members) and bi-located (from Lyon to Grenoble), further away from Amiens and my native Picardy. Although it requires rigorous organization and communication, the richness of this project is reflected for me in the complementarity of the newly formed team, motivated to work together and to act for the success of this project. I would like to thank the team members I collaborated with: Denis Uzio, Julien Bernard, Renaud Bouchet, and Didier Devaux, who enabled me to successfully carry this scientific adventure through their respective help and the trust they placed in me:

- Denis, I thank you for your daily presence, unwavering availability, and the transmission of your expertise in the field of heterogeneous catalysis by sulfides, specifically concerning MoS<sub>2</sub> from all angles. It was a leap into a new universe for me, of which you are passionate, resulting in a concentrated motivation and a genuine desire to understand this system. I also appreciate the time you spent reviewing and adding the beautiful yellow highlights to my document, even when you were off sick. This truly reflects your dedication to this thesis

- Julien, I want to express my gratitude for your kindness, optimism, and smile, indicating that the door was never closed despite your tightly scheduled agenda. You always had the right words to help me put the complexity of the Li-S system into perspective, which often contradicted my expectations. You were also able to mirror the project in the broader battery field. Your precious listening skills, even in the most difficult moments, have helped me succeed. This is an invaluable human quality that must be preserved.

- Renaud, it was a real pleasure collaborating with you: your vision and expertise in the field of batteries seem boundless. Your passion for electrochemical systems is contagious. It seemed that results held no secrets for you. Your pedagogy, wisdom, and desire to develop your students, encouraging them to question endlessly and build a rigorous scientific approach, are great qualities. Although our exchanges were mainly remote (and not around a "kf"), after my brief in-person visits to LEPMI, the working like did not fade. I learned a great deal from this collaboration, lessons that I hope to carry with me throughout my professional career.

- Didier, you supported me during various writing projects, providing precious advice, attentive, rigorous and rapid reviews even though the written projects multiplied (CSI, mid-thesis reports, conference abstracts, PhD manuscript), allowing me to bounce back and improve. A true Swiss Army knife, you ensured continuous communication with my office in Solaize, as if I had never left LEPMI. This was of great help to me.

From this collaboration, I will mainly remember that "a result is a result" and it is necessary to know how to keep a factual look at the responses of a complex multi-scale and multi-phase system to an experiment without taking to heart a result that seems initially negative always taking a step back to carry out an objective analysis. A big thank you to all four of you for your wise advice and motivation over the past three years.

This thesis work was therefore part of an environment conducive to scientific, human and introspective learning. During my collaboration between IFPEN and LEPMI, I met extremely competent, caring and smiling people. I would like to thank the departments R066 (including Denis B, Jean-Loulou, Marie-Paule, Marie-Claude, Julie, Candice, Pierre-Louis, Mathieu D), R064 (including Mélody « queen of KB », Elodie, Romain, Arnold, Cyril, Alain), R05 (including the girls of microscopy and Virgile, Saloua & Christèle, Denis R, Sébastien S, Mickael R and David G), Grégory for repairing the sulfidation cells, Noémie Caillol from Axel-One as well as the MIEL team whose (Fil, Mohamed, Ernest, Thomas, Justine, Tanguy, Toc, Sajad and James). I would like to express special thanks to the entire R173 department, which welcomed me with open arms, with a special mention for Romain for the translation of D.I.Y. and for accepting « my madness », Emma for Condrieu's cultural calendar, Philou for the culinary acceptance, Joseph for being Joseph, Laurie for the snap clip, Thierry for the discussions on economic recession, the Clacyclo team who allowed me to go go even further (by bike), Lolo and his advice on materials (for tents), Quentin M the embodied concentration, Quentin C for feeding me with Beaufort cheese, Niki for the brewing discussions, Rémy without whom there would have been no electrochemical results processing nor even viewing of the remaining 1/3 of the defense PowerPoint, Houssam our LBC purchasing expert..., David teammate during the IBA, Christophe P for guaranteeing me an office within R173, even in times of crisis.

Outside of the professional context, there are of course you, family and friends, who have always supported me in my choices and have helped me laugh very frequently. You are my source of inspiration and growing happiness. This success is also yours. Thank you for stopping by to listen to my fascinating work. To my long-time friends (including Julien L who stayed in Picardy, Aurélien D who moved to Besançon, Robin F and his family, Nono), to my Australian friends (including Fred, thanks mate for your jerky beef support), to my Parisian friends (including Julie C for the pies, Bruno Pelat for the reading recommendations for the next thirty years, Vincent F for the deer rutting), to the people of Bordeaux (including Céline my sunshine, Hadri, Pierro & Hélène and the goats, Yoann, Kévin, MaO, Julien D for the weekend in the Dordogne and Alexandre Guillot for his sarcasm), to Chuzelle's roommate (including Ben and Toto), Patricia & Walter my Italian guardian angels, to the Grenoble residents (Raph & Camille, Nathalie, Vincent M best AMM and promoter of soft mobility - long live the crappy hitchhiking - Robin A for the post-hike stove welcome and the alpine equipment, Michel's Teams for the self-improvement and night hikes), to my meetings under the surgeon's knife to get a functional wrist: Béa & Xavier, to the JDN team (including Julien and Luigi), to the oenology club of Serezin-de-Rhône, to Toto Sanchez, Baptiste R (known as the great), Clément for the psychological support, digital support, and so on. Thank you to the caving club for these extraordinary discoveries of the karst environment that make me rethink my vocation (including David my favorite « prez », Damien dopamine concentrate, Xavier for your self control, the cavities equipments and the pastries). Thanks to Romain M, once again, for the musical accompaniment, the post-dance meals, the bivouac in the heart of an oak grove, the mapping of the AURA bathing areas and the rest. Thank you to Baptiste Bobo, my adopted little brother, packed with laughs, who has remained present during these three years, thank you for introducing me to dub, psytrance, space techno, thank you for the bivouacs on or underground, for the flight in the air, for your support until the end. Thank you to the Pyrenees mountains and

the Northern Alps mountains for allowing me to travel, to gain height by reconnecting with the essentials.

My thoughts are also with my family (including Domi for the treks and trips to the sea, Bernard for the battery articles cut out of the Courrier Picard, Eric & Françoise for the PhD farewell, the Balay family, Matt, Mél & Liam). I can only conclude this list with you, my fan club: Christophe, almost paternal support since primary school, you are really one of the person who contributed in my academic success since you were already present from CM1 to teach me rigor and correct my grammar, which was very useful for this scientific career. MP (Mummy), I do not have the appropriate words to express my gratitude to you, from the bottom of my heart thank you for the education provided, your support during these ten years of study, the proofreading year after year. Lucky you ....the PhD manuscript was written in English this time.

Knowledge takes time, you must take the time to take time.

With smile,

Célestine Desoeurbrun, at Grenoble, 09/02/2024.

*« C'est pas demain la veille qu'on fera marche arrière.  
On a même commencé à polluer les déserts » - Mickey 3D*

## Remerciements

C'est avec beaucoup d'émotions que j'ai rédigé ces quelques lignes afin de remercier les personnes ayant contribué, à mes côtés, à la réussite de ce beau projet. Ces remerciements s'adressent également aux personnes qui m'ont aidée, au fil des années, à affiner mes études, mon projet de thèse, mes projets professionnels et à grandir. Comme si le manuscrit de thèse n'était déjà pas une synthèse assez difficile... je me rends compte que ces remerciements le sont tout autant, avec l'appréhension d'oublier, à l'écrit, des membres clés, membres qui colorent pourtant mon parcours et l'ADN de ma pensée. Aux personnes que j'aurais oublié de mentionner, je vous prie de m'en excuser par avance. Vous vous retrouverez certainement dans mes mémoires, éditées aux éditions « La grande traversée » en 2195, dans notre monde toujours plus orchestré. Être synthétique, c'est ce qui est demandé à un chercheur ? Je vous laisse apprécier ma maîtrise de l'exercice.

Je commence, tout d'abord, par remercier les membres du jury, qui a répondu positivement à l'évaluation de mon travail de recherche, dans un ordre particulier dont la subtilité sera exprimée plus tard dans ce propos. Je remercie premièrement Claude Guéry du LRCS et Philippe Barbox de l'IRCP qui ont pris le temps de rapporter mes travaux, qui ont su en souligner les points clés et m'orienter sur certains points d'amélioration du propos. Mes remerciements sont également adressés à Christian Jordy, ingénieur de l'équipe Prospective de la SAFT et à Jean-Claude Leprêtre, membre de l'UGA et président du jury. La soutenance de thèse a été, pour moi, un réel moment de plaisir, un moment d'échanges scientifiques riche et constructif reflétant l'engouement de chacun pour la connaissance et la compréhension des systèmes complexes tant du point de vue académique qu'industriel. Cette soutenance fut également pour moi l'opportunité de rassembler les acteurs m'ayant permis, formation après formation, de la licence de chimie de l'UPJV, en passant par l'école d'ingénieur Chimie Paris Tech, les stages de terrain, jusqu'à la formation de l'école doctorale de l'UGA, de réaliser mon parcours d'études supérieures avec une grande satisfaction. J'y ai toujours rencontré des personnes motivées, sachant transmettre leurs connaissances, leur passion et m'ayant ainsi procuré l'envie de constamment apprendre à toutes les échelles, et avec le sourire. Je tiens à souligner d'un accent particulier la formation de chimie de l'UPJV, qui a été la première marche de mes études supérieures. C'est durant ces trois années de licence que je me suis prise de passion pour les matériaux et leurs applications, avec une appétence pour la chimie du solide, qui a été rendue agréablement ludique et l'électrochimie qui a été enseignée avec une grande rigueur, enseignement qui ne fait pourtant pas rêver tout le monde. A partir de ce solide bagage universitaire transmis, mes études ont été un réel bonheur d'apprentissage, sur lequel j'insiste car il n'est rien de plus important que de faire quelque chose qui fait sens pour soi, que l'on fait avec joie.

D'une manière plus générale, car le nombre de membres du jury de thèse était limité, je remercie chronologiquement tous les corps enseignants des formations suivies, la confiance des équipes et des structures dans lesquelles j'ai effectué mes six stages de la France aux Pays-Bas, les membres du CSI (Mathieu Morcrette et Lorenzo Stievano), sans qui je ne serais pas arrivée jusqu'au choix de la thèse et sa réalisation. L'idée de la thèse a germé en moi en fin de dernière année de licence (merci à Thibaut Chartrel et Franck Dolhem) et s'est confirmée au cours de mes études. C'est ainsi que j'ai choisi, avec soin, mon sujet de thèse sur la thématique Li-Soufre.

Pour replacer la thèse dans son contexte, elle s'est inscrite dans le cadre d'une nouvelle collaboration pluripartites (5 membres actifs) et bi-localisée (de Lyon à Grenoble), toujours plus loin d'Amiens et de ma Picardie d'origine. Bien que demandant une organisation et une communication rigoureuses, la richesse de ce projet se reflète pour moi dans la complémentarité de l'équipe nouvellement formée, motivée à « faire ensemble » et à acter pour la réussite de cette entreprise. Je tiens donc à remercier les membres de l'équipe avec qui j'ai travaillé et collaboré : Denis Uzio, Julien Bernard, Renaud Bouchet et Didier Devaux qui m'ont permis, de par leurs aides respectives et la confiance qu'ils m'ont accordée, de réaliser avec succès cette aventure scientifique :

- Denis, je te remercie pour ta présence au jour le jour, ta disponibilité sans faille, la transmission de ton expertise concernant le domaine de la catalyse hétérogène par les sulfures et plus spécifiquement celle concernant le MoS<sub>2</sub> sous tous ses angles. Cela a été pour moi un saut dans un nouvel univers, dont tu es passionné, ce qui aura eu pour conséquence le développement d'un concentré de motivation, d'une réelle volonté de compréhension de ce système. Je te remercie également pour le temps passé aux relectures et aux belles couleurs jaunes égaillant mon document, même lorsque tu étais en congé. Cela traduit réellement ton implication dans cette thèse.

- Julien, je tiens à te faire part de ma gratitude pour ta gentillesse, ton optimisme et ton sourire qui indiquaient que la porte n'était jamais fermée malgré ton emploi du temps millimétré. Tu as toujours eu les mots pour m'aider à relativiser la complexité de ce système Li-S, qui répondait très souvent à l'encontre de ce que j'espérais de lui. Tu as également su mettre en miroir le projet dans la thématique batterie au sens plus large. Tu as toujours fait preuve d'une écoute précieuse même dans les moments les plus difficiles, me permettant de tenir le cap jusqu'à la fin de mes travaux. C'est une qualité humaine inestimable qu'il faut préserver.

- Renaud, ce fut un réel plaisir de collaborer avec toi : ta vision, ton expertise du domaine des batteries me semble incommensurable. Ta passion pour les systèmes électrochimiques est contagieuse. Il semblait que les résultats n'avaient pas de secret pour toi. Ta pédagogie, ta sagesse, ton souhait de faire évoluer tes étudiants, qu'ils se questionnent inlassablement et construisent une démarche scientifique rigoureuse, sont de grandes qualités. Bien que les échanges furent principalement à distance (et pas autour d'un « kf »), après mes courts passages en présentiel au LEPMI, le lien ne s'est pas pour autant estompé. J'ai énormément appris de cette collaboration, enseignement que je souhaite emporter avec moi au cours de ma future carrière professionnelle.

- Didier, tu as su m'épauler durant mes différents projets de rédaction, m'accompagner de tes conseils précieux, de tes relectures attentives, rigoureuses et toujours rapides, bien que les projets écrits se soient multipliés (CSI, rapports de mi-thèse, abstracts pour les conférences, manuscrit de thèse), afin que je puisse rebondir et m'améliorer. Véritable couteau-suisse, tu as su, comme si je n'avais pas quitté le LEPMI, assurer la continuité de la liaison jusqu'à mon bureau de Solaize. Cela m'a été d'une grande aide.

De cette collaboration, je retiendrai principalement « qu'un résultat est un résultat » et qu'il faut savoir garder un regard factuel sur les réponses à une sollicitation d'un système complexe multi-échelles et multiphasiques, sans prendre à cœur un résultat paraissant négatif de prime abord. Il faut toujours prendre de la hauteur pour effectuer une analyse objective.

Un très grand merci à vous quatre pour vos conseils avisés et votre soutien au cours de ces trois années.

Ce travail de thèse s'est donc inscrit dans un environnement propice à l'apprentissage sur les plans scientifique, humain et introspectif. Lors de ma collaboration entre IFPEN et LEPMI, j'ai rencontré des personnes extrêmement compétentes, bienveillantes, souriantes. Je remercie les départements R066 (dont Denis B, Jean-Loulou, Marie-Paule, Marie-Claude, Julie, Candice, Pierre-Louis, Mathieu D), R064 (dont Mélody reine du KB, Elodie, Romain, Arnold, Cyril, Alain), R05 (dont les filles de la microscopie et Virgile, Saloua & Christèle, Denis R, Sébastien S, Mickael R et David G), Grégory pour la réparation des cellules de soufre, Noémie Caillol de chez Axel-One ainsi que l'équipe MIEL dont (Fil, Mohamed, Ernest, Thomas, Justine, Tanguy, Toc, Sajad et James).

Je remercie plus particulièrement l'entièreté du département R173 qui m'a accueillie de force ou de gré, avec une mention spéciale à l'attention de Romain pour la traduction de D.I.Y et pour avoir accepté « ma folie », Emma pour le calendrier culturel de Condrieu, Philou pour l'acceptation culinaire, Joseph pour Joseph, Laurie pour la pince à bouton-pression, Thierry pour les discussions sur la décroissance, l'équipe de la Clacyclo qui m'a permis d'aller toujours plus loin (à vélo), Lolo et ses conseils matériaux (de tente), Quentin M la concentration incarnée, Quentin C pour m'avoir nourrie au beaufort, Niki pour les discussions brassage, Rémy sans qui il n'y aurait pas eu de traitement des résultats électrochimiques, ni même de projection du tiers restant du powerpoint de soutenance, Houssam notre expert achat LBC..., David co-équipier de l'IBA, Christophe P pour m'avoir garanti un bureau au sein de R173, même en période de crise.

Hors du cadre professionnel, il y a bien sûr vous, famille et amis, vous qui m'avez toujours soutenue dans mes choix et qui m'avez aidée à rire très fréquemment. Vous êtes ma source d'inspiration et d'énergie croissante. Cette réussite est aussi la vôtre. Merci d'avoir fait le déplacement pour écouter mes travaux passionnants. A mes amis de longues dates (dont Julien L resté en Picardie, Aurélien D expatrié à Besançon, Robin F & sa famille, Nono), à mes rencontres australiennes (dont Fred, thanks, mate, for your jerky beef support), à mes rencontres parisiennes (dont Julie C pour les tartes, Bruno Pelat pour les conseils lectures pour les trente années à venir, Vincent F pour le brame du cerf), aux Bordelais (dont Céline mon rayon de soleil permanent, Hadri, Pierro & Hélène et les chèvres, Yoann, Kévin, MaO, Julien D pour le week-end en Dordogne et Alexandre Guillot pour son sarcasme), à la coloc de Chuzelle (dont Ben et Toto), Patricia & Walter mes anges gardiens italiens, aux Grenoblois (Raph & Camille, Nathalie, Vincent M, the best AMM, et promoteur de la mobilité douce - vive les stops foireux - Robin A pour l'accueil poêle post-rando et le matos d'alpi, la Michel's Teams pour le dépassement de soi et les randos nocturnes), à mes rencontres sur le billard pour l'obtention d'un nouveau poignet bionique : Béa & Xavier, à l'équipe de la JDN (dont Julien et Luigi), au club œnologie de Sérézin de Rhône, à Toto Sanchez, Baptiste R (dit le grand), Clément pour le soutien psychologique, soutien numérique, j'en passe et des meilleurs. Merci au club spéléo pour ces extraordinaires découvertes du milieu karstique qui me font repenser ma vocation (dont David mon « prez » préféré, Damien concentré de dopamine, Xavier pour ton self control, l'équipement des cavités et les viennoiseries). Merci à Romain M, de nouveau, pour l'accompagnement musical, les repas post-danse, le bivouac au cœur d'une chênaie, la cartographie des zones de baignade AURA et le reste. Merci à Baptiste Bobo, mon petit frère d'adoption, boule d'énergie positive qui a su rester présent durant ces trois années, merci pour la conversion à la dub, psytrance, techno spatiale, merci pour les bivouacs sur ou sous terre, pour l'envol dans les airs, pour ton soutien jusqu'à la fin. Merci au Massif des Pyrénées et au Massif des Alpes du Nord de m'avoir fait voyager, permis de prendre de la hauteur en me reconnectant à l'essentiel.

Mes pensées se dirigent aussi vers ma famille (dont Domi pour les treks et les virées à la mer, à Bernard pour les articles batteries découpés dans le Courrier Picard, à Eric & Françoise pour

le pot de thèse, à la famille Balay, à Matt, Mél & Liam).

Je ne peux que terminer cette liste par vous, mon fan club : Christophe, soutien quasi paternel depuis l'école primaire, tu es vraiment l'une des personnes qui a participé à ma réussite scolaire puisque tu étais déjà présent dès le CM1 à m'enseigner la rigueur et à corriger ma grammaire, ce qui me fut bien utile pour ce parcours scientifique. MP (Maman), je n'ai pas de mot pour t'adresser ma reconnaissance. Du fond du cœur, merci pour l'éducation fournie, pour la manière dont tu m'as épaulée durant ces dix années d'études, pour les relectures années après années. Heureusement pour toi que le manuscrit de thèse était en anglais cette fois.

La connaissance prend du temps, il faut prendre le temps de prendre du temps.

Avec le sourire,

Célestine Desoeurbrun, à Grenoble, le 09/02/2024.

*« D.I.Y, till the day I die (x2), I keep my style, my style low-fi on your high-fi » - Biga Ranx*

## Table of contents

<b>CONTEXT OF THE STUDY</b> .....	<b>1</b>
<b>ENERGY SCENE IN 2023</b> .....	<b>1</b>
<b>I. CHAPTER I - STATE-OF-THE-ART</b> .....	<b>7</b>
<b>1.1 INTRODUCTION TO LITHIUM-SULFUR BATTERIES</b> .....	<b>7</b>
1.1.1 PRINCIPLE AND MECHANISM.....	7
1.1.2 LI-S MAJOR DRAWBACKS TO OVERCOME.....	12
<b>1.2 ROUTES TO TRAP POLYSULFIDES</b> .....	<b>15</b>
1.2.1 FUNDAMENTAL APPROACHES .....	15
1.2.2 DESCRIPTION OF THE STRATEGIES FROM LITERATURE .....	16
<b>1.3 MoS<sub>2</sub> AND CARBON LITERATURE STUDY</b> .....	<b>22</b>
1.3.1 MOLYBDENUM DISULFIDE .....	22
1.3.2 CARBON SUPPORT.....	30
<b>1.4 THE PROJECT RESEARCH STRATEGY</b> .....	<b>32</b>
<b>1.5 CONCLUSION AND OBJECTIVES</b> .....	<b>36</b>
<b>II. CHAPTER II – SYNTHESIS AND CHARACTERIZATION OF MoS<sub>2</sub>-KB</b> .....	<b>39</b>
<b>1.1 INTRODUCTION</b> .....	<b>39</b>
<b>1.2 CHARACTERIZATION OF KETJENBLACK SUPPORT</b> .....	<b>40</b>
<b>1.3 SYNTHESIS AND CHARACTERIZATION OF MoS<sub>2</sub>-KB HOST STRUCTURES</b> .....	<b>46</b>
1.3.1 VARIATION OF MoS <sub>2</sub> LOADING ON MoS <sub>2</sub> -KB .....	47
1.3.2 VARIATION OF SULFIDATION CONDITIONS ON MoS <sub>2</sub> -KB.....	62
<b>1.4 CONCLUSION</b> .....	<b>74</b>



<b>III. CHAPTER III – STUDY OF THE MOS<sub>2</sub>-KB STRUCTURE/POLYSULFIDES ADSORPTION RELATIONSHIP BY UV-VISIBLE WITH AN <i>IN SITU</i> PROBE SETUP .....</b>	<b>77</b>
<b>1.1 INTRODUCTION .....</b>	<b>77</b>
<b>1.2 STUDY OF THE Li<sub>2</sub>S<sub>6</sub> EQUIVALENT SOLUTION .....</b>	<b>78</b>
1.2.1 EXPERIMENTAL PROTOCOL USED TO PREPARE S <sub>8</sub> , Li <sub>2</sub> S AND Li <sub>2</sub> S <sub>6</sub> SOLUTIONS .....	78
1.2.2 UV-VIS PROTOCOL : COMPARISON OF CLASSICAL <i>EX SITU</i> QUARTZ CUVETTE VS <i>IN SITU</i> OPTICAL FIBER SETUP .....	81
1.2.3 DATA ANALYSIS, SPECTRAL DECOMPOSITION .....	88
1.2.4 QUANTITATIVE ANALYSIS OF S <sub>8</sub> AND Li <sub>2</sub> S <sub>6</sub> SOLUTIONS .....	92
<b>1.3 STUDY OF THE ADSORPTION .....</b>	<b>99</b>
1.3.1 EXPERIMENTAL PROTOCOL .....	99
1.3.2 DISCUSSION .....	105
<b>1.4 CONCLUSION .....</b>	<b>121</b>
<b>IV. CHAPTER IV – ELECTROCHEMICAL PERFORMANCES OF S-MOS<sub>2</sub>-KB COMPOSITE ACTIVE MATERIAL AS POSITIVE ELECTRODE.....</b>	<b>125</b>
<b>1.1 INTRODUCTION .....</b>	<b>125</b>
<b>1.2 SYNTHESIS AND CHARACTERIZATION OF S- MOS<sub>2</sub>-KB COMPOSITE MATERIAL.....</b>	<b>126</b>
<b>1.3 ELECTRODE FORMULATION AND COIN-CELL MAKING .....</b>	<b>131</b>
1.3.1 OPTIMIZATION OF THE FORMULATION .....	132
1.3.2 OPTIMIZATION OF THE COATING AND DRYING STEP .....	134
1.3.3 OPTIMIZED PROTOCOL FOR ELECTRODE MAKING .....	136
1.3.4 COIN CELL ASSEMBLY .....	137
1.3.5 CALCULATION OF PERCENTAGE OF Li <sub>2</sub> S <sub>6</sub> AND Li <sub>2</sub> S <sub>4</sub> TRAPPED IN THE EXPERIMENTAL CONDITIONS CONSIDERING THE ADSORPTION CAPACITIES .....	138
1.3.6 CHOICE OF THE E/S RATIO .....	141
<b>1.4 ELECTROCHEMICAL PERFORMANCES.....</b>	<b>144</b>
1.4.1 GALVANOSTATIC CURVE TREATMENT METHODOLOGY .....	144
1.4.2 REPEATABILITY TESTS .....	146
1.4.3 ELECTROCHEMICAL RESULTS .....	149
1.4.4 DISCUSSION WITH LITERATURE DATA .....	154
<b>1.5 CONCLUSION .....</b>	<b>156</b>

<b>V.</b>	<b>GENERAL CONCLUSION .....</b>	<b>159</b>
<b>VI.</b>	<b>REFERENCES .....</b>	<b>165</b>
<b>VII.</b>	<b>APPENDICES–.....</b>	<b>177</b>
	<b>APPENDIX A - COMPARISON BETWEEN DIFFERENT MOS<sub>2</sub> POLYTYPES .....</b>	<b>179</b>
	<b>APPENDIX B - EXPERIMENTAL PART .....</b>	<b>181</b>
<b>1.1</b>	<b>MATERIAL CHARACTERIZATION .....</b>	<b>181</b>
1.1.1	ELEMENTAL ANALYSIS .....	181
1.1.2	MORPHOLOGY ANALYSIS.....	182
1.1.3	TEXTURAL ANALYSIS .....	184
1.1.4	LASER DIFFRACTION GRANULOMETRY .....	185
1.1.5	HELIUM PYCNOMETRY.....	185
1.1.6	SPECTROSCOPIC ANALYSIS .....	185
1.1.7	CONDUCTIVITY.....	187
<b>1.2</b>	<b>SYNTHESIS OF UNSUPPORTED MOS<sub>2</sub>.....</b>	<b>188</b>
	<b>APPENDIX C – UV-VIS.....</b>	<b>191</b>
	<b>APPENDIX D – CALCULATION INSTRUCTIONS.....</b>	<b>193</b>
	<b>APPENDIX E - FIGURES CAPTIONS.....</b>	<b>195</b>
	<b>APPENDIX F - TABLES CAPTIONS.....</b>	<b>199</b>
	<b>ABSTRACT .....</b>	<b>201</b>



## Tables of abbreviations

Abbreviations	Meaning
BET	Brunauer-Emmett-Teller
BF	Bright field
BSE	Backscattered electron
CAM	Composite active material
CB	Carbon black
CE	Coulombic efficiency
CHNS	Carbon, Hydrogen, Nitrogen, and Sulfur
CMC	Carboxymethylcellulose
CNF	Carbon Nano Fiber
CNT	Carbon Nanotube
CUS	Coordinated Unsaturated Site
CV	Cyclic voltammetry
DFT	Density Functional Theory
DME	1,3-dioxolane
DOL	1,2-dimethoxyethane
EC	Ethylene Carbonate
EDS	Energy-Dispersive Spectroscopy
EDX	Energy-Dispersive X-ray Spectroscopy
EIS	Electrochemical Impedance Spectroscopy
EPR	Electron Paramagnetic Resonance
ESCA	Electron Spectroscopy for Chemical Analysis
ESR	Electron Spin Resonance
EV	Electric Vehicle
HAADF	High-Angle Annular Dark Field
HDS	Hydrodesulfurization
HER	Hydrogen Evolution Reaction
HF	High Frequency
HPLC	High-Performance Liquid Chromatography
HPLS	High-Power Laser System
HR	High Resolution
IFPEN	Institut français du pétrole et des énergies nouvelles
IR	Infrared
IUPAC	International Union of Pure and Applied Chemistry
IWI	Incipient wet impregnation
JEM	Japan Electron Microscope
JEOL	Japan Electron Optics Laboratory
KB	Ketjenblack
LA	Longitudinal acoustic
LF	Low frequency
LFMP	Lithium manganese iron phosphate
Li	Lithium
LiPS	Lithium polysulfides

Li-S	Lithium sulfur
LiTFSI	Lithium Bis(trifluoromethanesulfonyl)imide
LiNO <sub>3</sub>	Lithium nitrate
LMNO	Lithium Manganese Nickel Oxide
LMR-NCM	Lithium –Manganese Rich
MF	Medium Frequency
Mo	Molybdenum
MoS <sub>2</sub> -KB	Supported MoS <sub>2</sub> on Ketjenblack
MSI	Metal Support Interaction
NCA	Nickel Cobalt Aluminum
NCMA	Nickel Cobalt Manganese Aluminum
NIR	Near-Infrared
NMC	Nickel Manganese Cobalt
NMP	N-Methyl-2-pyrrolidone
NMR	Nuclear Magnetic Resonance
OCV	Open Circuit Voltage
OER	Oxygen Evolution Reaction
PCA	Principal Component Analysis
PEDOT	Poly(3,4-ethylenedioxythiophene)
PEIS	Potentiostatic Electrochemical Impedance Spectroscopy
PMA	Phosphomolybdic acid
PP	Polypropylene
PSS	Polystyrene Sulfonate
PVDF	Polyvinylidene Difluoride
RAMAN	Raman Spectroscopy
SBR	Styrene-Butadiene Rubber
SE	Secondary electron
SEI	Solid Electrolyte Interphase
SEM	Scanning Electron Microscope
SHE	Standard Hydrogen Electrode
STEM	Scanning Transmission Electron Microscopy
TEGDME	Tetraethylene Glycol Dimethyl Ether
TEM	Transmission Electron Microscopy
TGA	Thermogravimetric Analysis
TMS	Transition metal sulfide
TPR	Temperature-Programmed Reduction
UV	UV-Visible
XANES	X-ray Absorption Near-Edge Structure
XAS	X-ray Absorption Spectroscopy
XDR	X-ray Diffraction
XPS	X-ray Photoelectron Spectroscopy
XRD	X-ray Diffraction
XRF	X-ray Fluorescence

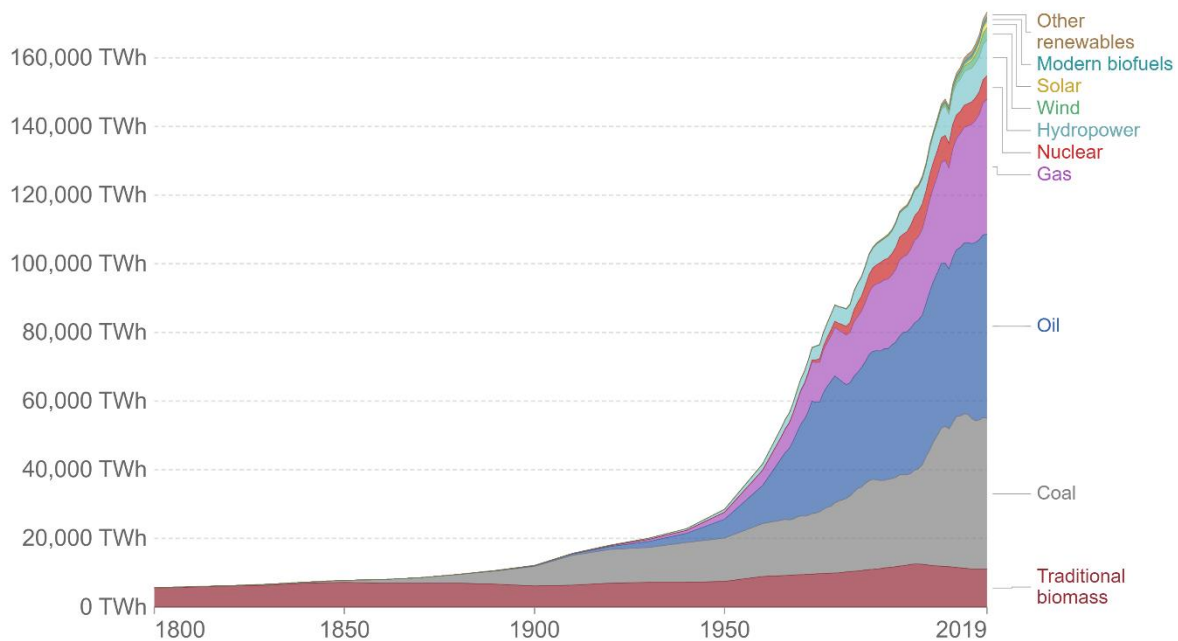




## Context of the study

### Energy scene in 2023

Global population was 1.6 billion in 1900, 2.5 billion fifty years later, and more than 7 billion human beings today. Due to demographic and economic growth, the energy demand is increasing continuously. **Figure 0-1** shows the global primary energy consumption from 1800 to 2019. Today coal, oil and gas are the dominant resources in the global energetic mix. So far, they give the highest energy density with practical values typically higher than  $1 \text{ kWh.kg}^{-1}$  while batteries fall well below. However, the stocks of these not-renewable energies are dramatically decreasing over the years and a switch to renewable one is now mandatory to meet the COP21 objectives. In 2019, modern renewables (wind, solar, biomass, hydropower and geothermal power represented 11.2% of total primary energy consumption <sup>1</sup>. These changes are not significant in the global energy mix, but renewable energy use tend to increase with growing concerns about climatic changes. Our energetic supply will definitely face several challenges in the coming decades. For instance, wind power, solar photovoltaic system deployment lead to a growing production of intermittent low carbon electricity. This electricity must be stored in real time when it is not directly used. Energy storage and conversion are two means to ensure intermittent energy electricity storage and restitution.



Source: Vaclav Smil (2017) & BP Statistical Review of World Energy

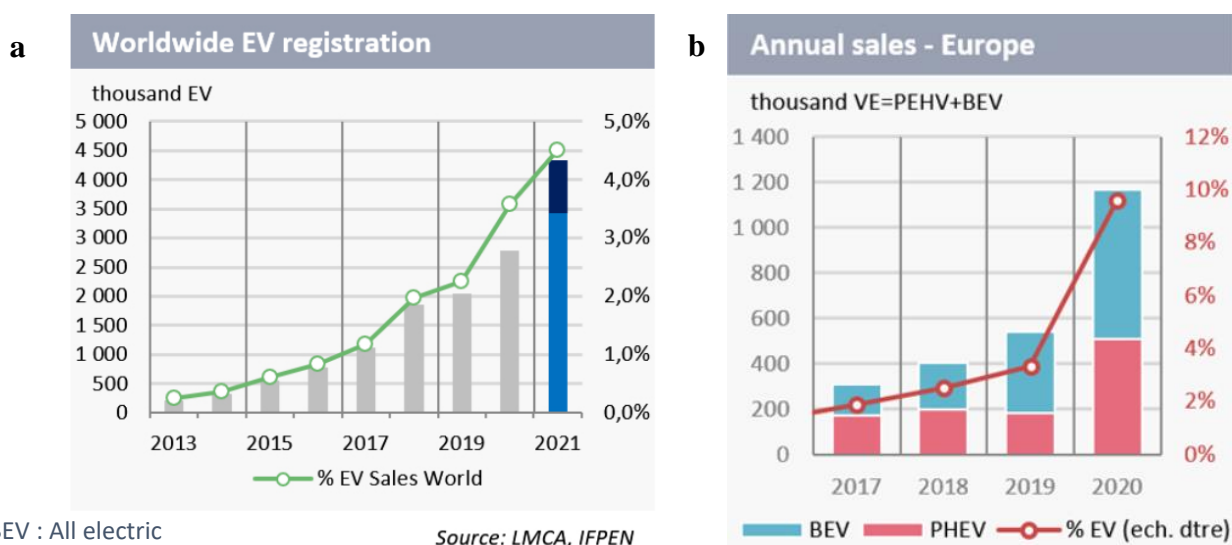
OurWorldInData.org/energy • CC BY

**Figure 0-1. Global primary energy consumption by source <sup>2</sup>.**



Based on reversible electrochemical reactions, batteries are excellent solutions to store electricity. Therefore, battery technologies can be used either for electric mobility or stationary energy storage applications. Batteries are already ubiquitous in our phones, laptops and cars. Growth in the markets for electric vehicles and stationary storage will make them even more important in the future.

In order to achieve a sustainable mobility by reducing greenhouse gas emissions, hybrid and electric vehicles have been developed. **Figure 0-2-a** describes the number of electric vehicles (EV) registration in the last decade. Worldwide, less than 500 thousand of electric vehicles have been sold in 2013. This number is increasing year by year and global electric vehicle deliveries reached 2.8 million units in 2020<sup>3</sup> which represent 3.6 % of light vehicle available. Even if this level is still low, 2020 appears to be a pivotal year for the EV market. **Figure 0-2-b** describes the remarkable increase of the annual EV sales in Europe. Despite the economic and covidcrisis, the sales doubled to reach 1.1 million vehicles. The same trend is observed worldwide. The amounts invested in 2020 in the electric vehicle sector exceeded 12 billion dollars<sup>3</sup> According to specialists, by 2040, 55% of all new car sales and 33% of the global fleet will be electric. Policies play a critical role in the EV market growth. Leading countries use a variety of measures such as fuel economy standards coupled with incentives for zero- and low-emissions vehicles, economic instruments that help to bridge the cost gap between electric and conventional vehicles and support the deployment of charging infrastructures<sup>4</sup>.



BEV : All electric  
 PHEV : Plug-in hybrids

**Figure 0-2. Global EV market growth a) worldwide b) in Europe<sup>3</sup>.**

Between 2005 and 2018, patenting activity in batteries and other electricity storage technologies grew at an average annual rate of 14% worldwide <sup>5</sup>, four times faster than the average of all technology fields. This trend highlights the great interest for battery development.

Sony commercialized the lithium-ion (Li-ion) batteries first in the early 1990s. Until now, Li-ion batteries have powered most of the electronic devices as well as electric cars due to their energy densities and durability. Several optimizations have been made to increase their practical energy density over the years. **Figure 0-3** compares the gravimetric performance of different battery technologies. With a constant energy density rise from 75 Wh.kg<sup>-1</sup> to 275 Wh.kg<sup>-1</sup>, conventional Li-ion battery chemistries (lithium cobalt oxide / graphite) are reaching the practical limits of their performances. To meet the requirements of the automotive sector, it is essential to maximize the energy density. For that, new materials have been developed:

At the positive electrode: LiNi<sub>0.6</sub>Mn<sub>0.2</sub>Co<sub>0.2</sub>O<sub>2</sub> (NMC 622), NMC 811, LiNi<sub>0.84</sub>Co<sub>0.12</sub>Al<sub>0.04</sub>O<sub>2</sub> (NCA) and LiNi<sub>0.89</sub>Co<sub>0.05</sub>Mn<sub>0.05</sub>Al<sub>0.01</sub>O<sub>2</sub> (NCMA)

At the negative electrode: silicium/carbon composite

It is expected that by 2035, Li<sub>1.2</sub>Mn<sub>0.55</sub>Ni<sub>0.15</sub>Co<sub>0.1</sub>O<sub>2</sub> (LMR-NMC), LiMn<sub>1.5</sub>Ni<sub>0.5</sub>O<sub>4</sub> (LMNO) or even LiFe<sub>0.5</sub>Mn<sub>0.5</sub>PO<sub>4</sub> (LFMP) positive electrode without nickel will be used. This will lead to a slight rise of energy density and a reduction of battery costs.

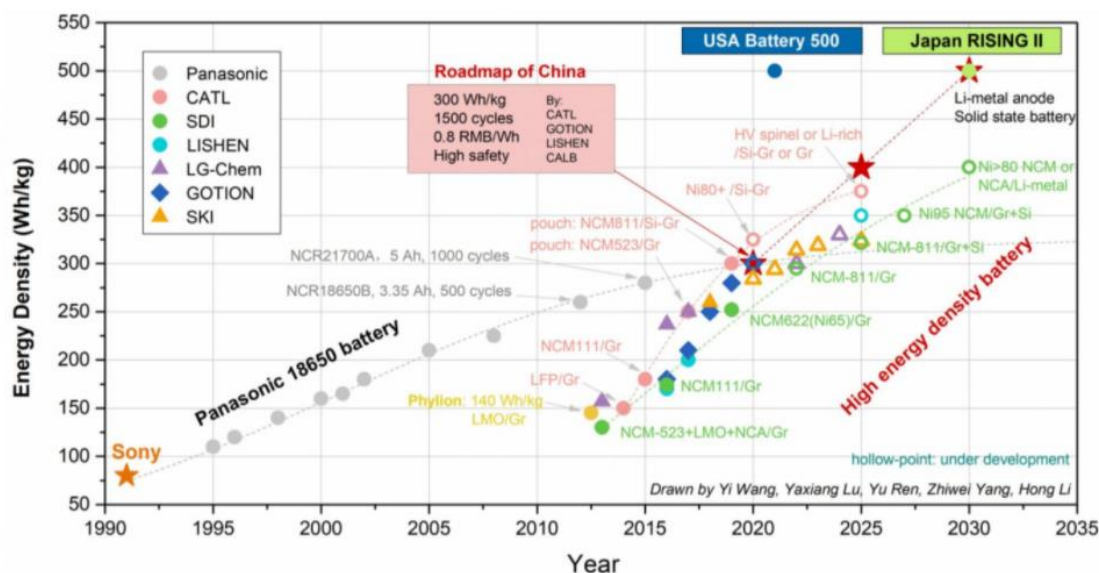


**Figure 0-3.** Comparison of the gravimetric performance of different battery technologies for automotive applications and performances expected up to 2035. <sup>6</sup>

In spite of the progress made over the past decades, the limited Li-ion capacity hinders the fast deployment of this technology. An increase in energy density from present-day values to the target of  $400 \text{ Wh.kg}^{-1}$  for 2030 <sup>6</sup>, requires exploration of new materials and chemistry. To answer this challenge, new generation of battery technologies are foreseen. **Figure 0-4** shows next battery candidates. Among those, lithium-sulfur (Li-S) is attracting an increasing attention.

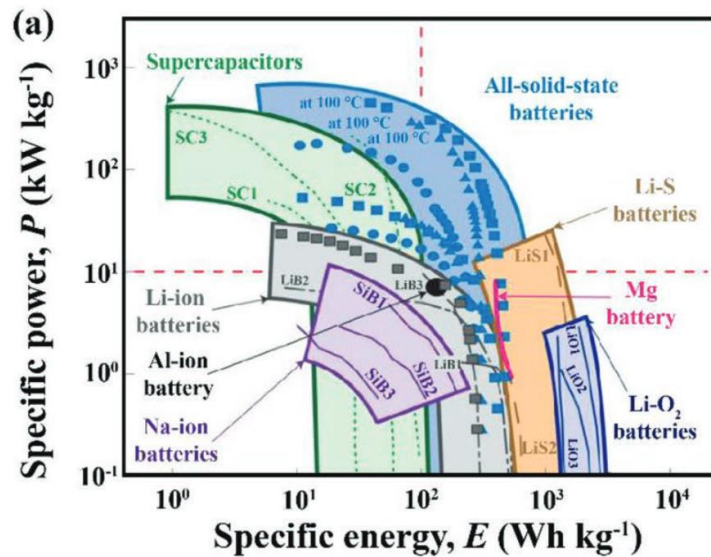


**Figure 0-4.** Ragone plot for different types of electrochemical energy storage devices<sup>7</sup>.





## Chapter I - State-of-the-art

### 1.1 Introduction to lithium-sulfur batteries

#### 1.1.1 Principle and mechanism

Lithium-sulfur battery (Li-S) consists of the assembly of a sulfur based composite positive electrode, a porous polyolefin separator filled with an ether-based electrolyte and a Li negative electrode as depicted in **Figure I-1**. This technology differs from conventional Li-ion batteries for two main reasons: i) the source of lithium is not the positive electrode material, but the Li metal itself and ii) the cell does not operate based on Li intercalation/desintercalation process. During discharge,  $S_8$  undergoes stepwise reduction reactions toward  $Li_2S$  when reacting with  $Li^+$  from the negative electrode. The overall reaction is  $S_8 + 16 Li^+ + 16 e^- \rightarrow 8 Li_2S$ .

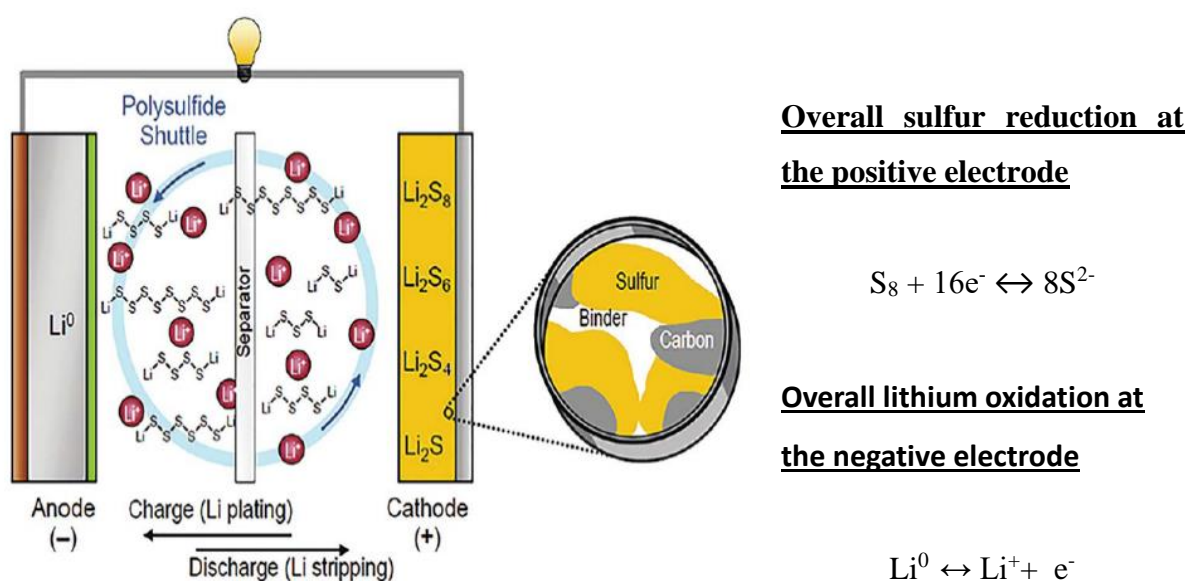


**Figure I-1. Schematic diagram of a Li-S battery.**

The cell voltage lies near 2.2 V vs.  $Li^+/Li^0$ , which is about 2/3 of the conventional Li-ion positive electrode voltage. However, this is offset by the high sulfur theoretical specific capacity of  $1675 \text{ mAh.g}^{-1}$ , leading to theoretical gravimetric and volumetric energy densities of  $2500 \text{ Wh.kg}^{-1}$  and  $2800 \text{ Wh.L}^{-1}$ , respectively. Compared to conventional Li-ion batteries, Li-S could provide 3 to 5 times higher gravimetric energy density assuming a complete reaction to  $Li_2S$  <sup>9</sup>.

Moreover, although sulfur constitutes only about 0.052 wt% of the Earth's crust, elemental sulfur is a readily available material. Its current worldwide production exceeds 70 million metric tons per year. Elemental sulfur was extracted from underground deposits by the Frasch process, but nowadays most of the available sulfur is recovered from natural gas and crude oil desulfurization<sup>10</sup>. Sulfur is therefore a by-product from the oil refinery, available at low cost, large scale and is not classified as a critical raw material (such as cobalt and nickel). Indeed, material criticality will become even more important in the nearest future since the demand for energy storage increases exponentially.

### **Sulfur reduction mechanism**

The sulfur reduction mechanism is a complex multistep (multiphasic and multielectronic) process during which soluble lithium polysulfide intermediates ( $\text{Li}_2\text{S}_x$   $8 < x < 2$ ) are produced via a redox cascade. **Polysulfides will be simplified by "LiPS" for the rest of the report.**

The typical galvanostatic discharge and cyclic voltammogram (CV) profiles are shown in **Figure I-2**. The discharge profile is composed of two plateaus and three regions:

At the beginning of region I,  $\text{S}_8$  is initially reduced to soluble  $\text{Li}_2\text{S}_8$  in a plateau at a potential higher than 2.3 V vs.  $\text{Li}^+/\text{Li}$ . Long chain  $\text{Li}_2\text{S}_8$  is then reduced to  $\text{Li}_2\text{S}_6$  and  $\text{Li}_2\text{S}_4$  short-chains between 2.3-2.1 V vs.  $\text{Li}^+/\text{Li}$ . This corresponds to the first cathodic peak at around 2.1–2.4 V vs.  $\text{Li}^+/\text{Li}$  in the CV curves.

At region II  $\text{Li}_2\text{S}_4$  is reduced to  $\text{Li}_2\text{S}_2$  or directly to  $\text{Li}_2\text{S}$  at 1.9–2.1 V vs.  $\text{Li}^+/\text{Li}$ . This corresponds to the second cathodic peak at around 2.0 V vs.  $\text{Li}^+/\text{Li}$  in the CV curves.

At region III  $\text{Li}_2\text{S}_2$  is completely reduce to  $\text{LiS}_2$ .

During charge process the short-chains LiPS are converted back to  $\text{S}_8$  with a mechanism that differ from the discharge process. Both cycling curve and CV profile exhibit an asymmetric behavior between discharge and charge profiles. The assuming electrochemical reactions of the discharge process are summarized in **Table I-1**.

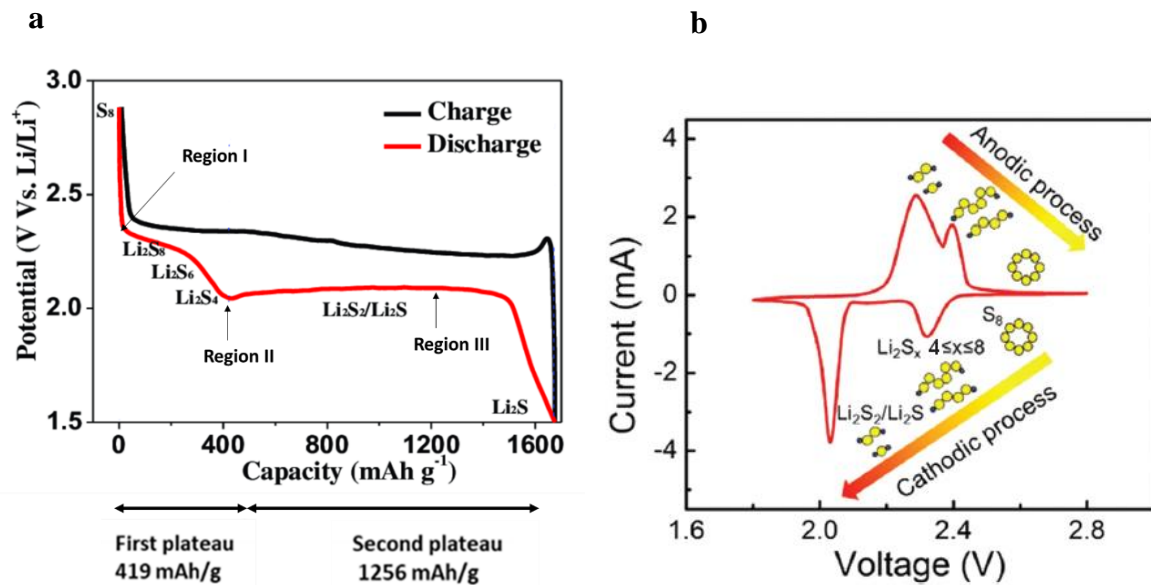
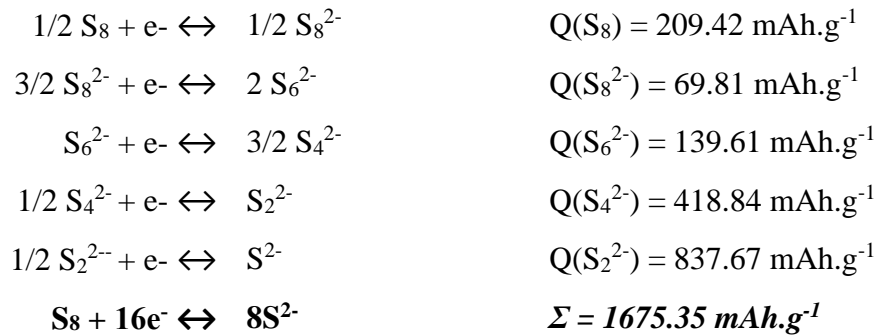


**Figure I-2.** a) Typical two-plateau cycling curve of Li-S<sup>11</sup> and the corresponding b) CV profile<sup>12</sup>.

**Table I-1.** Principal electrochemical reactions occurring at the positive electrode during discharge<sup>13</sup>.



Many polysulfide species are present in the electrolyte due to these electrochemical equilibria. Additional complexity arises because polysulfides can transform into other sulfur species spontaneously by disproportionation reactions<sup>14</sup>. **Equations I-1** to **I-3** describes the disproportionation reactions and points out the formation of additional radical anion ( $S_3^{\cdot-}$ ) which is subject of some debate concerning its stability and reactivity.





The reduction of sulfur therefore results in a succession of electrochemical and chemical equilibria in which the coexistence of various soluble polysulfides ( $\text{Li}_2\text{S}_x$ ,  $8 < x < 4$ ), low soluble ( $\text{Li}_2\text{S}_2$ )<sup>15</sup> and insoluble species ( $\text{S}_8$ ,  $\text{Li}_2\text{S}$ ) complexifies the overall mechanism. Many studies seek to shed light on this mechanism. Currently, there is no consensus on the steps of the mechanism and their kinetics due to their complexities and also because successive equilibria depend on the electrode composition, intermediate species stability, discharge/charge rate, electrolyte composition<sup>16 17</sup>, electrolyte/sulfur ratio<sup>18</sup>, temperature conditions<sup>19</sup> which hence might differ from one configuration to another.

Indeed, Zheng *et al.*<sup>20</sup> investigated the mechanism by HPLS and confirmed that in the region I (at 2.3V), long-chain  $\text{S}_8^{2-}$   $\text{S}_7^{2-}$   $\text{S}_6^{2-}$   $\text{S}_5^{2-}$  are formed. They pointed out the coexistence of almost all the polysulfides  $\text{S}_n^{2-}$  with  $4 \leq n \leq 7$  between 2.3-2.1V and an initial precipitation of  $\text{Li}_2\text{S}_2/\text{Li}_2\text{S}$  before 2.1V (region II). At the end of the discharge, traces of  $\text{S}_5^{2-}$   $\text{S}_4^{2-}$  and  $\text{S}_3^{2-}$  remained (see **Figure I-3 a and b**). No identification of  $\text{S}_3^\bullet$  have been made while Barchasz *et al.*<sup>14</sup> demonstrated their presence during the first reduction plateau due to the disproportionation of  $\text{S}_8^{2-}$  and  $\text{S}_6^{2-}$  into  $\text{S}_5^{2-}$  and  $\text{S}_3^\bullet$ , also confirmed by Wang *et al.*<sup>21</sup> and Zheng *et al.*<sup>22</sup> works. However, the electrolyte natures being different from one series of work to another, radicals can be stabilized in the TEGDME rather than in DME, explaining the specie nature differences.

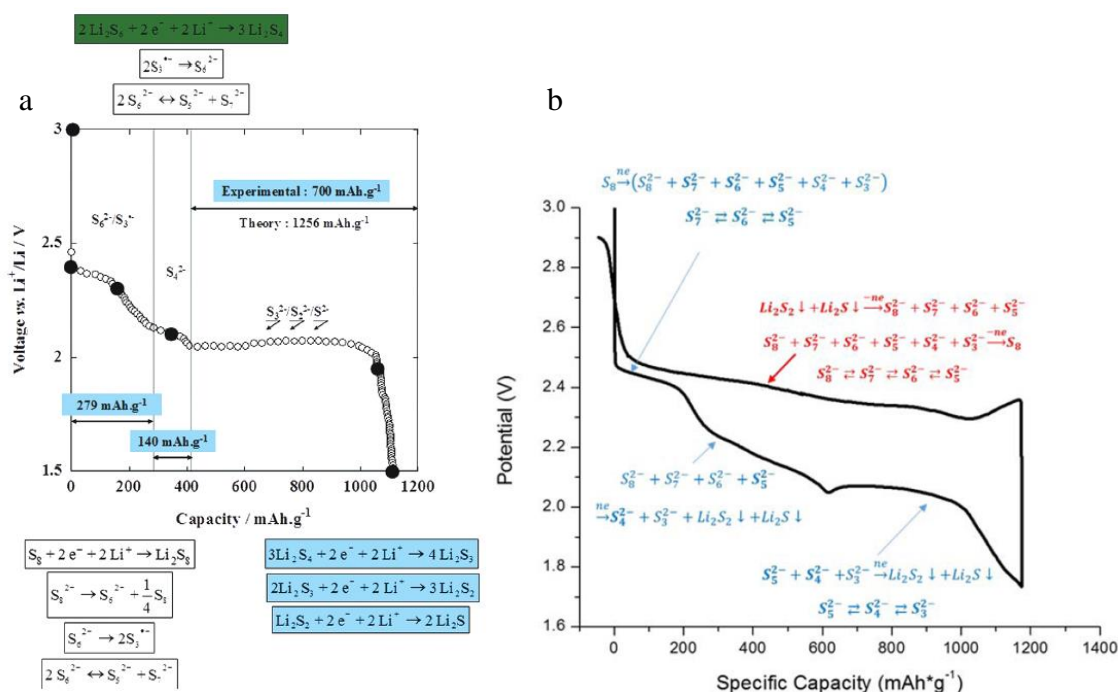


**Figure I-3. Proposition of Li-S mechanism a) discharge mechanism in TEGDME<sup>14</sup> b) discharge/charge mechanism in 0.5 M  $\text{LiClO}_4/\text{DME}$  solution<sup>20</sup>.**

Mechanisms mentioned above treat the polysulfide species as “non-lithiated”, meaning that polysulfide anions remain fully dissociated from  $\text{Li}^+$  cations and are fully solvated by the electrolyte solvent. However, Korff *et al.*<sup>18</sup> suggested the existence of another mechanism involving “lithiated” intermediates, assuming association between the  $\text{Li}^+$  and sulfur anions. Both reduction mechanism models fit the experimental discharge curves setting aside a “non-lithiated” mechanism exclusively. They even pointed out a shift on the dominant pathway during discharge, depending on the  $\text{Li}^+$  availability. In addition, Manthiram *et al.*<sup>23</sup> showed that these LiPS are not necessarily individually solvated but tends to aggregate, which impedes the electrochemical conversion kinetics of LiPS, particularly at low electrolyte/sulfur (E/S:  $\mu\text{L}/\text{mg}$ ) ratio.

In addition, the polysulfide species produced during the discharge are not motionless, they diffuse within the positive electrode and the bulk electrolyte due to their solubility. Consequently, they are not only located within the positive electrode porosity and their concentration varies overtime due to this diffusion. Sadd *et al.*<sup>24</sup> studied the kinetic mechanisms using in situ tomography and pointed out a rapid dissolution of sulfur, a rapid generation of polysulfides species at the early discharge step and an unequal LiPS diffusion kinetics between the positive electrode and the bulk electrolyte. LiPS have a diffusion coefficient of  $D_c = 9.5 \cdot 10^{-8} \text{ cm}^2 \cdot \text{s}^{-1}$  in the positive electrode and  $D_e = 7.5 \cdot 10^{-6} \text{ cm}^2 \cdot \text{s}^{-1}$  in the bulk electrolyte. This unequal diffusion is the result of higher tortuosity of the diffusion pathways and of the increased electrolyte viscosity due to higher local concentration polysulfides within the 3D positive electrode network. The LiPS dissolution within the electrolyte leads to a sharp increase in the electrolyte viscosity<sup>15</sup> which will also impede the LiPS diffusion coefficient value, decreasing it. Sadd *et al.* even demonstrated an inhomogeneous diffusion of LiPS within positive electrode thickness. At the surface of the electrode (electrode-electrolyte interface), LiPS diffuse quickly to the electrolyte while in the center of the electrode the diffusion is slowed down by longer diffusion pathway through the carbon-binder matrix.

In any case, this LiPS diffusion phenomenon has a negative impact on Li-S cycling performances. This drawback is described in **1.1.2 section**.

### 1.1.2 Li-S major drawbacks to overcome

Although Li-S batteries have many advantages, there are several critical issues hindering their commercial development. These limitations are described below and summarized in **Figure I-4-a**.

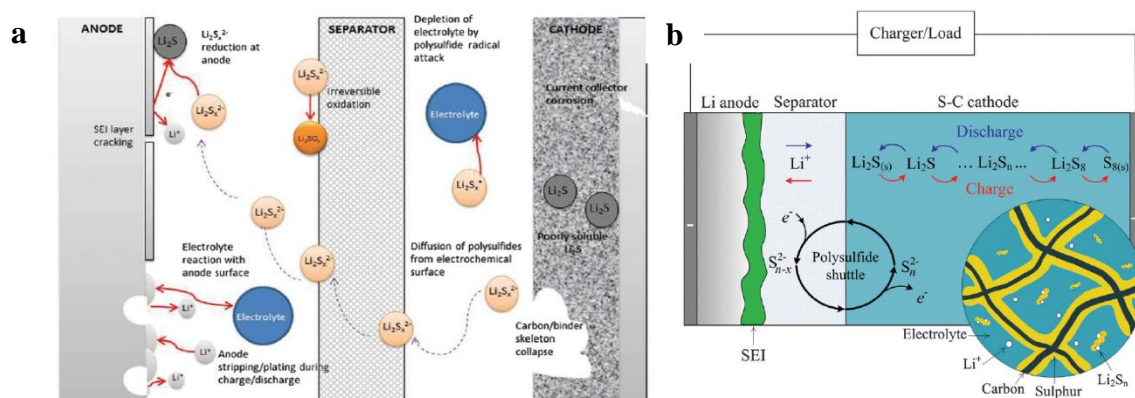


**Figure I-4.** (a) Summary of degradation mechanism inside a Li-S battery (b) scheme of the shuttle effect upon cycling <sup>10</sup>.

The low conductivity properties of solid sulfur species ( $\text{S}_8$ ,  $\text{Li}_2\text{S}_2$ ,  $\text{Li}_2\text{S}$ ) both ionic and electronic ones, result in poor electrode reaction kinetics and high internal resistance. Indeed, the intrinsic electronic conductivities of  $\text{S}_8$  ( $5 \cdot 10^{-30} \text{ S.cm}^{-1}$ ) and  $\text{Li}_2\text{S}$  ( $10^{-13} \text{ S.cm}^{-1}$ ) impede the electron transfer, resulting in sluggish electrochemical reactions. To optimize the continuous electronic network, carbon additives must be used to increase intimate sulfur-carbon contact enabling reversible electrochemical reactions <sup>25</sup>. However, the amount of conductive additives needs to be controlled due to direct impact on the overall specific energy, by increasing of the dead weight (referring to material that are not electrochemically active as well as binder and separator). To overcome the insulating nature of the end-products of reaction in both oxidation (charge / delithiation) and reduction (discharge / lithiation), it is possible to use sulfur nanoparticles to optimize the sulfur particle dispersion (high surface/volume (S/V) ratio) to increase the contact between carbon additive and sulfur and the electronic percolation.

The electroactive polysulfides formed at the positive electrode during the reduction of  $\text{S}_8$  (discharge) are soluble and their undesired mass transport within the electrolyte is at the origin of three major performance barriers <sup>10</sup>.

- 1) At open-circuit, the spontaneous reduction (self-discharge process) of  $S_x^{2-}$  on the surface of the negative electrode.  $Li_2S$  may gradually form a thick layer on the anode surface after prolonged cycling or ageing and become electrochemically inaccessible causing irreversible active material loss, lithium corrosion and passivation by  $Li_2S$ , electrolyte consumption.<sup>26</sup> This self-discharge causes, loss of capacity, poor coulombic efficiency and a shorten cycle life of the battery<sup>27</sup>.
- 2) The LiPS can easily diffuse towards the negative electrode where they are reduced and diffuse back to the positive electrode, due to concentration gradient or electric field, to be re-oxidized without having carried out the complete redox cycle limiting the overall efficiency as shown in **Figure I-4-b**. This redox shuttle, known as “shuttle effect”, can proceed endlessly and therefore causes poor coulombic efficiency and may prevent complete charging of the cell as well.

In addition,  $Li_2S$  is insoluble in ether-based electrolyte, resulting in a precipitation in the porosity of the composite electrode at the end of the discharge. This accumulation of insoluble and insulator compounds on the electrode surface during repeated charge and discharge cycles increases the cell polarization and leads to higher possibility of device failure caused by blocking  $Li^+$  or  $e^-$  pathways.

A significant volume expansion (+ 80%) occurs during the discharge after complete reduction of  $S_8$  into  $Li_2S$ . Indeed,  $S_8$  crystallizes in orthorhombic Bravais lattice, Fddd space group with lattice parameters of  $a = 10.43 \text{ \AA}$ ,  $b = 12.84 \text{ \AA}$  and  $c = 24.36 \text{ \AA}$ , while  $Li_2S$  belongs to Fm-3m space group and exhibits lattice parameters  $a = 5.71 \text{ \AA}$ <sup>28</sup>. The reduction comes with a crystalline structure transformation from orthorhombic  $S_8$  to the cubic  $Li_2S$  (**Figure I-5**). This has a consequence on the final density, the latter is reduced from  $2.07 \text{ g.cm}^{-3}$  to  $1.66 \text{ g.cm}^{-3}$ , contributing sulfur particles disconnection from the conductive network leading to dramatic electrode pulverization.

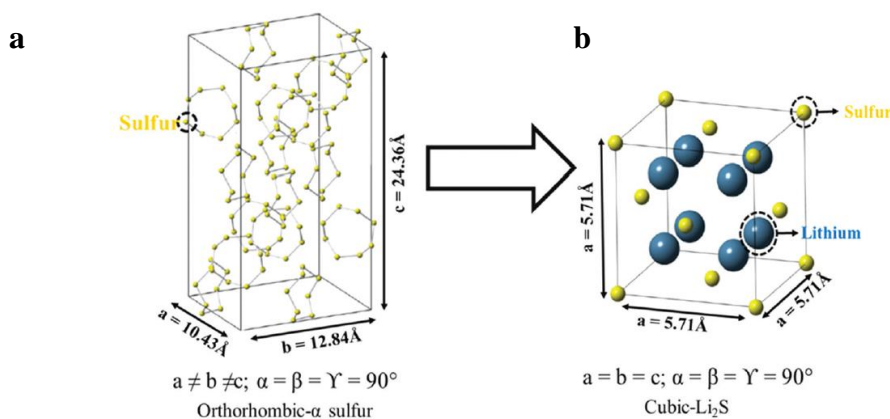


**Figure I-5. Crystal structure of a) sulfur b) lithium sulfide <sup>28</sup>.**

In addition to limitations at the positive electrode, one must keep in mind some phenomena occurring at the negative electrode as well. For instance, inhomogeneous Li deposition during plating/stripping and Li dendrite growth lead to repeated breaking and formation of the solid–electrolyte interphase (SEI), which consumes lithium and the electrolyte. Moreover, lithium dendrites may cause short-circuit, leading to safety issues. <sup>29</sup>.

In conventional Li-ion batteries, this Li dendrite growth especially appears at high current density. On the contrary, the high sulfur capacity implies already a high current density at low C-rate<sup>1</sup>, high enough to rapidly favor dendrite growth, event at low C-rate.

Among the listed drawbacks the “shuttle effect” is one of the main issues. Indeed, it is the cause of most of the failure modes of Li-S batteries (continuous loss of active material, infinite charge during cycling, Li metal passivation, etc.). Therefore, several strategies have been developed to trap them to avoid their diffusion within the battery electrolyte during cycling.

<sup>1</sup> C-rate can be defined as the normalized current at which a battery is discharged relative to the nominal capacity of the cell (given by the manufacturer and measured from standards such as ISO 124-05-1). 1C for a 1Ah battery means that the discharge at 1A will take one hour. For Li-S prototype, the “nominal capacity” is often calculated using the amount of sulfur in the electrode and its theoretical capacity. However, the calculation method remains undescribed or confused in most of the publications. It is then difficult to compare cycling performance from one publication to another.

## 1.2 Routes to trap polysulfides

Based on polysulfide properties: solubility in ether-based solvent and polarity, two fundamental approaches are possible to trap polysulfides upon cycling hence to tackle the shuttle-effect: physical confinement and entrapments through chemisorption or electrostatic interactions.

### 1.2.1 Fundamental approaches

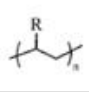
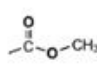
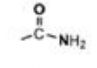
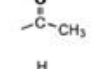
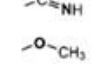
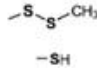
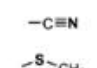
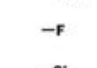
#### Physical confinement

Long chain LiPS are soluble in ether-based solvent, to avoid their movement within the electrolyte, they can be physically confined by a barrier such as a non-permeable LiPS membrane/separator or an encapsulating material containing the initial sulfur such as : a porous or a hollow encapsulating structure.

#### Entrapments through chemisorption or electrostatic interactions

*Electrostatic interaction based mainly on  $\text{Li}^+$  and polar units*

The electrostatic interaction is a chemical interaction between polar LiPS (*e.g.*  $\text{Li}^+$  and  $\text{S}_x^{2-}$ ) and an electron-rich element (*e.g.* electronegative heteroatom N, O, S, P, halogen...). Ab initio calculations show that high binding energies are obtained with atom displaying lone pair of electron as listed in the table displayed in **Figure I-6**. This results in the formation of Li–O, Li–N, Li–S interactions, with electron accepting and donating taking place between lithium or sulfur and an heteroatom<sup>9</sup>. Using these interactions, host material may be tuned to include such electronegative heteroatoms to specifically interact with LiPS.

	Chemical Class	Binding Energy with LiS (eV)	Binding Energy with Li <sub>2</sub> S (eV)
R = $-\text{CH}_2-\text{NH}_2$	Amine	1.29	1.10
	Ester	1.26	1.10
	Amide	1.23	0.95
	Ketone	1.20	0.96
	Imine	1.02	0.88
	Ether	1.01	0.71
	Disulfide	0.85	0.92
$-\text{SH}$	Thiol	0.84	0.76
$-\text{C}\equiv\text{N}$	Nitrile	0.77	0.60
	Sulfide	0.66	0.87
$-\text{F}$	Fluoroalkane	0.62	0.40
$-\text{Cl}$	Chloroalkane	0.46	0.26
$-\text{Br}$	Bromoalkane	0.42	0.23
$-\text{CH}_3$	Alkane	0.30	0.23

**Figure I-6.** Ab-initio binding energies of LiS and Li<sub>2</sub>S calculation<sup>9</sup>.

*Chemisorption by Lewis acid-base interaction*

Instead of relying on electrostatic interactions that involve  $S_x^{2-}$  and polar groups, a material can also bind LiPS via Lewis acid-base interactions. A Lewis base is an electron donor specie while a Lewis acid is an electron acceptor. According to this definition, polysulfide anions ( $S_x^{2-}$ ) are considered as Lewis bases owing to the sulfur lone electron pairs to bind on a Lewis acid site. Host materials that exhibit Lewis acid characteristics are therefore able to interact strongly with LiPS to trap them on the host surface (**Figure I-7**).

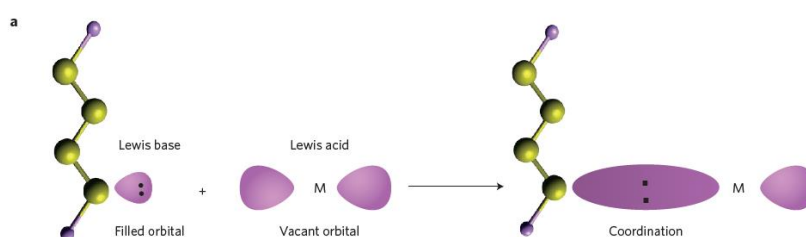


**Figure I-7.** : Lewis acid-base interactions to coordinate lithium polysulfides <sup>30</sup>.

From electrostatic and Lewis acid-base interactions, two dominant types of interactions with the surface of the absorbent are possible 1) interaction of the positively charged lithium ion in LiPS and 2) the negatively charged sulfur in LiPS. This offers two anchor points to interact with lithium polysulfides.

### 1.2.2 Description of the strategies from literature

Several strategies have been explored to develop material capable of efficient polysulfides trapping

- (1) physical confinement of polysulfide with porous nanostructures, polymers, hollow/yolk-shell nanoparticles
- (2) chemical interactions with polysulfides using polar polymers and inorganics
- (3) modify electrolyte composition to reduce polysulfide solubility,
- and (4) creating a stable solid electrolyte interphase (SEI) at lithium metal surface.

### 1.2.2.1 Positive electrode

In 2009, Nazar *et al.* in Canada re-stimulated attention toward Li–S batteries when they successfully combined high performance cathode materials of Li–S batteries with ordered mesoporous carbon CMK-3 and sulfur<sup>31</sup>. The literature reports different strategies that have been considered to improve Li-S battery electrochemical performance (**Figure I-8**). First strategies have been focused on a variety of carbon-based materials with some specific structures (*e.g.*, 0D carbon capsules, 1D carbon nanotubes, 2D graphene nanosheets and 3D porous graphitic carbon) using van der Waals force and confinement effect. The most popular approaches are to encapsulate sulfur within the porosity of carbon materials to improve the electronic wiring, decrease the domain size of insulating sulfur materials and trap polysulfides within the structure as well. However, the interactions between polysulfides and carbon are so weak that the long term performance is limited. The anchoring of polar LiPS on the nonpolar carbon hosts' surface thanks to physisorption is not energetically sufficiently to maintain the confinement. In this respect, hetero-atom (N, P, O, B, S etc.) doping and modification of surface functional groups have been employed to activate the surface of carbon materials. Indeed, chemical strategies that provide polar groups on the surface of the pores lead to stronger interactions between functional groups and lithium polysulfides.

Other strategies using conductive polymers (polyaniline (PANi)<sup>32,33</sup>, poly(3,4-ethylenedioxythiophene (PEDOT)<sup>34</sup>), metal organic frameworks (MOFs)<sup>35</sup>, various metal-based material such as oxides or hydroxides (MnO, MnO<sub>2</sub>, Ti<sub>4</sub>O<sub>7</sub>, TiO<sub>2</sub>, Fe<sub>2</sub>O M(OH)<sub>x</sub>)<sup>36</sup>, sulfides (NiCO<sub>2</sub>S<sub>4</sub><sup>37</sup>, CoS<sub>2</sub><sup>38</sup>, MoS<sub>2</sub><sup>39</sup>), nitrides or carbides (TiN, VN<sup>40</sup>, Co<sub>3</sub>Mo<sub>3</sub>N<sup>41</sup>, Ti<sub>3</sub>C<sub>2</sub>T<sub>x</sub><sup>42</sup>, Ti<sub>2</sub>C<sup>43</sup>) have been studied. Over the last years, numerous works have been dedicated to the development of metal-based materials which possess both strong affinity toward LiPS and potential catalytic activities to enhance electrochemical conversion kinetic between LiPS and Li<sub>2</sub>S<sub>2</sub>/Li<sub>2</sub>S (rapid charge transfer). The architecture design is also carefully considered when developing defect-engineered materials or breathable structures. To that purpose, Cui and co-workers pioneered the work of using sulfur– TiO<sub>2</sub> yolk–shell nanostructures<sup>44</sup> to create an internal void space for accommodating the volume expansion upon lithiation.

The sulfur active material can be replaced by alternative sulfur sources: Li<sub>2</sub>S or S grafted onto polymer (sulfurized polyacrylonitrile (SPAN))<sup>45</sup> involving a different mechanism.



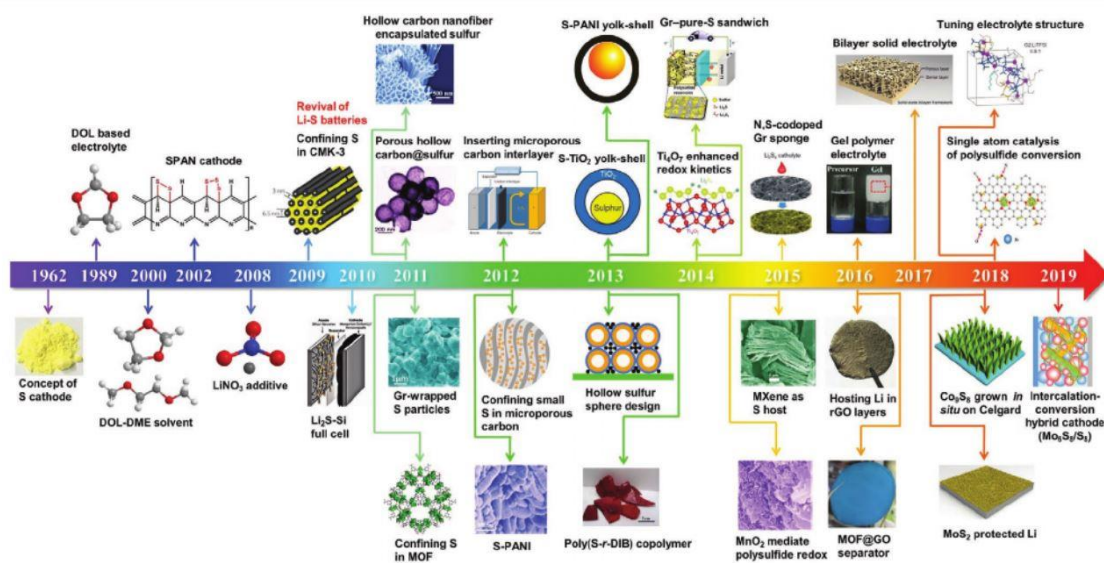


**Figure I-8. Overview of Li-S strategies developed to improve the performance of Li-S batteries<sup>46</sup>.**

### 1.2.2.2 Separator

In the same idea of material design for the positive electrode, interlayers have been developed by surface modification of the separators. This is achieved by applying functional materials, which include polymer-based, carbon-based, metal oxides, metal sulfides, and metal carbides/nitrides, as coating<sup>47</sup>. Strategies are mostly centered around enhancing the commercial PE/PP separator. These strategies are very closed by the one presented above and will not be further details.

### 1.2.2.3 Electrolyte

Many efforts have been made to trap LiPS inside the positive electrode, but some groups also focus on electrolyte optimization in order to solve the shuttling issue. The primary function of the electrolyte in a battery is to efficiently transport ions between the positive and negative electrodes. This implies a high ionic conductivity. In Li-S batteries, the electrolyte also serves unfortunately as medium for the polysulfide dissolution.

The typical Li-S electrolyte is an ether-based liquid electrolyte made of 1 M lithium bis(trifluoromethanesulfonyl)imide (LiTFSI) in a 1:1 mixture of 1,3-dioxolane (DOL) and 1,2-dimethoxyethane (DME). Indeed, conventional carbonate-based electrolyte cannot be use for Li-S applications because they are known to be unstable in the presence of dissolved nucleophilic polysulfides. On the contrary, DOL/DME mixture offers a better stability and good ionic conductivity. However, the LiPS still dissolve inside and easily diffuse within the electrolyte.

Several strategies have been elaborated to develop new electrolyte composition. Among them, it is possible to cite:

- **electrolyte/sulfur (E/S:  $\mu\text{L.mg}^{-1}$ ) ratio optimization** aiming to reduce the amount of electrolyte from E/S=50 (standard value) to E/S=3-10  $\mu\text{L.mg}^{-1}$  <sup>48,49</sup> to minimize inactive weight in the cell and increase the final energy density of a practical Li-S battery.
- **sulfur salt concentration modification** used to modulate/suppress the solubility of LiPS.
- **physical state modification toward solid-state electrolytes** targets to physically (mechanically) block the LiPS shuttle and Li dendrite growth.
- **ionic liquid based electrolyte** with potentially lower LiPS solubilization to suppress the shuttle effect.

#### 1.2.2.4 Negative electrode

Lithium is the lightest metal and displays a very low standard reduction potential (-3.04 V vs SHE). These features produce an ideal negative electrode which possesses a low operating voltage and high specific capacity. This low potential therefore makes it very reactive and therefore unstable in contact with the polysulfides leading to active material consumption and passivation of the negative electrode.

Significant efforts have been made to improve lithium metal stabilization with in-situ additives decomposition to form a protective layer on the top of lithium or with ex-situ artificial anode/electrolyte interface. Artificial anode/electrolyte interface development acting as a barrier layer to deal with dendrite growth. High conductivity, insolubility, stability, flexibility are required to lower internal resistance, not to dissolve within the electrolyte, to avoid polysulfide side-reactions, to accommodate volume change during cycling, and to not impact the final dead weight of the cell.

### 1.2.2.5 Questions concerning the comprehension of the polysulfides trapping

To understand the influence of these strategies on polysulfides trapping (physical confinement and/or entrapments through chemisorption or electrostatic interactions) and to answer this series of questions: how polysulfides are trapped by Li or S atoms or both? What is the nature of polysulfides involved? How disproportionation and electrochemical equilibria are impacted? various techniques have been employed: UV–Visible absorption spectroscopy (UV-Vis)<sup>14,50–52</sup>, high-performance liquid chromatography (HPLC)<sup>14,20</sup>, X-ray absorption spectroscopy (XAS)<sup>53–55,56</sup>, nuclear magnetic resonance spectroscopy (NMR)<sup>57</sup>, Raman spectroscopy<sup>58,59</sup>, X-ray photoelectron spectrometry (XPS) or electron paramagnetic spin resonance spectroscopies (ESR/EPR)<sup>14</sup>, X-ray diffraction (XRD)<sup>60</sup>. Each method offers only part of the information of the working mechanism.

Among them, UV-Vis is a useful technique to observe soluble polysulfides in solution. Indeed, polysulfides solutions are inherently colored, making them highly responsive this spectroscopic method. That is why it is systematically used to prove LiPS interaction at the material-scale design. Although, polysulfide species are not stable when exposed to air or moisture<sup>51</sup>, UV-Vis investigations are frequently carried out by employing an *ex situ* setup with a quartz cuvette and measurements are not performed under perfect airtight conditions. Thus, this raises the question of potential artifacts associated with this measurement approach and the limitations of this method. **Figure I-9** shows an example of typically UV-Vis signal recorded.

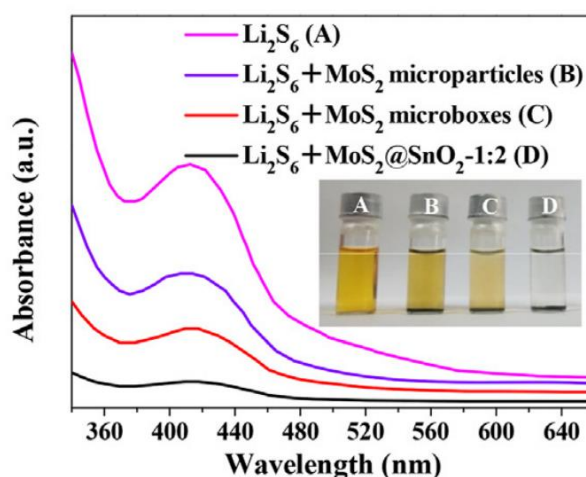


**Figure I-9.** Example of usual UV-Vis signal obtained after new material designed to trap LiPS and  $\text{Li}_2\text{S}_6$  equivalent solution. (Reproduced from <sup>61</sup>).

From these UV-Vis measurements, only qualitative observations are made, confirming the adsorption of LiPS by the reduction of signal intensity, and allowing for a relative comparison of the synthesized materials with each other without taking into account the nature of polysulfides involved in these interactions while some studies attempt to identify the wavelengths associated with the different types of LiPS. UV-Vis spectrum are mainly confined from the 350-700 nm range (corresponding mainly to  $\text{Li}_2\text{S}_4$ ,  $\text{Li}_2\text{S}_6$  and  $\text{S}_3^{\bullet}$  signals) with a predominant focus on signal changes around 400 nm although some studies identify sulfur species ( $\text{S}_8$  and  $\text{Li}_2\text{S}_4$ ) between 250 and 350 nm<sup>62,63</sup>.

Cui's group<sup>51</sup> developed a quantitative approach which represents a significant step forward UV-Vis quantitative study. This quantitative approach would facilitate the determination of the appropriate amount of material to be incorporated into electrode design or used to prepare modified-separator in Li-S batteries. In the existing literature, studies are predominantly focused on material synthesis and the selection of the electrolyte-to-sulfur ratio for battery use. However, there is a notable absence of quantitative measurements to establish the ideal quantity of material needed for visualizing the actual effects of material-LiPS interactions.

Although this quantitative methodology is interesting, it excludes a fraction of polysulfides under 400 nm, making it somewhat imprecise in characterizing the nature of the polysulfides involved. The material-LiPS interactions comprehension study conducted in these literature conditions are not completely adapted to give a complete answer to: what are the polysulfides involved? Do we have new equilibria? Are there speciation phenomena?

Therefore, a comprehensive understanding of the interactions mechanisms requires a thorough study across the entire UV spectrum. **In this PhD work, we propose a robust methodology to do so and to try to answer these questions by looking at the adsorption phenomenon and the alteration of polysulfide species in LiPS solution using supported  $\text{MoS}_2$  incorporated into a carbon network as model material.**

The next section focuses on the literature available on each of the components ( $\text{MoS}_2$  and carbon support) of the composite material structure targeted.

### 1.3 MoS<sub>2</sub> and carbon literature study

#### 1.3.1 Molybdenum disulfide

Molybdenum disulfide (MoS<sub>2</sub>) materials has a large range of applications and it has attracted a lot of attention in many fields starting from catalysis (hydrotreatment reactions),<sup>64</sup>) to electrocatalysis, photocatalysis<sup>65</sup>, sensors<sup>66</sup> or tribology<sup>67</sup> (see **Figure I-10**)

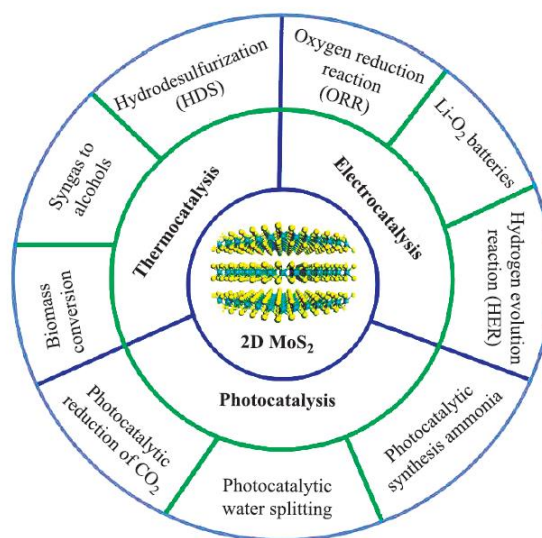


**Figure I-10. MoS<sub>2</sub> applications<sup>65</sup>.**

MoS<sub>2</sub> has proven also to be a good candidate for rechargeable batteries. Mostly used to improve the total reversible capacity of carbon negative electrode<sup>68</sup> MoS<sub>2</sub> has also gained interest in sodium-ion batteries research due to its interlayer space modulation<sup>69</sup>. The structures and properties of this versatile material are described in the next section.

##### 1.3.1.1 Structures and properties

###### MoS<sub>2</sub> structure

Molybdenum disulfide (MoS<sub>2</sub>) belongs to the dichalcogenides family, classified as a transition metal sulfide (TMS) made of S-Mo-S slabs. The electronegativity difference between sulfur and molybdenum lead to covalent bonds that are partially polarized. The Mo cations give up (primarily d-band) valence electrons to the sulfur anions. The Mo oxidation state is considered (+IV) while S anions are (-II). For an individual slab, the Mo - Mo distance is 3.16 Å (in the plane) and 2.36 Å from Mo to S<sup>70</sup> and consists of a predominant hexagonal structure (**Figure I-11-a**) where each Mo atom is coordinated with six sulfur atoms while each S atom becomes coordinated with three Mo atoms in a trigonal prismatic coordination to give the

thermodynamically stable 2H-MoS<sub>2</sub> phase. These slabs or layers are stacked parallelly and separated from 65 Å (**Figure I-11-c**). The sheets are weakly held by van der Waals interactions.

The MoS<sub>2</sub> architecture results in distinct atomic planes/positions: basal planes, edges and corners. (**Figure I-11-d**). In addition, two chemically non-equivalent edges can be distinguished: the (1 0 -1 0) molybdenum edge (hereafter also called the “M-edge”) and the (- 1 0 1 0) sulfur edge (“S-edge”).

The proportion of M-edge rather S-edge sites is directly correlated to MoS<sub>2</sub> morphology which can vary between pure triangular to a perfect hexagonal shape through intermediate truncated hexagonal forms<sup>64</sup>. Triangular MoS<sub>2</sub> crystallites are supposed to expose only M-edges, whereas hexagons expose both types alternatively (**Figure I-11-b**).

MoS<sub>2</sub> is then a complex and anisotropic material which displays different reactivities/properties from basal, edges to corners. The corner and edge sites give the “coordinatively unsaturated sites” (CUS) after removing of their labile S neighbors and are considered as the active sites in catalysis. They are considered as vacant Lewis adsorption sites accessible to sulfur containing molecules.<sup>65,71,72</sup>

CUS can be covered totally or partially by S atoms or hydrogen atoms depending on the the sulfidation of MoS<sub>2</sub> usually involving a mixture of H<sub>2</sub>S/H<sub>2</sub> gas and operating conditions. The sulfur coverage rate depends on the synthesis conditions and may vary from 0% to 100% (**Figure I-11-e**), high coverage rates lowering the total CUS available on the final structure.

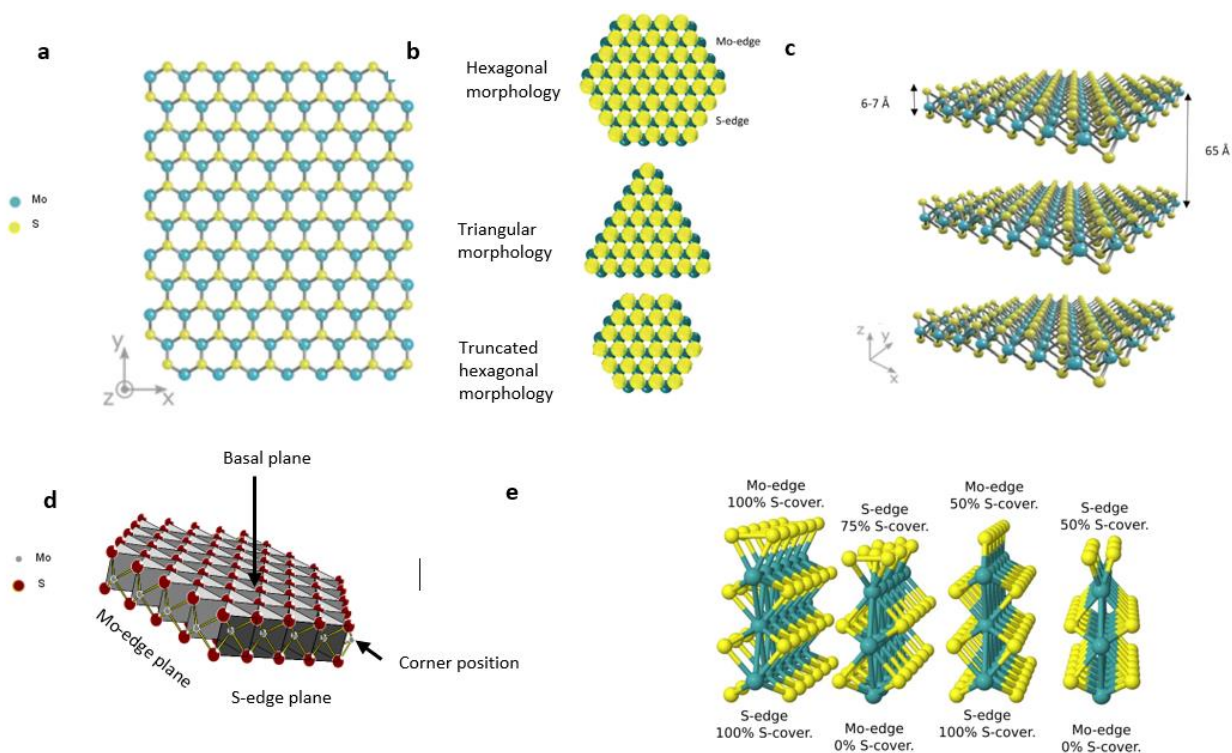


**Figure I-11.** MoS<sub>2</sub> structure a) Single slab of S-Mo-S<sup>73</sup> b) with different morphologies<sup>74</sup> c) stacking<sup>73</sup> d) distinct atomic planes/positions and e) with different sulfur coverages<sup>75</sup>.

### MoS<sub>2</sub> polytypes

MoS<sub>2</sub> can also exist under several polymorphic phases also called polytypes: 1T, 2H and 3R (Figure I-12). In these polytypes, the first digit represents the number of layers present in the arrangement and the alphabet indicates the crystallographic Bravais lattice structure. “T” represents the trigonal, “H” represents hexagonal and “R” represents rhombohedral arrangement.

Due to these crystallographic differences, Mo atoms within the structure have several configurations. Mo atoms are coordinated by S in an octahedral geometry in 1T whereas Mo centers change to trigonal prismatic coordination with S in 2H and 3R<sup>76</sup>. The 1T polytype shows lattice parameters of  $a=3.17 \text{ \AA}$ ,  $c=5.99 \text{ \AA}$ . 2H crystallizes in a space group P63/mmc with lattice parameters of  $a=3.15 \text{ \AA}$ ,  $c=12.30 \text{ \AA}$  while 3R belongs to R3m space group and exhibits lattice parameters  $a=3.17 \text{ \AA}$  and  $c=18.38 \text{ \AA}$ <sup>76</sup>. The comparison between different MoS<sub>2</sub> polytypes is given in Appendix A.

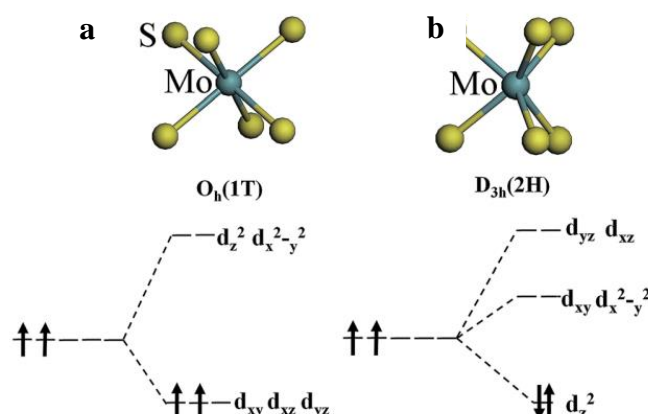


**Figure I-12.** Occupation of electrons in Mo 4d orbitals under the crystal fields of (a) 2H phase and (b) 1T phase <sup>77</sup> .

These polymorphs have different electronic properties. 1T-MoS<sub>2</sub> is metallic whereas 2H and 3R are semiconductors. These properties are highly dependent on the coordination of the Mo metal and its d-electrons orbital filling. In the trigonal prismatic coordinated 2H-MoS<sub>2</sub>, the non-bonding d orbitals are fully occupied and have antiparallel spin-electron while octahedrally coordinated 1T-MoS<sub>2</sub> exhibits d orbitals partially filled with parallel spin-electron (**Figure I-12**). From this occupation, 2H-MoS<sub>2</sub> is a nonmagnetic semiconductor whereas 1T-MoS<sub>2</sub> appears as paramagnetic and metallic <sup>78</sup>. Due to its electron configuration, 1T-MoS<sub>2</sub> has the highest conductivity, 10<sup>5</sup> times higher than 2H-MoS<sub>2</sub> <sup>76</sup>. For that reason, 1T phase is considered as better candidate to enhance electron transfer. The latter one is preferentially used in Hydrogen Evolution Reaction (HER) <sup>79-82</sup> where electronic conductivity is primordial, similarly to the battery field. However, 1T-MoS<sub>2</sub> is metastable and tends to rapidly return to 2H form. Several strategies have been developed to stabilize the 1T-MoS<sub>2</sub>. Palencia-Ruiz *et al.* <sup>83</sup> suggested a stabilization of 1T-MoS<sub>2</sub> induces by intercalation of a molecule, the ethylene glycol used during solvothermal preparations. Other strategies are described in the bibliographic report.



Other strategies to achieve high MoS<sub>2</sub> conductivity have been developed by playing on:

- **MoS<sub>2</sub> low stacking:** when MoS<sub>2</sub> slabs are stacked, electrons must cross each slab to reach the top-slab before being involved in reaction. This leads to higher resistance and lower the conductivity.
- **MoS<sub>2</sub> perpendicular growth on a support:** resistivity (reverse of the conductivity) perpendicular to the planes has been measured to be 2200 times larger compared to the parallel to the planes (0.1-1 Ω.cm<sup>-1</sup>)<sup>84</sup>. This can be achieved when MoS<sub>2</sub> is supported onto a matrix / interacts with a support.

As-mentioned metal-support interactions (MSI) provide completely new properties. This special interaction, well-known in heterogenous catalysis, is explained below and few examples of new properties achieved are listed.

### **Metal-support interactions (MSI)**

At the interface between the metal and the support, electrons of the first atomic layers are involved in a charge redistribution. The magnitude and direction of the charge transfer is driven by differences in the Fermi level of the metal and the support, ultimately seeking equilibration of the electron chemical potentials<sup>85</sup>. These interactions can be of two natures: weak interactions (van der Waals, hydrogen bonds or strong interactions which can lead to the creation of a covalent chemical bond with the support.

In heterogenous catalysis, it has been demonstrated that often Mo species creates Al-O-Mo chemical bonds with Al<sub>2</sub>O<sub>3</sub> support. Beyond this, Bara *et al.*<sup>86</sup> have shown a relationship between  $\alpha$ -Al<sub>2</sub>O<sub>3</sub> crystalline face orientation and the strength of metal-support interactions. This metal-support interaction tunes the electronic structure of the active sites, which in turn control the adsorption strength of reactants, LiPS in our case. If Mo is involved in covalent bonding such as -C-O-Mo, the Lewis character of Mo may be enhanced because oxygen atom is strongly electronegative and polarizes the chemical bonds. Thus metal-support interaction will be reinforced. This metal-support interaction modulates the electronic structure of the sites, resulting in various properties of the supported metals that strongly differ from non-supported metals.

New properties are given by MSI :

- **MoS<sub>2</sub> vertically oriented**

The support is also a useful surface to control MoS<sub>2</sub> layer growth. Shimada *et al*<sup>87</sup> demonstrated epitaxial growth with edge-bonded MoS<sub>2</sub> clusters (vertically oriented) on an anatase-type TiO<sub>2</sub> support. They discovered better catalytic performance with edge-bonding rather than basal-bonding (**Figure I-13**). The upper edge sites of the edge-bonded MoS<sub>2</sub> clusters have less steric hindrance than edge sites of the basal-bonded. With vertical configuration, the number of active sites accessible and available for the reaction is increased. This behavior is confirmed by Wang *et al.*<sup>88</sup>.

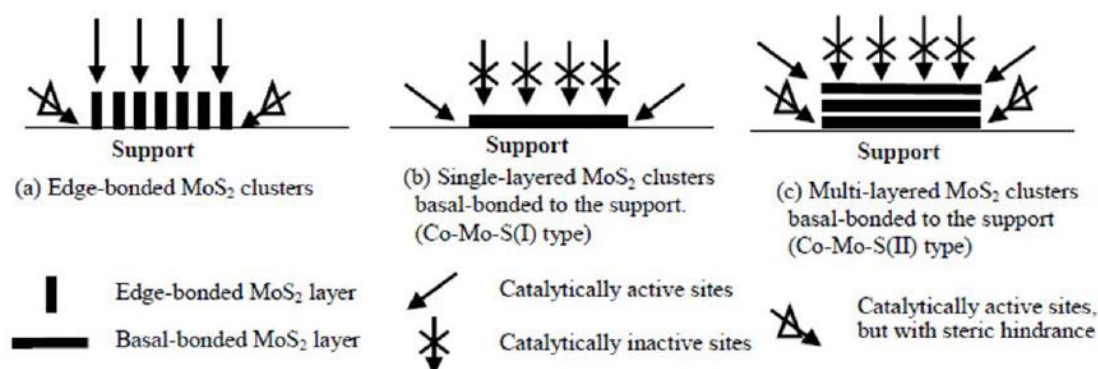


**Figure I-13.** Scheme of different possible orientations of MoS<sub>2</sub> clusters on supports<sup>86</sup>.

- **particle size / dispersion**<sup>2</sup>

Bara *et al.*<sup>70</sup> also demonstrate a relation between Al<sub>2</sub>O<sub>3</sub> plane orientations and particles' dispersion. The weak interaction with (0001) Al<sub>2</sub>O<sub>3</sub> planes and Mo oxide particles leads to large particles clusters and aggregates (low MoS<sub>2</sub> dispersion onto the support) while (0-102) planes exhibiting stronger metal-support interactions offer smaller oxide particles (high dispersion) that are well dispersed and anchored to the surface. The relationship has also a consequence on the sulfidation degree, MoS<sub>2</sub> size and stacking. For instance, low metal-support interactions lead to a higher sulfidation degree and provide larger MoS<sub>2</sub> slabs.

<sup>2</sup> The dispersion corresponds to a ratio of surface occupied by Mo per surface of support and is expressed in %.

### Sulfur species LiPS - MoS<sub>2</sub> interactions

MoS<sub>2</sub> structure modification leads to numerous reactivities. MoS<sub>2</sub> has been identified to specifically interact with sulfur species as known in HDS. In the same way, MoS<sub>2</sub> reacts with polysulfides species. Wang *et al.*<sup>89</sup> calculated that Mo-edge exposed surface should be beneficial for sulfur interactions more than S-edge or basal plane. Calculated binding energies increased as follow Mo-edge > S-edge > basal plane (>> carbon) (**Figure I-14**). From that perspective, it may be interesting to selectively synthesize a edges rich MoS<sub>2</sub> for Li-S application.

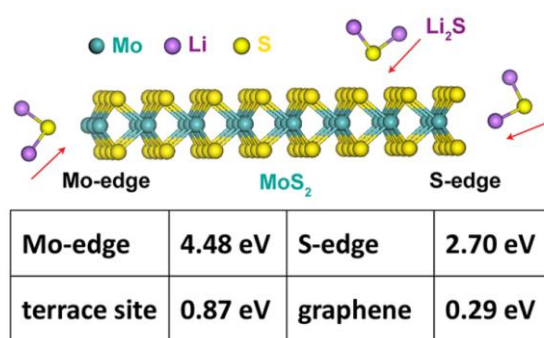


**Figure I-14.** Binding energies for the interaction between Li<sub>2</sub>S molecules and different MoS<sub>2</sub> atomic position<sup>89</sup>.

MoS<sub>2</sub> is a versatile material, its structure can be greatly modified to develop new characteristics for an optimization of the interactions with LiPS.

The concepts of MoS<sub>2</sub> structuration to play on the nature and the number of active sites well known in heterogenous catalysis and HER/OER. Indeed, it several strategies have been developed to modify MoS<sub>2</sub> structure: slab length variation<sup>90,91</sup>, stacking control<sup>92</sup> and epitaxial growth<sup>88</sup> enable to play on the number of active sites whereas vacancies engineering<sup>93,94</sup>, edge engineering<sup>95</sup> phase transition engineering<sup>96</sup> and modification of the metal support interaction<sup>97</sup> are used to modify the nature active sites as shown on **Figure I-15**. The solutions are interesting routes to improve polysulfides adsorption and their conversion into Li<sub>2</sub>S. In addition, the previously described properties of the MoS<sub>2</sub>-carbon are not very much disclosed in the literature dedicated to Li-S battery.

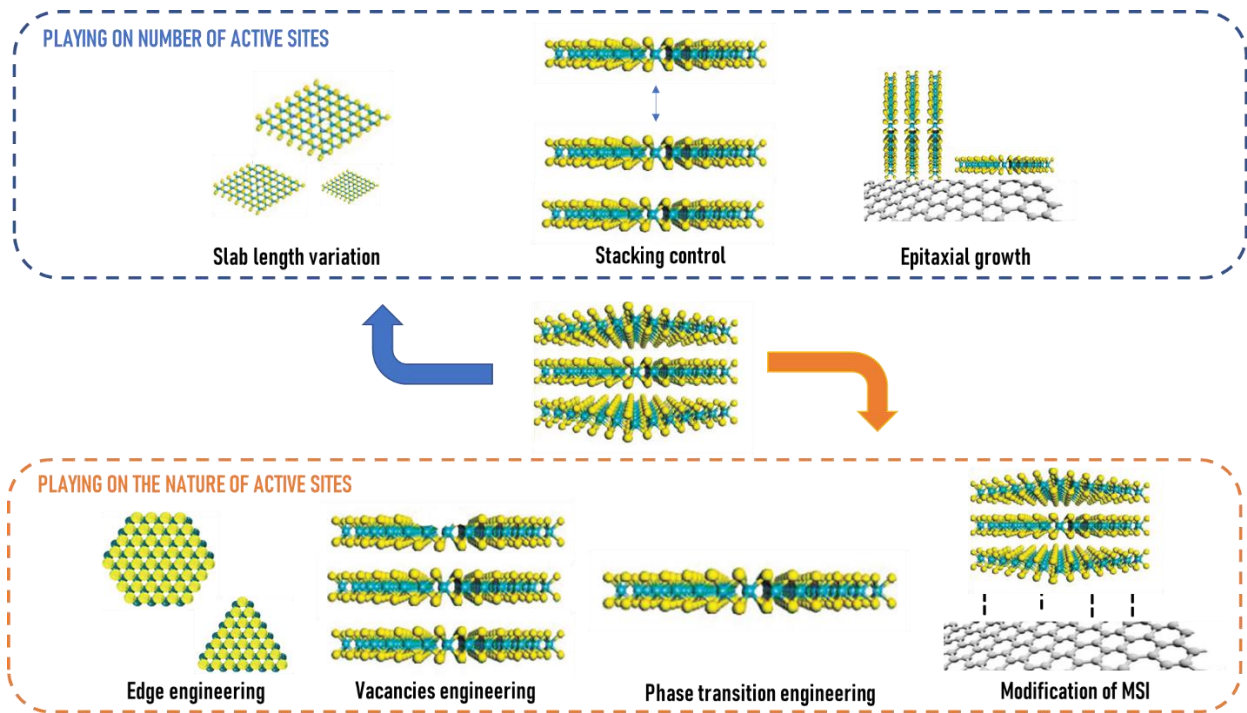
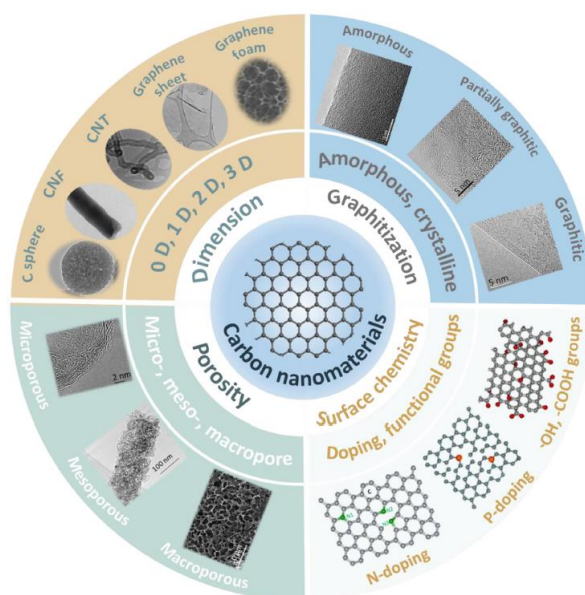


Figure I-15. Design approaches to modify MoS<sub>2</sub> structure.

## 1.3.2 Carbon support

### 1.3.2.1 Carbonaceous material employed for Li-S battery applications

Carbon materials are attractive due to their relatively high chemical stability, electroconductive properties and large variety of structure, texture, and morphology. Carbon nanomaterials have already played an important role in enhancing performances of Li-S batteries. **Figure I-16** illustrates the carbonaceous materials that have been already used for Li-S applications.



**Figure I-16. Carbon nanomaterials used for Li-S batteries applications** <sup>98</sup>.

In this project, the specifications for such carbon are:

- **High conductivity** to maintain continuous electrical pathways;
- **Adequate pore volume** to load supported MoS<sub>2</sub> and to host elemental sulfur active material;
- **Large surface area** to provide enough contact surface to anchor MoS<sub>2</sub> and polysulfides species.

Nazar group<sup>31</sup> first published the development of ordered mesoporous carbon CMK-3 carbon scaffold (1976 m<sup>2</sup>.g<sup>-1</sup> of surface area) for Li-S batteries. This has led to a strong interest in the development of other porous carbons for Li-S applications. These materials are versatile, and their syntheses enable to adjust the pore size, pore volume and ordered pore architecture.

However, such porous carbons are often combined with carbon additives in the electrode manufacturing to compensate for the poor electronic conductivity of sulfur. Majority of the porous carbons developed for Li-S applications, are not part of the carbon additives usually

chosen for electrode making. Consequently, working with carbon additives is an interesting alternative avoiding to completely modify the electrode manufacturing processes. This also limits the total number of interfaces within the electrode. **Table I-2** shows the characteristics of carbon additives already used in the battery field for electrode formulation. Among the varieties of carbon available, only few carbons developed a large surface area, e.g. graphene, Ketjenblack, Printex-2.

**Table I-2. Characteristics of carbon additives used in battery electrode formulation**

Carbon additives	Specific surface area (m <sup>2</sup> .g <sup>-1</sup> )	Conductivity (S.cm <sup>-1</sup> )	Reference
Timrex KS6 (Timcal)	21	-	99
Printex A	30	-	100
Super C45	45	-	99
Super C65	65	1.3	99,101
Carbon nano fiber (CNF)	50-120	-	99
Carbon nanotubes (CNT)	80-120	-	99
Reduced graphene oxide (rGO)	422-500	-	99
Graphene	400-800	-	99
Ketjenblack EC300J	988	1.2	101
Printex-2	1000	-	100
Ketjenblack EC600J	1270-1400	0.6	99-101

After studying the properties of available carbon additives, Ketjenblack EC-600JD ® (KB) appears to be an advantageous candidate for supporting MoS<sub>2</sub> and host S<sub>8</sub> active material. Its 6 cm<sup>3</sup>g<sup>-1</sup> porous volume and 1379 m<sup>2</sup>g<sup>-1</sup> large specific surface area are favorable textural properties for these purposes. With its conductivity of 0.25 S.cm<sup>-1</sup> it facilitates electron transport and maintains a continuous electrical pathway.

## 1.4 The project research strategy

This PhD project is dedicated to the design of supported MoS<sub>2</sub>-Ketjenblack (MoS<sub>2</sub>-KB) for Li-S positive electrode to conduct a comprehensive study of the MoS<sub>2</sub>-Ketjenblack structure – electrochemical performance relationships in lithium sulfur batteries. As specified in **section I-1.2.2.5**, a robust quantitative methodology is presented in order to answer some non-elucidated questions from literature and to better understand the adsorption phenomenon and how the MoS<sub>2</sub>-KB modify the LiPS equilibria in solutions to design an optimized MoS<sub>2</sub>-KB electrode to i) mitigate polysulfide shuttling, and ii) favor their reduction into Li<sub>2</sub>S.

The S<sub>8</sub>-MoS<sub>2</sub>-KB material is designed on the basis of the following hypotheses leading to a its specific architecture:

- Hypothesis 1: sulfur needs to be hosted in the porous volume of KB to ensure continuous electrical pathway and to maximize the contact and interactions of LiPS with MoS<sub>2</sub>

In order to maximize the probability of contact between LiPS released during lithiation process and MoS<sub>2</sub> deposited in the porosity of the KB, it is obvious that S<sub>8</sub> active phase must be inside the KB porous volume.

- Hypothesis 2: adsorption of LiPS may occur on MoS<sub>2</sub> edges or edge + basal planes

In order to assess the amount (and surface area) of MoS<sub>2</sub> necessary to adsorb all the produced LiPS the amount of Li<sub>2</sub>S<sub>4</sub> adsorbed (μmol) is determined assuming two main hypotheses: adsorption by the CUS (edge + corner sites) or via sulfur atom of the total slab surface (edges+corner+basal plane) considering only one side.

Edges + corners adsorption scenario is given by **Figure I-17-a** whereas whole slab surface scenario by **Figure I-17-b**. The amount of Li<sub>2</sub>S<sub>4</sub> adsorbed varies with the slab size only for edges + corners adsorption scenario.

**Figure I-17** shows higher adsorption capacity (μmol) for the total surface slab surface adsorption assumption than edges adsorption only. Reducing the stacking of MoS<sub>2</sub> slab on the support to produce MoS<sub>2</sub> monolayers might then be advantageous to make both basal plane sides available. Nevertheless, Wang *et al.* simulations<sup>89</sup> showed that edge sites (especially Mo-edges) are energetically favored for sulfur interactions compared to basal plane. Consequently,

if this is confirmed, MoS<sub>2</sub> slabs with small size must be preferred to maximize the edges Mo/total Mo ratio (dispersion). **Figure I-17** also compares the amount of Li<sub>2</sub>S<sub>4</sub> adsorbed for two MoS<sub>2</sub> loadings: 40 and 60 wt.% and the maximum number of moles of Li<sub>2</sub>S<sub>4</sub> that can be generated in the electrode made with our protocol. The maximum number of moles of Li<sub>2</sub>S<sub>4</sub> produced is calculated as followed:

- experimental electrodes contain  $\approx 1 \text{ mgs.cm}^{-2}$  of S<sub>8</sub> in average generating a maximum of  $8 \text{ }\mu\text{mol.cm}^{-2}$  of Li<sub>2</sub>S<sub>4</sub> during discharge

**Maximum of Li<sub>2</sub>S<sub>4</sub> produced ( $\mu\text{mol}$ )**

$$= 2 * \frac{\text{mass of S}_8 \text{ in the electrode (g)}}{Mw_{S_8} \text{ (g.mol}^{-1}\text{)}} = 2 * \frac{1 * 10^{-3}}{256} * 10^6 \approx 8 * \mu\text{mol}$$

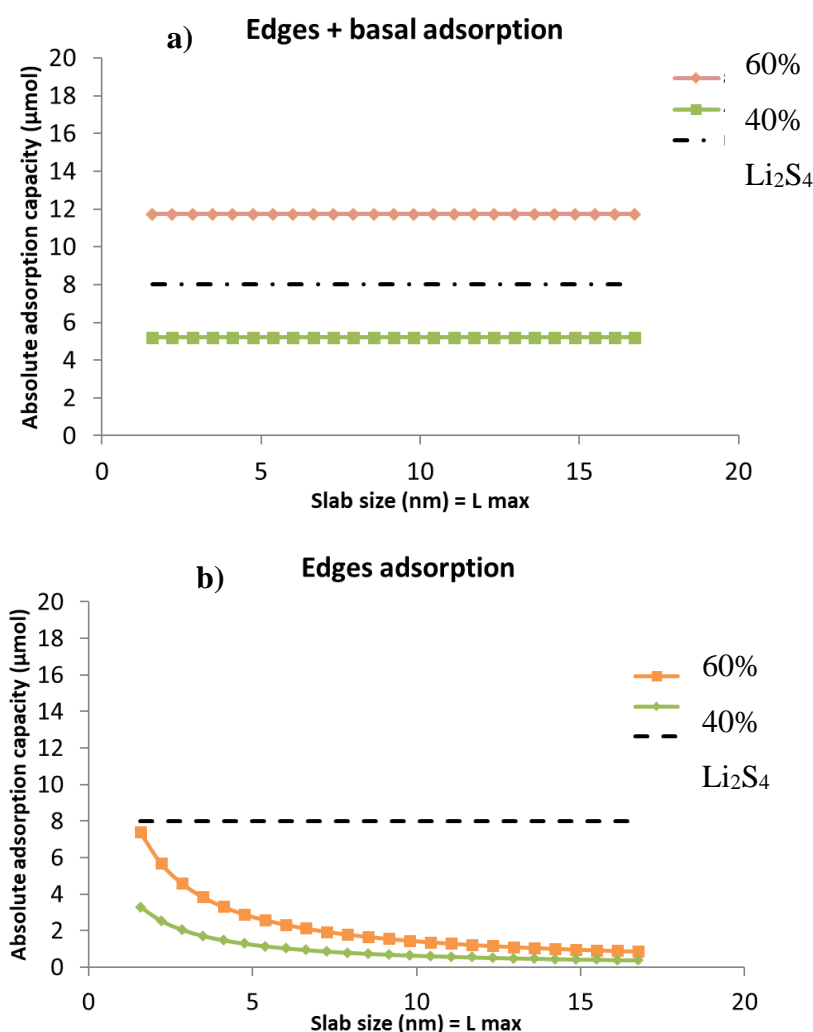


**Figure I-17.** Variation of adsorption capacity with the MoS<sub>2</sub> loading for a) edges/corners adsorption only and for b) edges/corners + basal plane adsorption.



Logically, both absolute adsorption capacities (edge or total surface) are higher for 60 wt.% than 40 wt.% Mo loading and much higher adsorption capacity is observed for the (total surface) mode. However, to trap the 8  $\mu\text{mol}$  value we would need very high MoS<sub>2</sub> loading > 60 wt.% which is probably too much since the porous volume of KB would decrease dramatically leading to low residual space for S hosting and diffusion limitation (Li<sup>+</sup>). Therefore, working with lower MoS<sub>2</sub> loading than 60 wt.% and increasing the fraction of MoS<sub>2</sub>-carbon in the final electrode formulation will be probably necessary. Samples with MoS<sub>2</sub> loading, slab length variations and MoS<sub>2</sub> morphology modifications are synthesized to verify these hypotheses.

In addition, this simplified calculation and assumptions does not take into account the dynamic of the process, since one given adsorption site might be used by several polysulfides successively if the turnover number is high enough compared to the diffusion rate of soluble species.

**Figure I-18** summarizes the organization of the overall experimental protocol, starting from MoS<sub>2</sub>-Ketjenblack (MoS<sub>2</sub>-KB) synthesis by incipient wet impregnation and sulfidation, sulfur impregnation, MoS<sub>2</sub>-KB /s electrode making and its use during battery cycling.

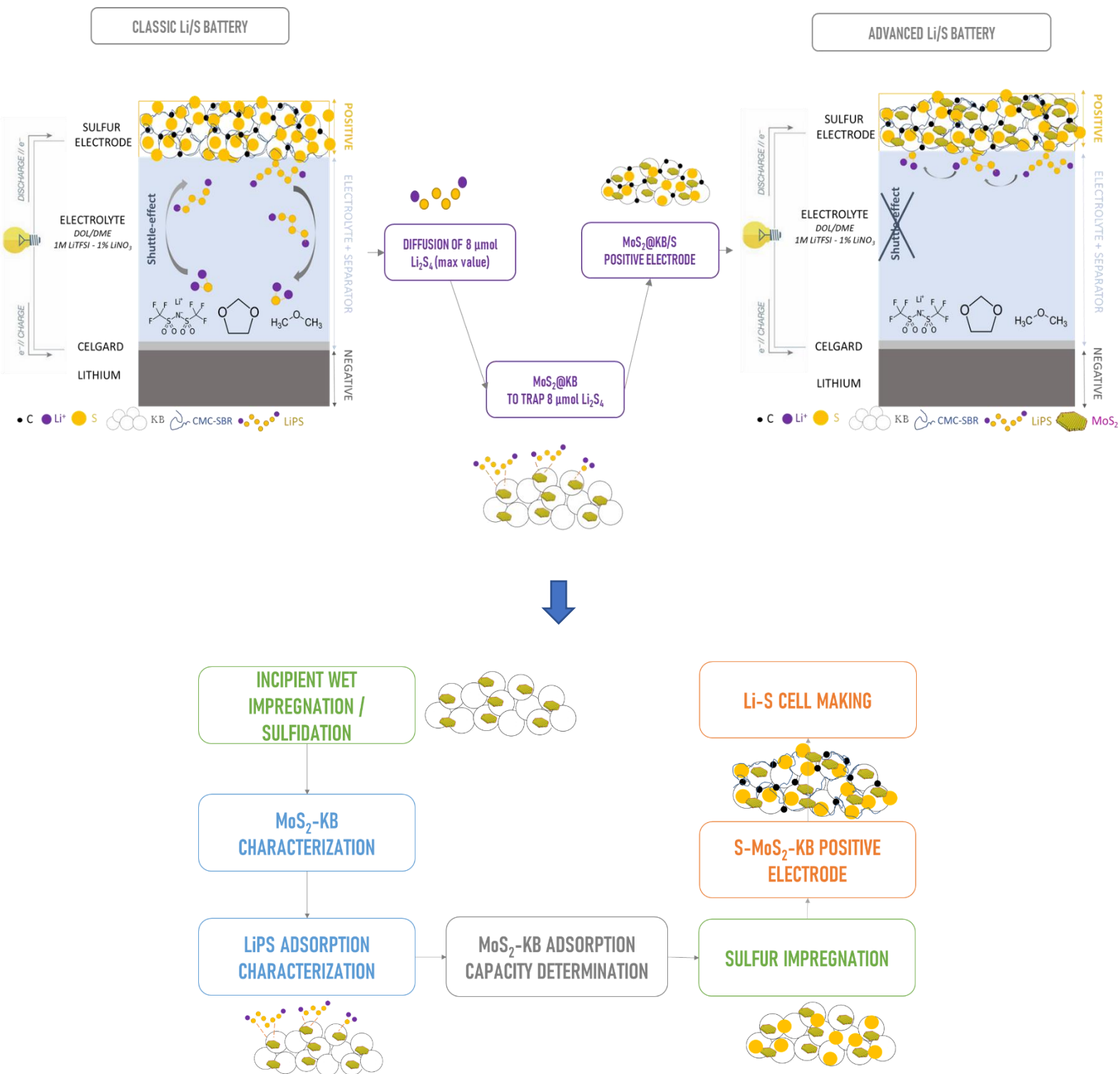


**Figure I-18.** Schematic organization of the overall strategy to develop S-MoS<sub>2</sub>-KB material for Li-S battery application. Green, blue, grey, orange corresponds to synthesis, characterization, adsorption characterization and electrode/battery making respectively.

## 1.5 Conclusion and objectives

Nowadays, the excessive use of fossil fuel in our energy consumption mix has triggered air pollution and global warming issues. Efforts toward international reduction of CO<sub>2</sub> have been made to limit this. It has led to a paradigm shift and a growing demand for modern renewable energies. Intermittent character of these modern renewable energies as well as constant demand for electricity have led to rapid development of energy storage devices and conversion. Among the electrochemical storage devices, lithium-sulfur (Li-S) batteries are attracting an increasing attention due to their superior energy density and high specific energy over the other rechargeable battery technologies. However, their commercial development is hindered by several challenges such as the insulation nature of sulfur and lithiation product Li<sub>2</sub>S, large volume expansion of the sulfur in the positive electrode and the shuttle effect of polysulfides Li<sub>2</sub>S<sub>x</sub> (4 ≤ x ≤ 8). In this survey, a focus has been made on the “shuttle-effect” which causes low sulfur utilization, rapid capacity fading and poor cyclability. To date, tremendous efforts have been attempted to solve this issue. At the sulfur positive electrode, the development of new materials used to trap polysulfides upon cycling by physical confinement and chemical entrapments (chemisorption and electrostatic interaction) have been studied using variety of carbon-based materials, conductive polymers, metal organic frameworks, metal-based material such as oxides or hydroxides, sulfides, nitrides or carbides. Significant efforts have also been made to improve lithium metal stabilization with in-situ additives decomposition or with ex-situ artificial anode/electrolyte interface as well as new electrolyte compositions to play on the solubility/precipitation equilibrium of polysulfides.

The Li/S<sub>8</sub> topic is rather “hot” with an intense activity and competition. The number of publications continues to increase on that field and new designs of positive electrode based on porous structure, yolk-shell, core-shell embedded with additives keep emerging. Nevertheless, the full comprehension of the mechanisms underlying the interactions between polysulfides, and materials remains incomplete due to a lack of quantitative studies. In this study, we propose a novel quantitative UV-VIS methodology to do so and to study the adsorption phenomenon and the alteration of polysulfide species in LiPS solution using supported MoS<sub>2</sub> incorporated into a carbon network as model.





## Chapter II – Synthesis and characterization of MoS<sub>2</sub>-KB

---

### 1.1 Introduction

As discussed in Chapter I, an efficient capture of polysulfides produced during the discharge of Li-S batteries is essential to maintain the electrochemical activity of the sulfur material. The materials developed to address polysulfides shuttle effect can be classified into two categories: physical barrier or chemical adsorbent. In this study, the chosen material aims to combine both effects by using MoS<sub>2</sub> layers (adsorbent) supported on Ketjenblack (adsorbent/encapsulating material) (MoS<sub>2</sub>-KB).

This chapter, divided into two main sections, describes the synthesis protocol and characterization results of the targeted materials. The first section is dedicated to the characterization of a commercial Ketjenblack EC-600JD used as a support. The second section encompassed the synthesis of MoS<sub>2</sub>-KB by an incipient wetness impregnation followed by a gas phase sulfidation and the associated characterizations results. Incipient wetness impregnation (IWI) and sulfidation step is usually used for heterogeneous catalysts preparation in petroleum refining. These catalysts typically consist in molybdenum disulfide clusters dispersed on a support surface (alumina and silica) and promoted by cobalt or nickel in the case of hydrotreating applications. Based on this expertise, the synthesis protocol is adapted to carbon support for our study. Among the various approaches to modify the MoS<sub>2</sub> structure, described in the literature and outlined in **Chapter I**, two synthesis parameters are varied: the Mo loading and the sulfidation conditions. The results are presented in this second section.

## 1.2 Characterization of Ketjenblack support

This section presents the characterization results of the commercial Ketjenblack EC-600JD (Safic Alcan) characterization (referred as KB hereafter), which is used as carbonaceous support throughout the study. Scanning Electron microscopy (SEM), Transmission Electron microscopy (TEM), elemental analysis (CHNS), laser diffraction granulometry, mercury intrusion porosimetry (Hg porosimetry), N<sub>2</sub>-adsorption-desorption measurement, Raman spectroscopy and impedance spectroscopy are performed to get valuable information about the morphology, textural properties, and the electrical conductivity of the support, prior the MoS<sub>2</sub> incorporation. The characterization protocols applied for each method are detailed in **Appendix B**.

Morphological images of the KB are displayed in **Figure II-1**. KB is composed of agglomerates ranging from 50 to 200  $\mu\text{m}$  (as shown on SEM image in **Figure II-1-a**), more or less compact. Analyzing the inner sample using TEM images enables to observe primary aggregates of carbon nodules ranging from 100 to 1000 nm (**Figure II-1-b**). At higher magnification, arrangements of graphite planes in onion-like layers are observed (**Figure II-1-c**), which is a typical arrangement of carbonaceous material, inside 30-50 nm primary particles. The multi-scale configuration of KB is schematically depicted on **Figure II-1-d**. The sample is composed of carbon (98 wt.%) with traces of oxygen (2 wt.%), as determined from elemental analysis (**Table II-1**).

**Table II-1. KB elemental analysis using CHNS**

(error associated is about  $\pm 0.1\%$  between 0-10 wt.% and  $\pm 0.3\%$  between 10-50 wt.%)

<b>C</b> wt. %	<b>H</b> wt. %	<b>N</b> wt. %	<b>S</b> wt. %	<b>Total</b> wt. %	<b>O deduced</b> wt. %
98	0	0	0	98	2
* the approximation of O content from CHNS is obtained using: $100 - \sum_{C,H,N,S} \text{wt.}\%$ assuming that O is the only element left					

The error associated to the CHNS method is about  $\pm 0.1\%$  between 0-10 wt.% and  $\pm 0.3\%$  between 10-50 wt.%.

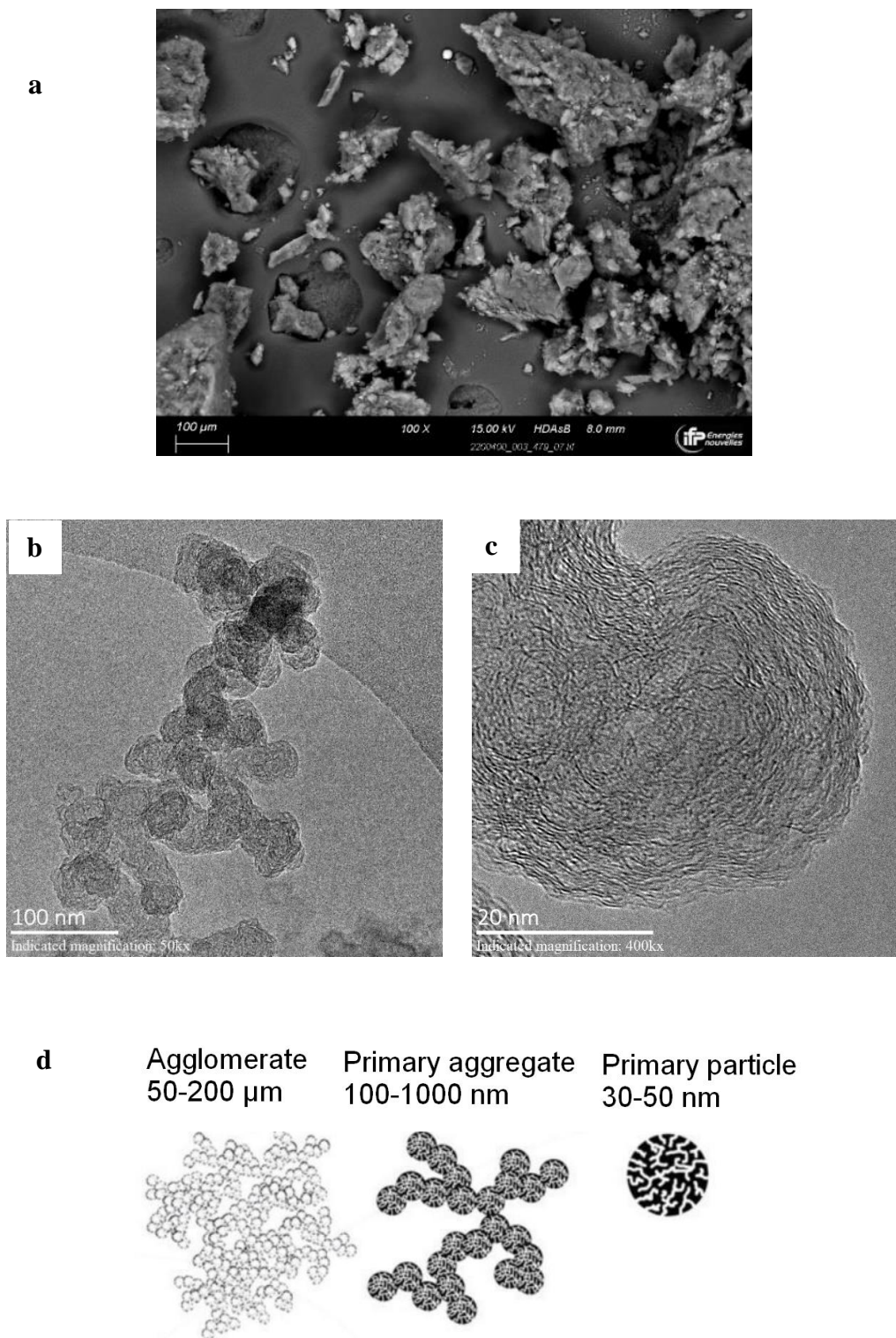


**Figure II-1.** KB morphology characterizations a) SEM image before ultrasound treatment, b and c) Bright Field TEM images of KB d) schematic structures of the three scales <sup>102</sup>.



**Figure II-2-a-b** shows the KB particles size distribution determined by laser diffraction granulometry. The median particle size corresponds to 5.4  $\mu\text{m}$  in volume which refers to primary aggregates seen on SEM image (**Figure II-1-a**). In terms of volume weighted distribution, 50% of the KB sample is composed of particles smaller than 76.6  $\mu\text{m}$ . Therefore, most of the volume is developed by large particles that are less numerous in number.

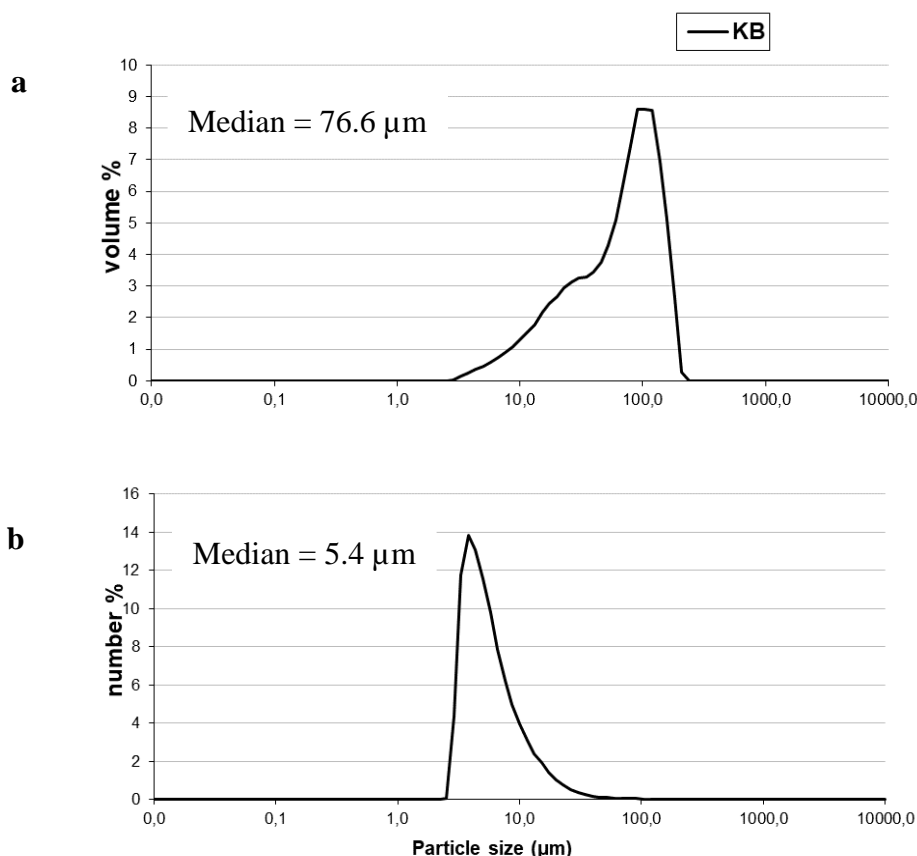


**Figure II-2. Ketjenblack particles size distribution a) in volume b) in number.**

Hg porosimetry and  $\text{N}_2$  adsorption-desorption measurements are carried out to explore the texture of the KB. These measurements provide information on the pore volume and pore size distributions at the different scales. Hg porosimetry is appropriate for evaluating the volume of macropores ( $> 50 \text{ nm}$ ) and mesopores (2-50 nm), while it has been decided to use  $\text{N}_2$  adsorption-desorption isotherms to determine the contribution of micropores ( $< 2 \text{ nm}$ ).

**Figure II-3-a** shows that Ketjenblack develops a total pore volume of  $4.1 \text{ cm}^3 \cdot \text{g}^{-1}$  considering the intra-particle macro and mesoporosity only (calculated between 7  $\mu\text{m}$  and 3.3 nm). Volumes of 3.0 and  $1.0 \text{ cm}^3 \cdot \text{g}^{-1}$  and mean pore diameter of 359 nm and 19 nm are developed by macro and mesopores respectively.  $\text{N}_2$  adsorption-desorption isotherm, depicted in **Figure II-3-b**,

reveals a type IV isotherm with a H3 hysteresis. This isotherm is the specific signature of solid containing mesopores, with non-uniform-sized slit-shaped pores<sup>103</sup>. A micropore volume of 0.35 cm<sup>3</sup>.g<sup>-1</sup> is calculated using the “t plot method”, by extrapolation of the adsorption branch to the adsorbed N<sub>2</sub> axis (blue curve). Consequently, 69%, 23% and 8% of the porous volume belonged to macro, meso and micropores respectively. A surface area of 1364 m<sup>2</sup>.g<sup>-1</sup> is determined by applying the Brunauer–Emmett–Teller (BET) method. These data are grouped by pore family in **Table II-2**. The textural values obtained are in line with Neffati *et al*<sup>104</sup> who deeply characterized KB sample.

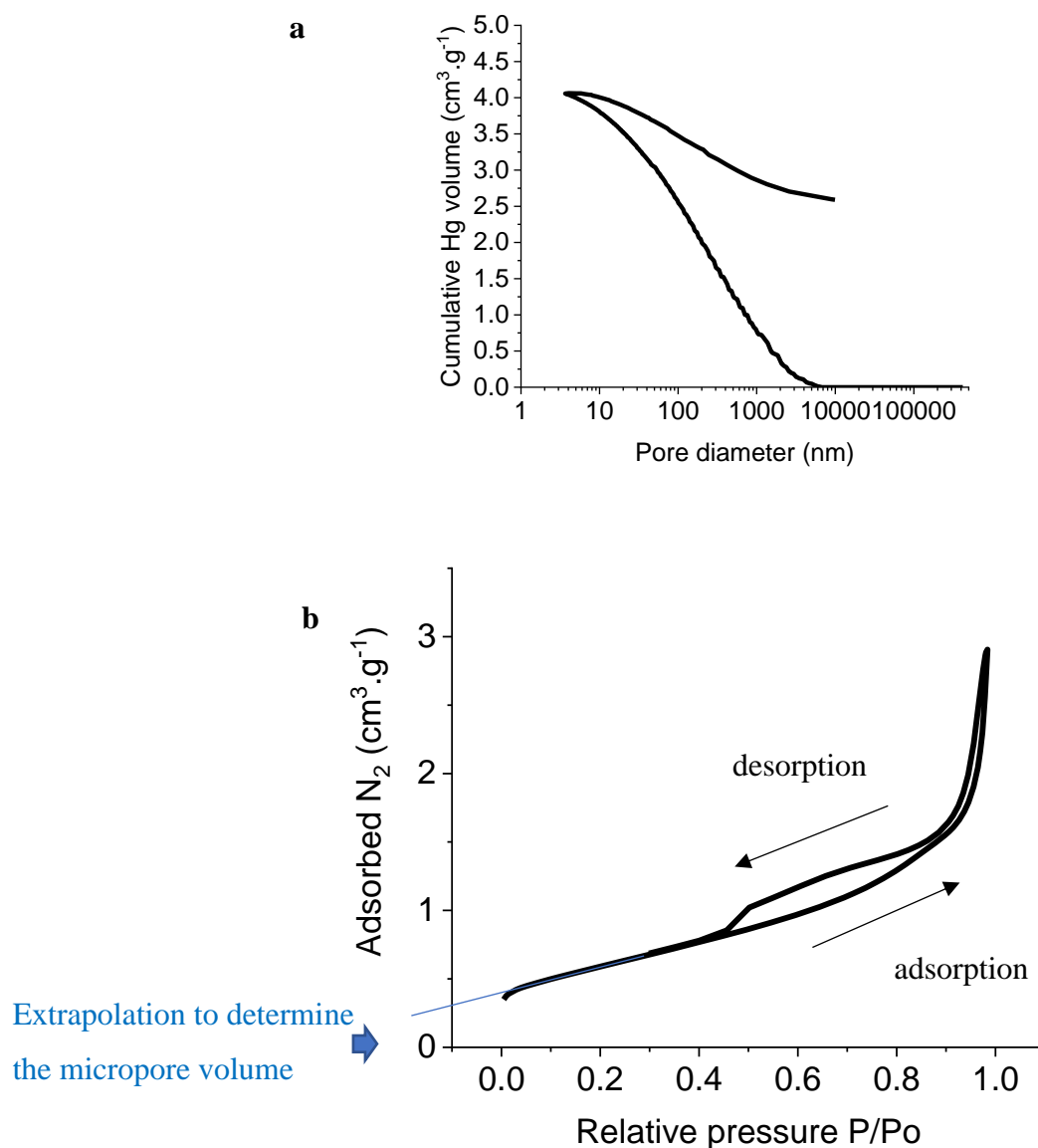


**Figure II-3. Textural analysis of KB a) Hg porosimetry d) N<sub>2</sub> adsorption-desorption isotherm.**

**Table II-2.** KB textural characteristics. Results are obtained from <sup>a</sup> Hg porosimetry, <sup>b</sup> N<sub>2</sub> adsorption-desorption isotherm.

<b>Surface area (m<sup>2</sup>.g<sup>-1</sup>)</b>	
BET <sup>b</sup>	1364
<b>Pores volume per family (cm<sup>3</sup>.g<sup>-1</sup>)</b>	
Macropore (7 μm – 50.4 nm) <sup>a</sup>	3.0
Mesopore (50.4 – 3.3 nm) <sup>a</sup>	1.0
Micropore (< 3.3 nm) <sup>b</sup>	0.4
<b>Total pore volume (cm<sup>3</sup>.g<sup>-1</sup>)</b>	<b>4.4</b>
<b>Mean pore diameter (nm) per family</b>	
<b>(at V<sub>macro</sub>/2 and V<sub>meso</sub>/2)</b>	
Macropore <sup>a</sup>	359
Mesopore <sup>a</sup>	19
Micropore	< 2

In an electrochemical application, it is also necessary for the support selected to be a good electronic conductor to enable the electron transfer. Conductivity measurements are therefore carried out using impedance spectroscopy and a sphere cell setup (see **Appendix B**) to characterize this key parameter. KB exhibits an intrinsic resistivity ( $\rho$ ) equal to  $3.9 \Omega \cdot \text{cm}^{105}$  ( $\sigma = 0.25 \text{ S} \cdot \text{cm}^{-1}$ ). This value is lower than the carbon “Super C65” conductivity ( $\sigma = 1.13 \text{ S} \cdot \text{cm}^{-1}$ )<sup>101</sup> or “Super C45” ( $\sigma = 1.77 \text{ S} \cdot \text{cm}^{-1}$ )<sup>106</sup>, carbon additives mainly used in the formulation of batteries electrodes to improve the electronic percolation, but we assume that the KB conductivity could ensure sufficient electronic conduction. Nevertheless, to enhance the electronic percolation, a 2 wt.% percent of carbon black “C65” will be added to the electrode formulation (described in **Chapter IV**).

To finalize the set of characterizations, the graphitization state is determined by Raman spectroscopy. The obtained spectrum shows two broad absorption bands in the region between 1000 and 1800 cm<sup>-1</sup> (**Figure II-4**). The D-band is observed at 1344 cm<sup>-1</sup> and is more intense than the G-band at 1602 cm<sup>-1</sup>. D-band and G-band correspond to defect-rich (D) and defect-

free (G) state respectively. The difference of intensity indicated that Ketjenblack is not an highly ordered graphite and presented defaults<sup>101,107,108</sup> that can be due to (tetrahedral carbon sp<sup>3</sup> and clustering<sup>109</sup>) which lower the electronic conductivity compared to highly graphitized carbon like Super C65 (G-band > D-band intensity)<sup>110</sup>.

The ratio of intensity between D and G-band ( $I_D/I_G$ ) is equal to 1.10 which in line with KB literature<sup>111</sup>

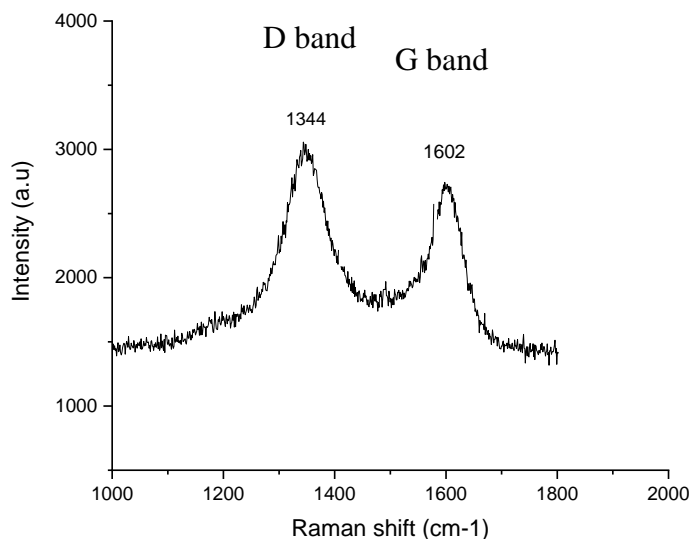


**Figure II-4. Raman spectrum of KB.**

In summary, the KB material is composed of primary particles of 30-50 nm with arrangements of graphite planes in onion-like layers. These primary particles are aggregated into larger primary aggregates (100-1000 nm) and finally in large agglomerates of 50-200  $\mu\text{m}$ . The material featured internal voids with several levels of porosity, including macro, meso, and microporosity. KB exhibits a total pore volume of 4.4  $\text{cm}^3\text{g}^{-1}$ , of which 69%, 23% and 8% are developed by macro, meso and micropores respectively. A large BET surface area of 1364  $\text{m}^2\text{g}^{-1}$  is calculated. These characterizations confirm that the KB texture should be suitable i) to offer a substantial surface area for optimal dispersion of the MoS<sub>2</sub> particles, ii) to host a significant volume of sulfur active material (sulfur), iii) to store the excess of electrolyte inside KB macropores and iv) to provide residual space to accommodate volumetric variations observed upon cycling (+/- 80%). Its 0.25  $\text{S}\cdot\text{cm}^{-1}$  conductivity is also sufficient to ensure a sufficient electronic conductivity withing the positive electrode. That is why numerous studies in literature chose this carbon in the electrode formulation<sup>112-114</sup>.

### 1.3 Synthesis and characterization of MoS<sub>2</sub>-KB host structures

To assess the MoS<sub>2</sub> structure/ polysulfide adsorption relationship, two main synthesis parameters are varied to play on MoS<sub>2</sub> structure: i) Mo loading and the ii) sulfidation conditions as summarize on **Figure II-5**. The aim is to customize the number and nature of the active sites. Each modification of the synthesis parameter will be the subject of a subsection.

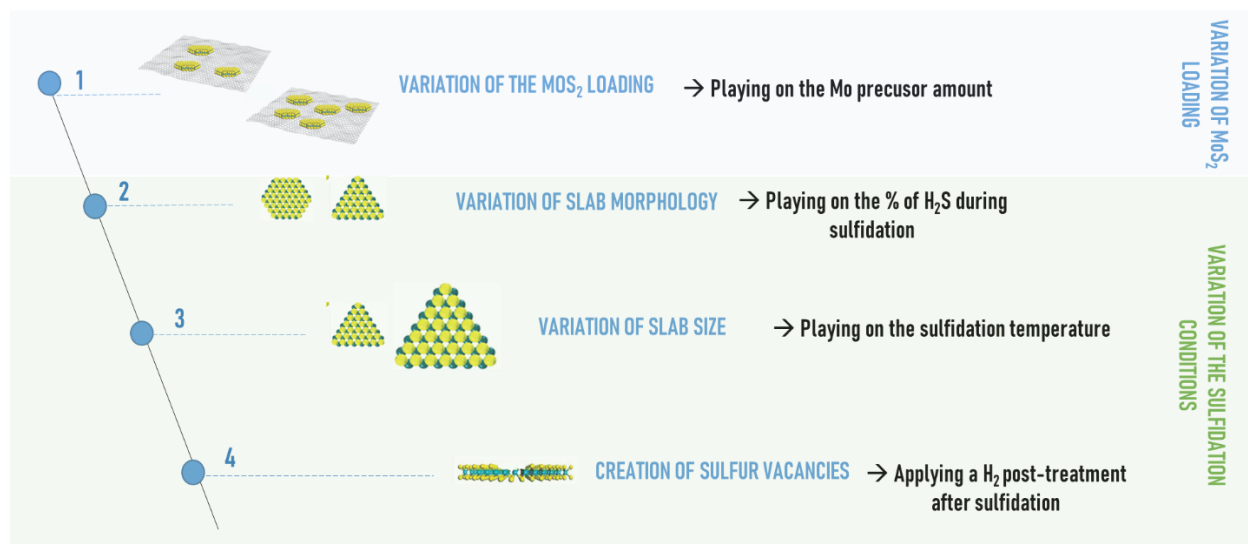


**Figure II-5.** Overview of the parameters chosen to modify the MoS<sub>2</sub>-KB structure and the related synthesis settings.

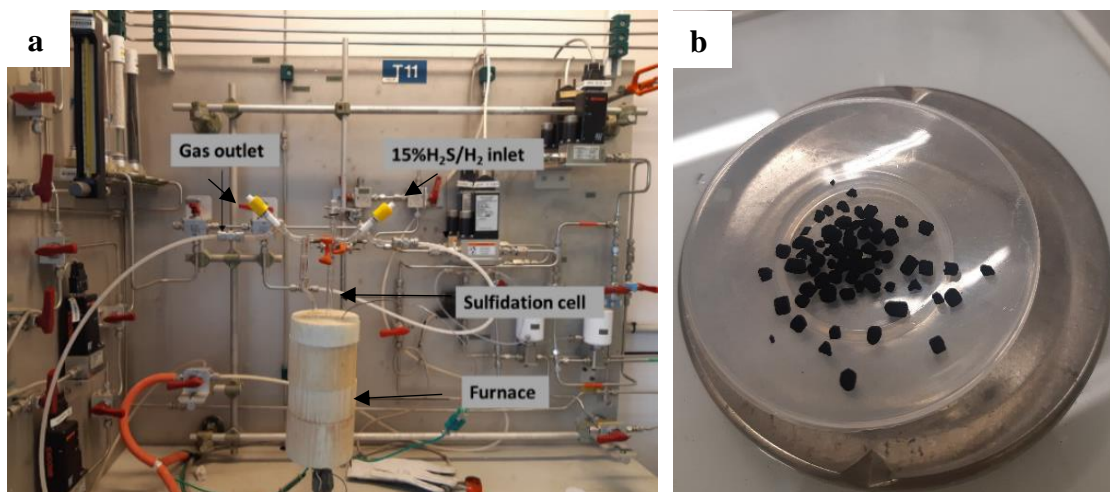
The protocol chosen to synthesize supported MoS<sub>2</sub> on Ketjenblack (MoS<sub>2</sub>-KB) is a combination of incipient wetness impregnation (IWI) method followed by a gas phase sulfidation step. This method saves a considerable amount of solvent during the synthesis and enables to only fill the pore volume of the support, without any excess.

The IWI consists of filling KB pore volume with a solution containing the desired amount of phosphomolybdic acid (H<sub>3</sub>PMo<sub>12</sub>O<sub>40</sub>, 30.5 H<sub>2</sub>O, PMA, Alfa Aesar) dissolved in 18.5 mL of ethanol (see **Table II-3**). The impregnation solution migrates into the support by capillary forces during the ageing step, performed under saturated ethanol vapor atmosphere for 12 h. The solvent is then evaporated during a final drying under air at 120°C for 3 h in an oven. At the end of this drying step, molecular Mo species are impregnated inside the support porosity.

**Table II-3.** Mass of PMA used in the impregnation solution for a targeted percentage of supported MoS<sub>2</sub>.

Percentage of MoS <sub>2</sub> targeted (wt.%)	30	50
Percentage of MoS <sub>2</sub> obtained (wt.%)	32	48
Mass of PMA (g) used in the impregnation solution	2.6	10.3

Standard gas phase sulfidation is performed in a 30 cc glass reactor adapted with a P3 frit (10-16  $\mu\text{m}$  pore size). The sulfidation is realized under 15% H<sub>2</sub>S/H<sub>2</sub> flow (2 L.h<sup>-1</sup>g<sup>-1</sup>) for 2h at 400°C to get final MoS<sub>2</sub>. The reactor is then cooled to 80°C under H<sub>2</sub>S/H<sub>2</sub> flow. An argon atmosphere is applied between 80 and 20°C cooling step to remove H<sub>2</sub>S/H<sub>2</sub> atmosphere and kept under vacuum before storage inside an argon-filled glove box. **Figure II-6-a** shows the sulfidation step which is settled inside a fume hood equipped with H<sub>2</sub>S detector and alarms and **Figure II-6-b** displays the agglomerated powder obtained after sulfidation.

**Figure II-6.** MoS<sub>2</sub>-KB synthesis a) Sulfidation reactor containing molecular MoS<sub>2</sub>-KB b) MoS<sub>2</sub>-KB material obtained after sulfidation

### 1.3.1 Variation of MoS<sub>2</sub> loading on MoS<sub>2</sub>-KB

The variation of MoS<sub>2</sub> loading aims to increase to number of active sites. The materials are prepared by varying the Mo content are synthesized using the standard IWI and sulfidation protocol under 15% H<sub>2</sub>S/85% H<sub>2</sub> v/v flow at 400°C during 2h, prior to argon cooling (from 80°C to 20°C). Host materials with different MoS<sub>2</sub> loadings from 32 and 48 wt. % are synthesized. The sample nomenclature is given in **Table II-4**. For instance, 32Mo-400-H<sub>2</sub>S(15) is

decomposed as follows: percentage of MoS<sub>2</sub> content (XMo)-temperature of sulfidation(400)-percentage of H<sub>2</sub>S in the gas mixture (H<sub>2</sub>S(15)).

**Table II-4. Sample nomenclature according to their MoS<sub>2</sub> loading obtained using XRF**

Sample names	Sulfidation conditions
32Mo-400-H <sub>2</sub> S(15)	15% H <sub>2</sub> S/85% H <sub>2</sub> 400°C 2h, argon cooling (80-20°C)
48Mo-400-H <sub>2</sub> S(15)	15% H <sub>2</sub> S/85% H <sub>2</sub> 400°C 2h, argon cooling (80-20°C)

After IWI and sulfidation, series of characterization are made to verify the chemical composition of the samples, to characterize MoS<sub>2</sub> slab length and stacking, the textural properties and the samples chemical composition homogeneity.

The chemical composition determination of the samples is made combining two techniques X-ray fluorescence (XRF) and CHNS. These methods are complementary as XRF provides information on molybdenum (Mo), phosphorous (P) and sulfur (S) contents while CHNS provides access to carbon (C), hydrogen (H) and nitrogen (N).

**Table II-5** exhibits the XRF and CHNS results. The Mo content are determined to be 19 and 29 wt.% which leads to 32 and 48 wt.% of MoS<sub>2</sub>. 1 wt.% of P and 66 and 36 wt.% of C are detected for **32Mo-400-H<sub>2</sub>S(15)** and **48Mo-400-H<sub>2</sub>S(15)**. The phosphorous, most likely present as P<sub>2</sub>S<sub>5</sub>, content originates from the H<sub>3</sub>PMo<sub>12</sub>O<sub>40</sub> precursor used during the IWI while the presence of carbon is associated with the KB support.

**Table II-5. Elemental analysis of MoS<sub>2</sub>-KB with Mo loading**

Obtained from XRF (the relative error associated to semi-quantitative analysis is approximately ± 20%)

Sample	Mo wt. %	P wt. %	S wt. %	MoS <sub>2</sub> calculated wt. %
32Mo-400-H <sub>2</sub> S(15)	19	1	12	<b>32</b>
43Mo-400-H <sub>2</sub> S(15)	29	1	21	<b>48</b>

Obtained from CHNS (error associated is about  $\pm 0.1\%$  between 0-10 wt.% and  $\pm 0.3\%$  between 10-50 wt.%)

Sample	C	H	S	Total
	wt. %	wt. %	wt. %	wt. %
32Mo-400-H <sub>2</sub> S(15)	66	0	13	79
43Mo-400-H <sub>2</sub> S(15)	36	0	26	62

The experimental amount of sulfided Mo (MoS<sub>2</sub>) is determined by X-ray Photo-electron Spectroscopy (XPS). The spectra are analyzed using the methodology reported by Gandubert *et al*<sup>115</sup>. Contributions of the different Mo oxidation states are then extracted. The proportion of MoS<sub>2</sub> is calculated by considering the Mo(IV) species to be only involved in the sulfide form. The XPS measurement has been done for 32Mo-400-H<sub>2</sub>S(15) and this sulfidation degree is assumed to be the same for all the samples.

**Figure II-7** exhibits the 32Mo-400-H<sub>2</sub>S(15) XPS spectral decomposition of Mo 3d. The spectrum is composed of four contributions. Each Mo contribution accounts for a doublet, with two positions for 3d<sub>5/2</sub> and 3d<sub>3/2</sub>. Peaks at 233.06 eV and 229.92 eV are attributed to Mo<sup>5+</sup> oxysulfide (MoO<sub>x</sub>S<sub>y</sub>)<sup>95</sup>. The two main intense peaks at 232.07 (3d<sub>3/2</sub>) and 228.93 (3d<sub>5/2</sub>) eV are characteristic of Mo<sup>4+</sup> in MoS<sub>2</sub><sup>111,116</sup>. Finally, the higher binding at 235.15 and 232.00 eV refer to Mo<sup>6+</sup> which may result either from the oxidation of the sample<sup>117</sup> that can be rapidly formed after only 10 min of exposure to ambient<sup>118</sup> or incomplete sulfidation. Peaks at 227.16 and 226.06 eV correspond to S 2s (-1) and (-2) of the MoS<sub>2</sub><sup>116,117</sup>. Quantification of Mo species is presented in **Table II-6**.

32Mo-400-H<sub>2</sub>S(15) sample is composed of 81% MoS<sub>2</sub> accounting for 2.61% atomic Mo (16.4 wt.% Mo). Additionally, there are 11% oxide species<sup>118</sup> and 9% oxysulfides<sup>95</sup>. All the Mo atoms from the phosphomolybdic acid (H<sub>3</sub>PMo<sub>12</sub>O<sub>40</sub>) used during the synthesis are not converted into MoS<sub>2</sub>. The sulfidation degree of approximately 0.8 is achieved, it is a high and “conventional” value for supported catalysts.



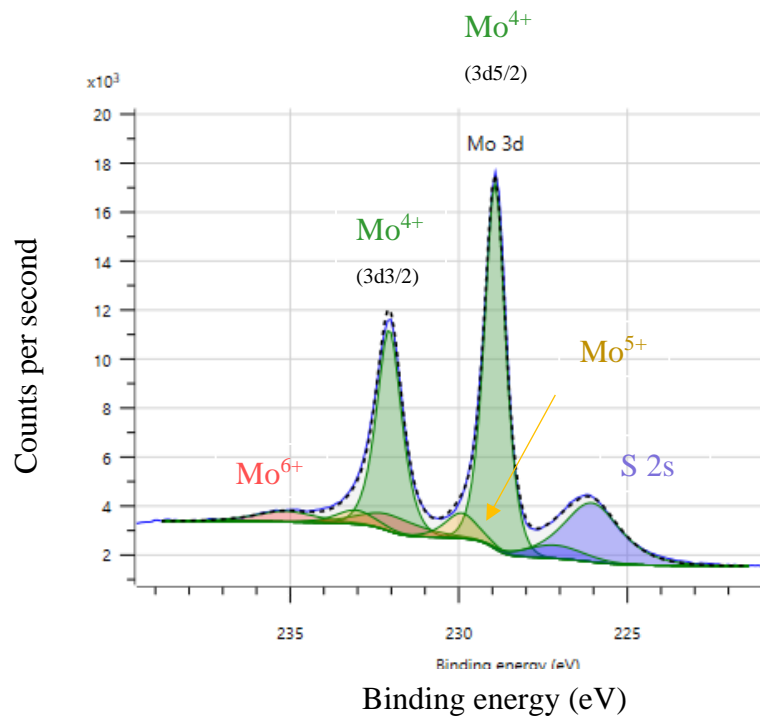


**Figure II-7.** 32Mo-400-H<sub>2</sub>S(15) XPS spectral decomposition.

**Table II-6.** Decomposition of Mo 3d XPS spectra for 32Mo-400-H<sub>2</sub>S(15). The data express the relative percentage of atoms according to their oxidation state.

	Mo <sup>6+</sup> (MoO <sub>3</sub> ) (%)	Mo <sup>5+</sup> (MoO <sub>x</sub> S <sub>y</sub> ) (%)	Mo <sup>4+</sup> sulfided (MoS <sub>2</sub> ) (%)	Total Mo (% atomic)
32Mo-400-H <sub>2</sub> S(15)	11	9	81	2.61

**Figure II-8 a** and **b** show the particles size distribution weighted in volume and number obtained, using the same conditions than KB, for the two MoS<sub>2</sub>-KB sample compared to pure KB. After Mo impregnation the particle size distribution in volume is slightly shifted to smaller values for 32Mo-400-H<sub>2</sub>S(15) compared to KB with a median particle size of 60  $\mu\text{m}$  instead of 76.6  $\mu\text{m}$ . For 48Mo-400 H<sub>2</sub>S(15), the distribution is modified. Two populations are visible, one centered around 90  $\mu\text{m}$ , and the other one distributed between 1-20  $\mu\text{m}$ . The median particle size is equal to 32.2  $\mu\text{m}$  in volume.

In terms of number weighted distribution, 50% of the 32Mo-400-H<sub>2</sub>S(15) and 48Mo-400-H<sub>2</sub>S(15) samples are smaller than 2.4 and 1.4, respectively, making them smaller in number than the KB particles. The impregnation of MoS<sub>2</sub> does not enlarge the particles, which suggests that the MoS<sub>2</sub> has penetrated the porosity of the KB and have a slight “deagglomeration” effect.

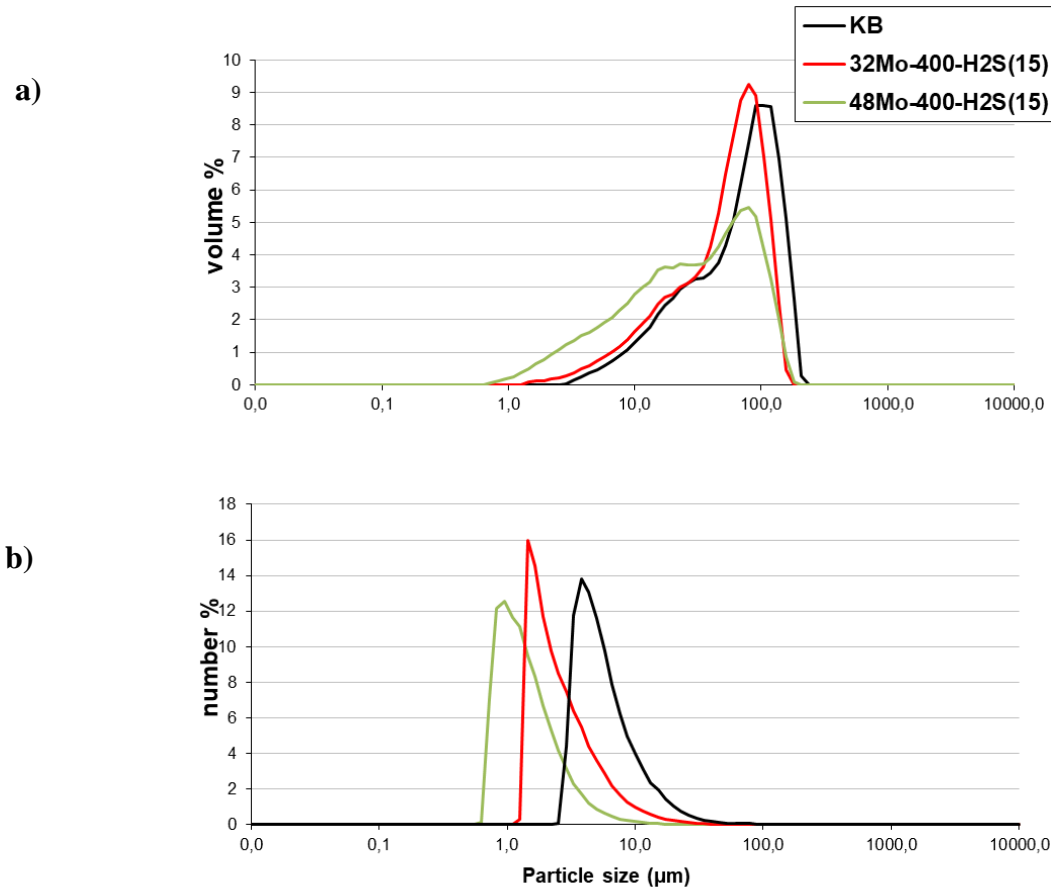


**Figure II-8.** MoS<sub>2</sub>-KB compared to pure KB particles size distribution a) weighted in volume b) weighted in number.

**Figure II-9-a** shows the particles direct observation using SEM. The chemical contrast is obtained with energy dispersive x-ray spectroscopy (EDX). The chemical contrast confirmed that, each KB particles contained Mo atoms. **Figure II-9-b** and **Table II-7** display the particle cross section along with a corresponding semi-quantitative study performed on a grain-by-grain basis. The weight percentage of each atom is calculated using oxygen (O) normalization. These results reveal that MoS<sub>2</sub> concentration is inhomogeneous between MoS<sub>2</sub>-KB particles from the same batch synthesis (shade of white reflected the Mo concentration). This heterogeneity is particularly accentuated at low MoS<sub>2</sub> concentrations (32 wt.%). Such variations could stem from an underestimation of the porous volume available of the initial KB carrier.

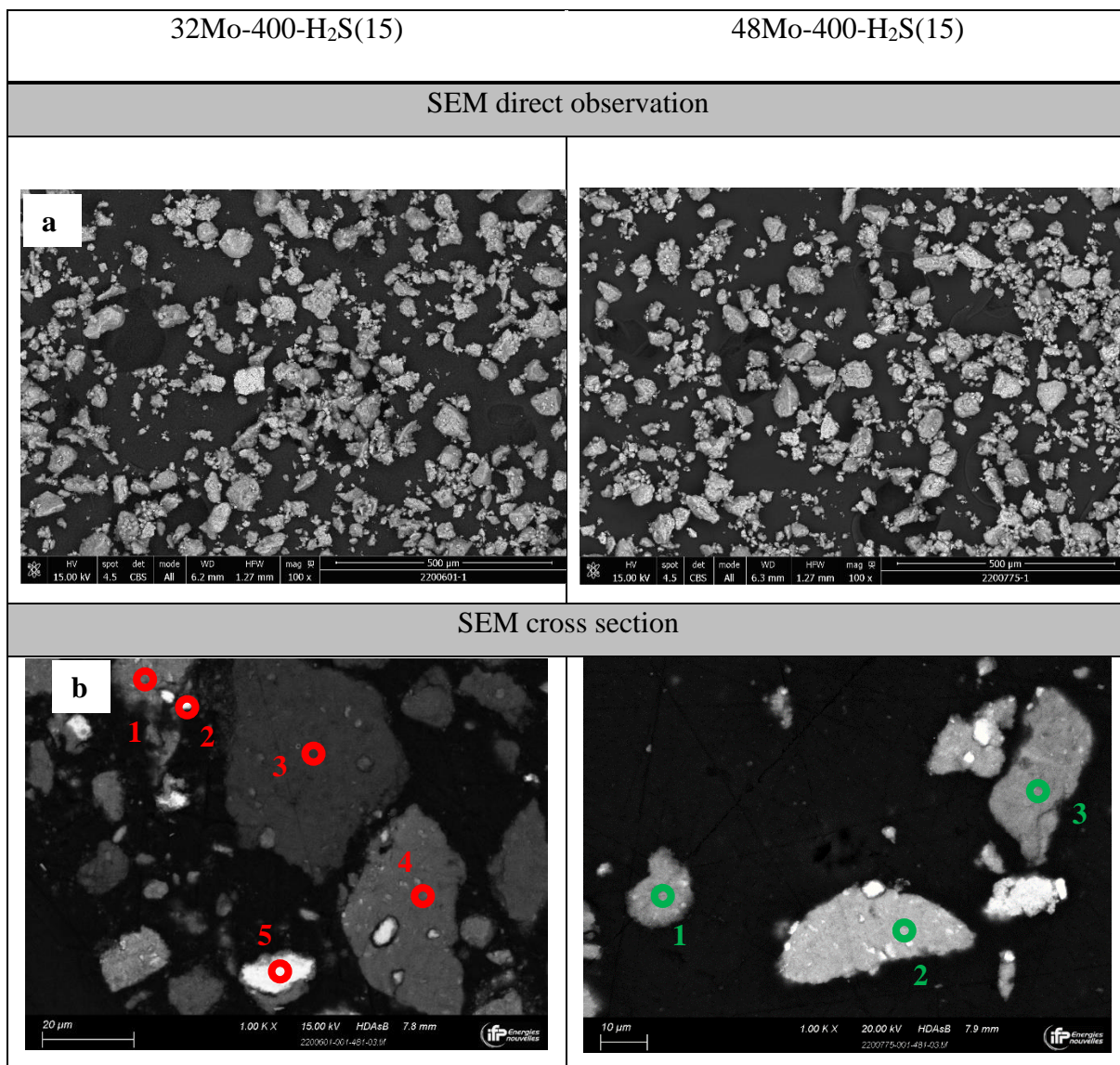


**Figure II-9.** SEM images of 32Mo-400-H<sub>2</sub>S(15) and 48Mo-400-H<sub>2</sub>S(15) a) direct observation of a particles b) cross section.

**Table II-7. Semi quantitative study of C, O, P, Mo contents grains by grains for SEM cross section of a) 32Mo-400-H<sub>2</sub>S(15) and b) 48Mo-400-H<sub>2</sub>S(15).****a. 32Mo-400-H<sub>2</sub>S(15)**

Spectrum	C	O	P	Mo
	wt. %	wt. %	wt. %	wt. %
1	63.8	10.1	0.2	25.9
2	53.9	7.5	0.4	39.2
3	75.4	11.5	0.0	13.1
4	66.0	10.5	0.2	23.3
5	31.4	6.3	0.2	62.0

**b. 48Mo-400-H<sub>2</sub>S(15)**

Spectrum	C	O	P	Mo
	wt. %	wt. %	wt. %	wt. %
1	71.2	11.9	0.1	16.8
2	60.7	9.8	0.2	29.2
3	57.3	9.1	0.2	33.3

The results of Raman measurements are shown in **Figure II-10**. The signature of Ketjenblack is found at the same Raman modes as KB itself (presented in the previous section) with peaks at 1344 and 1602 cm<sup>-1</sup>. The peak at 765 cm<sup>-1</sup> remains unassigned. MoS<sub>2</sub> can be recognized by characteristic peaks at 380, and 405 cm<sup>-1</sup>. They belong to two characteristic modes, E<sub>2g</sub><sup>1</sup> at 380 cm<sup>-1</sup> and A<sub>1g</sub> at 405 cm<sup>-1</sup> <sup>119-121</sup>. E<sub>2g</sub><sup>1</sup> emerges from in-plane (opposite S atoms vibrations bonded with Mo atoms) and A<sub>1g</sub> from out-of-plane (vibrations of two S atoms in opposite direction of Mo atom) from hexagonal MoS<sub>2</sub> <sup>122,123</sup>. The peak at 214 cm<sup>-1</sup> is less described in MoS<sub>2</sub> literature but the vibration can be assigned to in-plane longitudinal acoustic (LA) an acoustic branches <sup>124</sup>. Zhang *et al* <sup>123</sup> even demonstrated that these two Raman modes exhibited sensitive thickness dependence, with the frequency of the former decreasing and that of the latter increasing with thickness. The  $\Delta = 25$  cm<sup>-1</sup> between these two peaks is the signature for a MoS<sub>2</sub> stacking close to 1. Further, TEM is conducted to characterize the stacking and slab length of MoS<sub>2</sub>.

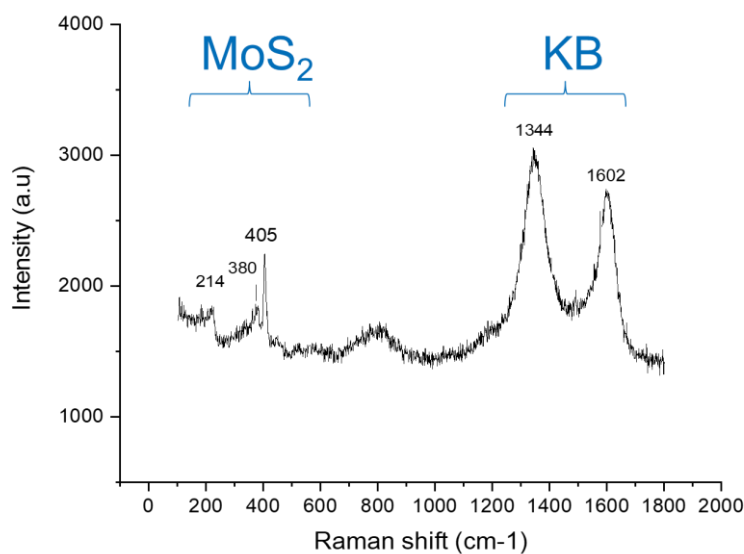


**Figure II-10. Raman spectra of 32Mo-400-H<sub>2</sub>S(15).**

TEM microscopy is performed using Bright Field (BF) mode, which is useful to highlight the morphology of the support (Ketjenblack) while scanning transmission electron microscope (STEM) images (High-angle annular dark-field imaging - HAADF) highlights the metallic phase which appeared darker than KB<sup>124</sup>. **Figure II-11-a** shows TEM BF images of **32Mo-400-H<sub>2</sub>S(15)** and **48Mo-400-H<sub>2</sub>S(15)**. MoS<sub>2</sub> slabs are marked by red circles on TEM images. The MoS<sub>2</sub> is observed in the form of "classic" hexagonal slabs, which can be seen either 'edge-on' or 'flat'. The slabs are positioned between the graphite planes and follows the curvature of the carbon sheets. Differences in stacking and slab length can only be noticed with High Resolution (HR) HAADF STEM (**Figure II-11 b-c**). **32Mo-400-H<sub>2</sub>S(15)** shows a lower density of MoS<sub>2</sub> slabs within the KB porosity. For both samples, the entanglement of MoS<sub>2</sub> does not allow for a clear distinction in the morphology of slabs (whether triangular or hexagonal) from flat MoS<sub>2</sub>. To achieve this, it is necessary to work with lower MoS<sub>2</sub> loading as shown in **section II-1.3.2.2**. The TEM images confirm the MoS<sub>2</sub> successful anchoring inside the KB's porosity.

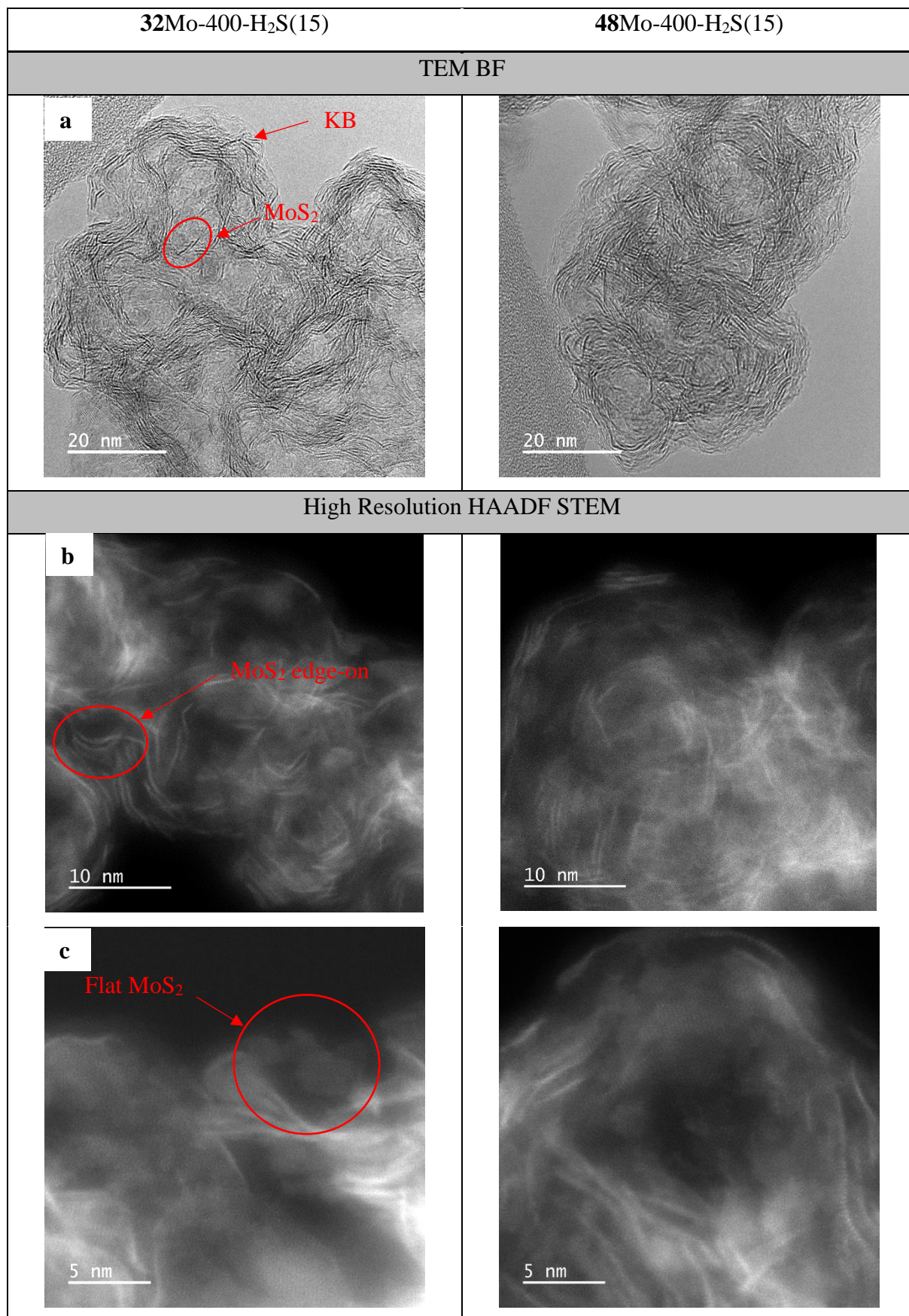


**Figure II-11.** TEM images of 32Mo-400-H<sub>2</sub>S(15) and 48Mo-400-H<sub>2</sub>S(15) using a) BF TEM b) and c) HR HAADF-STEM.

To obtain the average MoS<sub>2</sub> stacking and slab length, a statistical analysis<sup>117,125</sup> is made by analyzing a large number of HR HAADF-STEM images (details on the statistical analysis developed by B.Baubet *et al.*<sup>125</sup> is depicted in **Appendix B**). 13 and 26 images are manually analyzed to get 224 and 172 measurements of MoS<sub>2</sub> slabs for **32Mo-400-H<sub>2</sub>S(15)** and **48Mo-400-H<sub>2</sub>S(15)** respectively (using LOGRAMI software from IFPEN). The statistical results are shown in **Figure II-12 a and b**.

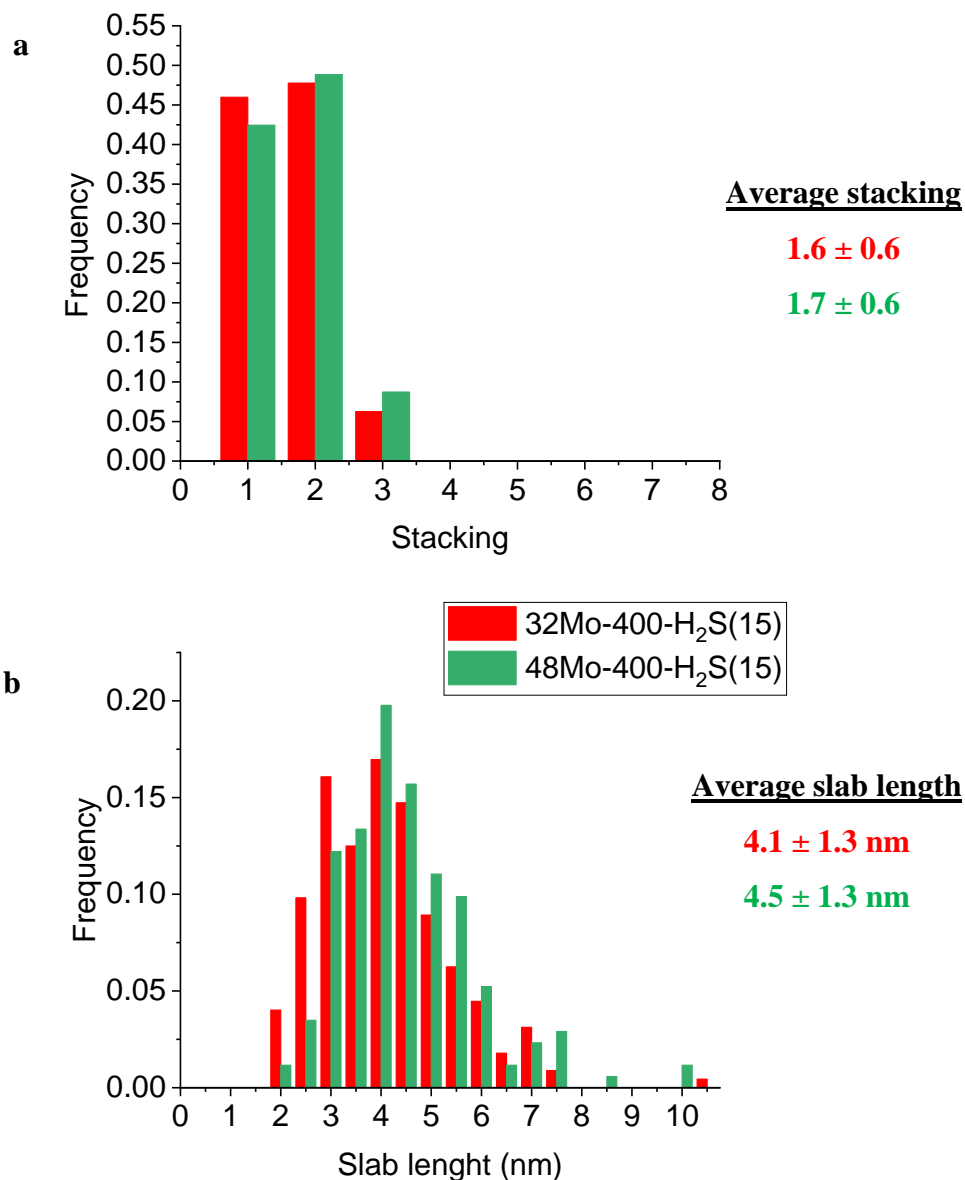


**Figure II-12.** MoS<sub>2</sub> a) stacking and b) slab length distributions of **32Mo-400-H<sub>2</sub>S(15)** and **48Mo-400-H<sub>2</sub>S(15)**.

(Histograms obtained from the analysis of 16 and 26 HR HAADF-STEM images and 224 and 172 measurements)

As shown on **Figure II-12-a** both samples are composed of majority of mono and double MoS<sub>2</sub> slabs. Only few triple layers are counted. An average staking of 1.6 and 1.7 nm is obtained for **32Mo-400-H<sub>2</sub>S(15)** and **48Mo-400-H<sub>2</sub>S(15)** respectively, in agreement with stacking number deduced from Raman's results. **Figure II-12-b** shows that a slab length of 4.1 nm is achieved for **32Mo-400-H<sub>2</sub>S(15)** while 4.5 nm are obtained for **48Mo-400-H<sub>2</sub>S(15)**. As a result, the increase of the loading does not lead to a significant increase of the mean slab length and stacking. This may be due to the very large initial surface area developed by the KB able to accommodate at these high loading the Mo as very small single slabs. The increase of the loading then allows to increase the accessible Mo surface area keeping other parameters constants.

Using the previous results and the geometric model developed by S.Kasztelan *et al.*<sup>126</sup>, it is possible to calculate the the total amount of atoms (edge+basal plane) in the particle and the fraction of atoms located on the edges+corners (dispersion, *D*) and the surface developed by MoS<sub>2</sub> slabs. These parameters are calculated from equation of **Figure II-13**. The results are given in **Table II-8**.

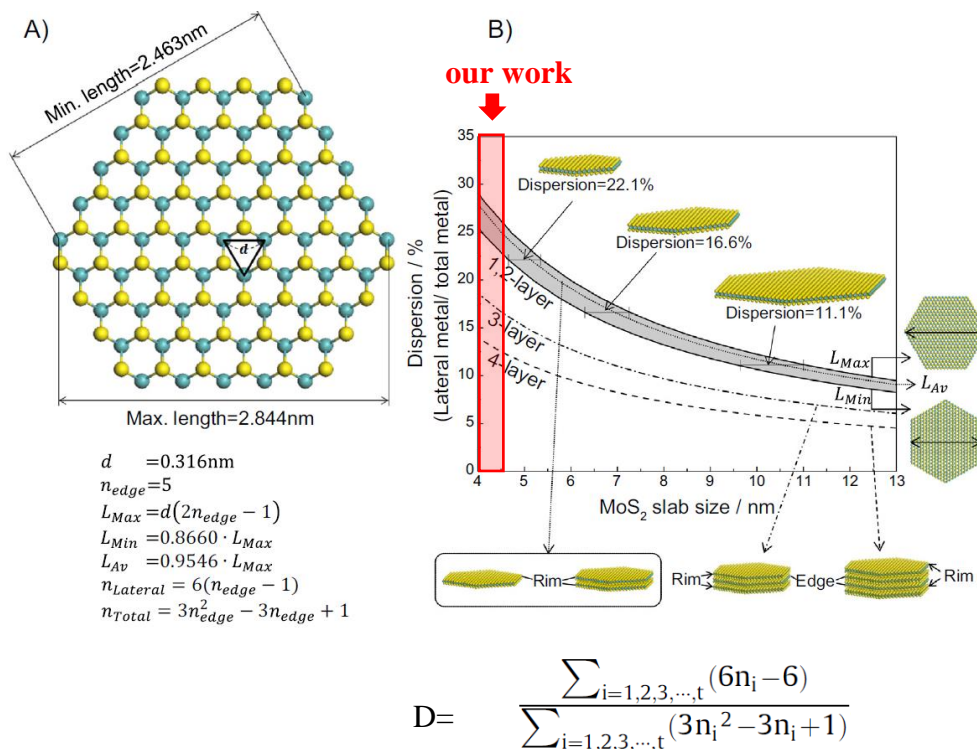


**Figure II-13.** Correlation of dispersion [(edges+corners)/(edges+corners+basal plan)] total with MoS<sub>2</sub> slab size and scheme of hexagonal MoS<sub>2</sub> slab. Reproduced from K-D Kim, Y-K Lee<sup>127</sup>.



**Table II-8. Slabs characteristics with MoS<sub>2</sub> loading.**

Sample	Slab length (nm)	Average stacking	Dispersion (%)	Slabs surface* (m <sup>2</sup> / g MoS <sub>2</sub> -KB)
	From experiments		From geometric model calculations	
32Mo-400-H <sub>2</sub> S(15)	4.1 ± 1.3	1.6 ± 0.6	28	118
48Mo-400-H <sub>2</sub> S(15)	4.5 ± 1.3	1.7 ± 0.6	26	179

\* calculation instructions are given in **Appendix D**

A dispersion of 28 and 26% are determined for **32Mo-400-H<sub>2</sub>S(15)** and **48Mo-400-H<sub>2</sub>S(15)** respectively, in line with D Kim *et al.*<sup>19</sup> (a red rectangle is drawn on **Figure II-13** to position our experimental results). Both samples have similar dispersion due to their similar small slab length. However, the higher loading of **48Mo-400-H<sub>2</sub>S(15)** results in a greater number of MoS<sub>2</sub> slabs, leading to 12.5 wt.% of edge-corners content (*calculated as following* : MoS<sub>2</sub> content in the sample \* dispersion = 48 \* 0.26) instead of 9 wt.% for **32Mo-400-H<sub>2</sub>S(15)** sample. This 1.4-fold increase in edge-corners content is beneficial for enhancing the interaction with polysulfides. Indeed, Wang *et al.*<sup>89</sup> calculated that Mo-edge exposed surface should be beneficial for sulfur interactions more than S-edge or basal plane. Calculated binding energies increased as follow Mo-edge > S-edge > basal plane (>> carbon). However, one can not exclude the basal plane as adsorption sites then one should consider the total surface developed by MoS<sub>2</sub> slabs as well. The total surface developed by all the slabs also varies by a factor of 1.4-1.5 from one sample to the other, which lead to an increase of the number of active sites increasing the MoS<sub>2</sub> loading. The fraction of edges+corners and the total MoS<sub>2</sub> surface increasing in the same way, it will not be possible to distinguish their respective influence on the LiPS adsorption phenomenon.

A textural analysis after the MoS<sub>2</sub> incorporation is conducted to evaluate how the pristine KB textural properties are modified. **Figure II-14** shows the Hg porosimetry measurement. Volume of 2.4 and 1.2 cm<sup>3</sup>.g<sup>-1</sup> is developed by macro + mesopores for 32 and 48 wt.% MoS<sub>2</sub> samples respectively. This leads to a porous volume decrease by 45 and 75 % with MoS<sub>2</sub> loading compared to pristine KB. After impregnation, samples depicted isotherm type IV isotherm with H<sub>4</sub> hysteresis loop as shown on **Figure II-15**. Therefore, the signature of mesopore, with non-uniform-sized slit-shaped pores<sup>103</sup>, remained after MoS<sub>2</sub> incorporation. 0.1 cm<sup>3</sup>.g<sup>-1</sup> micropore volumes are determined for both **32Mo-400-H<sub>2</sub>S(15)** and **48Mo-400-H<sub>2</sub>S(15)**.

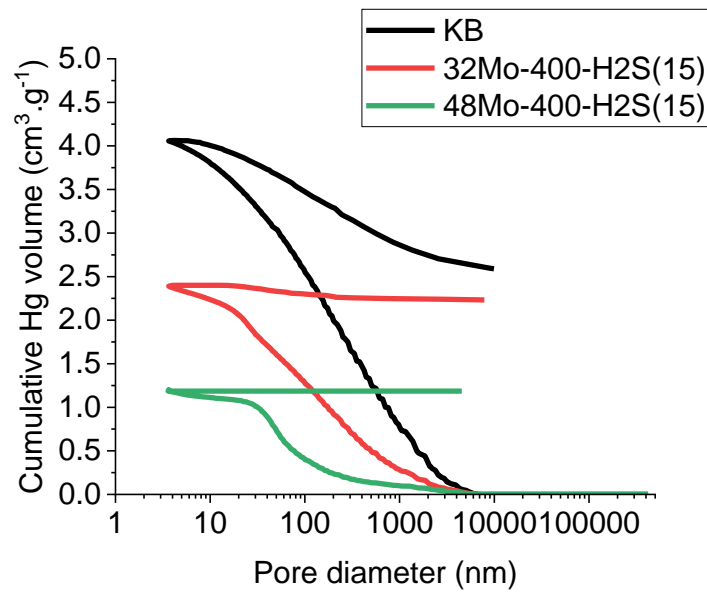


**Figure II-14.** Hg porosimetry of MoS<sub>2</sub>-KB with different MoS<sub>2</sub> loading.

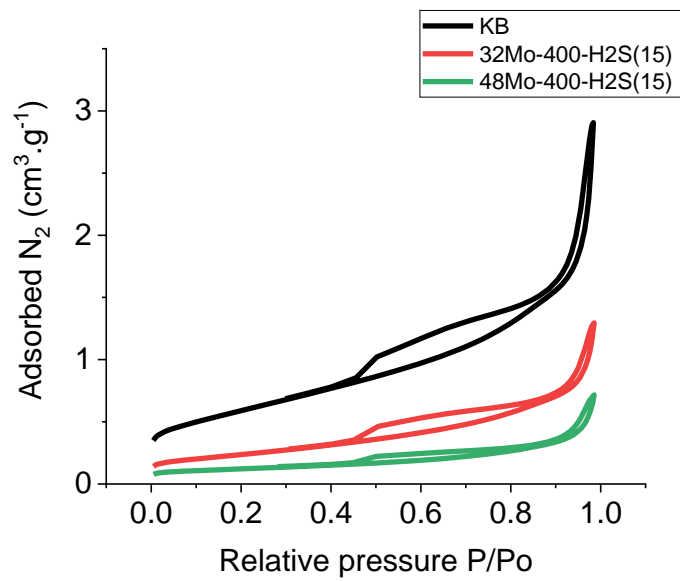


**Figure II-15.** N<sub>2</sub> adsorption-desorption isotherm MoS<sub>2</sub>-KB with different MoS<sub>2</sub> loading.

**Figure II-16 a** and **b** depict the evolution of the porous volume per pore family with Mo impregnation. When Mo is impregnated inside KB, each porous volume decreases as shown in **Figure II-16-a**, because MoS<sub>2</sub> lodges itself inside the KB pores, filling the voids. In relative terms, all pore families are similarly impacted (**Figure II-16-b**). Samples still exhibit approximately 60% of macro, 30% of meso and 10% of micropores in volume.

The remaining volume achieved after impregnation is not a limiting factor for the subsequent impregnation of active sulfur. Theoretical ratios  $V_{\text{host}}/V_{\text{Li}_2\text{S}}$  of 8 and 5 are reached for **32Mo-400-H<sub>2</sub>S(15)** and **48Mo-400-H<sub>2</sub>S(15)** respectively, assuming that the complete conversion of S<sub>8</sub> into Li<sub>2</sub>S, accompanied by a volumetric expansion 1.8, can still be accommodated without causing structural pulverization for a sulfur loading of  $\approx 1 \text{ mg}_s.\text{cm}^2$ .

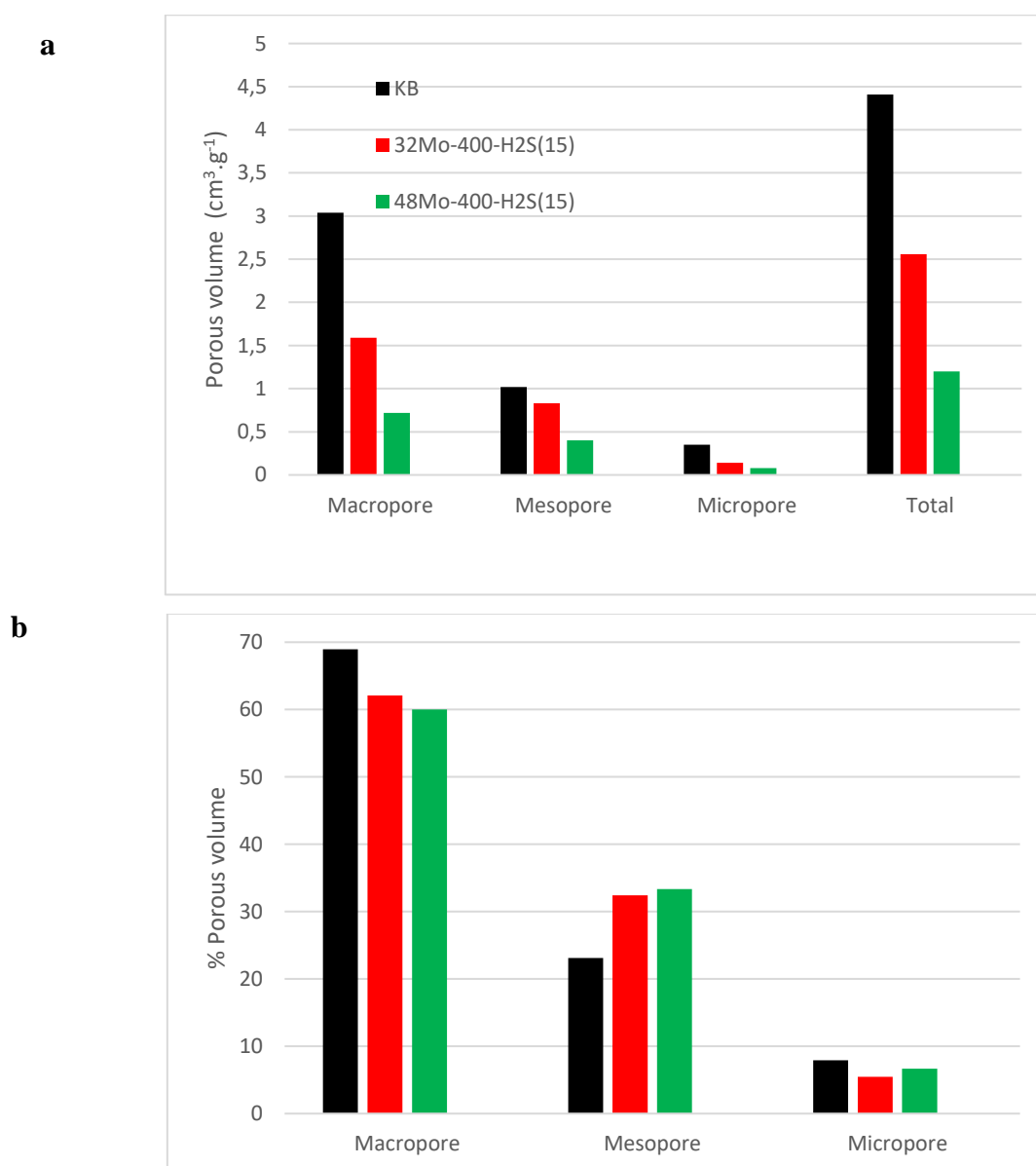


**Figure II-16.** Evolution of the porous volume per pore family after Mo impregnation **a)** in volume **b)** in percentage.

**32Mo-400-H<sub>2</sub>S(15)** shows 253 nm macropores and 23 nm mesopores whereas **48Mo-400-H<sub>2</sub>S(15)** has 113 nm macropores and 40 nm mesopores. As a reminder, the pristine KB shows 359 nm macropores and 19 nm mesopores. The Mo impregnation results in a reduction of the macropore diameters compared to pristine KB and an increase of the mesopore diameters. The residual BET surface area ranges from 543 to 276 m<sup>2</sup>.g<sup>-1</sup> for **32Mo-400-H<sub>2</sub>S(15)** and **48Mo-400-H<sub>2</sub>S(15)** respectively. Details of textural characteristics are summarized in **Table II-9**.

**Table II-9. Evolution of MoS<sub>2</sub>-KB textural characteristics with MoS<sub>2</sub> loading. Results are obtained from <sup>a</sup> Hg porosimetry, <sup>b</sup> N<sub>2</sub> adsorption-desorption isotherm.**

	32Mo-400-H <sub>2</sub> S(15)	48Mo-400-H <sub>2</sub> S(15)
<b>Surface area (m<sup>2</sup>.g<sup>-1</sup>)</b>		
BET <sup>b</sup>	543	276
<b>Pores volume per family (cm<sup>3</sup>.g<sup>-1</sup>)</b>		
Macropore (5.2 μm – 50.4 nm) <sup>a</sup>	1.6	0.7
Mesopore (50.4 – 3.3 nm) <sup>a</sup>	0.8	0.4
Micropore (< 3.3 nm) <sup>b</sup>	0.1	0.1
<b>Total pore volume (cm<sup>3</sup>.g<sup>-1</sup>)</b>	2.6	1.2
<b>Mean pore diameter (nm) per family</b>		
<b>(at V<sub>macro</sub>/2 and V<sub>meso</sub>/2)</b>		
Macropore <sup>a</sup>	253	113
Mesopore <sup>a</sup>	23	40
Micropore	< 2	< 2

To conclude, the set of characterization confirmed that MoS<sub>2</sub>-KB structure with 32 and 48 wt.% of MoS<sub>2</sub> loading are successfully achieved. Within these structures, small mono and double MoS<sub>2</sub> slabs ranging from 4.1 to 4.5 nm are anchored inside each KB's pore families. Playing on the MoS<sub>2</sub> loading contributes to a proportional increase in the total slab surface and the fraction of edges+corners by a factor of  $\approx 1.4 - 1.5$ . This, in turn, results in a higher number of adsorption active sites when MoS<sub>2</sub> loading increases.

The samples exhibit a 2.6 and 1.2 cm<sup>3</sup>g<sup>-1</sup> total pore volume, comprising 60% of macro, 30% meso and 10% micropores in volume and develop a large BET surface of 543 and 276 m<sup>2</sup>.g<sup>-1</sup> for 32Mo-400-H<sub>2</sub>S(15) and 48Mo-400-H<sub>2</sub>S(15) respectively. It is essential to set aside some unoccupied space within MoS<sub>2</sub>-KB to infiltrate electroactive sulfur and electrolyte and keep enough void to accommodate the volumetric expansion of sulfur during cycling. The remaining pore volumes are still significant to infuse the 30 wt.% used in the Li-S positive electrode formulation, shown in [chapter IV](#). Even after this sulfur incorporation of structure S-MoS<sub>2</sub>-KB retains 8 and 5 the volume of Li<sub>2</sub>S.

The following section will detail the synthesis and characterization of other samples for which the sulfidation conditions have been modified to alter the nature of the active sites.

### 1.3.2 Variation of sulfidation conditions on MoS<sub>2</sub>-KB

Variation of the sulfidation conditions have been selected to modify the nature of the MoS<sub>2</sub> active sites by i) modifying the surface state and ii) generating triangular MoS<sub>2</sub> with higher edges+corners fraction<sup>95,125</sup>. The modifications of the standard setup and their roles are displayed in [Table II-10](#). The selected sulfidation conditions, which include post-treatment, the type of sulfidation gas, and temperature adjustments, are outlined in [Table II-11](#) along with the corresponding sample identification names. The sulfidation program associated is presented in [Figure II-17](#). For example, the sample sulfided in pure H<sub>2</sub>S at 400°C with a H<sub>2</sub> and N<sub>2</sub> post-treatment at 300°C is designated 400- H<sub>2</sub>S(100)-NH.

**Table II-10. Targeted modification of the MoS<sub>2</sub> structure with variations of the standard incipient wetness impregnation-sulfidation protocol.**

Aims	Variation of sulfidation conditions	Impact on MoS <sub>2</sub> structure
Modifying the surface state	<p><b>Application of a post-treatment at 300°C</b></p> <ul style="list-style-type: none"> <li>- Under pure N<sub>2</sub> flow</li> <li>- Under H<sub>2</sub> and N<sub>2</sub> successive flows</li> </ul>	<ul style="list-style-type: none"> <li>- Removal of H<sub>2</sub> (from H<sub>2</sub>S/H<sub>2</sub> sulfidation gas) adsorbed at the surface of MoS<sub>2</sub></li> <li>- Creation of “CUS“ by removal of labile S neighbors on the edge</li> </ul>
	<p><b>Modification of the gas nature from 15% H<sub>2</sub>S/85% H<sub>2</sub> to 100% pure H<sub>2</sub>S</b></p>	Formation of triangular MoS <sub>2</sub> with rich-edges+corners
Generating triangular MoS <sub>2</sub>	<b>Sulfidation from 400 to 600°C</b>	Increase the fraction of triangular MoS <sub>2</sub>

**Table II-11. Sample nomenclature according to their sulfidation conditions.**

Sample name	Sulfidation conditions
<b>Post-treatment variation</b>	
21Mo-400-H <sub>2</sub> S(15)-N	15% H <sub>2</sub> S/H <sub>2</sub> 400°C 2h, N <sub>2</sub> 300°C, 1h
28Mo-400-H <sub>2</sub> S(15)-HN	15% H <sub>2</sub> S/H <sub>2</sub> 400°C 2h, H <sub>2</sub> 300°C 1h, N <sub>2</sub> 300°C, 1h
<b>Gas nature and sulfidation temperature variation</b>	
22Mo-400-H <sub>2</sub> S(100)-HN	100% H <sub>2</sub> S 400°C 2h, H <sub>2</sub> 300°C 1h, N <sub>2</sub> 300°C, 1h
21Mo-600-H <sub>2</sub> S(100)-HN	100% H <sub>2</sub> S 600°C 2h, H <sub>2</sub> 300°C 1h, N <sub>2</sub> 300°C, 1h

The gases flow applied are for:

- the post-treatment: 1 L.h<sup>-1</sup>g<sup>-1</sup> for both N<sub>2</sub> or under H<sub>2</sub> and N<sub>2</sub> flow
- the sulfidation gas nature: 2 L.h<sup>-1</sup>g<sup>-1</sup> under a pure H<sub>2</sub>S flow

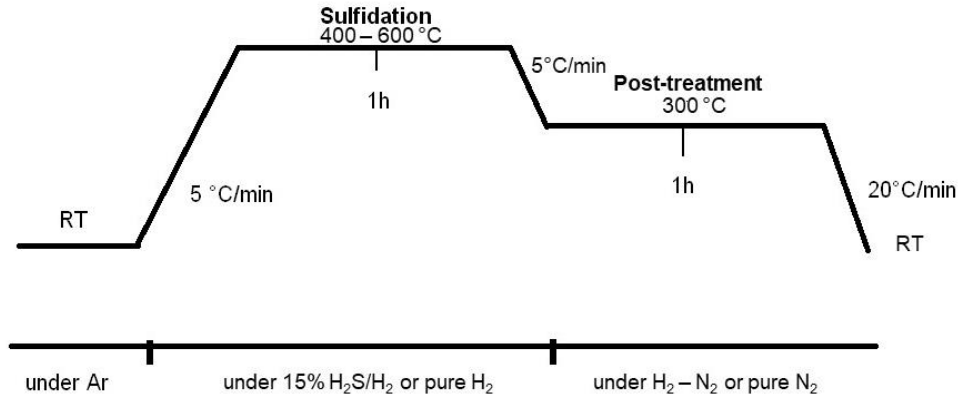


**Figure II-17. Sulfidation program**

The morphology characterization is a key-point in this study. Based on what we have learned in the previous subsection, it is needed to work with low MoS<sub>2</sub> loading < 32 wt.% to distinguish triangular vs hexagonal slabs from MoS<sub>2</sub> flat. Working with low loading avoids slabs overlaps and enables shape detection possible from hexagonal to triangular. For that reason, the sample loadings are set at 14 -21 wt.% for this entire subsection. The results obtained at these low Mo loadings may be assumed to be extrapolated to higher ones.

This subsection is divided in three parts detailing the results obtained and indicates whether the target MoS<sub>2</sub> structure has been obtained.

### 1.3.2.1 Post-treatment effect

Two post-treatments performed under 300°C, one under pure N<sub>2</sub>, and the other under H<sub>2</sub> followed by N<sub>2</sub>, are chosen to modify the surface state of MoS<sub>2</sub>. These choices are explained below:

- Post-treatment under N<sub>2</sub> (N)

In the standard IWI-sulfidation synthesis protocol, after the sulfidation at 400°C, the temperature is decrease down to 80°C under 15H<sub>2</sub>S/85%H<sub>2</sub> gas flow. During the cooling step between 400°C and 80°C, H<sub>2</sub> gas can be adsorbed at the surface of MoS<sub>2</sub>. The adsorption of species on the surface of the material would indeed be detrimental to the targeted application,

rendering the sites less accessible for polysulfides adsorption. To prevent this potential limitation, a post treatment under N<sub>2</sub> is applied to desorb H<sub>2</sub>.

- Post-treatment under H<sub>2</sub> and N<sub>2</sub> (NH)

Working under reducing H<sub>2</sub> conditions allowed for the removal of some part of the adsorbed sulfur in the form of H<sub>2</sub>S<sup>128, 94</sup>. The H<sub>2</sub>S desorption from the edge gives rise to the formation of a “coordinatively unsaturated sites” (CUS) after removing of the labile S neighbors on the Mo atom, modifying the Mo reactivity. P.Afanasiev<sup>128</sup> demonstrated that with a H<sub>2</sub> treatment at 300°C uncovered S- and Mo-edges are obtained for unsupported MoS<sub>2</sub> catalyst. In addition, these CUS are considered as vacant Lewis adsorption sites accessible to sulfur containing molecule<sup>65,72</sup>. **Table II-12** displays the element analysis of the two samples synthesized. Mo and S contents of 13 and 9 wt.% are obtained for **21Mo-400-H<sub>2</sub>S(15)-N** while **28Mo-400-H<sub>2</sub>S(15)-NH** displays 17 wt.% of Mo and 12 wt.% of S. The fraction of S on the KB support is negligible as it is calculated to be < 1 wt.%. From XRF results, the atomic ratio S/Mo are calculated to be 2.1 in both cases while an S/Mo ratio is theoretically expected to be < 2 after sulfur edge removal under H<sub>2</sub> and N<sub>2</sub>. CHNS results, no significant variation of H and S are observed for both samples. The XRF and CHNS measurements do not enables to confirm the sulfur desorption induced by the post treatment due to the accuracy of the measurement.

**Table II-12. MoS<sub>2</sub>-KB elemental analyses with post-treatment**

Obtained from XRF (relative error associated to semi-quantitative analysis is approximately ± 20%)

Sample	Mo wt. %	P wt. %	S wt. %	nS/nMo*	MoS <sub>2</sub> calculated wt. %
21Mo-400-H <sub>2</sub> S(15)-N	13	1	9	2.1	21
28Mo-400-H <sub>2</sub> S(15)-NH	17	1	12	2.1	28

\*nS/nMo ratio is calculated using **equation (II-1)**.

$$\frac{nS}{nMo} = \frac{\%S}{Mw_S} / \frac{\%Mo}{Mw_{SMo}} = \frac{\%S}{32} / \frac{\%Mo}{96} \quad (\text{II-1})$$

With Mw: molecular weight



Obtained from CHNS (error associated is about  $\pm 0.1\%$  between 0-10 wt.% and  $\pm 0.3\%$  between 10-50 wt.%)

Sample	C	H	S	Total
	wt. %	wt. %	wt. %	wt. %
21Mo-400-H <sub>2</sub> S(15)-N	64	4	13	81
28Mo-400-H <sub>2</sub> S(15)-NH	64	3	13	80

N<sub>2</sub> adsorption-desorption isotherms are shown on **Figure II-18**. BET surface areas of 732 and 682 m<sup>2</sup>.g<sup>-1</sup> are calculated for 28Mo-400-H<sub>2</sub>S(15)-NH and 21Mo-400-H<sub>2</sub>S(15)-N which account for a variation of 50 m<sup>2</sup>.g<sup>-1</sup>. Given that the MoS<sub>2</sub> loadings differ between the two samples, the reduction in surface area observed with the NH treatment is likely due to higher surface coverage in the case of 28 wt.% MoS<sub>2</sub> supported on KB.

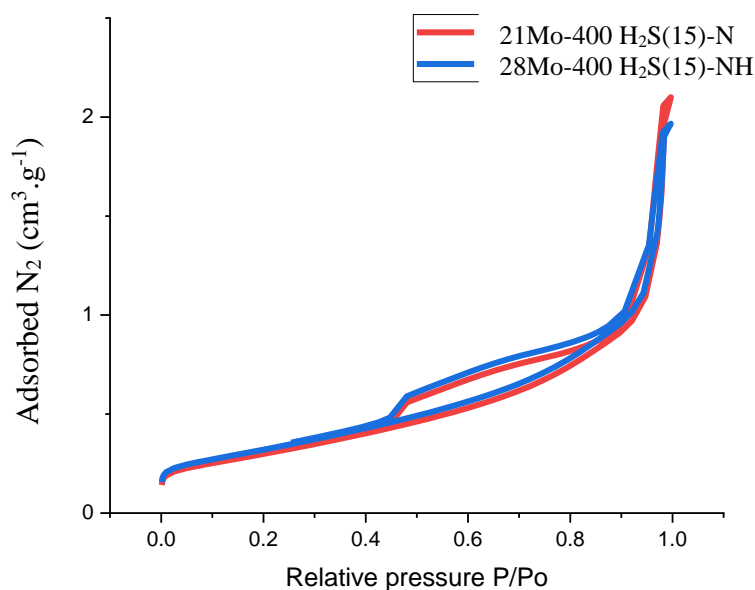


**Figure II-18.** Evolution of the MoS<sub>2</sub>-KB N<sub>2</sub> isotherms with different post-treatments.

The analyses carried out do not enable to confirm the post-treatment targeted. The use of temperature-programmed reduction (TPR) should have been more beneficial for that purpose<sup>128</sup>. Nevertheless, given the large number of studies in the literature conducted on this topic, it can be assumed that the post-treatments allowed different surface properties of the MoS<sub>2</sub> nanoparticles to be obtained.

### 1.3.2.2 Sulfidation gas nature effect

Varying the gas nature from 15% H<sub>2</sub>S/85% H<sub>2</sub> to pure H<sub>2</sub>S aims to promote the formation of truncated triangular MoS<sub>2</sub>, which exhibits a high fraction number of edges+corners, energetically favored for sulfur interactions compared to S-edges<sup>89</sup>. The effect of the sulfidation gas nature of the morphology of MoS<sub>2</sub> is investigated using HR HAADF STEM.

The XRF elemental analyses of the two sample are shown in **Table II-13**. Both samples are composed of 14 wt.% of MoS<sub>2</sub>. An increase of nS/nMo ratios of from 2.0 to 2.6 is observed for the 14Mo-400-H<sub>2</sub>S(100)-HN synthesized. Even with a NH post-treatment extra-sulfur are deposited on the MoS<sub>2</sub> edges as well as on the KB support under pure H<sub>2</sub>S.

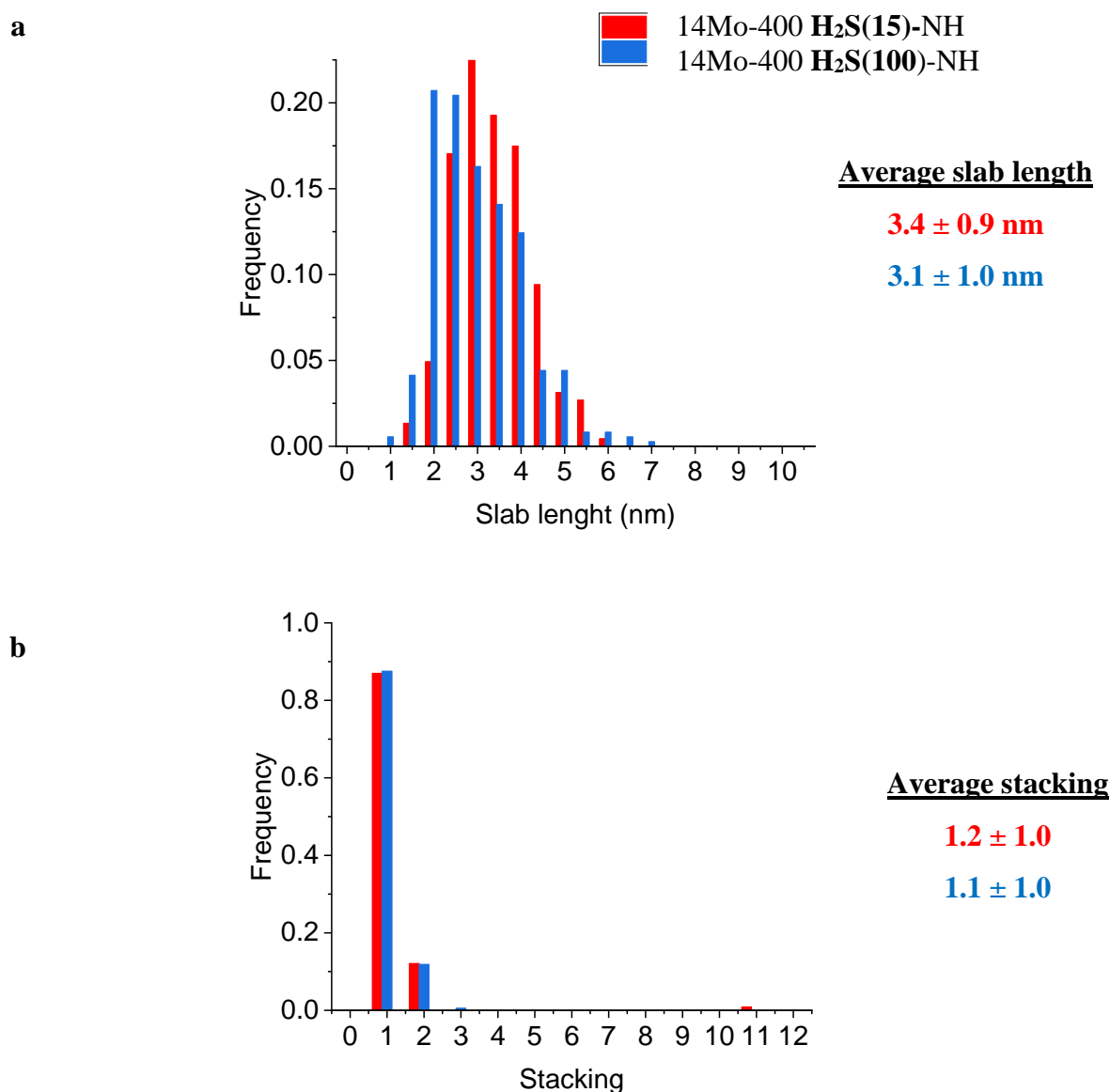
**Table II-13. MoS<sub>2</sub>-KB XRF elemental analysis with sulfidation gas nature.**

Sample	Mo wt. %	P wt. %	S wt. %	nS/nMo	S deposited on KB* wt. %	MoS <sub>2</sub> calculated wt. %
14Mo-400-H <sub>2</sub> S(15)-HN	8	0	6	2.0	0	14
14Mo-400-H <sub>2</sub> S(100)-HN	8	0	7	2.6	2	14

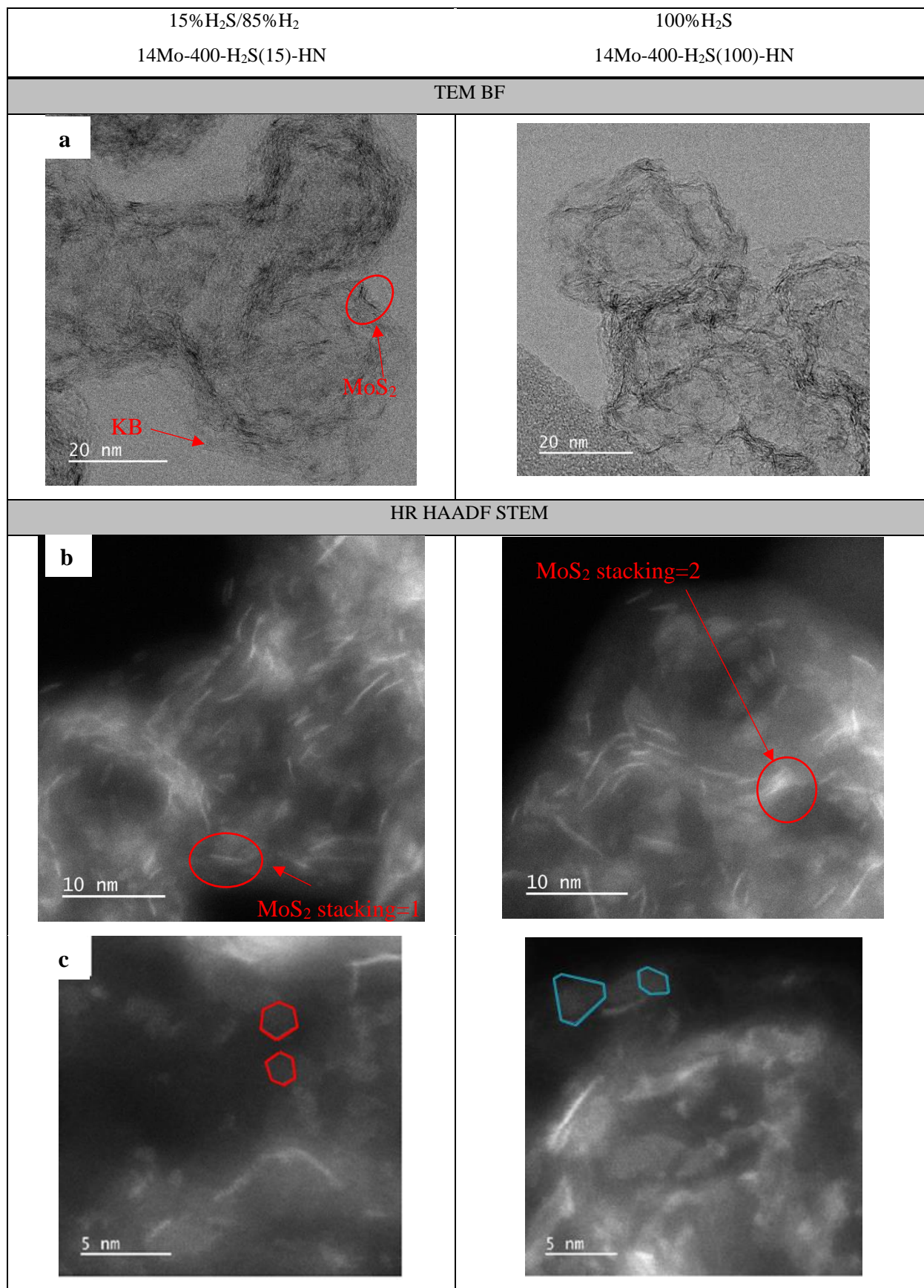
\* the sulfur content deposited on KB is calculated using **equation (II-2)**.

$$\begin{aligned}
 S \text{ content on KB (wt. \%)} &= \text{total S content from XRF} - S \text{ content from MoS}_2 \\
 &= \text{total S content from XRF} - \left( 2 * \frac{\text{Mo from XRF}}{96} * 32 \right) \quad \text{(II-2)}
 \end{aligned}$$

TEM images are displayed on **Figure II-20**. As previously noticed with the study of MoS<sub>2</sub> loading, MoS<sub>2</sub> slabs are positioned between the graphite planes showing onion-like structure. Samples are composed of well-defined MoS<sub>2</sub> monolayers, mainly fringes-oriented (**Figure II-20-a** and **b**). The average length size exhibits a decrease from 3.4 to 3.1 nm under pure H<sub>2</sub>S compared to the corresponding samples prepared under mixture of 15% H<sub>2</sub>S/85% H<sub>2</sub> (**Figure II-19-a**). The average stackings are similar between both samples. A majority of single and few double layers are recorded (**Figure II-19-b**). The monolayer arrangements attest a good dispersion of the active phase.

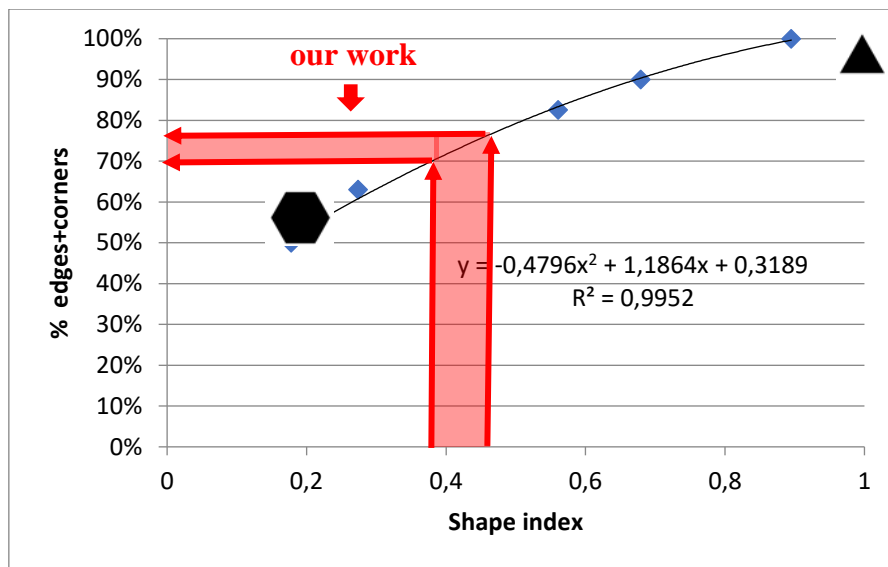







**Figure II-19.** MoS<sub>2</sub> a) slab length and b) stacking distributions on MoS<sub>2</sub>-KB with different sulfidation conditions. (Histograms obtained from the analysis of 22 and 28 HR HAADF-STEM images and 223 and 362 measurements)



**Figure II-20.** SEM images of MoS<sub>2</sub>-KB sulfided under pure H<sub>2</sub>S and 15% H<sub>2</sub>S/H<sub>2</sub> a) BF TEM, b) HR HAADF-STEM and c) at higher magnification (MoS<sub>2</sub> slabs are marked by the red circles and KB by the red arrow).

From HR-HAADF STEM images, it is clearly possible to distinguish a sufficient number of individual slabs. The MoS<sub>2</sub> morphology quantification to distinguish hexagonal from triangular is performed via Principal Component Analysis (PCA) method as described by Baubet *et al*<sup>125</sup> and led to the calculation of a *shape index*. The purpose of the shape quantification establishes a connection with a MoS<sub>2</sub> shape and provide an estimate of the proportion of edges+coners in the slab. **Figure II-21** shows the theoretical correlation reproduced from *PKS01-002*, internal IFPEN document. The shape index for a triangular form is 0.89, while a perfect hexagon has a shape index of 0.18.



Shape models					
Name		Triangular	Triangular truncated	Real hexagonal	Perfect hexagonal
% edges+corners		100%	90%	63%	50%
Shape index	0.0	0.89	0.68	0.27	0.18

**Figure II-21.** Theoretical relation between shape factor and % edges+corners using the PCA method for different shape models. Reproduced from *PKS01-002* internal IFPEN document.

**Figure II-22** reveals the shape index distribution obtained from SEM measurements and PCA analyses. Under 100% H<sub>2</sub>S sulfidation, the MoS<sub>2</sub> tends to contain more particles with a shape index between 0.5 and 0.9 than 15% H<sub>2</sub>S/85% H<sub>2</sub>. However, no shape index of 1 is visible, the triangular truncated shape better reflects the morphology of MoS<sub>2</sub>. Average shape indexes of 0.38 and 0.45 are calculated under 15% H<sub>2</sub>S/85% H<sub>2</sub> and 100% H<sub>2</sub>S sulfidation respectively as seen in **Table II-14**. Our results are reported on the **Figure II-21**. Under pure H<sub>2</sub>S gas, MoS<sub>2</sub> slab tends to form more truncated triangles in line with literature<sup>128</sup>. This treatment enables to slightly increase the percentage of edges+corners for a given MoS<sub>2</sub> loading and confirm connections between gas nature and MoS<sub>2</sub> morphologies.

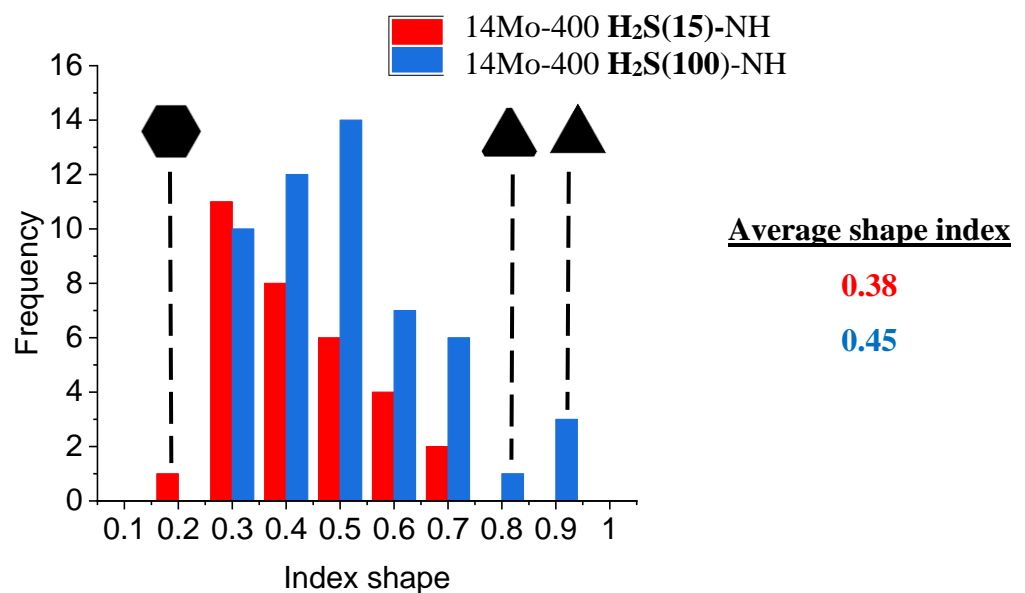


**Figure II-22. Shape index distribution with sulfidation gas nature**

(Histograms obtained from the analysis of 22 and 28 HR HAADF-STEM images and 223 and 362 measurements)

**Table II-14. Experimental shape index calculated**

Sample	Shape index <sup>125</sup>	% edges+corners
14Mo-400-H <sub>2</sub> S(15)-HN	0.38	70
14Mo-400-H <sub>2</sub> S(100)-HN	0.45	76

STEM and PCA analyses confirm connections between gas nature and MoS<sub>2</sub> morphologies. This treatment enables to slightly increase the weight percentage of edges+corners for a given MoS<sub>2</sub> loading.

### 1.3.2.3 Sulfidation temperature effect

The last study aims to increase the fraction of triangular MoS<sub>2</sub> by increasing temperature applied during the sulfidation step<sup>95</sup>. The temperature is increased by 200°C compared to the standard sulfidation protocol (ranging from 400 to 600°C). This modification enlarges the slab lengths as shown on **Figure II-23-a**. **Table II-15** points out that the average slab length is raised from 3.1 to 3.8 nm. The temperature enhancement acts as thermal sintering leading to particle coalescence and slabs expansion and by consequence decrease of the relative amount of the edge planes available as demonstrate before. No PCA analysis has been conducted so far to assess the shape index and corresponding percentage of edges+corners. The sulfidation temperature has no significant impact on the stacking. A majority of single MoS<sub>2</sub> slabs are visible as depicted in **Figure II-23-b**.

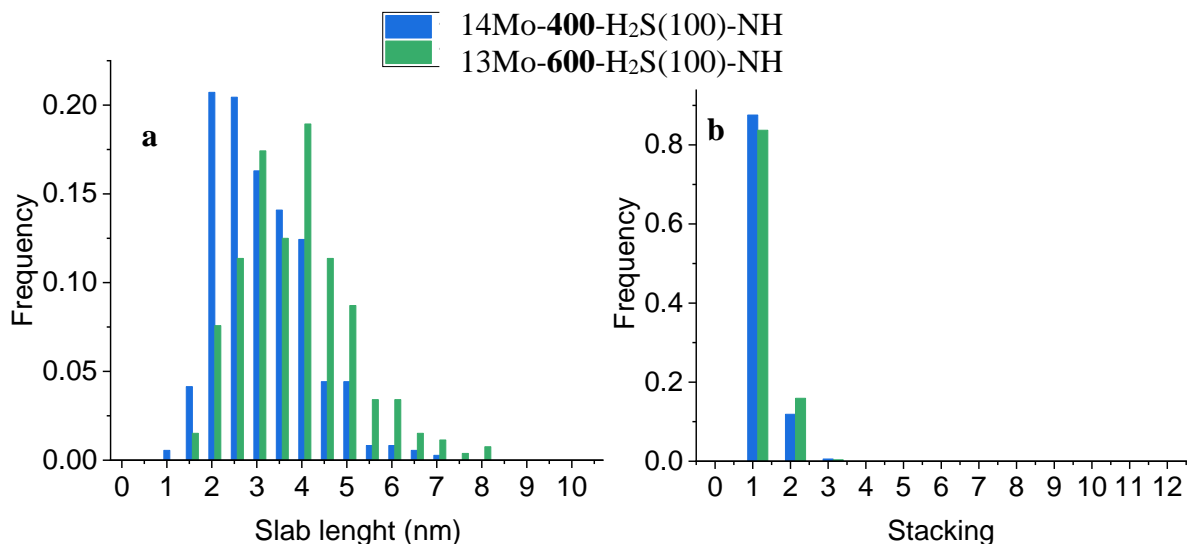


**Figure II-23.** MoS<sub>2</sub> a) slab length and b) stacking on MoS<sub>2</sub>-KB with sulfidation temperature. (Histograms obtained from the analysis of 28 and 19 HR HAADF-STEM images and 362 and 264 measurements)

**Table II-15.** Average slab length, stacking with sulfidation temperature

Sample	Slab length (nm)	Average stacking
14Mo-400-H <sub>2</sub> S(100)-HN	3.1 ± 1.0	1.1 ± 0.4
13Mo-600-H <sub>2</sub> S(100)-HN	3.8 ± 1.2	1.2 ± 0.4

The samples used to study the effect of the sulfidation gas nature and sulfidation temperature on MoS<sub>2</sub>-KB surface properties and morphologies have a MoS<sub>2</sub> loading of 14 wt.%, which has been slightly decreased compared to the sample used in chapter III (22-28 wt.%) due to STEM limitations to observe MoS<sub>2</sub> morphologies. As shown with MoS<sub>2</sub> loading study (see section I-1.3.1), the loading does not significantly impact of slab length and the stacking when the loading is increase from 32 wt.% to 48 wt.%. Then, here we assume an increase of 14 to 22-28 wt.% loading has no strong influence on the study. Only the exposed surface will proportionally increase from 14 to 22 wt.% MoS<sub>2</sub>-KB sample. They have been calculated using the geometric model<sup>127</sup> as the morphology of MoS<sub>2</sub> as only an impact of the percentages of edges+corners exposed and not on the surface. The results are gathered in Table II-16.

**Table II-16. MoS<sub>2</sub> slab nature for 21-28 wt. % of MoS<sub>2</sub> on KB calculated by extrapolation of the results obtained for 14 wt. %.**

Sample	Slab length (nm)	Average stacking	Slabs surface* (m <sup>2</sup> / g MoS <sub>2</sub> -KB)
<b>Gas nature</b>			
28Mo-400-H <sub>2</sub> S(15)-HN	3.4 ± 0.9	1.2 ± 1.0	180
<b>Sulfidation temperature</b>			
22Mo-400-H <sub>2</sub> S(100)-HN	3.1 ± 1.0	1.1 ± 0.4	147
21Mo-600-H <sub>2</sub> S(100)-HN	3.8 ± 1.2	1.2 ± 0.4	142

\* calculation instructions are given in Appendix D

The ratios of surface between samples for gas nature variation and sulfidation temperature variation is equal to 1.3 and 1.1 respectively mainly correlated to the MoS<sub>2</sub> content as previously demonstrated.



## 1.4 Conclusion

The KB carbonaceous support develops a substantial total pore volume of 4.4 cm<sup>3</sup>g<sup>-1</sup> and a specific surface area of 1364 m<sup>2</sup>g<sup>-1</sup>. It is therefore a material that perfectly met the specifications and is well-suited as a support for the dispersion of MoS<sub>2</sub> phase. Furthermore, the incipient wetness impregnation-sulfidation gas phase method has proven to be a versatile approach for synthesizing MoS<sub>2</sub>-KB with several structures.

In any case, supported MoS<sub>2</sub> shows small slabs < 5 nm with stacking of 1 or 2 are obtained. These small slabs are favorable to promote a high fraction of edges active that are supposed to be more efficient for LiPS adsorption<sup>89,127</sup> while a low stacking improves the access to the basal site also supposed to adsorb LiPS.

MoS<sub>2</sub> structure is efficiently modified by playing on MoS<sub>2</sub> loading and the sulfidation conditions applied. The number of active sites successfully is enhanced by 1.4 by increasing the MoS<sub>2</sub> loading from 32 to 48 wt.% while the nature of the active sites is modified by creating more truncated triangular MoS<sub>2</sub> monolayers under pure H<sub>2</sub>S sulfidation conditions at 400°C with a post treatment under H<sub>2</sub> and N<sub>2</sub> at 300°C. This triangular morphology exhibited more edges than usual hexagonal morphology which may be beneficial to the specific adsorption of polysulfides species.

Finally, the sulfidation step performed at 600°C under pure H<sub>2</sub>S enlarges the slab length. The thermal sintering without modification of the morphology compared to the experiment performed at 400°C.

To assess the relation MoS<sub>2</sub> structure/LiPS adsorption relationship regarding polysulfides adsorption, the as-synthesized materials described in this chapter are brought into contact with polysulfide solutions. The polysulfide-adsorbent material interactions are quantified by UV-Vis spectroscopy. The study is details in the next chapter.





## Chapter III – Study of the MoS<sub>2</sub>-KB structure/polysulfides adsorption relationship by UV- Visible with an *in situ* probe setup

---

### 1.1 Introduction

To assess on the relationships between MoS<sub>2</sub>-KB structure and the polysulfides adsorption properties, UV-Vis measurements are conducted. This technique is widely employed in literature to develop new materials dedicated to polysulfides trapping<sup>14,50,51,121,129</sup>. Indeed, polysulfides solutions are inherently colored, making them highly responsive to spectroscopic methods, both in the visible range (400 to 800 nm) and in the UV range (200 to 400 nm). UV-Vis investigations are frequently carried out typically by employing an *ex situ* setup with a quartz cuvette, where measurements are generally confined from the 350-700 nm range, with a predominant focus on signal changes around 400 nm<sup>50,51,130</sup>. However, it is well-known that there are multiple equilibria among polysulfides<sup>14</sup>, including species that absorb below 400 nm. Therefore, a comprehensive understanding of the mechanisms requires a thorough study across the entire UV spectrum.

For a deeper insight into the adsorption properties of materials, we propose a robust methodology employing an *in situ* probe to minimize setup-related artifacts. Indeed, using conventional *ex situ* setup where the investigated solution is placed in a quartz cuvette. Moreover, the methodology presented in the first part of this chapter permits to consider the entire UV-Vis spectrum from 200 to 600 nm with a much better resolution in the range 200-300 nm than the classical UV-vis analysis with quartz cuvette. This facilitates a better understanding on the influence of the nature of adsorbents (MoS<sub>2</sub>, MoS<sub>2</sub>-Ketjenblack, silica) on the adsorption phenomenon and thus on the modification of the polysulfides species in solution, e.g. specific adsorption, disproportionation etc.

This chapter is organized into two sections. The first section presents the UV-Vis methodology performed to extract quantitatively the specific polysulfides contribution and details the spectral decomposition study of Li<sub>2</sub>S<sub>6</sub> equivalent solution to identify the polysulfides natures in solution and their potential concentration. The last section is dedicated to the study of the adsorption on

three types of adsorbents fumed-silica, 32 wt.% and 48 wt.% of MoS<sub>2</sub> supported on KB, followed by a mechanistic study of the adsorption phenomena which can alter the equilibria of polysulfides in solution and the determination of the overall adsorption capacity for the different materials synthesized in [chapter II](#).

## 1.2 Study of the Li<sub>2</sub>S<sub>6</sub> equivalent solution

### 1.2.1 Experimental protocol used to prepare S<sub>8</sub>, Li<sub>2</sub>S and Li<sub>2</sub>S<sub>6</sub> solutions

#### 1.2.1.1 Preparation of S<sub>8</sub> and Li<sub>2</sub>S precursors solutions

To record the UV-Vis spectra of the precursors, it is necessary to identify solvents capable of dissolving these precursors. Y.Liu *et al.*<sup>131</sup> report a maximum solubility of elemental sulfur S<sub>8</sub> in 1,3-dioxolane (DOL) : 1,2-Dimethoxyethane (DME) of 10 mM. Hence, S<sub>8</sub> based solutions using DOL-DME are successfully prepared at 0.4, 0.8, 4 mM. Elemental sulfur (S<sub>8</sub>, 99,5% refined, Acros Organics) is dissolved in mixture of dry solvents DOL (99,5%, stab, Alfa Aesar) / DME (99%, extra dry, AcroSeal, Acros Organic) (1:1 v/v) and stirred vigorously with a magnetic stirrer at room temperature overnight inside the argon filled glove box (Jacomex, H<sub>2</sub>O/O<sub>2</sub> < 1 ppm). By contrast, P.Andrei *et al.*<sup>132</sup> and D.Zheng *et al.*<sup>133</sup> report low solubility for lithium sulfide (Li<sub>2</sub>S) < 0.02 mM in DME and DOL. A.Robba<sup>134</sup> succeed Li<sub>2</sub>S solubilization in ethanol (EtOH). Solubility tests are performed using DOL, DOL:DME and EtOH. Similarly, to S<sub>8</sub> solutions, Li<sub>2</sub>S (99.98%, Sigma Aldrich) is dissolved in the three solvents separately and stirred overnight. **Figure III-1** shows the different solutions obtained after the solubilization tests. 0.4 mM S<sub>8</sub> solution appears clear without remaining sulfur yellow powder. The same clear solutions are obtained for 0.8 et 4 mM. In contrast, we confirm that the dissolution of 32 mM Li<sub>2</sub>S is only possible in EtOH. Consequently, the solubilization of Li<sub>2</sub>S is carried out in ethanol. The UV-Vis spectrum of Li<sub>2</sub>S is presented in [Appendix C](#) but is not exploited here.

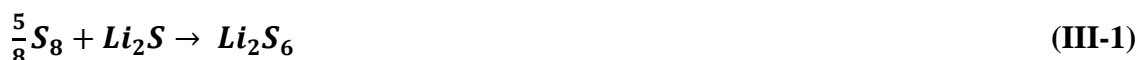


**Figure III-1.** Images of 0.4 mM S<sub>8</sub> in DOL:DME and 32 mM Li<sub>2</sub>S in different solvents.

### 1.2.1.2 Preparation of Lithium Polysulfides (Li<sub>2</sub>S<sub>6</sub>) solutions

Intermediate-chain Li<sub>2</sub>S<sub>6</sub> is selected ahead of short-chain species that exhibit lower solubility<sup>131</sup> in DOL/DME. The choice of Li<sub>2</sub>S<sub>6</sub> is also based on the greater documentation of this polysulfides in the literature.

Li<sub>2</sub>S<sub>6</sub> equivalent polysulfides solutions (60 mM) is obtained by mixing S<sub>8</sub> and lithium sulfide Li<sub>2</sub>S at a molar ratio of 5:1 in a mixture of dry solvents made of DOL:DME. The solution is stirred vigorously with a magnetic stirrer at 60°C inside the argon glove box. **Equation III-1** gives the corresponding chemical reaction to produce Li<sub>2</sub>S<sub>6</sub> :



After the mixing step, no trace of elemental sulfur has been observed suggesting a complete reaction. **Figure III-2** exhibits the evolution of color of the solution during the reaction time from yellow to dark red over time in agreement with literature results<sup>21</sup>. Complete reaction is considered when a persistent dark red color is achieved with no solid particle remaining in solution (herein after 24h).

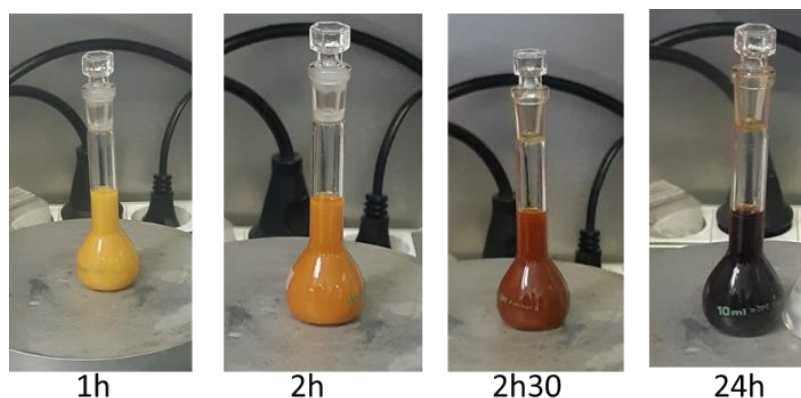
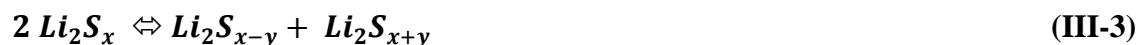


**Figure III-2.** Color evolution of 60 mM initial Li<sub>2</sub>S<sub>6</sub> polysulfides solution over reaction time.

Polysulfides species are in equilibrium and can transform into other sulfur species spontaneously by disproportionation reactions such as **equation (III-2)** and **(III-3)** or can generate radicals by an homolytic cleavage of the S-S bound as shown in **equation (III-4)**<sup>14,135</sup>.



Applied to our case (x=6), it yields to the following set of equations:



The exact nature and concentration of each polysulfides in solution is not known up to now and depends on the concentration, temperature, and solvents. Therefore, it is not possible to affirm that one unique polysulfides nature exists within the prepared solutions which are thus considered as an 'equivalent' to the targeted polysulfides nature (e.g. Li<sub>2</sub>S<sub>6</sub> equivalent) during the entire study.

Afterward, series of 0.5, 1, 2, 3, 4 mM polysulfides solutions are prepared by dilution from the 60 mM mother solution to be used as reference solutions for UV-Vis calibration. For concentration higher than 4 mM the UV-Vis signal saturates. Li<sub>2</sub>S<sub>6</sub> diluted solutions exhibit a gradient of color from light orange at 4 mM to colorless at 0.5 mM as shown in **Figure III-3**.

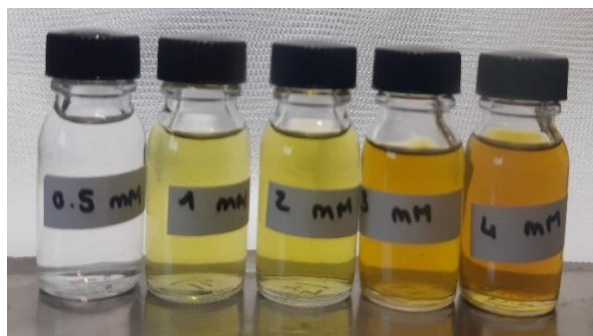


**Figure III-3. Standard equivalent polysulfides solutions Li<sub>2</sub>S<sub>6</sub>.**

### 1.2.2 UV-Vis protocol : comparison of classical *ex situ* quartz cuvette vs *in situ* optical fiber setup

The use of quartz cuvette (1 mm optical path) induces the filling of the cuvette in the glove box with 1 mL of the as-prepared solution, then the sealing of the cuvette, prior to carried out UV-Vis analysis outside the glove box. This protocol is quite long and delicate.

As DOL-DME exhibits a slight absorbance in the UV range below 280 nm, the spectrum of DOL-DME is therefore subtracted from all the UV-Vis spectra presented in this chapter. Thus, **Figure III-4** shows the signal of a 3 mM Li<sub>2</sub>S<sub>6</sub> solution after filling and sealing the cuvette.

The solution is colored in light orange (see **Figure III-3**). In the UV range, below 260 nm the detector saturates, then a large massif is observed between 280 to 350 nm. A broad peak is observed in between 360 and 480 nm. The absorption occurs towards the blue spectrum which is expected since blue is the complementary color of yellow. In addition, no contribution above 500 nm is discernable.



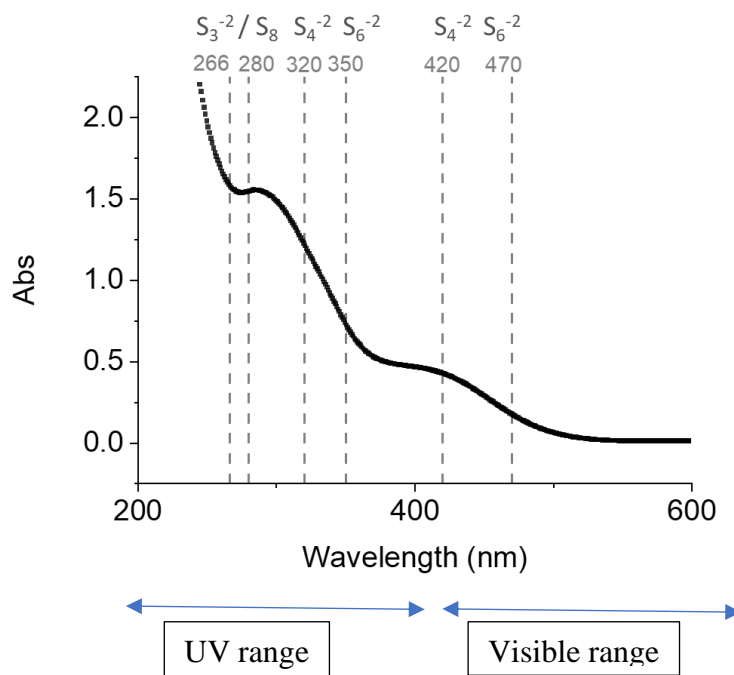


**Figure III-4.** Li<sub>2</sub>S<sub>6</sub> (3 mM in DOL-DME) UV-Vis signal using a quartz cuvette.

These observations confirmed that the Li<sub>2</sub>S<sub>6</sub> equivalent solution has a complex UV-Vis signal embedding several contributions. In literature, Patel and Dominko<sup>48</sup> noticed that long-chain polysulfides absorbed at higher wavelengths than short-chains. This trend is confirmed by various other studies that have assigned specific wavelengths to polysulfides species.

**Table III-1** shows long-chain polysulfides at 560 nm, mid-chain polysulfides between 470 and 300 nm and short-chain polysulfides between 340 and 265 nm. The radical S<sub>3</sub>• signs at 617 nm. The elemental sulfur (S<sub>8</sub>) dissolved in the solvent has absorbance peaks between 240 and 280 nm.

**Table III-1** also highlights that S<sub>8</sub><sup>2-</sup>; S<sub>5</sub><sup>2-</sup>; S<sub>3</sub><sup>2-</sup>-S<sub>3</sub>• and S<sub>3</sub><sup>2-</sup> have a unique absorption peak while S<sub>6</sub><sup>2-</sup> and S<sub>4</sub><sup>2-</sup> have multiple: contributions around 470 and 350 nm and at 420 and 310 nm, respectively. It is worth noting that there is also a peak shift with concentration<sup>48</sup> and solvent nature<sup>16,106</sup>. Hence the specific wavelengths slightly vary when using different ether solvents (such as DOL-DME, TEGDME, etc).

The polysulfides peak attributions from **Table III-1** are added to **Figure III-4**. Main contributions are identified at 270 nm, 320 nm, and 350 nm, which suggests the presence of S<sub>8</sub>,

S<sub>6</sub><sup>2-</sup> and S<sub>4</sub><sup>2-</sup> respectively. These polysulfides species are coherent with the disproportionation equations (**equations (III-5) (III-6) and (III-7)**).

The polysulfides radical S<sub>3</sub><sup>•-</sup> (617 nm) is not detected at all, which is in agreement with the results of *Zou et al*<sup>62</sup>. The formation of stable S<sub>3</sub><sup>•-</sup> radical depends on the solvent<sup>62,135</sup> and is favored at elevated temperature<sup>136</sup> and at low polysulfides concentration<sup>136</sup>.

**Table III-1. Attribution of absorption peak of polysulfides according to literature.**

Solvent	S <sub>2</sub> <sup>2-</sup>	S <sub>3</sub> <sup>2-</sup>	S <sub>4</sub> <sup>2-</sup>	S <sub>5</sub> <sup>2-</sup>	S <sub>6</sub> <sup>2-</sup>	S <sub>8</sub> <sup>2-</sup>	S <sub>3</sub> <sup>•-</sup>	S <sub>8</sub>	Reference
DOL/DME		266	300, 420					265-285	63
DOL/DME			320, 420		350			264	129
DOL/DME			320,420		470, 350	560	617		62
TEGDME			315,410		315, 355, 475	475, 570	-	240, 280	106
TEGDME	265	340	420	450	470	560	617	280	14

**Figure III-5** displays the evolution of the UV-Vis signal over a period of time (*t*) of 72 h along with pictures of the cuvette after sealing and after 72 h. The solution become colorless after 72 h indicating that the polysulfides equilibria are evolving over time. Accordingly, the intensity of the absorption in the visible part of the spectrum becomes nearly zero (purple curve). A decrease in intensity in the UV range is also observed, along with the formation of two maxima at 265 and 280 nm suggesting the presence of S<sub>8</sub> (see **Table III-1**).

This temporal evolution has also been observed when the cuvettes are stored in the argon filled glove box, thus it is not due to some experimental artifacts such as bad air-tightening of the cuvette. Alternatively, it may be due to polysulfides interactions with the silica quartz cuvette surface<sup>60</sup>.

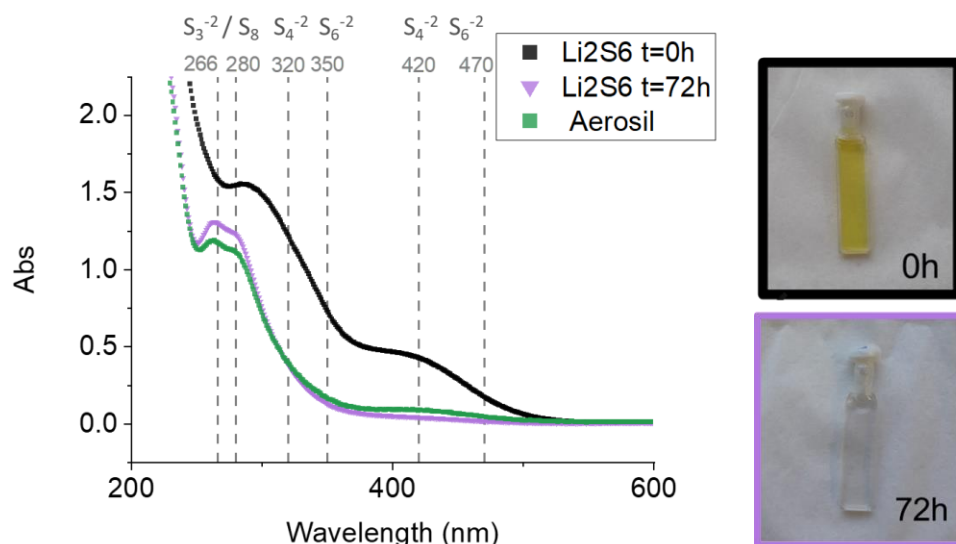


**Figure III-5.** Li<sub>2</sub>S<sub>6</sub> (3mM) UV-Vis signal evolution after 72h when using quartz cuvette.

To further investigate this assumption, the polysulfides solution is brought into contact with 10 mg of fumed silica (Aerosil 200<sup>137</sup>) overnight, and the supernatant is collected and analyzed. The corresponding UV-Vis signal is added in **Figure III-5** (green curve). Both purple (Li<sub>2</sub>S<sub>6</sub> solution after 72h) and green signal have comparable shape which demonstrate that polysulfides interact with silica-based materials. According J.Conder *et al.*<sup>60</sup>, silica materials are effective adsorbent for LiPS species. **Therefore, the use of thin quartz cuvette can modify the solution composition due to a low ratio  $\frac{\text{volume of PS}}{\text{surface of silica}}$  which can lead to measurement artefacts. In addition, the region below 300nm is not well resolved due to cuvette absorption.**

These issues are tackled when using a deported UV-Vis optical fiber directly inside the glove box. The *in situ* UV-Vis probe setup is displayed in **Figure III-6**. The setup connects the spectrometer, the light source, and the probe through optical fibers. This optical fiber is connected directly to the glovebox between the light source and the probe. The vials containing the solutions to be analyzed are sealed hermetically until the moment of measurement when the probe is immersed in the vial for 1 minute (3 measurements). With this setup, large sample volume can be analyzed (increasing the ratio  $\frac{\text{volume of PS}}{\text{surface of silica}}$ ), without air contamination.

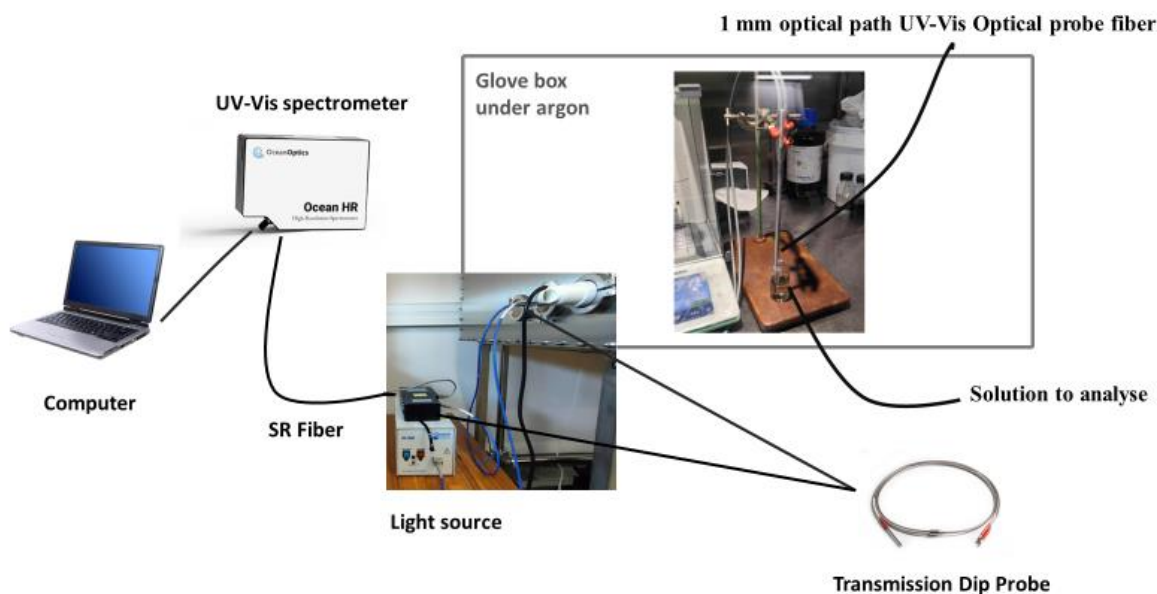


**Figure III-6.** *In situ* UV-Vis probe setup connected to the glove box.

Unlike the quartz cuvette setup, the signal remained constant over time as illustrated in **Figure III-7** for three samples of Li<sub>2</sub>S<sub>6</sub> equivalent solution at different concentrations (1, 2, 3 mM).

For each concentration, the signals are almost perfectly superposed after 72 h, with minor shifts due to variations in the intensity of the deuterium lamp. In addition, the spectral region below 300 nm is well resolved compared to results obtained with the quartz cuvette (see **Figure III-8**).

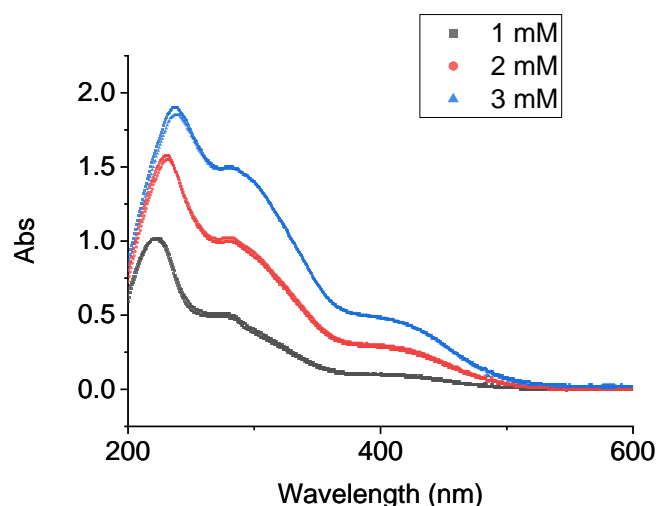


**Figure III-7.** Superposition of Li<sub>2</sub>S<sub>6</sub> (3mM) UV-Vis signals at time=1h and 72h using an *in situ* probe.

Artefact signal with quartz cuvette due to saturation

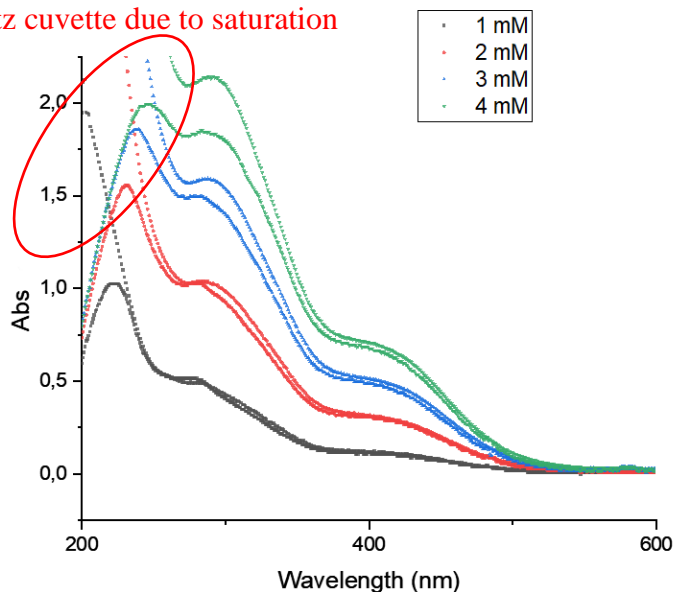


**Figure III-8.** Li<sub>2</sub>S<sub>6</sub> UV-Vis signal comparison between *ex situ* cuvette quartz (dash) and *in situ* probe (line).

Then, we choose to use *in situ* UV-Vis methodology to conduct our study because it extends the range of analysis in the UV and gives repeatable and reproducible results (see [Appendix C](#)).

In the literature, UV-Vis adsorption phenomena for Li-S system have been only qualitatively, demonstrating interactions through changes in solution color and a decrease in signal intensity and UV-Vis spectra are generally limited to the 350-700 nm<sup>50,51,130</sup> UV-Vis range. Only Cui's group<sup>51</sup> has developed a quantitative method for assessing the overall adsorption capacity by integrating UV-Vis spectra from 400-700 nm and conducted in on 16 commercial powders as potential adsorbents candidate for Li-S batteries (including metal oxides, sulfides, nitrides and carbon black). In our first approach, we reproduce this method.

**Figure III-9** displays UV-Vis spectra of Li<sub>2</sub>S<sub>6</sub> standard solutions from 1 to 4 mM. Li<sub>2</sub>S<sub>6</sub> spectra exhibit three absorption massifs. The first adsorption massif shows a maxima that shift from 210 to 230 nm with concentration, the second massif presents two sub-maxima at 260 and 285 nm and the last one is broadened between 370 and 500 nm. As expected, the overall signal intensity increases with concentration, with no additional peak appearing between 1 and 4 mM. However, the most intense peak in the UV shifted from 220 to 240 nm with concentration.

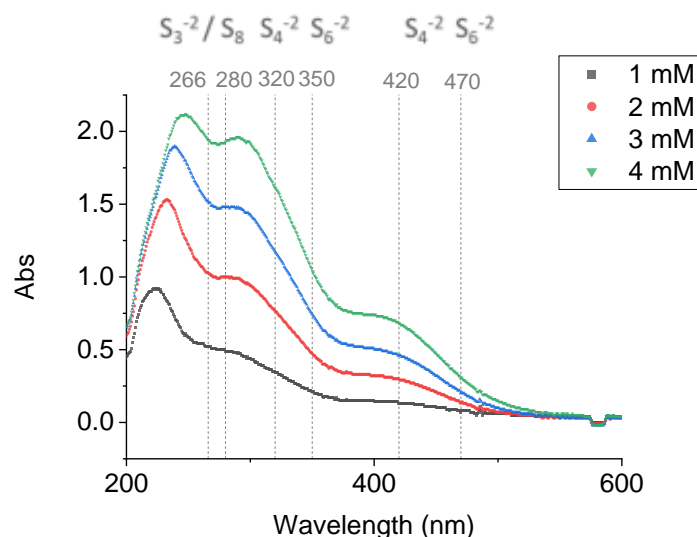


**Figure III-9.** UV-Vis spectrum of Li<sub>2</sub>S<sub>6</sub> solutions in DOL/DME (v/v 50/50).

**Figure III-10** gives the calibration curve obtained from the spectra in **Figure III-9**. They are obtained by integrating the entire massif curve from 200 to 600 nm (where the absorbance is close to zero).

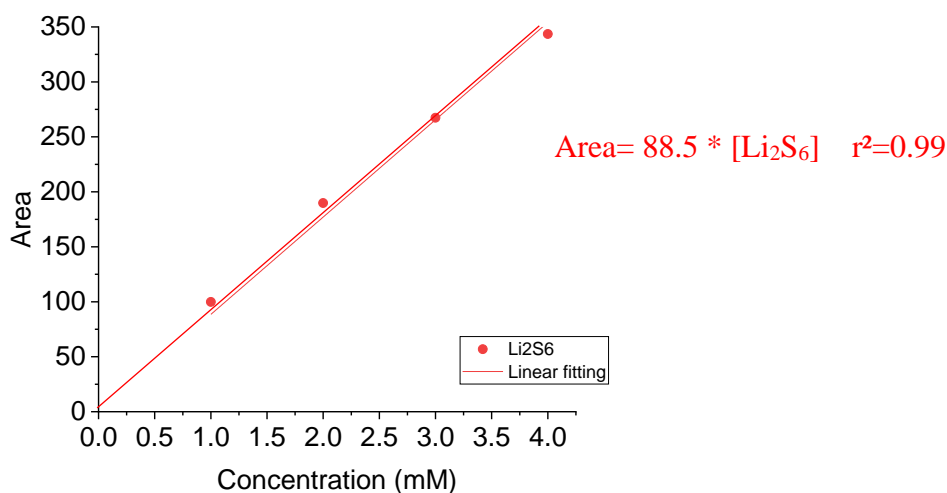


**Figure III-10.** Calibration curve: Area of the Li<sub>2</sub>S<sub>6</sub> solutions spectra integration as a function of concentration.

As the calibration curve is linear, the Beer-Lambert Law (**equation (III-8)**) is applicable to our study for each peak. Indeed, when the area is considered instead of the absorbance intensity, greater accuracy is achieved. We suppose that if multiple contributions are present, the sum of each of the contributions is calculated; they are linear with respect to C, and their sum follow the same linearity.

$$Area_i = \log_{10} \frac{I_0}{I} = \epsilon_i * c_i * l \quad (III-8)$$

With

A : absorbance area

$\epsilon$  : molar absorption coefficient ( $M^{-1}cm^{-1}$ )

c : molar concentration (M)

l : optical path length (cm) =  $1 * 10^{-1}$  cm

The molar extinction coefficient  $\epsilon$  is specific to each species in the mixture, they have not been reported in literature. In a first order approximation, thus can be treated as a sum of compositions, which will be considered constant for any particular wavelength as proposed in Cui's group<sup>51</sup>.

While Cui's<sup>51</sup> approach represents a significant step forward UV-Vis quantitative study, it excludes a fraction of polysulfides under 400 nm, making it somewhat imprecise in characterizing the nature of the polysulfides involved. This method is not completely adapted to a comprehensive study of the influence of adsorbent nature on the adsorption phenomenon and the alteration of polysulfide species in solution. Then, we decided to conduct a spectral decomposition of the UV-Vis spectrum to identify the specific contributions present in the Li<sub>2</sub>S<sub>6</sub> equivalent solution to properly determine their evolution i) with LiPS concentration (calibration curves) and ii) in the presence of adsorbent.

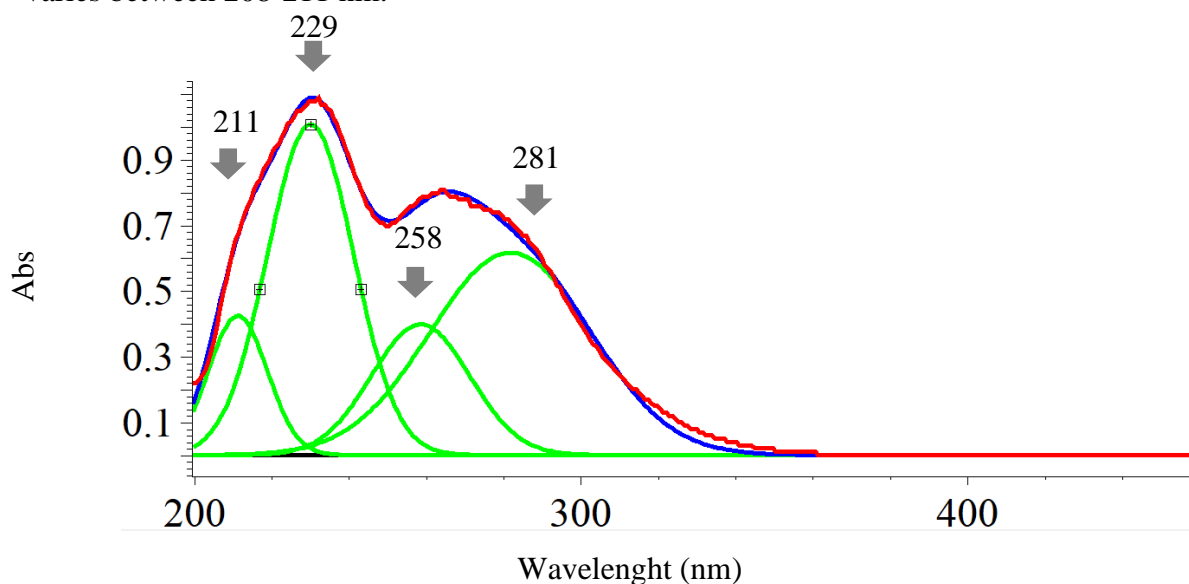
### 1.2.3 Data analysis, spectral decomposition

The spectral decomposition is performed step-by-step to determine the number of decomposition peaks, their positions, widths, heights, curve types, and to establish an initial and common set of parameters for use during *spectral curve fitting*. Spectral decomposition is carried out using Renishaw's Raman Environment (WiRE 3.3™) software, typically designed for Raman spectroscopy. Peak fitting is performed using only Gaussian curve types as expected from UV-Vis absorption<sup>138</sup>.

There are several sources of experimental errors (partial reaction of Li<sub>2</sub>S with S<sub>8</sub>, errors in the concentration of Li<sub>2</sub>S<sub>6</sub> solutions), as well as measurement uncertainties (UV-Vis measurement uncertainty, fluctuations in lamp signal, signal noise), and uncertainties related to spectral decomposition that can lead to fluctuations in the results. The margin errors are 5% on x-axis and 10% for y-axis.

- Step 1 : positioning of individual peaks and choice of initial parameters for spectral decomposition using *spectral curve fitting* on 0.8 mM S<sub>8</sub> solution

**Figure III-11** illustrates the peak decomposition in four individual contributions, the simulation of the total curve (in blue), and experimental results (in red). The fit is really satisfactory. The dataset obtained after minimization using WiRE 3.3 software are added in the table in **Figure III-11**. Four contributions are observed at 211, 229, 258 and 282 nm. The last three peaks correspond to the signal of S<sub>8</sub> found in the literature (**Table III-1**), which confirms that there is no S<sub>3</sub><sup>2-</sup> in the Li<sub>2</sub>S<sub>6</sub> equivalent solution. Again, the peak at 211 nm is not identified in the literature. The peaks at 210 ± 5 nm and 260 ± 5 nm are probably not associated with any specific species since its intensity remains constant and does not vary with the incremental additions S<sub>8</sub> or Li<sub>2</sub>S<sub>6</sub> (see **Figure III-11**). Nevertheless, the inclusion of this peak is necessary to complete the fit at the edge, as the baseline does not reach 0 after 200 nm. The peak position at 210 may varies between 208-211 nm.



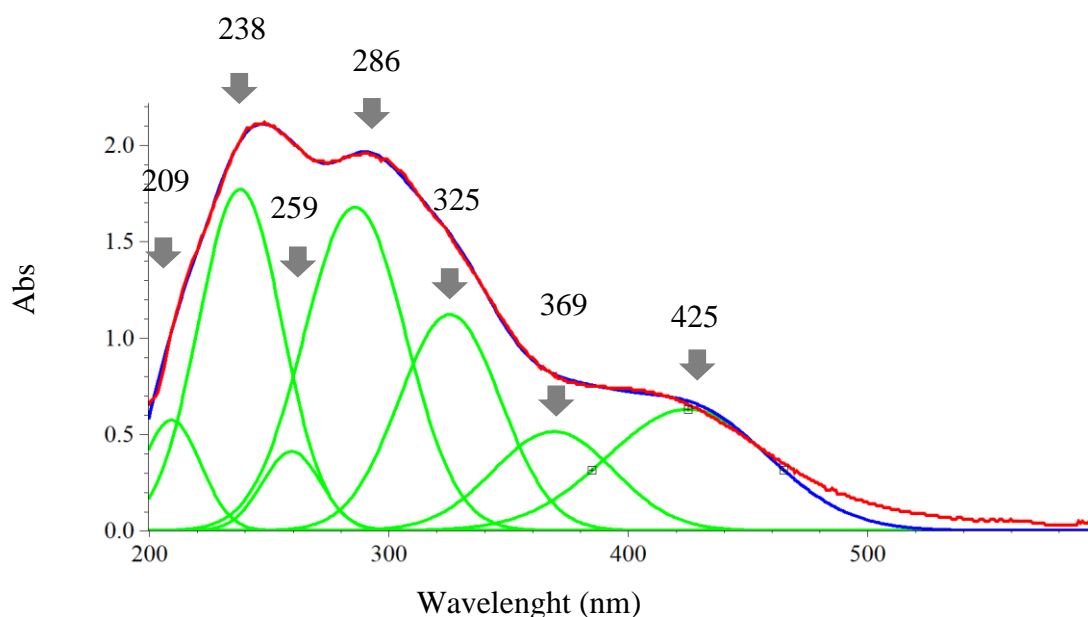
Peak position	Width	Height	Area
211	18	0,4	13
229	26	1,0	28
258	30	0,4	13
281	49	0.6	32

**Figure III-11.** Spectral decomposition and fitting of 0.8 mM S<sub>8</sub> (red curve refers to experimental curve, green curves to the individual peaks and blue curve to simulated Gaussian curve).



- Step 2 : performing the spectral decomposition on 4 mM Li<sub>2</sub>S<sub>6</sub> solution

On **Figure III-12** six sub-maxima 209, 238, 259, 286, 325 and 425 nm are observed on the the UV-Vis signals of Li<sub>2</sub>S<sub>6</sub> at 4mM. The fit is not satisfactory in the region 350-400 nm (plateau region). Thus a seventh contribution is added at 369 nm which limits the artificial broadening of the 425 nm peak.



Peak position	Width	Height	Area
209	28	0,6	17
238	41	1,8	78
259	29	0,4	13
286	50	1,7	89
325	50	1,1	60
369	59	0,5	32
425	80	0,6	54

**Figure III-12.** Spectral decomposition and fitting of 4 mM Li<sub>2</sub>S<sub>6</sub> (red curve refers to experimental curve, green curves to the individual peaks and blue curve to simulated Gaussian curve).

To further adjust the initial parameter set (values and limits), and check the robustness of the parameters, the spectrum at lower concentrations is fitted using the same initial parameters. Especially, for each contribution, the peak width has been locked to limits its evolution at less than 10%, the position has been locked to a very narrowed range (below +/- 5 or 10 nm), while the intensity is kept free. In average the fit for each concentration is very good. This series of fit tends to validate the set of parameters used.

- Step 3: Comparison of peak position of each contribution with literature

If now, we compare the spectral decomposition and the peak assignments from the literature (see **Table III-2**), it is noticed that the positions of 6 out of the 7 peaks are reported: 240, 260, 285, 325, 365 and 425 nm, with a displacement of less than 10 nm between literature and our experimental results. The peak at 240, 260 and 285 are attributed to the elemental sulfur. As confirmed by the attribution of the elemental sulfur peaks (see **Figure III-11**). The peaks at 325 and 425 nm to the S<sub>4</sub><sup>2-</sup>, while the peak at 365 nm can be attributed to the S<sub>6</sub><sup>2-</sup>. The small peak at 208nm is not identified in literature. The peak at 208 and 260 nm are independent of the concentration (see **Figure III-13**) which suggests that this contribution is coming from an artefact of the measure.

**Table III-2. Wavelengths of polysulfides species obtained from the spectral curve fitting.**

Peak n°	Wavelength (nm)	Attribution from literature (from <b>Table III-1</b> )
1	210 ± 5	NA
2	<b>240 ± 10</b>	S <sub>8</sub>
3	<b>260 ± 5</b>	S <sub>3</sub> <sup>2-</sup> ; S <sub>8</sub>
4	<b>285 ± 5</b>	S <sub>8</sub>
5	<b>325 ± 5</b>	S <sub>4</sub> <sup>2-</sup>
6	<b>365 ± 5</b>	S <sub>6</sub> <sup>2-</sup> ?
7	<b>425 ± 5</b>	S <sub>4</sub> <sup>2-</sup>
NA : not available in literature		

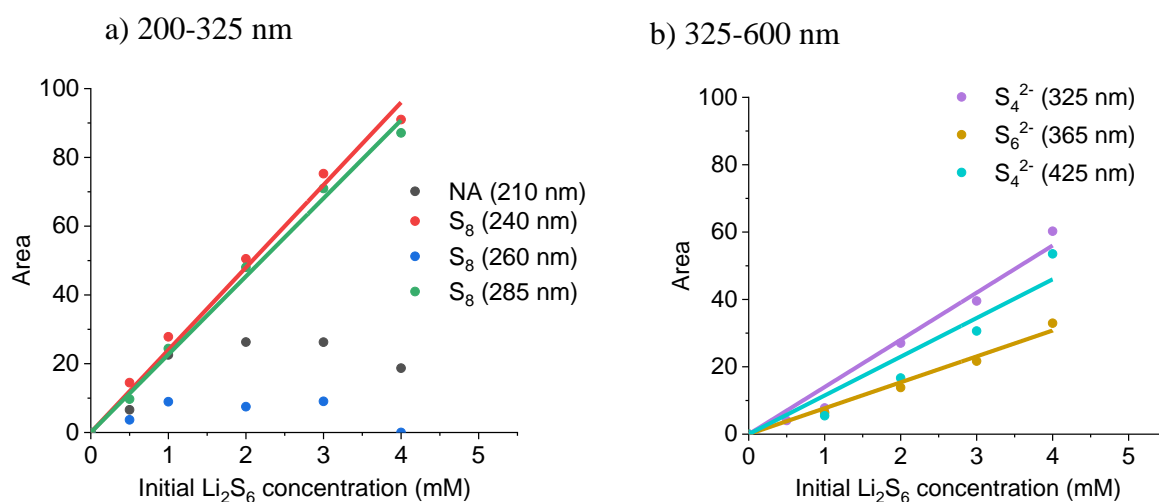


**Figure III-13.** Evolution of area of each contribution/peak as a function of initial Li<sub>2</sub>S<sub>6</sub> concentration in a) 200-325 nm b) 325-600 nm regions.

These results confirm the co-existence of at least 3 species in the equivalent Li<sub>2</sub>S<sub>6</sub> solution, i.e. S<sub>8</sub>, S<sub>4</sub><sup>2-</sup> and S<sub>6</sub><sup>2-</sup> in agreement with the disproportionation reaction of Li<sub>2</sub>S<sub>6</sub> (eq 5). In the range of concentration probed (0.5 – 4 mM), the relative amount of these 3 species stays almost constant because all the area obeys Beer Lambert law. Only the contribution at 425 nm, shows an increase of the slope at high concentration. This trend may come from the peak broadening with the concentration to compensate for the baseline and the presence of a small broad contribution of S<sub>6</sub><sup>2-</sup> around 470 nm as proposed by Zou *et al*<sup>62</sup>. However, we can not deduce the molar extinction coefficient and the concentrations since we do not know the partition of each species. Thus to go further in the quantitative analyses the spectra obtained with S<sub>8</sub> are now analyzed.

## 1.2.4 Quantitative analysis of S<sub>8</sub> and Li<sub>2</sub>S<sub>6</sub> solutions

### 1.2.4.1 Quantitative analysis of S<sub>8</sub> precursor

The UV-Vis spectra of S<sub>8</sub> solutions at 0.4, 0.8 and 4 mM in DOL-DME are given in **Figure III-14**. S<sub>8</sub> spectra exhibit two absorption massifs consistent with the literature' data<sup>63</sup>. The first adsorption region shows a maxima that shift from 210 to 230 nm with concentration, and the second massif presents two sub-maxima at 260 and 285 nm. As deduced from the spectral curve decomposition, three contributions at 230, 258 and 282 nm are related to sulfur species. The signal intensity varies proportionally with concentration between 0.4 and 0.8 mM, while at higher concentration (4 mM), the absorbance is no more proportional, and the second massif intensifies relatively to the first massif. This suggests that the limit of solubility of sulfur is

reached below 4 mM. **Figure III-15** shows the massif area evolution with S<sub>8</sub> concentration (obtained by integration of entire spectra). A linear trend is observed for 0.4 and 0.8 mM with similar slope. At 4 mM the solution is already saturated. Indeed, the limit of solubility is experimentally determined to be 1.5 mM (blue arrows on **Figure III-15**).

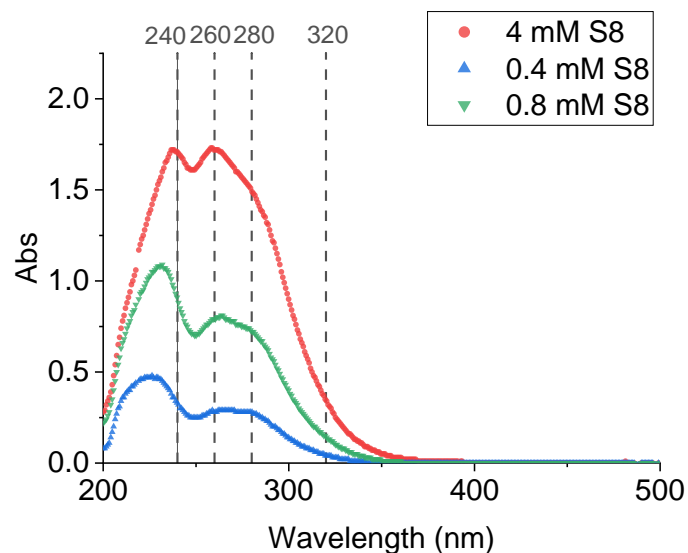


**Figure III-14.** UV-Vis signals of S<sub>8</sub> at different concentrations in DOL-DME.

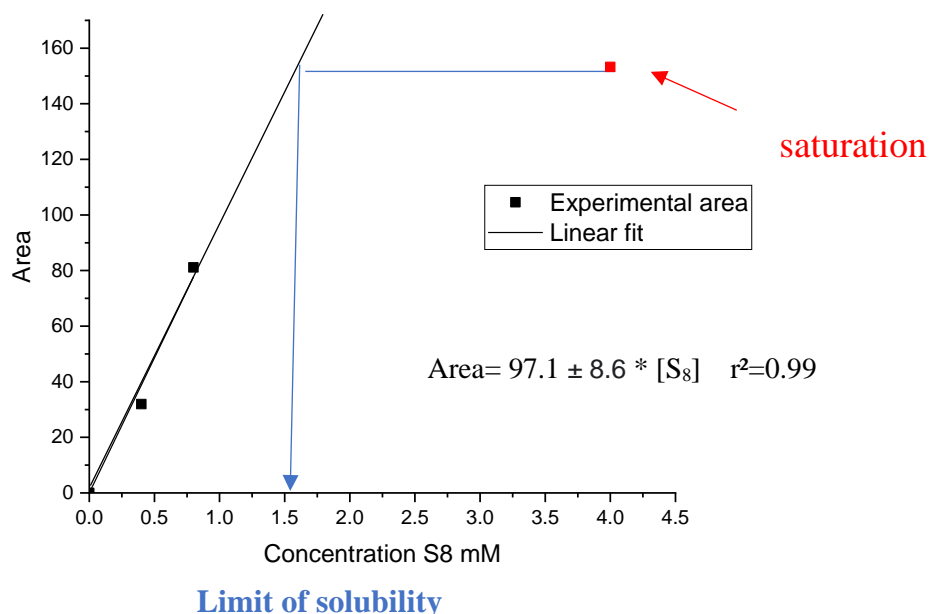


**Figure III-15.** Evolution of the massif area as a function of S<sub>8</sub> concentration.

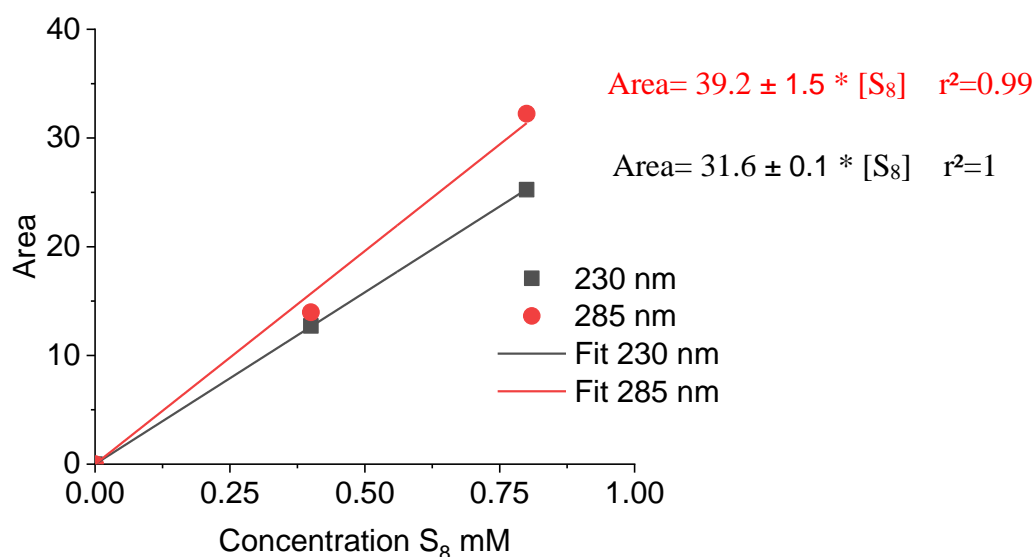


**Figure III-16.** Evolution of  $230 \pm 10$  and  $285 \pm 5$  nm peak area as a function of S<sub>8</sub> concentration

The molar extinction coefficients  $\epsilon$  ( $\text{mM}^{-1} \cdot \text{cm}^{-1}$ ) of S<sub>8</sub> is calculated from the slope of the experimental curve (see **Figure III-16**) using **equation (III-9)** :

$$\epsilon = \frac{\text{slope from } A=f(C S_8)}{l} = \frac{\text{slope from } A=f(C S_8)}{1 \cdot 10^{-1}} \quad \text{(III-9)}$$

We measured molar extinction coefficients of  $316 \pm 80 \text{ mM}^{-1} \cdot \text{cm}^{-1}$  for the peak at  $230 \pm 5$  nm and of  $392 \pm 100 \text{ mM}^{-1} \cdot \text{cm}^{-1}$  for the peak at  $285 \text{ nm} \pm 5$  nm. These molar extinction coefficients have not been compared to the literature due to the lack of papers on the subject, as far as we know. These coefficients will serve to determine S<sub>4</sub><sup>2-</sup> and S<sub>6</sub><sup>2-</sup> concentrations from Li<sub>2</sub>S<sub>6</sub> quantitative study presented below.

### 1.2.4.2 Quantitative study of Li<sub>2</sub>S<sub>6</sub>

Knowing signal intensities of  $230 \pm 10$  nm and  $285 \pm 5$  nm S<sub>8</sub> contributions in of 0.4 and 0.8 mM S<sub>8</sub> solutions and the molar extinction coefficient of S<sub>8</sub>, we can deduce the composition of the Li<sub>2</sub>S<sub>6</sub> equivalent solution assuming disproportionation reaction (**equation III-10**) as the main reason for the presence of S<sub>8</sub> and S<sub>4</sub><sup>2-</sup> contribution in the spectra. We propose a first estimation of S<sub>8</sub>, S<sub>4</sub><sup>2-</sup> and S<sub>6</sub><sup>2-</sup> concentration in Li<sub>2</sub>S<sub>6</sub> using the S<sub>8</sub> contribution  $230 \pm 10$  nm obtained from **Figure III-16**, as it is the more intense and it is no affected by the baseline compensation in S<sub>8</sub> solutions. **Table III-3** gives the stoichiometric relationship between the species.

- Disproportionation equilibrium (in solution)

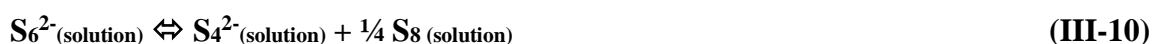


**Table III-3. Reaction stoichiometry table**

	Extent of reaction $\xi$ (in mol)	Li <sub>2</sub> S <sub>6</sub> $\rightleftharpoons$ Li <sub>2</sub> S <sub>4</sub>	$\frac{1}{4} S_8$
Initial	$\xi = 0$	n Li <sub>2</sub> S <sub>6</sub>	0
Intermediate At constant volume	$\xi$	n Li <sub>2</sub> S <sub>6</sub> = n Li <sub>2</sub> S <sub>6</sub> - $\xi$ [S <sub>6</sub> <sup>2-</sup> ] = C°(100- $\alpha$ )	n Li <sub>2</sub> S <sub>4</sub> = 0 + $\xi$ [S <sub>4</sub> <sup>2-</sup> ] = C° * $\alpha$
Final	$\xi_{\text{max}}$	n Li <sub>2</sub> S <sub>6</sub> - $\xi_{\text{max}}$ → limiting reactant	n S <sub>8</sub> = 0 + $\frac{1}{4} \xi_{\text{max}}$

$\alpha$  = percentage of the extent of reaction (expressed in %)

**Figure III-17** shows the superposition of the evolution of S<sub>8</sub> contribution at 230 ± 10 nm in Li<sub>2</sub>S<sub>6</sub> and S<sub>8</sub>, taken from **Figure III-13** and **Figure III-16** respectively.

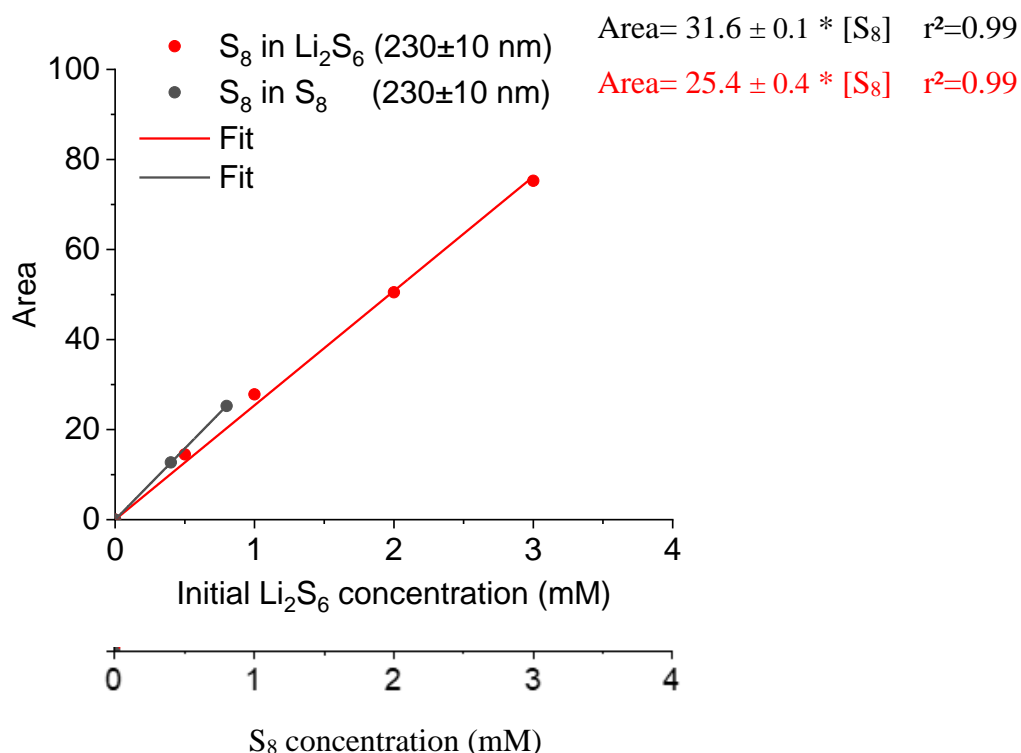


**Figure III-17.** Superposition of the evolution of 230 ± 10 nm S<sub>8</sub> contribution in S<sub>8</sub> and Li<sub>2</sub>S<sub>6</sub> solutions. In blue, evolution S<sub>8</sub> in elemental S<sub>8</sub> solution from **Figure III-16** and in red evolution in Li<sub>2</sub>S<sub>6</sub> from **Figure III-13**.

The slopes of the two fitting curves are considered similar except for experimental errors (5% on x-axis and 10% for y-axis) meaning that the concentrations of S<sub>8</sub> are comparable. For instance, 1 mM of equivalent Li<sub>2</sub>S<sub>6</sub> is composed of 1 mM of S<sub>8</sub>. **Table III-4** gives the S<sub>8</sub> and S<sub>4</sub><sup>2-</sup> concentrations in the range of the total concentration of Li<sub>2</sub>S<sub>6</sub> (C°).

**Table III-4.** Calculated concentration of S<sub>8</sub> and S<sub>4</sub><sup>2-</sup> in Li<sub>2</sub>S<sub>6</sub> equivalent (first estimation)

C° <sub>Li<sub>2</sub>S<sub>6</sub></sub> mM	Experimental		Theoretical if α=100%	
	[S <sub>8</sub> ] mM	[S <sub>4</sub> <sup>2-</sup> ] mM	[S <sub>8</sub> ] mM	[S <sub>4</sub> <sup>2-</sup> ] mM
0,5	0,5	1,8	0,1	0,5
1	0,9	3,5	0,2	1
2	1,6	6,4	0,5	2
3	2,4	9,5	0,7	3

The results obtained from this first estimation, do not allow to conclude regarding the concentrations in the solution. Indeed, the concentrations obtained are much higher than the theoretical ones if we assume  $\alpha = 100\%$  (total disproportionation reaction).

In addition, **Figure III-18** shows that it stays the peak at 365 nm which is attributed to S<sub>6</sub><sup>2-</sup> according to references <sup>62</sup> and <sup>129</sup>. Indeed, its area is similar to that of S<sub>4</sub><sup>2-</sup> peaks, meaning concentration of similar order of magnitude, which is not compatible with the previous results (where S<sub>6</sub><sup>2-</sup> ≠ 0).

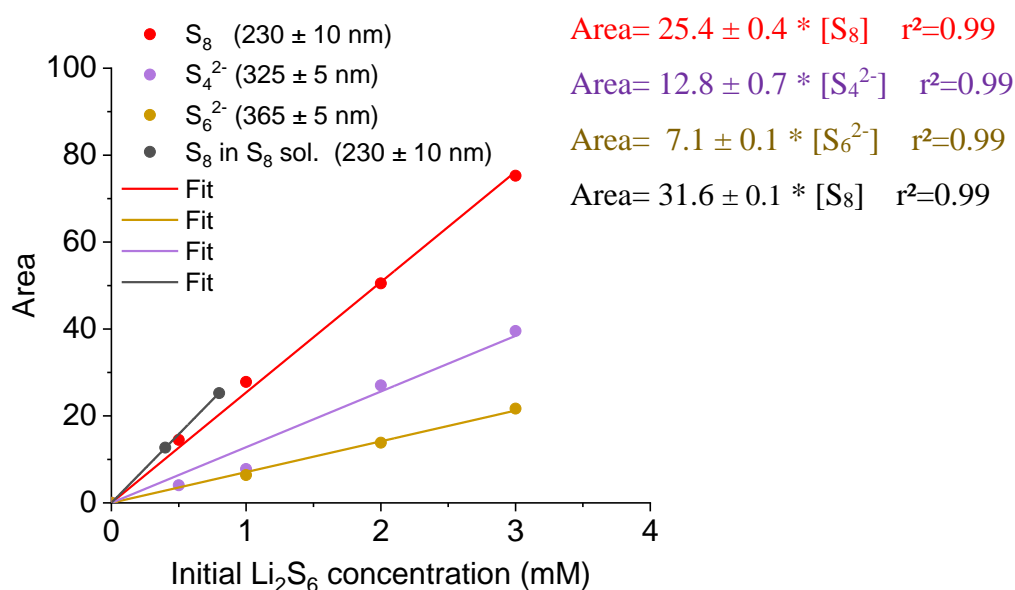


**Figure III-18. Evolution of several contributions as a function of Li<sub>2</sub>S<sub>6</sub> equivalent concentrations**

We propose a second estimation of the S<sub>4</sub><sup>2-</sup> by direct comparison of the fitting curves slopes using 230 ± 10 nm, 325 ± 5 nm and 365 ± 5 nm contributions (see **Figure III-18**). This assume that the molar extinction coefficients are similar between species, as assumed by Cui<sup>133</sup>. The slope ratio between S<sub>8</sub> (black curve) and S<sub>4</sub><sup>2-</sup> (purple curve) contributions gives a ratio of 2.5. In the solution of 1 mM of Li<sub>2</sub>S<sub>6</sub> equivalent, there would be a concentration of 1.00 / 2.5 = 0.40 mM of S<sub>4</sub><sup>2-</sup>. **Table III-5** shows the estimation of S<sub>4</sub><sup>2-</sup> and S<sub>8</sub> based on the stoichiometric relationship of **equation III-10**. A percentage of extent of reaction ( $\alpha$ ) of 40% is deduced the slop of C°=f(S<sub>4</sub><sup>2-</sup>). The remaining S<sub>6</sub><sup>2-</sup> concentration in solution is calculated using the extend of reaction.



**Table III-5.** Calculated concentration of S<sub>8</sub>, S<sub>4</sub><sup>2-</sup> and S<sub>6</sub><sup>2-</sup> in Li<sub>2</sub>S<sub>6</sub> equivalent (second estimation)

C° <sub>Li<sub>2</sub>S<sub>6</sub></sub> mM	[S <sub>4</sub> <sup>2-</sup> ] mM	[S <sub>8</sub> ] mM	[S <sub>6</sub> <sup>2-</sup> ] mM
0,5	0.20	0.05	0.30
1	0.40	0.10	0.60
2	0.80	0.20	1.20
3	1.20	0.30	1.80

This result suggests that a 40% of the S<sub>6</sub><sup>2-</sup> species undergo disproportionation reaction. However, the calculated concentration of S<sub>6</sub><sup>2-</sup> is higher than S<sub>4</sub><sup>2-</sup> which is not in line with what can be seen on **Figure III-18**. Several assumptions can be made: i) considering only the disproportionation equilibrium does not accurately reflect the equilibria in the solution in this concentration domain ii) the experimental errors may have been underestimated or iii) it is then possible to question whether the peak assignment is accurate. The concentrations of each contribution can not be accurately determined which could have provided valuable experimental data, not referred in literature to the best of our knowledge.

A careful analysis of the literature reports shows that this assignment is highly debated and remains ambiguous. For instance S<sub>3</sub><sup>2-</sup><sup>63</sup> and S<sub>8</sub><sup>129</sup> have been attributed at the same wavelength (266 nm). In our case, we are certain about the assignment of the two S<sub>8</sub> peaks at 230 ± 10 nm and 285 ± 5 nm thanks to the calibration with pure S<sub>8</sub> standard solutions. The attribution of the peaks at 320 and 420 nm to S<sub>4</sub><sup>2-</sup> has been reported and confirmed by several reports<sup>62,129</sup>. Thus in our equivalent Li<sub>2</sub>S<sub>6</sub> solutions, the presence of solid S<sub>8</sub> and Li<sub>2</sub>S<sub>4</sub> is confirmed, which can only be compatible with the disproportionation equilibrium. Whatever the peak at 365nm its behavior is parallel to the one of S<sub>4</sub><sup>2-</sup> peaks.

This result can explain the small wave in between the 2 plateaus during the reduction of sulfur (discharge, see **chapter I** and **chapter IV**). Indeed, it could correspond to the S<sub>8</sub>/Li<sub>2</sub>S<sub>4</sub> equilibrium as Li<sub>2</sub>S<sub>6</sub> tends to disproportionate into S<sub>8</sub>/S<sub>4</sub><sup>2-</sup>.

To go deeper, further experiments are required, especially by studying equivalent solutions of Li<sub>2</sub>S<sub>8</sub> and Li<sub>2</sub>S<sub>4</sub> to confirm both the positions of the S<sub>4</sub><sup>2-</sup> and evaluate the different disproportionation reactions with S<sub>8</sub><sup>2-</sup> and S<sub>4</sub><sup>2-</sup>. Another interesting direction would be to work with another solvent than DOL-DME, and at lower temperatures to stabilize S<sub>6</sub><sup>2-</sup> and to estimate the equilibrium constant.

Now, we have the tools necessary to properly analyze the adsorption of equivalent Li<sub>2</sub>S<sub>6</sub> solution on different adsorbents. It is worth to focus on adsorption capacity, *C<sub>ads</sub>*, that will be discussed in the next part.

### 1.3 Study of the adsorption

This section is divided in three parts. It starts with a description of the experimental protocol to trace the adsorption isotherms used to study of adsorption in presence of adsorbent synthesized in **chapter II**. The second part is devoted to the spectral study of the influence of adsorbent natures on the adsorption phenomenon and the polysulfides species equilibria to gain additional understanding into the specific interaction between adsorbent and each Li<sub>2</sub>S<sub>6</sub> contributions. This study is conducted on MoS<sub>2</sub>-KB sample from “MoS<sub>2</sub> loading” series (**32Mo-400-H<sub>2</sub>S(15)**, **48Mo-400-H<sub>2</sub>S(15)**) because both samples show notable difference in their adsorption capacity and enable to study two separate behavior. A fumed silica adsorbent (Aerosil 200) is also studied to understand the adsorbent nature influence as its interaction with polysulfides, as can be observed on the quartz cuvette surface, in line with work done by Conder *et al.*<sup>60</sup>

The last part is dedicated to the adsorption capacity determination.

#### 1.3.1 Experimental protocol

##### 1.3.1.1 Preparation of [adsorbent-Li<sub>2</sub>S<sub>6</sub> equivalent] solutions for adsorption isotherms

To prepare the adsorbent-Li<sub>2</sub>S<sub>6</sub> equivalent solutions, 40 mg of solid (adsorbent) are dispersed in 10 mL DOL:DME v/v 1/1 at room temperature using ultrasounds (1 min, 40 W). Several drops of known volumes of concentrated Li<sub>2</sub>S<sub>6</sub> equivalent solution (60 mM) are added to the initial dispersion to vary the equivalent Li<sub>2</sub>S<sub>6</sub> concentration from 0 mM to 4.9 mM according to the protocol shown in **Table III-6**. One can notice, that up to 1.9 mM, small volumes (10 &

40 $\mu$ L) are added to get a better resolution at low concentration where most of the adsorption occurs, then the volume of the drops is increased to 80  $\mu$ L to reach the full capacity of adsorption. In **Figure III-19** is plotted a characteristic kinetics curve of adsorbed amount (capacity of adsorption) as function of time using 48Mo-400-H<sub>2</sub>S for a total addition of 0.57 mL Li<sub>2</sub>S<sub>6</sub> solution. It shows that the equilibration is reached in less than 1h. We take this duration as our standard equilibrium time for all the systematic experiments. Thus, after each volume addition, the solution is stirred during 1 hour prior to decantation (30 min) and UV-Vis signal is recorded from 200 to 600 nm.

**Table III-6. Experimental Li<sub>2</sub>S<sub>6</sub> volume addition protocol to get adsorption isotherms.**

Time (h)	Volume of Li <sub>2</sub> S <sub>6</sub> added ( $\mu$ L)	Initial [Li <sub>2</sub> S <sub>6</sub> ] (mM)	Total volume (Vtot) (mL)
1	0	0	10 (pure DOL-DME)
1	10	0.1	10.01
2	40	0.3	10.05
3	40	0.5	10.09
4	40	0.8	10.13
5	40	1.0	10.17
6	40	1.2	10.21
7	40	1.5	10.25
8	40	1.7	10.29
9	40	1.9	10.33
10	80	2.4	10.41
11	80	2.8	10.49
12	80	3.2	10.57
13	80	3.7	10.65
14	80	4.1	10.73
15	160	4.9	10.89

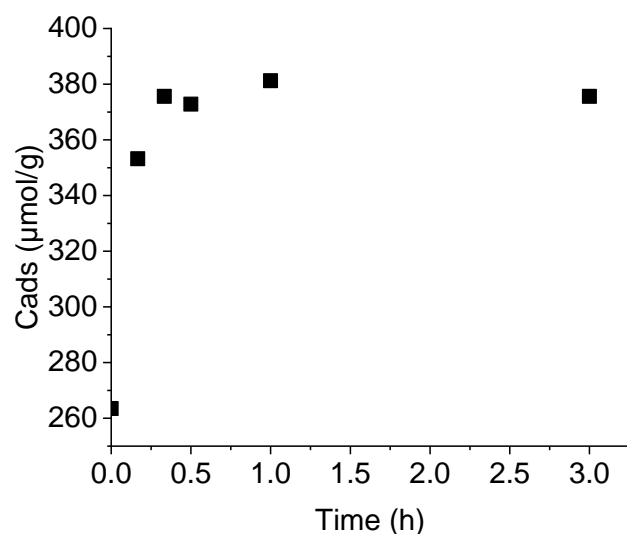
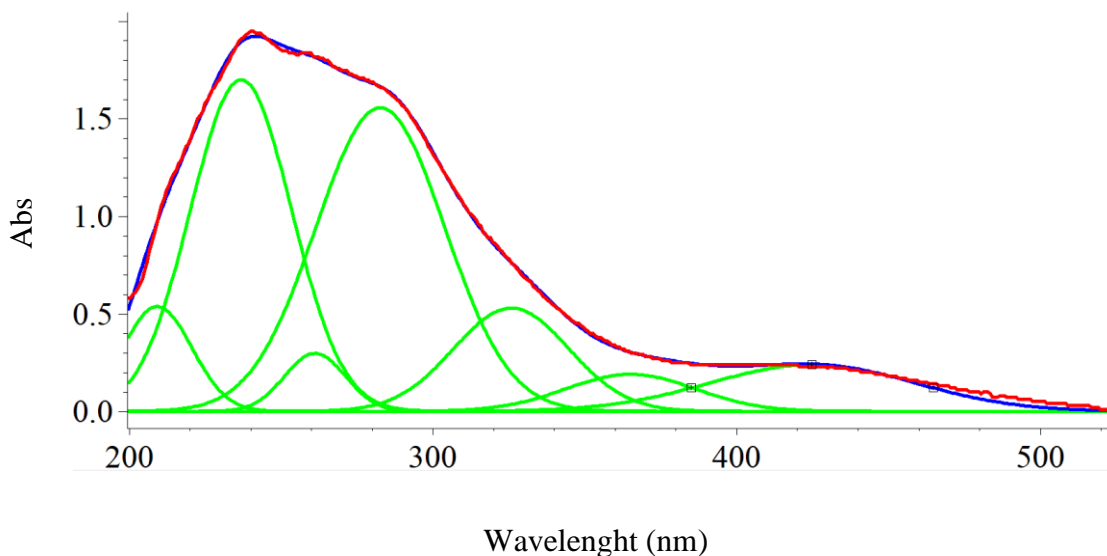


**Figure III-19.** Evolution of 48Mo-400-H<sub>2</sub>S adsorption capacity in (μmol/g) over time after addition of 0.57 mL of Li<sub>2</sub>S<sub>6</sub> solution (corresponding to 3.2 mM).

### 1.3.1.2 Verification of the spectral curve decomposition fitting with [adsorbent-Li<sub>2</sub>S<sub>6</sub> equivalent] solutions

The set of parameters is applied UV-VIS signal obtained in the presence of the adsorbent in contact with Li<sub>2</sub>S<sub>6</sub> solutions. **Figure III-20** gives an example obtained with 48Mo-400-H<sub>2</sub>S(15) in contact with 4.1 mM Li<sub>2</sub>S<sub>6</sub> solution. Excellent fit of the experimental curve is also obtained. Only the intensity of the peaks has been kept free to be adjusted. Therefore, this parameter set with a physico-chemical consistency seems robust and thus well-suited for our study. The spectral decompositions of spectra obtained after the addition of 0.5, 1, 1.5, 1.9, 2.4, 3.2, 4.1 and 4.9 mM of Li<sub>2</sub>S<sub>6</sub> are analyzed in the discussion.



Peak position	Width	Height	Area
209	27	0,5	15
236	39	1,7	71
261	24	0,3	7
282	50	1,6	83
325	45	0,5	25
365	50	0,2	10
425	80	0,2	20

**Figure III-20.** Example of fitting obtained after the adsorption of 4.1 mM Li<sub>2</sub>S<sub>6</sub> on 48Mo-400-H<sub>2</sub>S(15) adsorbent (red curve refers to experimental curve, green curves to the individual peaks and blue curve to simulated Gaussian curve).

### 1.3.1.3 Adsorption isotherm plots

Adsorption isotherms are plot as follow:  $n_{ads} = f(C_{eq})$  isotherms. Using the peak fit procedure described in **section III-1.2.3** of UV-Vis spectra, the individual peaks area can be measured, and compared with the calibration curves (**Figure III-13** in **section III-1.2.3**), in order to determine the equilibrium concentration of each species in solution ( $C_{eq}$ ) from measurements. To calculate to the remaining concentration of LiPS species ( $C_{ads}$ ) in solution and the equivalence in number of moles ( $n_{ads}$ ), we consider the initial Li<sub>2</sub>S<sub>6</sub> equivalent concentration ( $C^\circ$ ) (prior to adsorption). As shown in the previous section, the calculation of S<sub>8</sub>, S<sub>4</sub><sup>2-</sup> and S<sub>6</sub><sup>2-</sup> concentration is still ambiguous. The  $n_{ads}$  is then an approximation given at a  $\alpha$  factor.

**Equations (III-11) to (III-13)** show how is calculated  $n_{ads}$ .

$$C_{eq} = \frac{Area}{calibration\ slope} \quad (III-11)$$

$$C_{ads} = C^\circ - C_{eq} \quad (III-12)$$

$$n_{ads} = C_{ads} * V_{tot} \quad (III-13)$$

The experimental adsorption isotherms are fitted using the Langmuir model **equation (III-14)**. Langmuir adsorption isotherm is one of the simplest models that describe the behavior of a binary system (equilibrium between adsorbate and adsorbent). The main postulates of this model are as follows <sup>139</sup> :

- i) the adsorption rate  $\theta$  is limited to one molecular layer;
- ii) there is no lateral interaction between adjacent adsorbed molecules;
- iii) all the sites of the solid surface are equivalent;

**Langmuir equation:**

$$\theta = \frac{n_{ads}}{n_{ads\ sat}} = \frac{K_{ads} * C_{Li_2S_6\ eq}}{1 + K_{ads} * C_{Li_2S_6\ eq}} \quad \text{(III-14)}$$

With

$\theta$  : fractional adsorbent surface coverage

$n_{ads}$  : number of mole of Li<sub>2</sub>S<sub>6</sub> at the adsorbent surface ( $\mu\text{mol}$ )

$n_{ads\ sat}$  : number of mole of Li<sub>2</sub>S<sub>6</sub> required to saturate the adsorbent surface ( $\mu\text{mol}$ )

$C_{eq}$  : equilibrium Li<sub>2</sub>S<sub>6</sub> concentration ( $\mu\text{mol.L}^{-1}$ )

$K_{ads}$  : adsorption equilibrium constant

The  $n_{ads} = f(C_{eq})$  adsorption isotherm data are fitted using least squares method.

**1.3.1.4 Preparation of [adsorbent-Li<sub>2</sub>S<sub>6</sub> equivalent] solutions for adsorption capacity determination and XPS measurements.**

It has been also demonstrated in this study that a surface saturation is observed at 3-3.2 mM of Li<sub>2</sub>S<sub>6</sub> for the highest loaded MoS<sub>2</sub> samples (48 wt.%). Other samples saturate before reaching this concentration. Therefore, the choice of a 3 mM Li<sub>2</sub>S<sub>6</sub> solution is seen as optimal as it allows working at the saturation of solid surfaces to determine their adsorption capacities. Fortunately, this choice of concentration allows us to compare our results with Cui's paper<sup>51</sup> and, on a broader scale, with the rest of the publications presenting qualitative UV-Vis results. More than 70% of the studies work at a concentration of 3 mM without providing an explanation for this choice. For the direct determination of the capacity adsorption, the protocol is similar to the one described to plot the adsorption isotherm. 40 mg of solid are directly dispersed into 10 mL of 3

mM Li<sub>2</sub>S<sub>6</sub> at using ultrasounds (1 min, 40 W) at room temperature. Solutions are stirred magnetically overnight before particle settling. After decantation, the absorbance UV-Vis spectrum from 200 to 600 nm is recorded.

After adsorption, some samples have been selected and analyzed by X-ray photoelectron spectroscopy (XPS). Samples are washed with DOL/DME v/v 1/1 solvent, filtered with Büchner and dried during 12 h. As-obtained powders are manually pressed onto an indium sample holder and then mounted to carbon tape. Silica samples are directly mounted to carbon tape due to the non-adhesiveness on the indium substrate. All these preparation steps are made inside an argon-filled glove box to prevent surface contaminations.

### 1.3.1.5 Calculation of adsorption capacity determination

Considering that the UV-Vis area represents the remaining Li<sub>2</sub>S<sub>6</sub> concentration in solution after adsorption, it is possible to calculate the number of Li<sub>2</sub>S<sub>6</sub> moles resulting, knowing the initial volume of solution (**equation (III-15)**).

$$n_{Li_2S_6 \text{ remaining}} = \frac{Area}{Li_2S_6 \text{ calibration slope}} * V_{solution} \quad (III-15)$$

The number of moles of Li<sub>2</sub>S<sub>6</sub> adsorbed  $n_{ads}$ , the specific adsorption capacity  $N_{ads}$  (μmol of Li<sub>2</sub>S<sub>6</sub> adsorbed per gram of sample) are calculated following **equations (III-16) to (III-17)**.

$$n_{ads} (\mu mol) = (n_{Li_2S_6 \text{ initial}} - n_{Li_2S_6 \text{ remaining}}) \quad (III-16)$$

$$N_{ads} \left( \frac{\mu mol}{g} \right) = \frac{n_{ads}}{mass \text{ of sample}} \quad (III-17)$$

The number of moles of Li<sub>2</sub>S<sub>6</sub> adsorbed on MoS<sub>2</sub>  $n_{ads \text{ MoS}_2}$ , the MoS<sub>2</sub> contribution in the MoS<sub>2</sub>-KB and the MoS<sub>2</sub> specific adsorption capacity  $N_{ads \text{ MoS}_2}$  (μmol of Li<sub>2</sub>S<sub>6</sub> adsorbed per gram of MoS<sub>2</sub>) are calculated using **equations (III-18) to (III-19)**.

$$n_{ads \text{ MoS}_2} (\mu mol) = n_{ads} - \left( N_{ads \text{ KB}} * mass \text{ of sample} * \frac{\% \text{ wt KB}}{100} \right) \quad (III-18)$$

$$N_{ads \text{ MoS}_2} \left( \frac{\mu mol}{g \text{ MoS}_2} \right) = \frac{n_{ads \text{ specific Mo}}}{mass \text{ of sample} * \frac{\% \text{ wt MoS}_2}{100}} \quad (III-19)$$

In this equation, wt.% KB and wt. % Mo are taken from Chapter II.

### 1.3.2 Discussion

#### 1.3.2.1 Adsorption isotherms study

The UV-Vis spectra obtained after the successive volume additions listed in **Table III-6** are shown in **Figure III-21**. Each signal is named using the initial Li<sub>2</sub>S<sub>6</sub> concentration. Interestingly, the contribution in the visible range corresponding to S<sub>4</sub><sup>2-</sup> and S<sub>6</sub><sup>2-</sup> are negligible up to 1.9 mM for Aerosil 200 and **32Mo-400-H<sub>2</sub>S(15)** and up to 3 mM for **48Mo-400-H<sub>2</sub>S(15)** then they increase proportionally to the Li<sub>2</sub>S<sub>6</sub> addition demonstrating a full adsorption of these species up to 1.9 mM. On the contrary, in the UV range, corresponding mainly to the sulfur (on contribution of S<sub>4</sub><sup>2-</sup> is included at 325±5 nm), the intensities of the peaks seem always proportional to the Li<sub>2</sub>S<sub>6</sub> concentration, suggesting no or few adsorptions of dissolved elemental sulfur occurs on the solids, herein on both MoS<sub>2</sub> and Aerosil 200 based adsorbent.

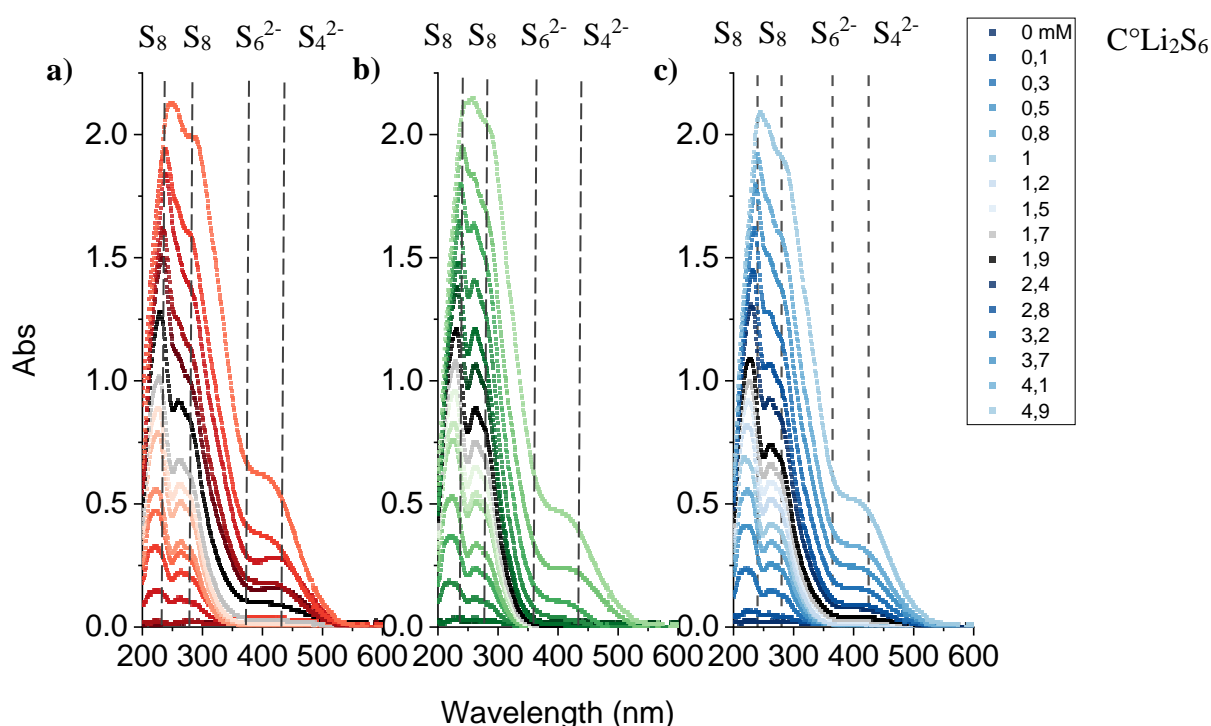


**Figure III-21.** Equilibrium UV-Vis spectra obtained on the supernatant of the a) **32Mo-400-H<sub>2</sub>S(15)** b) **48Mo-400-H<sub>2</sub>S(15)** and c) Aerosil 200 after (15) successive Li<sub>2</sub>S<sub>6</sub> equivalent additions.



Figure III-22 a, b and c show the result, i.e. the evolution of each peak area with the three adsorbents. For all three materials, the adsorption is very selective: S<sub>8</sub> seems not adsorbed or, at least, very few, as its peaks vary linearly with a similar slope within the error margin (the margin errors are 5% on x-axis and 10% for y-axis) to that of S<sub>8</sub> in standard Li<sub>2</sub>S<sub>6</sub> (black points) solutions for all adsorbents, while S<sub>4</sub><sup>2-</sup> (and S<sub>6</sub><sup>2-</sup>) strongly interact with the different surfaces. They are fully adsorbed (no peak) by the MoS<sub>2</sub>-KB samples up to a saturation value which increases with MoS<sub>2</sub> content and the exposed surface. In the case of Aerosil, the adsorption seems less strong with a slight non-linear increase of the intensity up to 2mM.

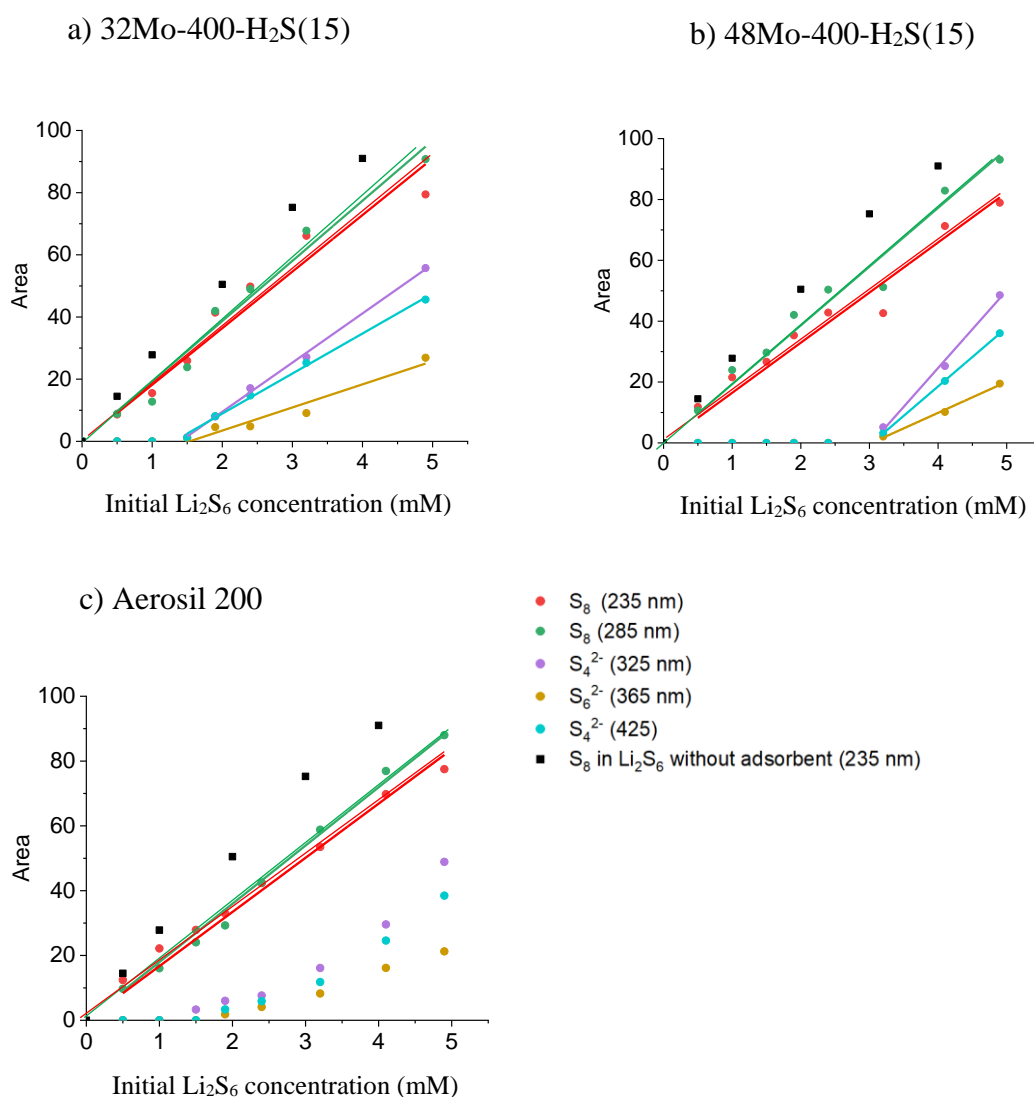
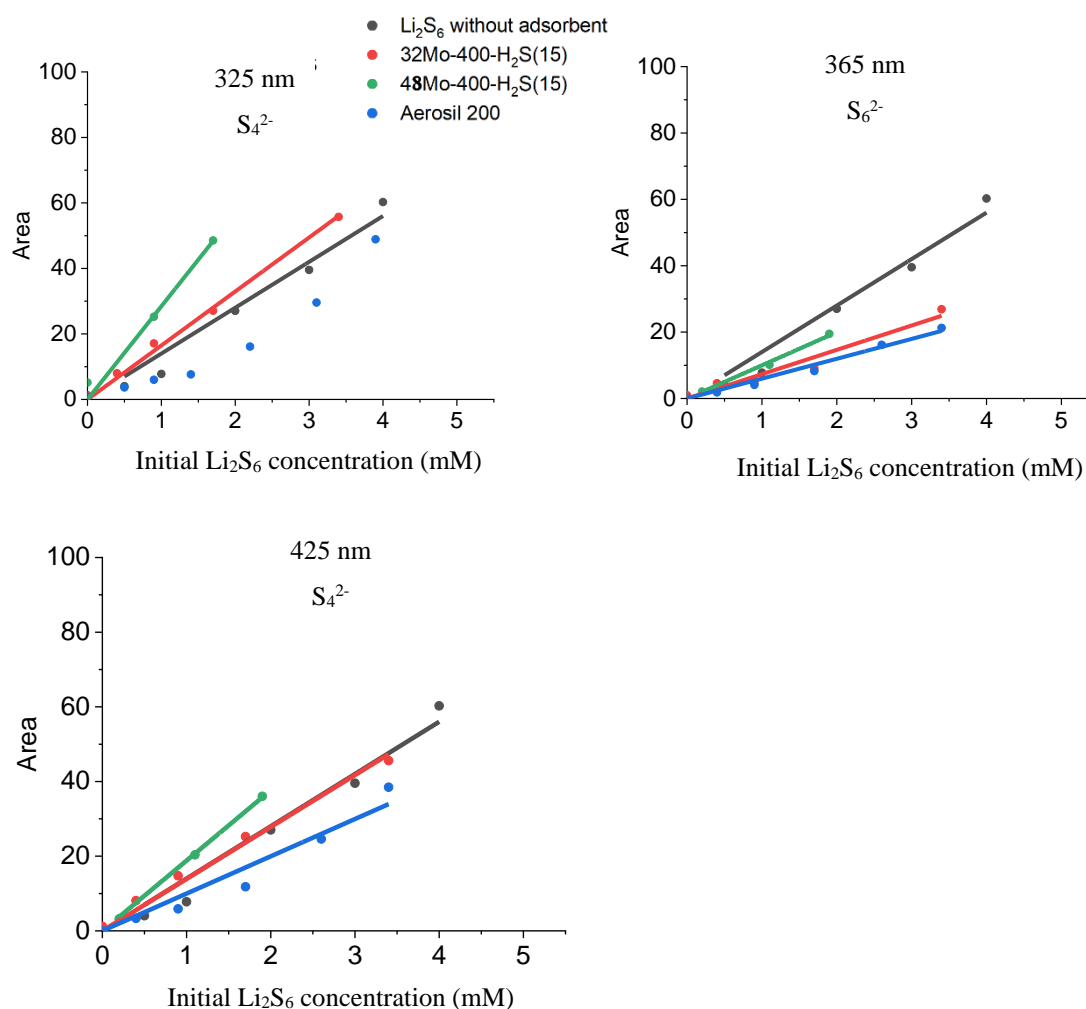


Figure III-22. Evolution of peak area of each specie contribution with the initial Li<sub>2</sub>S<sub>6</sub> concentration for a) 32Mo-400-H<sub>2</sub>S(15) b) 48Mo-400-H<sub>2</sub>S(15) c) Aerosil 200.

These results shows that elemental sulfur S<sub>8</sub> is not adsorbed and has little affinity for these solids (hydrophobic carbon, polar SiO<sub>2</sub>).

After the surface saturation, the contributions of S<sub>4</sub><sup>2-</sup> and S<sub>6</sub><sup>2-</sup> varies linearly with the concentration after Li<sub>2</sub>S<sub>6</sub> addition. A similar slope that in the Li<sub>2</sub>S<sub>6</sub> standard solution is expected. Only 32Mo-400-H<sub>2</sub>S(15) shows that behavior as shown in

**Figure III-23.** 48Mo-400-H<sub>2</sub>S(15) shows S<sub>4</sub><sup>2-</sup> higher slope while S<sub>6</sub><sup>2-</sup> slope is decreased. Aerosil 200 shows lower slopes variations for each contribution compared to Li<sub>2</sub>S<sub>6</sub>. This remains unclear.



**Figure III-23.** Evolution of the area of the different contributions after adsorbent saturation at a) 325 b) 365 and c) 425 nm compared to Li<sub>2</sub>S<sub>6</sub>.

An estimation of the adsorption constants (*k<sub>ads</sub>*) from equations (III-20) to (III-21) are calculated thanks to the classical Langmuir formalism.

- Adsorption equilibria (at the adsorbent surface)



The adsorption isotherms (*nads\*α* vs *C<sub>eq</sub>*) (according to equations III-13-14 shown in section III-1.3.1.3) are plotted in Figure III-24 taking the peak at 325, 365 and 425 nm (attributed to S<sub>4</sub><sup>2-</sup> and S<sub>6</sub><sup>2-</sup>). The isotherms are adjusted by a factor α (undetermined) because the calculation relies on C° Li<sub>2</sub>S<sub>6</sub> equivalent instead of [S<sub>4</sub><sup>2-</sup>] and [S<sub>6</sub><sup>2-</sup>] in the solution since their determination remains partially unresolved. However, the estimation of *k<sub>ads</sub>* is not affected by the factor α.

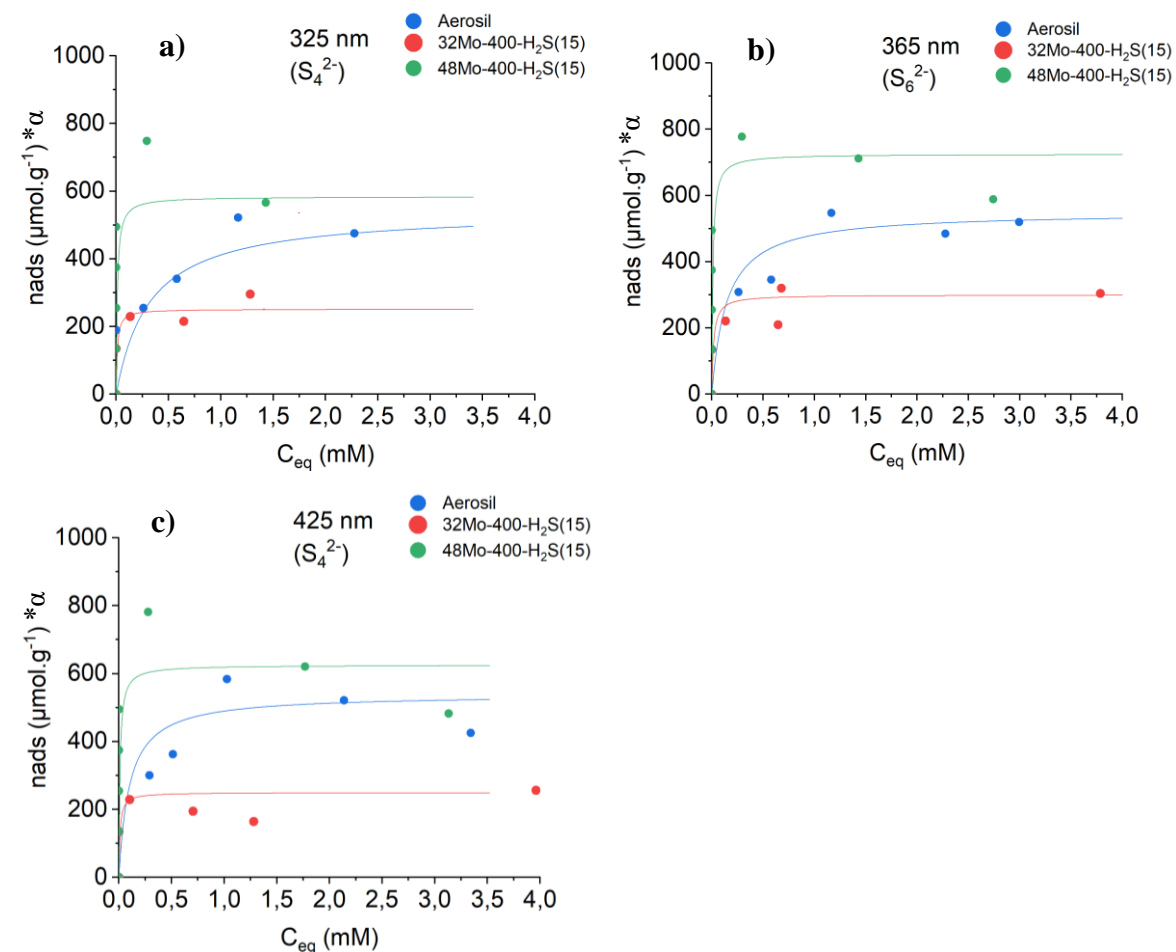


**Figure III-24.** Comparison of the adsorption isotherms per contribution at a) 325 nm b) 365 nm c) 425 nm for Aerosil 200, 32Mo-400-H<sub>2</sub>S(15) and 48Mo-400-H<sub>2</sub>S(15). Points represents experimental data and lines the Langmuir adsorption isotherm.

The Langmuir model provides quite a good fit of the adsorption isotherms for both MoS<sub>2</sub> based compounds 48Mo-400-H<sub>2</sub>S(15), and 32Mo-400-H<sub>2</sub>S(15), while for the Aerosil 200, isotherm shape suggest a more complex phenomenon. Nevertheless, it is still possible to asses the adsorption constant  $k_{ads}$  (see **equation III-14**), which is related to the adsorption strength, and the maximum of adsorption (supposed to be one monolayer in Langmuir model)  $n_{ads sat}$ , called the adsorption capacity. The three contributions in the visible range show very similar isotherms, giving according similar fitting parameters. The results are summarized in **Table III-7**.

**Table III-7. Adsorption equilibrium constant  $k_{ads}$  and  $n_{ads sat}$ .**

	Aerosil 200		32Mo-400-H <sub>2</sub> S(15)		48Mo-400-H <sub>2</sub> S(15)	
	$k_{ads}$	$n_{ads sat}$ ( $\mu\text{mol LiPS/g}$ of MoS <sub>2</sub> -KB)	$k_{ads}$	$n_{ads sat}$ ( $\mu\text{mol LiPS/g}$ of MoS <sub>2</sub> -KB)	$k_{ads}$	$n_{ads sat}$ ( $\mu\text{mol LiPS/g}$ of MoS <sub>2</sub> -KB)
325 nm (S <sub>4</sub> <sup>2-</sup> )	4 ± 1	625 ± 130	95 ± 20	250 ± 50	101 ± 20	615 ± 123
365 nm (S <sub>6</sub> <sup>2-</sup> )	7 ± 2	550 ± 110	62 ± 20	300 ± 60	93 ± 20	750 ± 150
425 nm (S <sub>4</sub> <sup>2-</sup> )	10 ± 5	550 ± 110	121 ± 20	250 ± 50	150 ± 20	725 ± 90

Materials can be compared to each other, with the adsorption constants varying as follows:  $k_{ads}$  48Mo-400-H<sub>2</sub>S(15) >> Aerosil 200, which reflect the differences in the behavior and illustrates the impact of the nature of the adsorbent on the adsorption thermodynamics. The  $k_{ads}$  S<sub>6</sub><sup>2-</sup> 48Mo-400-H<sub>2</sub>S(15) >  $k_{ads}$  S<sub>6</sub><sup>2-</sup> 32Mo-400-H<sub>2</sub>S(15) may be due to the limited experimental data points that induce artefact in the model. We can assume that, similarly to S<sub>4</sub><sup>2-</sup>, the  $k_{ads}$  values of MoS<sub>2</sub> are closed: 48Mo-400-H<sub>2</sub>S(15) # 32Mo-400-H<sub>2</sub>S(15). The amount of adsorbed S<sub>x</sub><sup>2-</sup> appears to remain relatively constant from one contribution to another. This time, the variation in  $n_{ads sat}$  follows the order: 48Mo-400-H<sub>2</sub>S(15) > Aerosil 200 > 32Mo-400-H<sub>2</sub>S(15), which is consistent with adsorption capacity  $N_{ads}$  measured. To our knowledge, we are the first to provide such set of data and analyses, thus the values of  $k_{ads}$  could not be compared and discussed with literature data.

In this study, the “S<sub>4</sub><sup>2-</sup>” and “S<sub>6</sub><sup>2-</sup>” species has been considered as dissociated from Li<sup>+</sup> cations. However, The theoretical 1D model of Korff *et al.*<sup>18</sup> pointed out that conventional mechanisms used to described polysulfides equilibria, treating species as “non-lithiated” (ie as polysulfide anion fully dissociated from Li<sup>+</sup> cations), is not totally true. They determined that molecular Li<sub>2</sub>S<sub>x</sub> species are existing. In addition, A.Gupta and A.Manthiram<sup>23</sup> showed experimentally that polysulfides can be found at clustered states such as Li<sub>x</sub>S<sub>y</sub>(-2y+x) ( $x \leq 2y$  and  $x > 2$ ) (especially under lean-electrolyte or at low temperature conditions). The existence of clustering and molecular Li<sub>2</sub>S<sub>6</sub> which might also change the adsorption mechanism operating in the battery.

### 1.3.2.2 X-ray photoelectron spectroscopy (XPS) measurements

X-ray photoelectron spectroscopy (XPS) measurements have been conducted on 32Mo-400-H<sub>2</sub>S(15) and Aerosil 200 to confirm the adsorption phenomena of theses adsorbents after the Li<sub>2</sub>S<sub>6</sub> equivalent adsorption. As example, Mo 3d, S 2p and Li 1s XPS spectra of 32Mo-400-H<sub>2</sub>S(15) are shown on **Figure III-25**. The results of the semi-quantitative analysis performed before and after adsorption are given in **Table III-8**. The relative quantification is achieved by normalizing all detected elements to 100% (averaging measurements from 3 data points). In addition, it should be noted that there is inherent contamination of carbon and oxygen in the samples originating from the device itself.

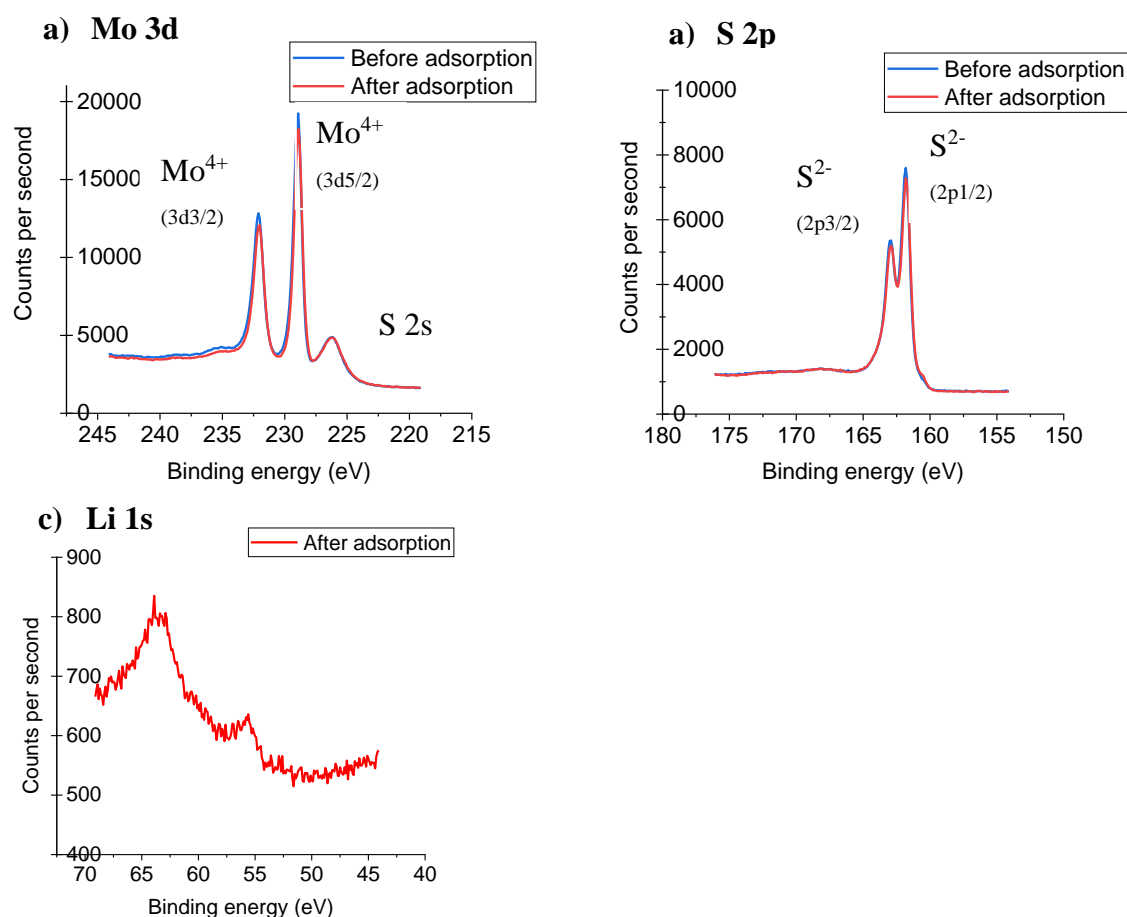


**Figure III-25.** <sup>32</sup>Mo-400-H<sub>2</sub>S(15) XPS spectra centered on a) molybdenum Mo 3d b) sulfur S 2p c) lithium Li 1s.

**Table III-8.** Semi-quantitative analysis of XPS spectra before and after polysulfides adsorption.

For <sup>32</sup>Mo-400-H<sub>2</sub>S(15)

	Before Li <sub>2</sub> S <sub>6</sub> adsorption		After Li <sub>2</sub> S <sub>6</sub> adsorption	
	Atomic conc. [%]	Mass conc. [%]	Atomic conc. [%]	Mass conc. [%]
C 1s	90.8	71.4	88.1	70.0
Li 1s	-	-	1.2	0.5
Mo	2.6	16.4	2.4	15.3
O 1s	1.5	1.6	3.1	3.3
P 2p	0.2	0.4	0.2	0.5
S 2p	4.9	10.2	4.9	10.4

For Aerosil 200

	Before Li <sub>2</sub> S <sub>6</sub> adsorption		After Li <sub>2</sub> S <sub>6</sub> adsorption	
	Atomic conc. [%]	Mass conc. [%]	Atomic conc. [%]	Mass conc. [%]
C 1s	2.5	1.5	15.1	9.9
Li 1s	-	-	1.9	0.7
O 1s	68.9	56.9	59.0	52.1
Si 2p	28.6	41.5	24.0	37.2

The detection of 1.2 and 1.9 atomic % of Li for both MoS<sub>2</sub>-KB and Aerosil 200 seems to confirm the LiPS adsorption on the surface even if no sulfur is detected for Aerosil after adsorption. The latter adsorbate may have been decomposed inside the glovebox because during the drying process under argon (in a glovebox), the sample, which has remained yellow after washing, turns white (approximately 2 hours). This decomposition might be attributed to reoxidation upon contact with H<sub>2</sub>O residual amount in the glove box, as suggested by the Li<sub>2</sub>S + H<sub>2</sub>O => Li<sub>2</sub>O + H<sub>2</sub>S reactions.

For MoS<sub>2</sub>-KB a slight increase of S/Mo ratio from 1.9 to 2 is observed. J.Luo *et al*<sup>140</sup>. performed the same kind of experiment and shows a new peak on the Mo 3d XPS spectrum decomposition at 22.9 eV included inside the Mo (3d<sub>5/2</sub>) contributions (see [section II-1.3.1](#)). They attributed this to Mo-S bond, which implies that LiPS can be adsorbed at least by sulfur.

### 1.3.2.3 Polysulfides adsorption capacity determination

The subsection subsequently is dedicated to the polysulfides adsorption capacities (*Nads*) determination of Li<sub>2</sub>S<sub>6</sub> equivalent taking into account the entire UV-Vis to evaluate the impact of MoS<sub>2</sub>-KB structures synthesized in [chapter II](#). This study presents the preliminary research conducted at the outset of the PhD work, before the development of the *spectral curve decomposition method*. It focuses only on the Li<sub>2</sub>S<sub>6</sub> equivalent and does not account the nature of the polysulfides involved in the adsorption. Nonetheless, this approach proves to be a rapid material screening process. It confirms the influence of MoS<sub>2</sub> loading observed with the spectral curve decomposition study and sheds light on the impact of various sulfidation conditions, including post-treatment, sulfidation gas composition, and sulfidation temperature variations, on LiPS adsorption, as the spectral curve decomposition has not been performed on these samples yet. The results are subsequently compared with pristine Ketjenblack and unsupported

MoS<sub>2</sub>. The synthesis protocol of this unsupported MoS<sub>2</sub> is given in **Appendix B**. The experimental conditions are given in **section 1.3.1.4** and **1.3.1.5**.

### *Influence of MoS<sub>2</sub> loading*

This experimental work enables to screen material with MoS<sub>2</sub> contents from 0% to 100% by using Ketjenblack, unsupported MoS<sub>2</sub>, 32Mo-400-H<sub>2</sub>S(15) and 48Mo-400-H<sub>2</sub>S(15) inside a 10 mL of 3 mM Li<sub>2</sub>S<sub>6</sub> solution. **Figure III-26** displays the color alteration of the Li<sub>2</sub>S<sub>6</sub> solution observed after the addition of the materials (images taken after 12 h). On the one hand, no observable color fading is associated with MoS<sub>2</sub> and KB, suggesting weak adsorption. It is worth noting that the presence of KB in the vial made difficult visual analysis (dark solution) and required a settling time decantation of one hour instead of few minutes for the other samples. On the other hand, the Li<sub>2</sub>S<sub>6</sub> color intensity decreases with 32Mo-400-H<sub>2</sub>S(15) and 48Mo-400-H<sub>2</sub>S(15) samples from orange to yellowish indicating that the concentration of species absorbing in the visible range (S<sub>6</sub><sup>2-</sup> at 365 nm and S<sub>4</sub><sup>2-</sup> at 425 nm) has been reduced. This is in line adsorption isotherms (see **section II-1.3.2.1**). The 32Mo-400-H<sub>2</sub>S(15) surface saturates at 1.9 mM while 48Mo-400-H<sub>2</sub>S(15) at 3 mM, this is why the 32Mo-400-H<sub>2</sub>S(15) solution is more colorful.

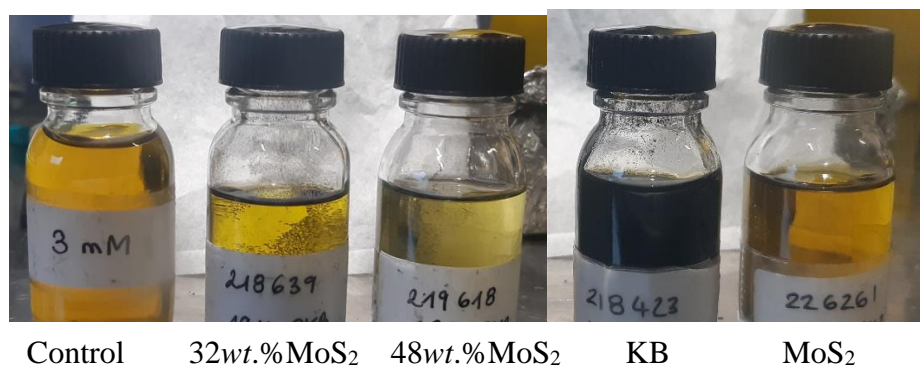


**Figure III-26.** Images of the 3 mM Li<sub>2</sub>S<sub>6</sub> color solution evolution after addition of 32Mo-400-H<sub>2</sub>S(15), 48Mo-400-H<sub>2</sub>S(15), Ketjenblack and MoS<sub>2</sub>.



**Figure III-27** shows UV-Vis spectra of Li<sub>2</sub>S<sub>6</sub> solutions before and after the addition of adsorbents. The UV-Vis results are in good agreement with the previous visual inspections.

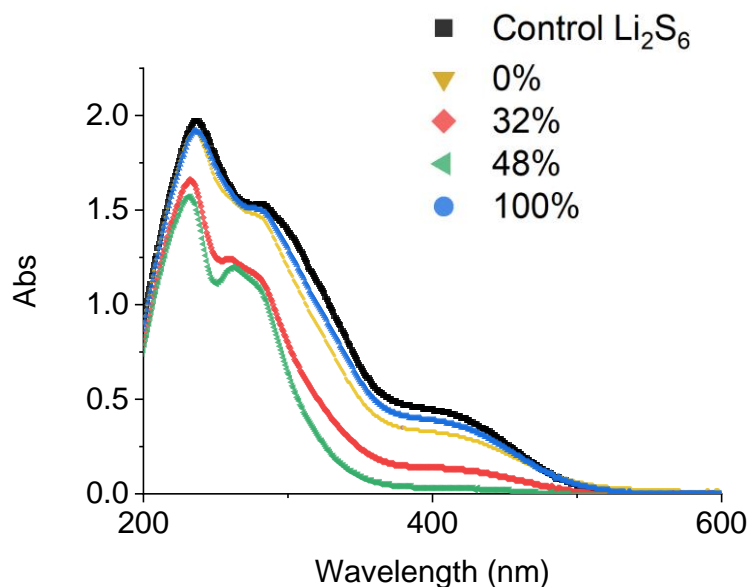


**Figure III-27.** UV-Vis spectra of Li<sub>2</sub>S<sub>6</sub> solution before and after the addition of KB, MoS<sub>2</sub>, 32Mo-400-H<sub>2</sub>S(15) and 48Mo-400-H<sub>2</sub>S(15).

**Table III-9** reports the adsorption capacities obtained. KB and MoS<sub>2</sub> displays a relatively low *N<sub>ads</sub>* of 87 and 88 ± 18 μmol/g<sub>sample</sub> while 32Mo-400-H<sub>2</sub>S(15) and 48Mo-400-H<sub>2</sub>S(15) exhibits 294 ± 59 and 389 ± 78 μmol/g<sub>sample</sub> respectively in which the supported MoS<sub>2</sub> contributes to 81 and 89% of the adsorption in MoS<sub>2</sub>-KB respectively.

**Table III-9.** Adsorption capacity with MoS<sub>2</sub> loading.

Sample	MoS <sub>2</sub> loading (wt. %)	N <sub>ads</sub> (μmol Li <sub>2</sub> S <sub>6</sub> /g <sub>sample</sub> )	n <sub>ads MoS<sub>2</sub></sub> (μmol Li <sub>2</sub> S <sub>6</sub> )	N <sub>ads MoS<sub>2</sub></sub> (μmol Li <sub>2</sub> S <sub>6</sub> /g supported MoS <sub>2</sub> )
KB	0	87 ± 17	-	-
32Mo-400-H <sub>2</sub> S(15)	32	294 ± 59	10 ± 2	754 ± 150
48Mo-400-H <sub>2</sub> S(15)	48	389 ± 78	14 ± 3	717 ± 143
Unsupported MoS <sub>2</sub>	100	88 ± 18	-	88 ± 18

The specific adsorption phenomenon ( $N_{\text{ads MoS}_2}$ ) induced by MoS<sub>2</sub> is significantly enhanced when using MoS<sub>2</sub> at supported state (MoS<sub>2</sub>-KB) compared to unsupported one. This can be explained by a different aggregation state. At supported state, a multitude of monolayers and bilayers of MoS<sub>2</sub> are obtained while for pure MoS<sub>2</sub> provides a high stacking (for instance of 11 in reference <sup>117</sup>). This inherently modifies the number of available sites for interaction with Li<sub>2</sub>S<sub>6</sub>. To get rid of this numerous works are dedicated to the exfoliation of MoS<sub>2</sub>.

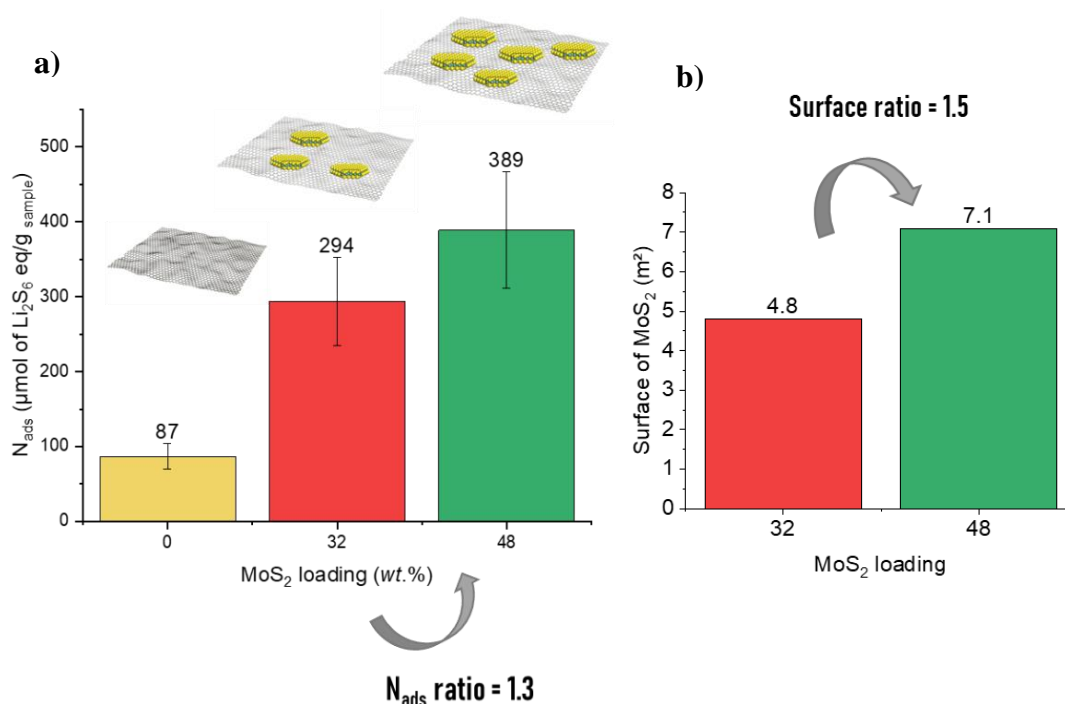


**Figure III-28.** Comparison of the evolution of a)  $N_{\text{ads}}$  and b) the MoS<sub>2</sub> surface ratio.

The **Figure III-28** illustrates the relationship between  $N_{\text{ads}}$  evolution and the MoS<sub>2</sub> surface area. The number of mol of Li<sub>2</sub>S<sub>6</sub> equivalent adsorbed by MoS<sub>2</sub> is 1.3 times greater with **48Mo-400-H<sub>2</sub>S(15)** (**Figure III-28-a**). When normalized by the mass of MoS<sub>2</sub>,  $N_{\text{ads}}$   $\mu\text{mol/g}$  supported MoS<sub>2</sub> is increased by 1.05 with **48Mo-400-H<sub>2</sub>S(15)** compared to **32Mo-400-H<sub>2</sub>S(15)**. These variations are of the same order of magnitude, taking in account the experimental errors.

The adsorption capacities enhancement is directly proportionally to the MoS<sub>2</sub> surface (**Figure III-28-b**). Increasing the MoS<sub>2</sub> loading leads to a higher number of exposed surface and, therefore, an increased number of accessible active sites<sup>127</sup> for similar MoS<sub>2</sub> nature (in slab length and stacking) between the two samples (as explained in **Chapter II**).

In our case, the use of KB to support layered MoS<sub>2</sub> is an effective strategy to hinder the aggregation of MoS<sub>2</sub> nanosheets. Moreover, increasing the MoS<sub>2</sub> content significantly enhances the adsorption activity for Li<sub>2</sub>S<sub>6</sub>.

### *Influence of sulfidation conditions*

Similar to what is observed in the previous section, partial discoloration of the Li<sub>2</sub>S<sub>6</sub> solution is observed (

**Figure III-29**). The difference in intensity between the samples is imperceptible, except for the sample 21Mo-600-H<sub>2</sub>S(100)-HN, treated at 600°C under pure H<sub>2</sub>S, which has the same color than the control vial. The adsorption capacities are calculated from the UV-Vis spectra presented in **Figure III-30** and the results are summarized in **Table III-10**.

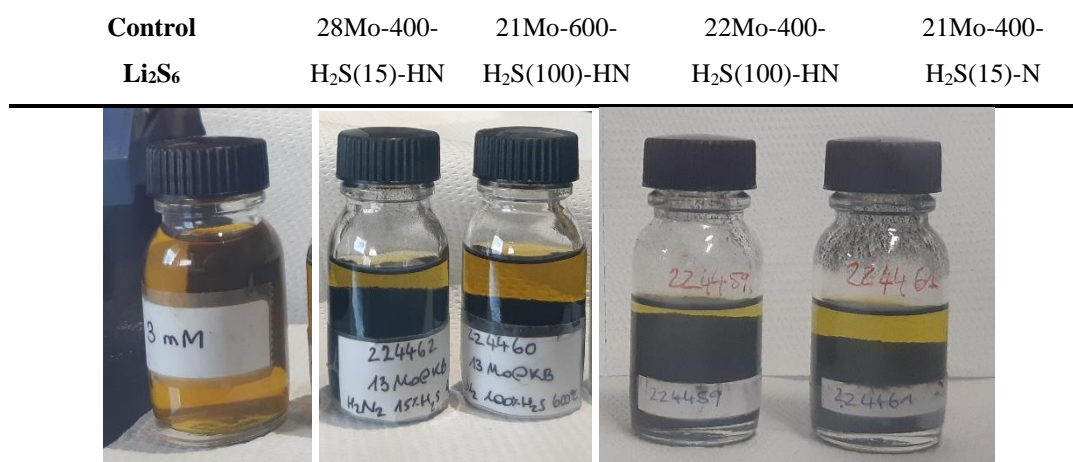


**Figure III-29.** Images of the 3 mM Li<sub>2</sub>S<sub>6</sub> color solution evolution after addition of MoS<sub>2</sub>-KB synthesized under varying sulfidation conditions.

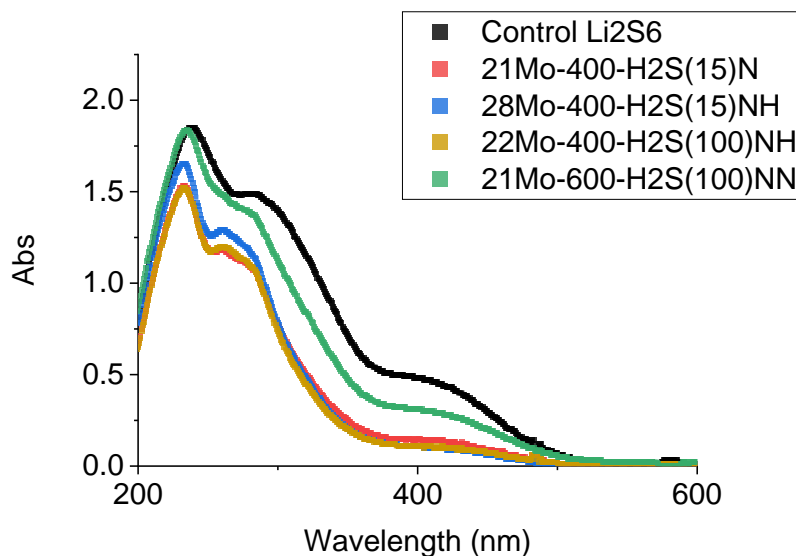


**Figure III-30.** UV-Vis spectra of Li<sub>2</sub>S<sub>6</sub> solution before and after the addition of adsorbent synthesized with various of sulfidation conditions.

**Table III-10.** Adsorption capacity with sulfidation conditions variations.

Sample	MoS <sub>2</sub> loading (% wt)	Nads (μmol/g <sub>sample</sub> )	nads with MoS <sub>2</sub> (μmol)	Nads (μmol/g supported MoS <sub>2</sub> )
<b>Post treatment</b>				
21Mo-400-H <sub>2</sub> S(15)-N	21	325 ± 65	10 ± 2	1204 ± 240
28Mo-400-H <sub>2</sub> S(15)-HN	28	310 ± 62	10 ± 2	899 ± 180
<b>Sulfidation temperature</b>				
22Mo-400-H <sub>2</sub> S(100)-HN	22	344 ± 69	11 ± 2	1292 ± 258
21Mo-600-H <sub>2</sub> S(100)-HN	21	119 ± 24	2 ± 1	253 ± 50

The samples can be relatively ranked as follows: *Nads* 22Mo-400-H<sub>2</sub>S(100)-HN > 21Mo-400-H<sub>2</sub>S(15)-N > 28Mo-400-H<sub>2</sub>S(15)-HN >> 21Mo-600-H<sub>2</sub>S(100)-HN.

Similarly, to “MoS<sub>2</sub> loading” series study, the ratio of  $N_{ads}$ ,  $n_{ads}$  and  $N_{ads MoS_2}$  are compared to the exposed surface ratios as shown in **Table III-11**.

**Table III-11. Ratio comparison of the different adsorption value calculated with the exposed surface area.**

Sample	Exposed surface ratio (from chapter II)	Nads ratio	n <sub>ads</sub> with MoS <sub>2</sub> ratio	N <sub>ads MoS<sub>2</sub></sub> ( $\mu$ mol/g supported MoS <sub>2</sub> ) ratio
<b>Post treatment</b>	<b>0.75</b>	1	1	1.3
<b>Gas nature</b>	<b>1.3</b>	0.9	0.9	0.7
<b>Sulfidation température</b>	<b>1</b>	2.9	5.5	5.1

For the « post-treatment » and « gas nature » variations, the difference in the exposed MoS<sub>2</sub> surface alone does not fully explain the result, as the ratios are slightly higher than the surface ratio. This theory is not sufficient to explain the results. For the “post-treatment” we do not have more characterization to found out a correlation with the adsorption.

In the case of “gas nature” series, more edges+corners are exposed for the sample obtained sulfured at 400°C under pure H<sub>2</sub>S instead of the conventional 15% H<sub>2</sub>S / 85% H<sub>2</sub> mixture. Between both samples, the edges+corners ratio is equal to 0.9 (see **chapter II**) which can better explain the results obtained more that the surface theory. This can be explained by a synergy between an increase in the number of edges (dispersion = 36% for 22Mo-400-H<sub>2</sub>S(100)-HN vs. 33% 28Mo-400-H<sub>2</sub>S(15)-HN) and the preferential formation of edges facilitated by the truncated triangular morphology of MoS<sub>2</sub>. Indeed, the binding energy between Li<sub>2</sub>S (that serves as polysulfides model) and Mo-edge is equal to 4.48 eV, compared to 2.70 eV for S-edge according to Wang *et al.*<sup>89</sup>. Working under pure H<sub>2</sub>S seems to be beneficial to create MoS<sub>2</sub>-KB structure that better interacts with LiPS. Nevertheless, increasing the temperature up to 600°C, leads to a complete drop in the measured adsorption capacity (119  $\mu$ mol/g recorded for **21Mo-600-H<sub>2</sub>S(100)-HN**). Even though this higher sulfidation temperature can increase the size of MoS<sub>2</sub> slabs through sintering, the stacking and exposed surface remain closed. Another possibility should be considered to explain the results.

The assumption we make is that increasing the sulfidation temperature could alter the metal-support interactions, thus modifying the adsorption forces due to changes in the electronic properties of MoS<sub>2</sub> (potentially modifying the quality of adsorption sites with temperature).

In addition, the “sulfidation conditions” series demonstrates a significantly higher  $N_{\text{ads MoS}_2}$  ( $\mu\text{mol/g}$  supported MoS<sub>2</sub>). The difference between these samples lies in the MoS<sub>2</sub> content and in the applied post-treatment. No post-treatment is conducted for 32 and 48Mo-400-H<sub>2</sub>S(15) as the cooling step is maintained under 15% H<sub>2</sub>S/85% H<sub>2</sub> gas flow until 80°C, sulfur vacancies have not been created in this conditions. This can explain the difference in the adsorption behavior.

To analyze at the overall MoS<sub>2</sub> nanoparticles engineering effects, it is possible to compared the intrinsic capacity of MoS<sub>2</sub> of the several samples synthesized (i.e., the capacity normalized per gram of MoS<sub>2</sub>). **Figure III-31** shows that the modification of the structure of MoS<sub>2</sub> supported on Ketjenblack has a significant impact on the adsorption capacity. The two samples with the highest adsorption capacity are characterized by the presence of sulfur vacancies or truncated triangular sheets. It is suggested that combinations of triangular sheets with high MoS<sub>2</sub> or CUS (coordination unsaturated sites) content could lead to an improvement in total adsorption capacity. The correlation between increased adsorption capacity and morphology is in line with Cui's group<sup>89</sup>, where a higher proportion of triangular shapes, and thus more Mo edge, is associated with improved adsorption. This study provides key insights into nanoparticle engineering to optimize the MoS<sub>2</sub>-KB structure for future work.

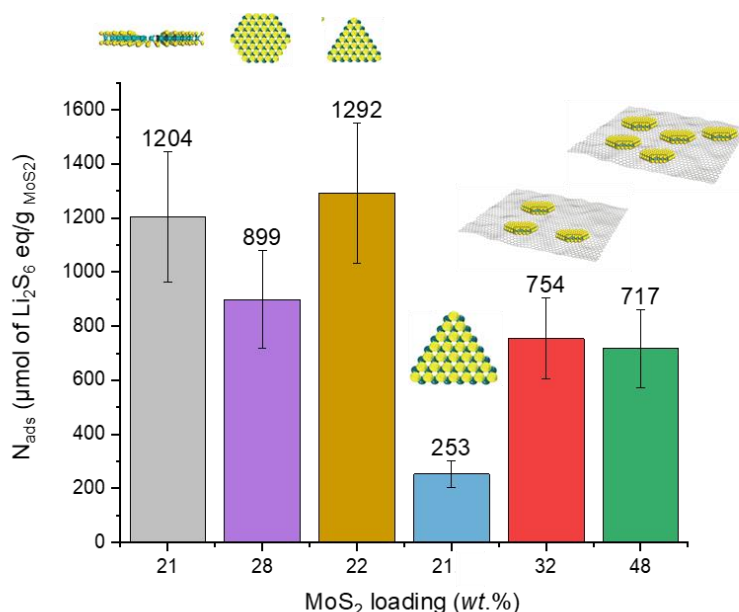


**Figure III-31.** Effect of MoS<sub>2</sub> nanoparticles engineering (comparison in terms of  $N_{\text{ads}}$  per gram of MoS<sub>2</sub>)

Among the available materials synthesized, the MoS<sub>2</sub>-KB with the highest adsorption capacity Nads ( $\mu\text{mol}/\text{g}_{\text{sample}}$ ) has been selected to design the Li-S positive electrodes (S-MoS<sub>2</sub>-KB). For that purpose, 48Mo-400-H<sub>2</sub>S(15) with its 389  $\mu\text{mol}$  Li<sub>2</sub>S<sub>6</sub> adsorbed per gram of sample has been selected as the best candidate. Therefore, the electrochemical study is focused on evaluating the influence of MoS<sub>2</sub> loading on electrochemical performance, with 32 and 48Mo-400-H<sub>2</sub>S(15) samples.

### *Comparison of the results with the literature*

We attempted to compare our results with those obtained by Cui's results<sup>51</sup>, performed under similar conditions. To do so, we initially chose Aerosil 200 as the silica material and synthesized unsupported MoS<sub>2</sub> for comparison with SiO<sub>2</sub> and the commercial MoS<sub>2</sub> used in Cui's results<sup>51</sup>. The UV-Vis results are given in **Figure III-32** and in **Table III-12**. Since the materials are not strictly identical (varying in the nature of the silica material, potentially differing aggregation states of MoS<sub>2</sub>, and differing surface areas), it is challenging to compare the materials.



**Figure III-32.** Images of the 3 mM Li<sub>2</sub>S<sub>6</sub> color solution evolution after addition of Aerosil 200 and MoS<sub>2</sub>.

**Table III-12. Nads comparison of the experimental data and the literature.**

Sample	Nads ( $\mu\text{mol/g}_{\text{sample}}$ )	BET ( $\text{m}^2/\text{g}$ )
<b>This work</b>		
MoS <sub>2</sub>	88 ± 18	26
48Mo-400-H <sub>2</sub> S(15)	389 ± 78	276
Aerosil 200	373 ± 74	200
<b>Cui (commercial powder)<sup>51</sup></b>		
MoS <sub>2</sub>	175	10
SiO <sub>2</sub> (not Aerosil)	39	5.9

## 1.4 Conclusion

A standard procedure using *in situ* probe has been established to minimize the artefact obtained with conventional quartz-cuvette, especially the adsorption of polysulfides at the cuvette surface, which prevents kinetic studies and poses a risk of air contamination outside the glove box, leading to polysulfides degradations. Indeed, the adsorption of polysulfides on the quartz cuvettes is confirmed by the high affinity of polysulfides for Aerosil 200, a fumed silica.

The spectral decomposition across the entire UV spectrum reveals that the Li<sub>2</sub>S<sub>6</sub> equivalent spectrum is composed of five contributions, with two accurately attributed to S<sub>8</sub> at 230 and 285 nm, and three others to S<sub>4</sub><sup>2-</sup> and S<sub>6</sub><sup>2-</sup>, as reported in the literature, at 325, 365, and 425 nm. It is therefore necessary to conduct UV-Vis studies across the entire spectrum range and not just focus on the variations in absorbance intensity between 350-700 nm, as it is commonly practiced in qualitative studies that demonstrate the interactions between polysulfides and adsorbents, to be precise in characterizing the nature of the polysulfides involved during adsorption.

The study highlights two major points:

- The proportion of each polysulfide species remains unchanged with the initial concentration of Li<sub>2</sub>S<sub>6</sub>. However, their respective concentrations vary in the mixture and the accurate determination is still challenging. These species are interconnected through a disproportionation equilibrium, where the S<sub>6</sub><sup>2-</sup> undergoes disproportionation reaction into S<sub>4</sub><sup>2-</sup> and S<sub>8</sub> under our conditions (ambient temperature in DOL-DME).



- The adsorption of Li<sub>2</sub>S<sub>6</sub> by adsorbents is selective, only the S<sub>4</sub><sup>2-</sup> and S<sub>6</sub><sup>2-</sup> species are being adsorbed up to the surface saturation. The adsorption constants ( $k_{ads}$ ) follows the relative order 48Mo-400-H<sub>2</sub>S(15) # 32Mo-400-H<sub>2</sub>S(15) >> Aerosil 200.

However, the adsorption capacity of the materials depends on the number of available active sites and thus sets the maximum value of the number of moles of Li<sub>2</sub>S<sub>6</sub> adsorbed (surface saturation),  $n_{ads sat}$ , which varies as follows: 48Mo-400-H<sub>2</sub>S(15) > Aerosil 200 > 32Mo-400-H<sub>2</sub>S(15). New equilibriums in the adsorbed state, therefore, compete with the disproportionation equilibrium. Our study shows that the addition of adsorbent alters the equilibria in the solution. The variation in the two contributions assigned to S<sub>4</sub><sup>2-</sup> (325 and 425 nm) does not change in exactly the same way in the case of Li<sub>2</sub>S<sub>6</sub> with and without adsorbent. This discrepancy underscores that the assignment of peaks for different polysulfides remains somewhat uncertain and that theoretical and quantitative work is desirable for a better understanding of this complex multiphase system.

This study also enabled to select, among the various synthesized candidates, material with the higher polysulfides adsorption capacity. Among the synthesized MoS<sub>2</sub>-KB materials, those with higher adsorption capacity ( $N_{ads}$ ) are **48Mo-400-H<sub>2</sub>S(15)** and **22Mo-400-H<sub>2</sub>S(100)-HN**, with values of 389 and 344 μmol of Li<sub>2</sub>S<sub>6</sub> per gram of the sample, respectively. The quantity of Li<sub>2</sub>S<sub>6</sub> equivalent adsorbate,  $N_{ads}$  appears to be directly proportional to the MoS<sub>2</sub> content in MoS<sub>2</sub>. This can be explained by the fact that 48Mo-400-H<sub>2</sub>S(15) offers larger surface (7.1 m<sup>2</sup> instead of 4.8 m<sup>2</sup>), resulting in a higher number of exposed surface and, therefore, an increased number of accessible active sites<sup>127</sup> for similar MoS<sub>2</sub> nature (in slab length and stacking).

In the second case, it is favored by better dispersion (36% compared to 26% for 48Mo-400-H<sub>2</sub>S(15)) and an increase in the number of M-edges formed under pure H<sub>2</sub>S, which enhances the adsorption of Li<sub>x</sub>S<sub>y</sub>.

This quantitative approach would facilitate the determination of the appropriate amount of material to be incorporated into electrode design or used to prepare modified-separator in Li-S batteries for potential future work. Due to the highest adsorption capacity of 48Mo-400-H<sub>2</sub>S(15), the "MoS<sub>2</sub> loading" series is subsequently selected and tested in the positive electrode of a Li-S battery to evaluate their performance during cycling. The results are presented in the next chapter.





## Chapter IV – Electrochemical performances of S-MoS<sub>2</sub>-KB composite active material as positive electrode

---

### 1.1 Introduction

In the previous chapter, it has been demonstrated that MoS<sub>2</sub> supported KB materials, show strong interactions with Li<sub>2</sub>S<sub>4</sub> and Li<sub>2</sub>S<sub>6</sub> to the best of our knowledge present in a Li<sub>2</sub>S<sub>6</sub> equivalent solution, while molecular S<sub>8</sub> is not or at least very few absorbed on the adsorbent. Among the various MoS<sub>2</sub>-KB syntheses to modify its structure and thus enhance interactions with polysulfides for maximum adsorption, the most relevant adsorption capacity (*C<sub>ads</sub>*) is achieved when increasing the MoS<sub>2</sub> loading up to 48 wt.%. Indeed, the number of moles of adsorbed S<sub>4</sub><sup>2-</sup>/S<sub>6</sub><sup>2-</sup> until surface saturation increase from *N<sub>ads</sub>* of 294 ± 59 to 389 ± 78 μmol S<sub>4</sub><sup>2-</sup>/S<sub>6</sub><sup>2-</sup> · g<sub>sample</sub><sup>-1</sup> when increasing the MoS<sub>2</sub> loading by a factor of 1.4 (from 32 to 48 wt.%).

This final chapter is dedicated to the incorporation of MoS<sub>2</sub>-KB material into a sulfur-based electrode to check its impact on the electrochemical behavior of the positive sulfur electrode. To assess to real impact of the adsorption phenomenon in Li-S batteries, we choose favorable conditions *C<sub>ads</sub>* #C(Li<sub>2</sub>S<sub>4</sub>) to see the real impact of MoS<sub>2</sub>-KB. This implies to work at low sulfur loading, with a weight *adsorbent/S ratio* of 2-3 and high volume of electrolyte/mass of sulfur (E/S). The aim is to bring new lights on how the electrochemical mechanism is impacted compared to a reference system without MoS<sub>2</sub>-KB adsorbent. The case of high sulfur loading *C<sub>ads</sub>* << C(Li<sub>2</sub>S<sub>4</sub>), with a low E/S ratio of 10 μL/mg<sub>s</sub> has been also studied in the PhD work. However, the lack of result reproducibility, likely stemming from issues related to sulfur wetting and accessibility, made them difficult to use.

This chapter is divided into three main sections. The first section focuses on the elaboration of sulfur impregnated into MoS<sub>2</sub>-KB porous network. The second section describes the elaboration of the composite positive electrode comprising the reservoir of energy, S-MoS<sub>2</sub>-KB (S<sub>8</sub> active material confined into the host and adsorbent microstructure), the binders to give proper dispersion, mechanical stability and adherence to the current collector, as well as carbon C65 additives to improve the electronic percolation. Different compositions have been

elaborated to properly reveals the effect(s) of MoS<sub>2</sub>-KB adsorbent on the electrochemical performance. In this section, formulation will be based on MoS<sub>2</sub>-KB's adsorption capacity (**Chapter III**), to evaluate the theoretical percentage of trapped polysulfides in the battery for a given S<sub>8</sub> loading. In the final section, the electrochemical characteristics of S- MoS<sub>2</sub>-KB composite electrodes are compared to a reference electrode without adsorbent to highlight how the adsorbent modifies the shuttle effect and the electrochemical phenomena.

## 1.2 Synthesis and characterization of S- MoS<sub>2</sub>-KB composite material

The MoS<sub>2</sub> 2D structure is known to be electrochemically active in between 0.7 and 1.1<sup>141,142</sup>. V vs. Li/Li<sup>+</sup>, thus the MoS<sub>2</sub> is stable in the potential window between 1,5 and 3 V vs. Li<sup>+</sup>/Li generally used to cycle Li-S batteries. To obtain a better intimacy between sulfur (responsible of polysulfide species) and the adsorbent, the elemental sulfur (S<sub>8</sub>) is infused into the MoS<sub>2</sub>-KB host structure by conventional melt diffusion, a method introduced by Nazar *et al.*<sup>8</sup> in the Li-S battery field. Before melt-diffusion process, S<sub>8</sub> (99,5% refined, Acros Organics) and MoS<sub>2</sub>-KB powders are sieved through a 60 μm mesh.

In order to compare the electrodes with each other, we decide to fix the sulfur loading in the electrode at (1 mg.cm<sup>-2</sup>) and we adjust sulfur S<sub>8</sub> mass and the MoS<sub>2</sub>-KB mass (m<sub>MoS<sub>2</sub>-KB</sub>) to meet this requirement and also to accommodate the volume expansion upon full lithiation to Li<sub>2</sub>S (expansion factor of 1.8)<sup>4</sup> and to enable the electrolyte infiltration. Indeed, if the remaining porous volume of the host structure is not large enough, the conversion of S<sub>8</sub> to Li<sub>2</sub>S during discharge might lead to a dramatic electrode pulverization. The corresponding calculations are display in **equation (IV-1)** and results are given in **Table IV-1**.

$$m(\text{MoS}_2 - \text{KB}) = \frac{\frac{m_{\text{S}_8} \cdot \text{expantion factor}}{\rho_{\text{S}_8}}}{V_{\text{porous MoS}_2 - \text{KB}}} \quad (\text{IV-1})$$

With

Expansion factor : 1.8

ρ<sub>S<sub>8</sub></sub> : the density of sulfur (2.07 g.cm<sup>-3</sup>)

V<sub>porous MoS<sub>2</sub>-KB</sub> : porous volume of MoS<sub>2</sub>-KB measured in the **chapter II**

Three materials are synthesized using this protocol:

- **S-0Mo** which serves as reference to formulate sulfur electrode without MoS<sub>2</sub>
- **S-32Mo-400-H<sub>2</sub>S(15)**
- **S-48Mo-400-H<sub>2</sub>S(15)**

Appropriate mass of sulfur and MoS<sub>2</sub>-KB powders are hand-grounded (see **Table IV-1**) together using a mortar and a pestle, then placed under vacuum at ambient temperature for 30 minutes to remove gases that could be trapped inside the porosity of MoS<sub>2</sub>-KB. Finally, the powder is heated to 155°C overnight under vacuum.

**Table IV-1. Mass of sulfur and MoS<sub>2</sub>-KB calculated from equation IV-1**

<b>Sample</b>	<b>S<sub>8</sub></b>	<b>MoS<sub>2</sub>-KB</b>
	<b>g</b>	<b>g</b>
S-0Mo (REF)	0.28	0.72
S-32Mo-400-H <sub>2</sub> S(15)	0.25	0.75
S-48Mo-400-H <sub>2</sub> S(15)	0.19	0.81

**Table IV-2** exhibits the elemental analysis of the powders after melt-diffusion and provides the actual content of each atom. The as-synthesized powders shows a S loading of 28, 37 and 39 wt.% S for S-0Mo, S-32Mo-400-H<sub>2</sub>S(15) and S-48Mo-400-H<sub>2</sub>S(15) respectively, which accounts for the total amount of sulfur (S<sub>active</sub>, S from MoS<sub>2</sub> and S deposited on KB during sulfidation).

**Table IV-2. Elemental analysis of S- MoS<sub>2</sub>-KB samples obtained from CHNS**  
(error associated is about ± 0.1% between 0-10 wt.% and ± 0.3% between 10-50 wt.%)

<b>Sample</b>	<b>C</b>	<b>H</b>	<b>S<sub>tot</sub></b>	<b>Total</b>
	<b>wt. %</b>	<b>wt. %</b>	<b>wt. %</b>	<b>wt. %</b>
S-0Mo (REF)	69	0	28	<b>97</b>
S-32Mo-400-H <sub>2</sub> S(15)	40	0	37	<b>77</b>
S-48Mo-400-H <sub>2</sub> S(15)	28	0	39	<b>67</b>

**Chapter IV – Electrochemical performances of S-MoS<sub>2</sub>-KB composite active material as positive electrode**

From these CHNS values and the MoS<sub>2</sub> loading determined from the XRF for MoS<sub>2</sub>-KB (**Chapter II**), the MoS<sub>2</sub> loading, MoS<sub>2</sub>-KB content and S<sub>active</sub> loading in the final S- MoS<sub>2</sub>-KB are calculated. Results are shown in **Table IV-3**.

**Table IV-3. Experimental MoS<sub>2</sub>, MoS<sub>2</sub>-KB and S<sub>active</sub> content in S- MoS<sub>2</sub>-KB and the corresponding adsorbent/S ratio.**

Sample	MoS <sub>2</sub> (calculated) wt. %	MoS <sub>2</sub> -KB (calculated) wt. %	S <sub>active</sub> (calculated) wt. %	Total wt. %	Adsorbent/ S ratio
S-0Mo (REF)	-	-	28	-	2.4
S-32Mo-400-H <sub>2</sub> S(15)	24	64	28	92	2.3
S-48Mo-400-H <sub>2</sub> S(15)	39	67	23	90	2.9

The as-synthesized active materials powders show a MoS<sub>2</sub>-KB loading of 64 and 67 wt.% for S-32Mo-400-H<sub>2</sub>S(15) and S-48Mo-400-H<sub>2</sub>S(15) and a S<sub>active</sub> loading of 28, 28 and 23 wt.% for S-0Mo, S-32Mo-400-H<sub>2</sub>S(15) and S-48Mo-400-H<sub>2</sub>S(15), respectively. We achieve to obtain the targeted S<sub>8</sub> loading (see **Table IV-1**) as shown in **Figure IV-1**. The sulfur contents obtained are in line with the recommendation of L. Li *et al.*<sup>143</sup> which have determined that above 67 wt.% of sulfur content, Li<sub>2</sub>S will not be completely accommodated by the pore host during the discharge (sulfur lithiation). From the elemental analysis, another important parameter is the weight *adsorbent/S ratio* which will be discussed in **section IV-1.3.5**. The adsorbents material is KB for S-0Mo, while it is MoS<sub>2</sub>-KB for 32Mo-400-H<sub>2</sub>S(15) and 48Mo-400-H<sub>2</sub>S(15). The experimental weight *adsorbent/ S ratio* are equal to 2.4, 2.3 and 2.9 for S-0Mo, S-32Mo-400-H<sub>2</sub>S(15) and S-48Mo-400-H<sub>2</sub>S(15), respectively, as shown in **Figure IV-2**.

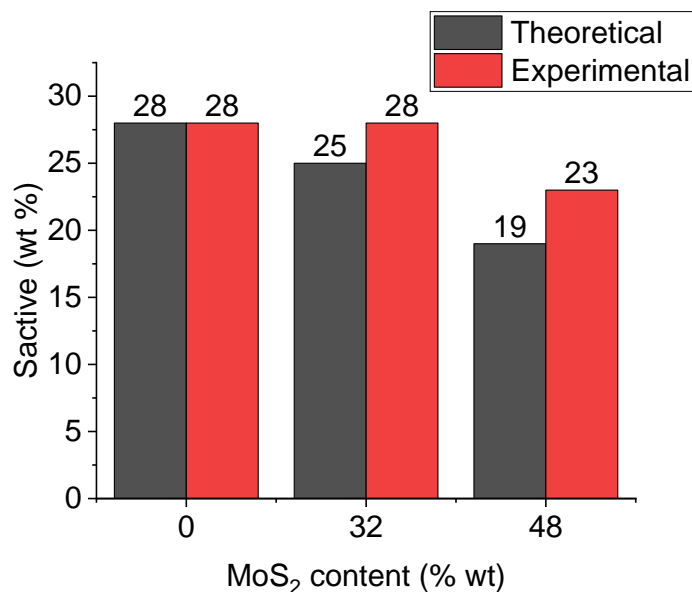


**Figure IV-1.** Comparison of experimental and theoretical electroactive sulfur content S<sub>8</sub>.

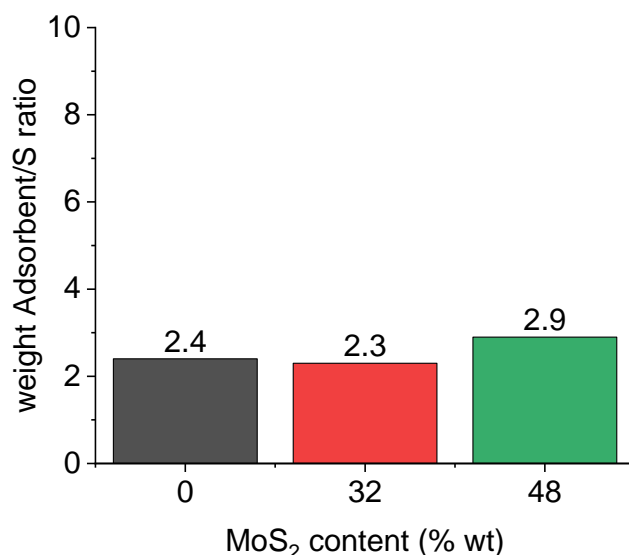


**Figure IV-2.** Adsorbent/S ratio obtained from S-MoS<sub>2</sub>-KB.

In addition, the skeletal density and porous volume of the S-MoS<sub>2</sub>-KB materials are determined. The skeletal density of the three materials, measured using helium pycnometry, range from 1.9 to 2.4 g.cm<sup>-3</sup>. This value is then used to calculate the volume of solids, in order to deduce the final electrode porosity. Hg porosimetry measurements are also performed to obtain the porous volume of S-MoS<sub>2</sub>-KB samples. A residual porous volume of 3.7, 2.1 and 1.2 cm<sup>3</sup>g<sup>-1</sup> remains for S-0Mo, S-32Mo-400-H<sub>2</sub>S(15) and S-48Mo-400-H<sub>2</sub>S(15) respectively. So, the initial KB porous volume (4.4 cm<sup>3</sup>g<sup>-1</sup>) is reduced by 23, 56 and 75 %.



If we consider the sulfur mass incorporated inside S-MoS<sub>2</sub>-KB, its volume can be calculated from **equation (IV-2)** and we can deduced the volume occupied by Li<sub>2</sub>S ( $V_{Li_2S}$ ) from **equation (IV-3)** and compared its value to the remaining porous volume ( $V_{S-MoS_2-KB}$ ) (see **Appendix D**).

$$V_{S_8} = m_{S_8} * \rho_{S_8} \quad (IV-2)$$

$$V_{Li_2S} = \text{expansion factor} * V_{S_8} \quad (IV-3)$$

**Figure IV-3** displays the ratios  $V_{S-MoS_2-KB}/V_{Li_2S}$ . For the three samples, after both MoS<sub>2</sub> and S<sub>8</sub> incorporation inside the KB pores, the  $V_{S-MoS_2-KB}/V_{Li_2S}$  ratios are significantly greater than 1.8. The porous volume is then sufficient to enable i) physical confinement of PS and accommodate Li<sub>2</sub>S formation inside the porosity when S<sub>8</sub> is reduced, ii) electrolyte infiltration to insure lithium-ion transport.

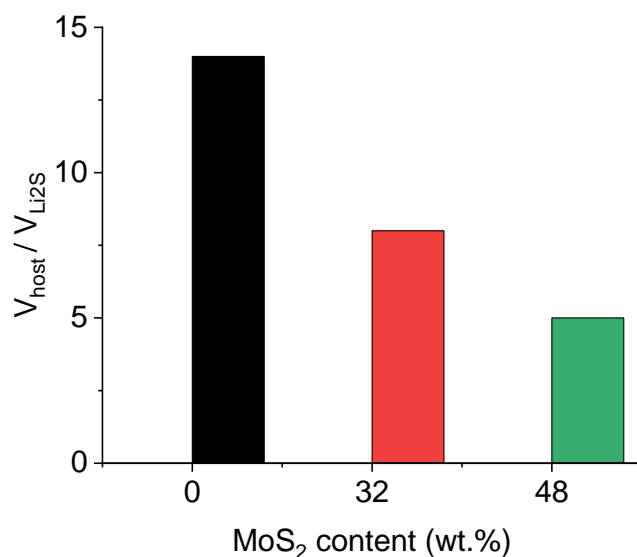


**Figure IV-3. Ratio of  $V_{host}/V_{Li_2S}$  from S-MoS<sub>2</sub>-KB samples**

These characterizations confirms that the S-MoS<sub>2</sub>-KB active materials are filled with the targeted sulfur content. Samples still exhibits enough pore volume to accommodate the volume change occurring during cycling and to host liquid electrolyte for a good wetting of the active material. The next step consists in the electrode formulation and coin cell making.

### 1.3 Electrode formulation and coin-cell making

Once the S-MoS<sub>2</sub>-KB micro-structured active materials are synthesized, they will go through a series of processes to produce electrode which includes the following stages: (1) formulation of a composite electrode, (2) creating a slurry by mixing the materials with solvents, (3) coating the slurry onto current collector foils and further drying to remove the solvent, and (4) cutting the electrodes. Finally, composite electrodes are assembled in Li-sulfur cells in coin cell configuration and the batteries are cycled to evaluate their electrochemical characteristics, as depicted in **Figure IV-4**.

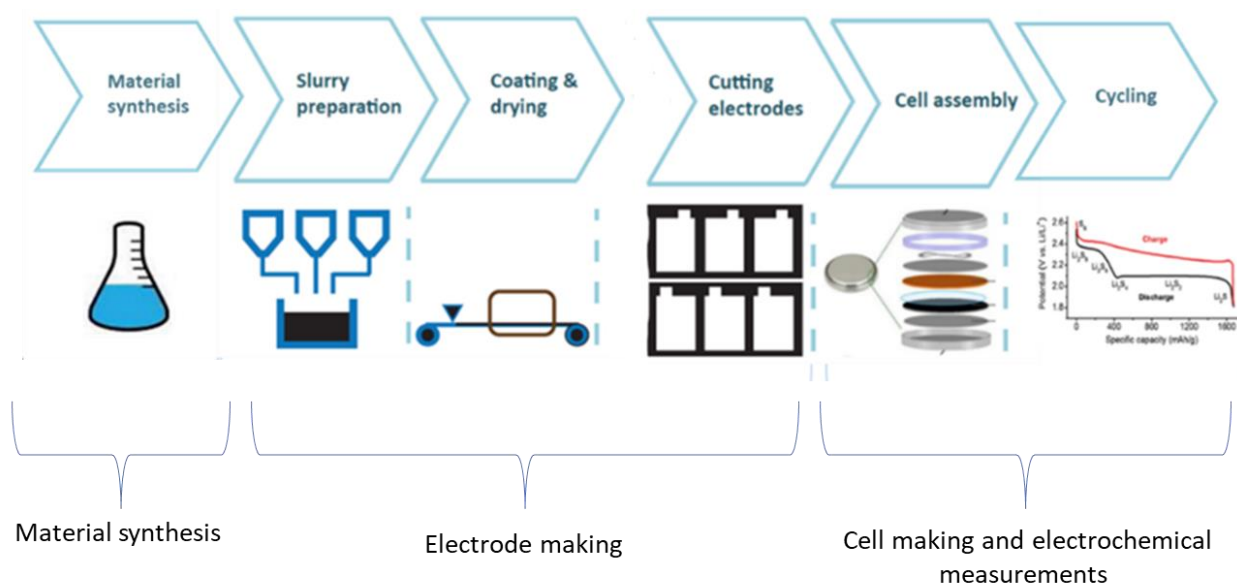


**Figure IV-4. From material synthesis to battery assembly, the processing chart**

The classical formulation of battery electrodes involves the use of active material, carbon black (CB) additives, and a polymer binder. For Li-S positive electrode, CB, polyvinylidene fluoride (PVDF) binder are commonly dispersed in N-Methyl-2-pyrrolidone (NMP) solvent<sup>8,144–146</sup>. Due to a high porous volume of Ketjenblack which drinks literally the solvent, it is difficult to obtain a homogeneous ink using NMP with classical amount of solids (>10%), **Figure IV-5** highlights four other drawbacks encountered during the electrode elaboration by displaying different photographs of the initial resulting electrodes after enduction & drying steps: (a) non-adherence on the current collector, (b) electrode peeling, (c) heterogeneous particle distribution, and (d) cracking. Therefore, a series of optimizations on the formulation and mixing, coating and drying steps are performed to address these issues and elaborate functional composite electrodes.

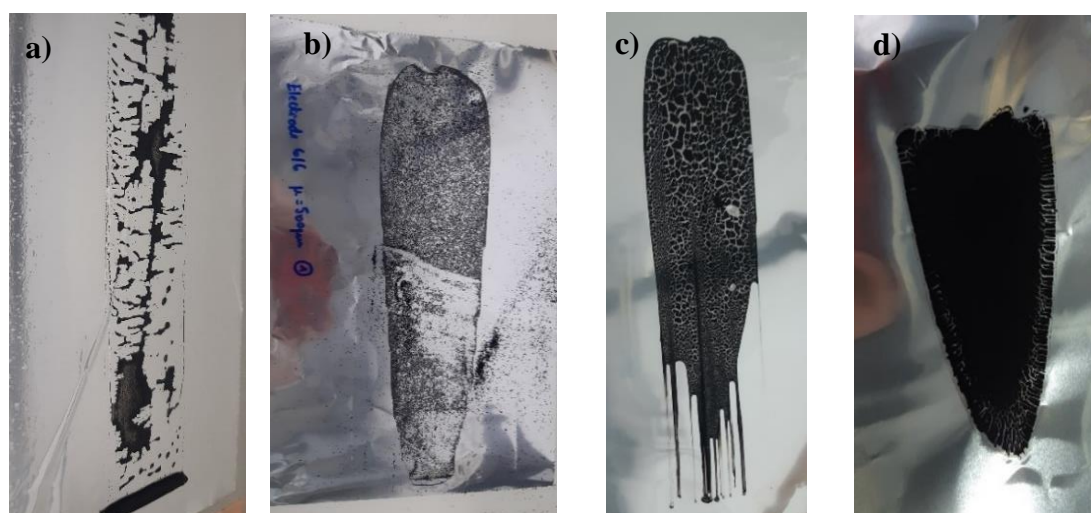


**Figure IV-5. Formulation issues a) non-adherence on the current collector b) electrode peeling, c) heterogeneous particle distribution and d) cracking.**

Five parameters are then investigated to optimize the electrode formulation i) the choice of the binder and solvent nature, ii) the binder ratio in the formulation, iii) the choice of the drying protocol, iv) the doctor blade coating gap, and finally v) the nature of the current collector. Only the four first investigations are detailed because the use of carbon coated current collector instead of a bare aluminum one does not have any effect on the issues mentioned.

### 1.3.1 Optimization of the formulation

#### 1.3.1.1 Choice of binder and solvent

Classical PVDF dispersion in NMP is replaced by two water soluble binders : CarboxyMethyl Cellulose (CMC) and Styrene-Butadiene Rubber (SBR). This mixture is widely used to formulate electrode with high carbon content because graphite particles interact favorably with CMC which improves particle dispersion<sup>147</sup>. Indeed, the fundamental role of a binder is the cohesion of electrode components as well as their adhesion to the current collector. On one hand, CMC polymer acts as a dispersant, improving particle interactions by creating CMC-KB interactions instead of KB-KB interactions that lead to particle aggregation. Consequently, its use enhances the slurry dispersibility to get an homogenous suspension<sup>147</sup>. On the other hand, SBR is an elastomer (latex) that exhibits strong binding force and high flexibility<sup>148</sup> which is beneficial for achieving better adhesion between the slurry and the current collector, enhancing the final flexibility of the electrode (preventing cracking). CMC carboxymethyl cellulose is

often used in conjunction with SBR. Indeed, CMC/SBR is widely used for graphite and silicon-based negative electrode in Li-ion batteries<sup>149</sup>. In addition, J. Häcker *et al.*<sup>106</sup> successfully applied this binder mixture to elaborate sulfur electrodes made of Ketjenblack EC 600-JD using the following formulation : 50/40/10 *wt. %* of S-KB/CB/CMC-SBR (ratio 1:2 of CMC:SBR).

### 1.3.1.2 Choice of CMC:SBR binder ratio

Usually, the percentage of CMC and SBR in the final electrode formulation is < 10 *wt %* and the ratio of CMC over SBR is 1:1. However the first trials using this ratio in a S-0Mo/CB/CMC-SBR mixture of 88/2/10 in water do not permit to reach a slurry with sufficient fluidity. Indeed, the slurry is too viscous with many agglomerates as displayed in the camera picture in **Figure IV-6**. This picture is taken just after the addition of SBR prior homogenization. Due to the non-negligible surface area and porous volume of the S-0Mo material composed of only 28 *wt%* of S and 69 *wt%* of KB, the aggregation of KB-KB particles generates a viscous gel. So, in an attempt to get an homogenous slurry, the overall binder percentage in the formulation is increased to 40 *wt%* following the approach of J. Häcker *et al.*<sup>106</sup> comprising 10 *wt. %* CMC and 30 *wt. %* SBR to improve adhesion onto the current collector.

a) 10 *wt %* CMC-SBR



b) 40 *wt %* CMC-SBR



**Figure IV-6.** Slurry viscosity when using a) 10 *wt. %* of CMC-SBR (5-5) and b) 40 *wt. %* of CMC-SBR (10-30).

In an important work, J-H. Park *et al.*<sup>147</sup> indicated that the slurry is better dispersed when adding CMC and SBR to the particles sequentially, instead of adding both binders at the same time. Therefore, the CMC binder is mixed with S-0Mo in a 5 wt.% ethanol solution in water using a Thinky® homogenizer at homogenization speed of 2000 rpm for 10 min, prior to SBR addition. The addition of 5 wt% of ethanol (EtOH) in water is found to be beneficial for dispersing the solids compared to pure water. From this optimization of CMC:SBR ratio and process to make the electrode slurry, a good ink viscosity is then obtained using 58/2/40 wt.% S-0Mo/CB/CMC-SBR (10:30, CMC:SBR) as shown in the camera picture in **Figure IV-6**.

### 1.3.2 Optimization of the coating and drying step

#### 1.3.2.1 Choice of the drying protocol

Conventional drying at 60 °C under air overnight resulted in a rapid solvent evaporation leading to a delamination from the current collector, due to the non-negligible solvent content in the slurry, as displayed in **Figure IV-5-d**. So, a new drying step with gentler conditions is implemented to allow for slower solvent evaporation. The process is composed of three successive steps:

- i) 5 h, 15 °C, atmospheric pressure, under air in temperature-controlled oven, to slowly dry the electrode;
- ii) 12 h, room temperature, under vacuum, to remove the remaining solvent in the electrode porosity;
- iii) 5 h, 100°C, under argon, to evaporate the water trapped inside the material micro/meso porosity.

#### 1.3.2.2 Choice of the doctor blade gap for the enduction

The doctor blade is the tape casting coater used to produce electrode films whose picture is displayed in **Figure IV-7-a**. The wet electrode thickness is determined by the doctor blade gap. After the drying step, the dry electrode thickness is reduced compared to its wet state. For instance, a 150 μm gap leads to a dry electrode of 50 μm (for a final solid content of around 13% including S-MoS<sub>2</sub>-KB, CB, dry 5 wt.% CMC and SBR) and a sulfur loading of 0.2-0.3 mg of sulfur.cm<sup>-2</sup>). The sulfur loading is calculated using the **equation IV-4**.

$$\text{loading (mg.cm}^{-2}\text{)} = \frac{\text{mass of sulfur within the electrode (mg)}}{\pi * \left(\frac{\text{electrode diameter (mm)} * 10^{-1}}{2}\right)^2} \quad \text{(IV-4)}$$

By widening the blade gap, it is possible to enhance the final electrode thickness, thereby increasing the final sulfur loading for a given electrode formulation.

To adjust the final sulfur loading, the doctor blade gap is varied from 150 to 250  $\mu\text{m}$ . **Figure IV-7-b** exhibits the wet electrode obtained using a 250  $\mu\text{m}$  doctor blade gap and **Table IV-4** gathers the dry electrode thickness and sulfur loading obtained depending on the selected doctor blade gap. After drying, the electrode thickness is approximately three times thinner than the blade gap and varies linearly with the doctor blade gap. It is possible to increase the doctor blade gap up to 250  $\mu\text{m}$  without any issues, leading to a sulfur loading of 0.3  $\text{mg}_\text{s}.\text{cm}^2$ . A blade gap  $> 300 \mu\text{m}$  leads to an intensification of the shrinkage phenomenon within the electrode thickness and the development of cracks, even with the optimization of the drying protocol. Therefore, a doctor blade gap of 250  $\mu\text{m}$  is selected for this work.

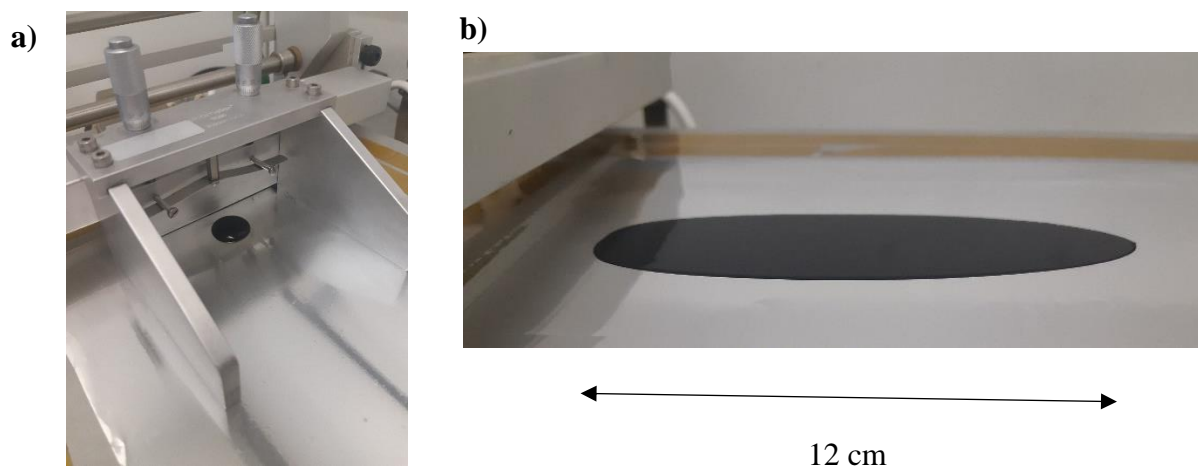


**Figure IV-7. a) Doctor blade device b) S-0Mo typic wet electrode film deposited on aluminum foil**

**Table IV-4. Electrode thickness and sulfur loading obtained for different doctor blade gaps.**

<b>Doctor blade gap (<math>\mu\text{m}</math>)</b>	<b>Dry electrode thickness with Al foil (<math>\mu\text{m}</math>)</b>	<b>Sulfur loading (<math>\text{mg}_\text{s}.\text{cm}^2</math>)</b>
150	$55 \pm 5$	$0.05 \pm 0.1$
200	$67 \pm 5$	$0.1 \pm 0.1$
250	$75 \pm 5$	$0.3 \pm 0.1$

After this series of optimizations on the binder-solvent natures, the CMC:SBR binder ratios, the doctor blade gap choice and the drying process selection, this new formulation protocol is employed to make S-MoS<sub>2</sub>-KB electrodes.

### 1.3.3 Optimized protocol for electrode making

To formulate the sulfur positive electrodes, a slurry containing S-MoS<sub>2</sub>-KB composite active material (CAM), CB C65 (Timcal) and 5 wt.% CMC (Battery Grade, > 99.5%, MSE Supplies) binder are mixed in 5 wt.% ethanol solvent using a Thinky homogenizer at homogenization speed of 2,000 rpm for 10 min. After obtaining a honey-like slurry texture, SBR (MSE Supplies) binder is added. The slurry is then slowly homogenized at of 400 rpm for 3 min to get the final composition of 58/2/40 wt.% CAM/CB/CMC-SBR (10:30, CMC:SBR).

The resulting slurries are casted onto an aluminum foil current collector (20 μm thick) using the doctor blade (with 250 μm of open gap). The electrodes are slowly dried using the optimized protocol.

**Figure IV-8** exhibits a S-0Mo electrode obtained with this protocol. The resulting electrode is uniform in thickness, without visible particle agglomerations, and cracking. The composite electrode is well adhesive to the current collector, with no detachment when the electrode is gently folded.

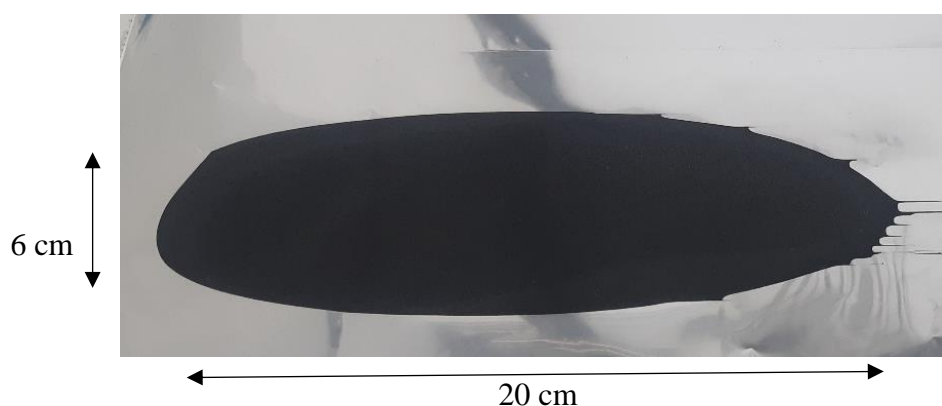


**Figure IV-8. S-0Mo electrode after optimization**

The dried electrodes are then cut into 15 mm diameter discs, which corresponds to 1.76 cm<sup>2</sup> electrode surface. In average, electrodes have a 50 μm thickness, 80 % porosity, 13 to 16 % sulfur active content leading to a sulfur loading of ~0.2-0.3 mg.cm<sup>-2</sup>. **Table IV-5** shows the S- MoS<sub>2</sub>-KB electrode properties of the three electrodes formulated.

**Table IV-5.** S-MoS<sub>2</sub>-KB electrode properties (average values obtained from 6 samples on the same electrode)

	S-0Mo(REF)	S-32Mo-400-H <sub>2</sub> S(15)	S-48Mo-400-H <sub>2</sub> S(15)
<b>Material scale</b>			
<b>S<sub>active</sub> wt. % (mat)</b>	28	27	23
<b>Electrode scale</b>			
<b>S<sub>active</sub> wt. % (electrode)</b>	16	16	13
<b>Mass of sulfur (mg)</b>	0.3 ± 0.1	0.6 ± 0.1	0.3 ± 0.1
<b>Sulfur loading (mg.cm<sup>-2</sup>)</b>	0.2 ± 0.1	0.3 ± 0.1	0.2 ± 0.1
<b>Electrode thickness (μm)</b>	55 ± 1	52 ± 1	54 ± 1
<b>Porosity (%)</b>	85 ± 5	78 ± 5	83 ± 5
<b>Electrode capacity</b>			
<b>Theoretical capacity (mAh)</b>	0.7 ± 0.1	1 ± 0.2	0.6 ± 0.1
<b>Areal capacity (mAh.cm<sup>-2</sup>)</b>	0.4 ± 0.1	0.6 ± 0.1	0.4 ± 0.1

The positive electrode discs are then assembled in coin-cells to perform the electrochemical characterizations presented in the [section IV-0](#).

### 1.3.4 Coin cell assembly

CR2032 coin cells are assembled inside an argon-filled glove box by stacking a composite electrode disk ( $\phi = 15$  mm), a Li foil ( $\phi = 16$  mm) and a coated polypropylene separator Celgard 3501 ( $\phi = 18$  mm) as displayed in [Figure IV-9](#). The electrolyte is consisting of a mixture of 1 M lithium bis(trifluoromethanesulfonyl)imide (LiTFSI, 99,95%, Aldrich) dissolved in 1,3-dioxolane (DOL, 99,5%, stab, Alfa Aesar) / 1,2-dimethoxyethane (DME, 99%, extra dry, AcroSeal, Acros Organic) (1:1, v/v) with 1 wt.% lithium nitrate (LiNO<sub>3</sub>, 99,95%, Aldrich). The electrolyte content is carefully added to match the chosen electrolyte volume to sulfur mass ratio (E/S ratio, expressed in  $\mu\text{L}_{\text{electrolyte}} \cdot \text{mg}_{\text{sulfur}}^{-1}$ ). The E/S ratio choice is determined in [section IV-1.3.6](#).



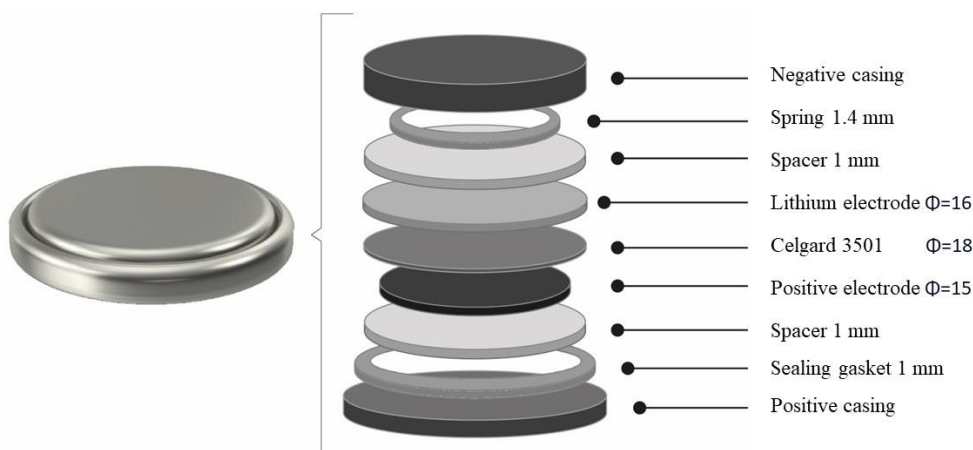


**Figure IV-9.** Schematic representation of a two-electrodes coin cell (CR2032)

### 1.3.5 Calculation of percentage of Li<sub>2</sub>S<sub>6</sub> and Li<sub>2</sub>S<sub>4</sub> trapped in the experimental conditions considering the adsorption capacities

The adsorption capacity calculated in **Chapter III** helps to calculate the theoretical percentage of polysulfide species that might be trapped within the MoS<sub>2</sub>-KB structure, allowing for a future analysis of the experimental effect on the electrochemical performance such as the reduction of the shuttle effect in the Li-S battery.  $88 \pm 18$ ,  $294 \pm 59$  and  $389 \pm 78$   $\mu\text{mol Li}_2\text{S}_6/\text{g}_{\text{sample}}$  adsorption capacities are measured (**Chapter III**) for KB, 32Mo-400-H<sub>2</sub>S(15) and 48Mo-400-H<sub>2</sub>S(15), respectively. Knowing, the mass of sulfur in the electrodes, the maximum number of moles of Li<sub>2</sub>S<sub>6</sub> can be calculated based on the equilibrium in **equation (IV-5)** and the resulting **equation (IV-6)-(IV-7)**. Same calculations can be made for Li<sub>2</sub>S<sub>4</sub> using **equations (IV-7)** and **(IV-8)**.

For Li<sub>2</sub>S<sub>6</sub>



$$n\text{Li}_2\text{S}_6 = \frac{4}{3} * \frac{\text{mass of S}_8 \text{ in the electrode}}{\text{Mw}_{\text{S}_8}} \quad (\text{IV-6})$$

For Li<sub>2</sub>S<sub>4</sub>



$$nLi_2S_4 = 2 * \frac{\text{mass of } S_8 \text{ in the electrode}}{Mw_{S_8}} \quad (IV-8)$$

**Table IV-6** shows the maximal Li<sub>2</sub>S<sub>6</sub> and Li<sub>2</sub>S<sub>4</sub> moles generated withing the formulated electrodes and compare the deduced ratio adsorbent over sulfur with the theoretical one necessary to fully trap them. The latters are much larger, between 36 (0% of MoS<sub>2</sub>) to 7 (48% of MoS<sub>2</sub>) times higher to trap Li<sub>2</sub>S<sub>4</sub> than the experimental ratios.

**Table IV-6. Comparison of theoretical and experimental weight adsorbent/S ratios**

	S-0Mo(REF)	S-32Mo-400-H <sub>2</sub> S(15)	S-48Mo-400-H <sub>2</sub> S(15)
Nads (μmol/g <sub>adsorbent</sub> )	88 ± 18	294 ± 59	389 ± 78
Mass of sulfur (mg)	0.3 ± 0.1	0.6 ± 0.1	0.3 ± 0.1
n Li <sub>2</sub> S <sub>6</sub> (μmol)	2	3	2
n Li <sub>2</sub> S <sub>4</sub> (μmol)	2	5	2
<b>Theoretical weight adsorbent/S ratio needed to trap 100% of Li<sub>2</sub>S<sub>4</sub> or Li<sub>2</sub>S<sub>6</sub></b>			
Li <sub>2</sub> S <sub>6</sub>	59	18	13
Li <sub>2</sub> S <sub>4</sub>	89	27	20
<b>Experimental weight adsorbent/S ratio</b>			
	2.4	2.3	2.9

$$\% \text{ of trapped } Li_2S_4 \text{ or } Li_2S_6 = \frac{\text{experimental ratio} \frac{\text{adsorbent}}{\text{active sulfur}}}{\text{theoretical ratio} \frac{\text{adsorbent}}{\text{active sulfur}}} * 100 \quad (IV-9)$$

The percentage of LiPS (Li<sub>2</sub>S<sub>4</sub> or Li<sub>2</sub>S<sub>6</sub>) experimentally trapped is calculated using **equation (IV-9)**. A maximum of 6%, 15%, and 38%, of the Li<sub>2</sub>S<sub>4</sub> generated in the battery can be effectively captured in our experimental conditions, as shown in **Figure IV-10**, especially for S-48Mo-400-H<sub>2</sub>S(15) which has the higher adsorption capacity.

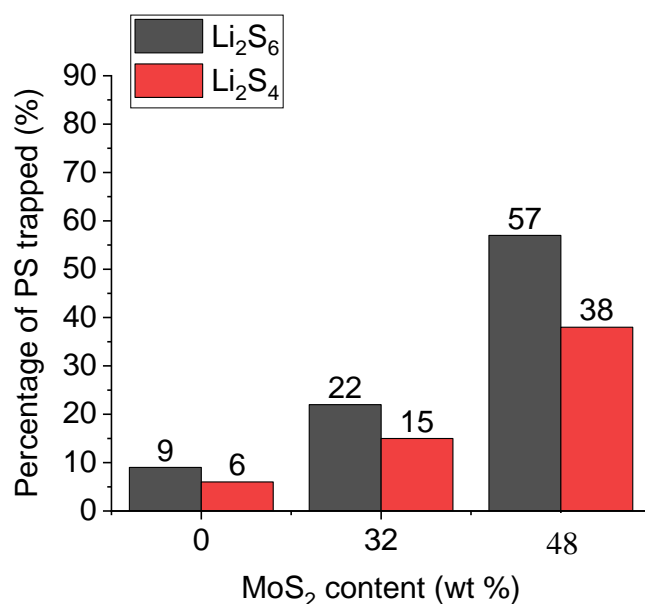


**Figure IV-10.** Percentage of polysulfides (Li<sub>2</sub>S<sub>6</sub> or Li<sub>2</sub>S<sub>4</sub>) trapped depending on the adsorbent nature.

Moreover, the maximum number of moles of polysulfides are not produced all at once during cycling, it is a dynamic process. Polysulfides are continuously produced during discharge. As demonstrated by Nazar group<sup>150</sup>, S<sub>6</sub><sup>2-</sup> is primarily formed in the initial discharge step in DOL-DME (v/v) (1/1), mainly due to the disproportionation of S<sub>8</sub><sup>2-14</sup> and its maximum concentration is observed when 300 mAh.g<sup>-1</sup> capacity is reached the slightly decrease up to 850 mAh.g<sup>-1</sup> where it drops to zero until the end of the discharge. On the other hand, S<sub>4</sub><sup>2-</sup> is produced with a slight delay, reaching its plateau concentration near 400 mAh.g<sup>-1</sup> at the beginning of the low-voltage plateau as displayed in **Figure IV-11**. The assignment of species by XANES has been extensively analyzed thereafter, and the differentiation between the various chemical states is very challenging<sup>151</sup>. Therefore, in these historical works, the attribution to a specific chemical state of the sample can be questioned.

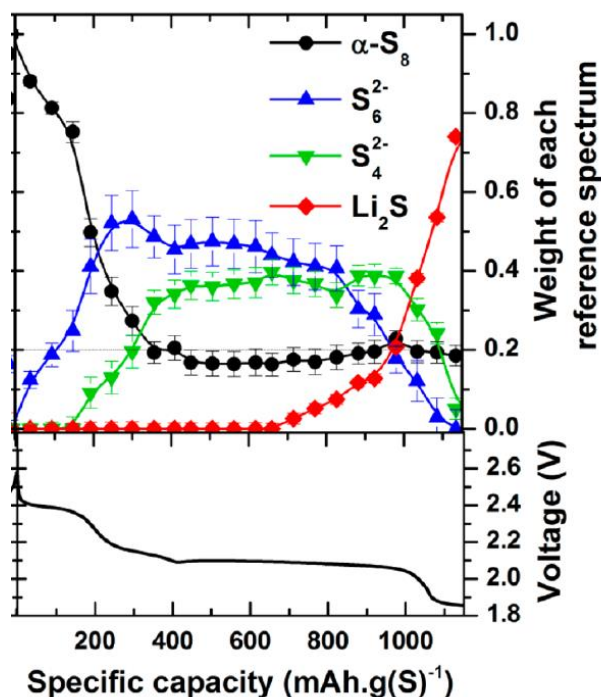


**Figure IV-11.** Evolution of sulfur species upon electrochemical discharge of sulfur electrode by XANES (reproduced from M.Cuisiner *et al.*<sup>150</sup>).

We hypothesize that the adsorbent's surface will behave dynamically, which is expected to limit the surface saturation. In addition, the choice of the amount of electrolyte used in the coin cell can also dilute the polysulfide species produced and alter the adsorption dynamics. The next section details the selection of the E/S ratio, which is directly correlated to the electrolyte volume.

### 1.3.6 Choice of the E/S ratio

From a practical point of view, to achieve a gravimetric energy density higher than 400 Wh.kg<sup>-1</sup>, the electrolyte volume to sulfur mass ratio (E/S ratio) needs to be less than 4 μL.mg<sup>-1</sup><sup>49</sup>. However, this low E/S ratio gives rise to underlying issues, including:

- **surpassing the solubility limit for lithium polysulfides in solution**, leading to sluggish Li<sub>2</sub>S deposition (i.e., slow interfacial charge transfer)<sup>152,153</sup>.
- **formation of LiPS aggregates**. Manthiram *et al.*<sup>23</sup> showed that the electrochemical conversion kinetics of LiPS are hindered by LiPS aggregation. The aggregation state directly contributes to an extreme loss in diffusion coefficient, which massively inhibits the ultimate conversion to Li<sub>2</sub>S.
- **viscosity increasing** which lead to diffusion issues.

To select the suitable E/S ratio for the study, the concentrations of polysulfides generated within both electrode (where electrochemical reactions occur) and electrode + separator system (in the case of polysulfides diffusion/migration out of the electrode) are calculated to determine the favorable conditions for observing the adsorption phenomenon and prevent the shuttle effect. At first, the porous volume of the electrode (determined based on its thickness and porosity) and the total porous volume ( $V_p \text{ tot}$ , electrode + separator) are calculated to ascertain the volume of electrolyte needed in the coin cell. **Table IV-7** provides an overview of the porous volumes for each compartment. Thus, the minimum volume of electrolyte must be at least equal to the overall porous volume, which is 8.2  $\mu\text{L}$ . For a sulfur masses of 0.3 and 0.6 mg within an electrode, this results in a E/S ratio of 27 and 14  $\mu\text{L}\cdot\text{mg}^{-1}$  (calculated using **equation (IV-10)**). Consequently, working with a lower E/S amount is not adequate.

**Table IV-7. Porous volume of the electrode, separator and electrode+ separator**

<b>Electrode thickness (<math>\mu\text{m}</math>)</b>	55
<b>Electrode porosity (%)</b>	84
<b><math>V_p</math> electrode (<math>\mu\text{L}</math>)</b>	5.2
<b><math>V_p</math> separator (<math>\mu\text{L}</math>)</b>	3
<b><math>V_p \text{ tot}</math></b>	8.2

$$\text{Minimal } \frac{E}{S} \text{ ratio} = \frac{\text{orevallporousvolume(electrode+separator)}}{\text{mass of sulfur within an electrode}} * 100 \quad \text{(IV-10)}$$

Then, the concentration of  $\text{Li}_2\text{S}_6$  and  $\text{Li}_2\text{S}_4$  in the electrode and in the electrolyte are calculated with the E/S ratio using a mass of sulfur of 0.3 mg. In the 5.2  $\mu\text{L}$  volume of electrode, high polysulfide concentrations of 400 and 600 mM of  $\text{Li}_2\text{S}_6$  and  $\text{Li}_2\text{S}_4$  are generated, respectively. These values drop to 207, 104, 56 mM of  $\text{Li}_2\text{S}_6$  for a 25, 50, 100 E/S ratio respectively. The same decrease in concentration is observed as the E/S ratio rises for  $\text{Li}_2\text{S}_4$ . (**Figure IV-12**).

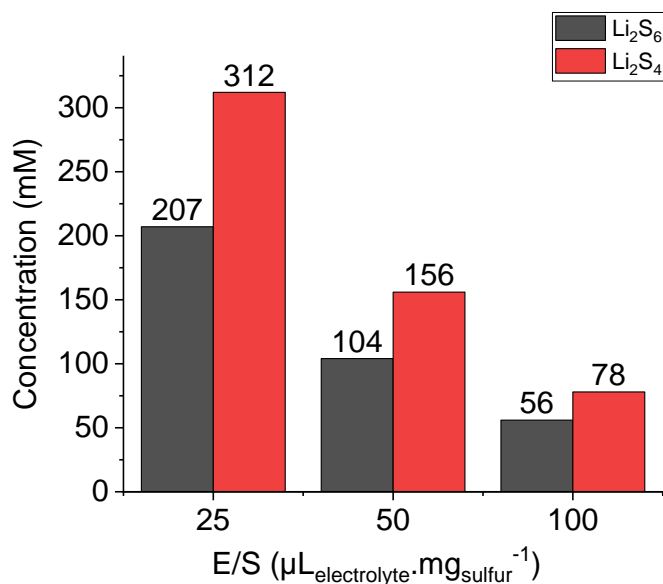


**Figure IV-12.** Evolution of the Li<sub>2</sub>S<sub>6</sub> and Li<sub>2</sub>S<sub>4</sub> concentrations in the electrolyte with E/S ratio, calculated for a sulfur mass of 0.3 mg.

Even with a low sulfur mass (0.3 mg), the concentration of polysulfides within the electrode volume remains high. A large portion of the polysulfides may end up in the electrolyte because the MoS<sub>2</sub>-KB surfaces saturate at 1.5 and 3 mM for **32**Mo-400-H<sub>2</sub>S(15) and **48**Mo-400-H<sub>2</sub>S(15) (see **chapter III**), respectively. It seems necessary to operate with a diluted system (with a high E/S ratio) to capture a larger portion of the generated polysulfides and assess the influence of MoS<sub>2</sub>-KB on electrochemical performance. Therefore, a E/S ratio of 100  $\mu\text{L}_{\text{electrolyte}}.\text{mg}_{\text{sulfur}}^{-1}$  is chosen to conduct the study. This corresponds to a  $V_{\text{electrolyte}}/V_{\text{electrode}}$  of 5. Working at higher E/S ratio is not relevant because the excess of electrolyte will be lost within the coin cell and may result in active material loss in the dead volumes of the cell. Even if this ratio is high compared to practical recommendations, it is better to work in a diluted system in this study to understand the real impact of MoS<sub>2</sub>-KB on the shuttle effect, rather than introducing additional limitations (i.e. diffusion) into an already complex system.

After the electrode formulation and coin-cell making, electrochemical characterizations are conducted to examine the effect of MoS<sub>2</sub>-Ketjenblack adsorbent present in the electrode on the electrochemical performance, especially to understand how this material impact the “shuttle-effect”.

## 1.4 Electrochemical performances

### 1.4.1 Galvanostatic curve treatment methodology

This section clarifies the methodology used for processing and plotting the galvanostatic curves. These precisions are necessary because there are various representations in the literature, which can be confusing, and the processing steps are often insufficiently explained, making difficult the comparison of the results<sup>154</sup>.

Coin cells are placed in an oven held at 25°C and cycled in the voltage range between 2-3 V vs Li<sup>+</sup>/Li on a BioLogic BCS-805 multichannel potentiostat. The C-rate applied to discharge and charge the coin cell, is selected taking into account the theoretical capacity ( $C_{th}$ ) of the electrode calculated using **equation (IV-11)**. A conditioning cycle at  $C_{th}/20$  is applied to the cell before cycling at  $C_{th}/10$ .

$$C_{th}(mAh) = 1675(mAh.g^{-1}) * mass\ of\ sulfur(g) \quad (IV-11)$$

**Figure IV-13** shows an example of the discharge curve of S-0Mo in the conditioning cycle at  $C_{th}/20$  (red curve). The first plateau and the potential drop until the second plateau (region A) is generally assigned to the full reduction of S<sub>8</sub> into S<sub>4</sub><sup>2-</sup> (S<sub>8</sub> + 4 e<sup>-</sup> ↔ 2 S<sub>4</sub><sup>2-</sup>) which gives a theoretical capacity of 419 mAh.g<sup>-1</sup> (see **Chapter I**). However, herein a higher practical capacity of 614 mAh.g<sup>-1</sup> is reach instead of the theoretical 419 mAh.g<sup>-1</sup>. This difference is likely related to large errors in sulfur content arising from the small masses that are weighed (eg, electrode mass = 130 mg, including 7.5 mg of Al). Consequently, to get rid of this mass incertitude, the cycling curves are normalized relatively to the theoretical capacity of region A (correction factor) leading to the normalized curve (black color in **Figure IV-13**). This correction factor allows to adjust the sulfur content in the electrode (see **Table IV-6**). The cycling rate is then corrected accordingly.

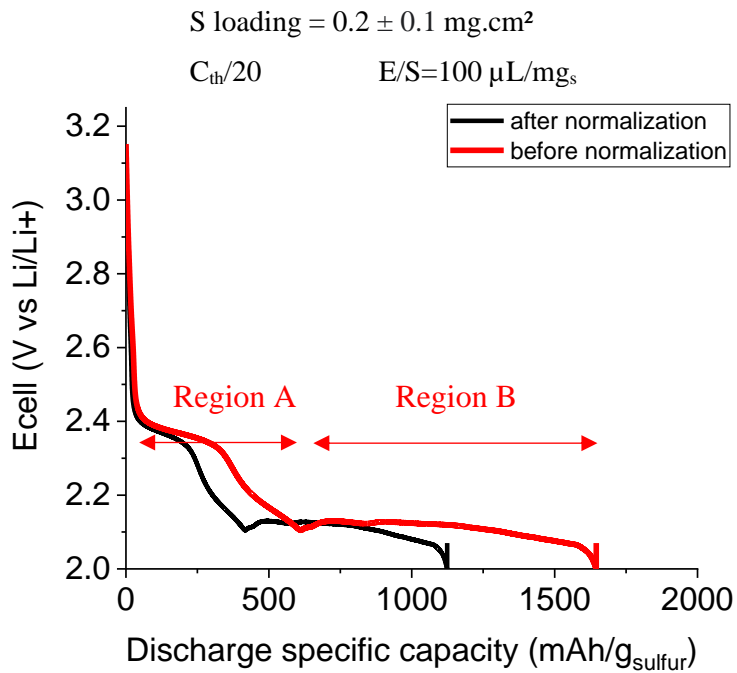


**Figure IV-13.** Galvanostatic discharge curves of S-0Mo before and after normalization – conditioning step . Conditions:  $25^\circ\text{C}$  in  $1 \text{ M LiTFSI}$ ,  $1 \text{ wt}\% \text{ LiNO}_3$ ,  $\text{DOL/DME v/v } 1/1$ .

Then, the typical galvanostatic discharge-charge curve of  $\text{Li} \parallel \text{S}_8$  cells is depicted in **Figure IV-14** for a  $C_{th}/10$  rate after applying the factor of normalization deduced at  $C_{th}/20$ .

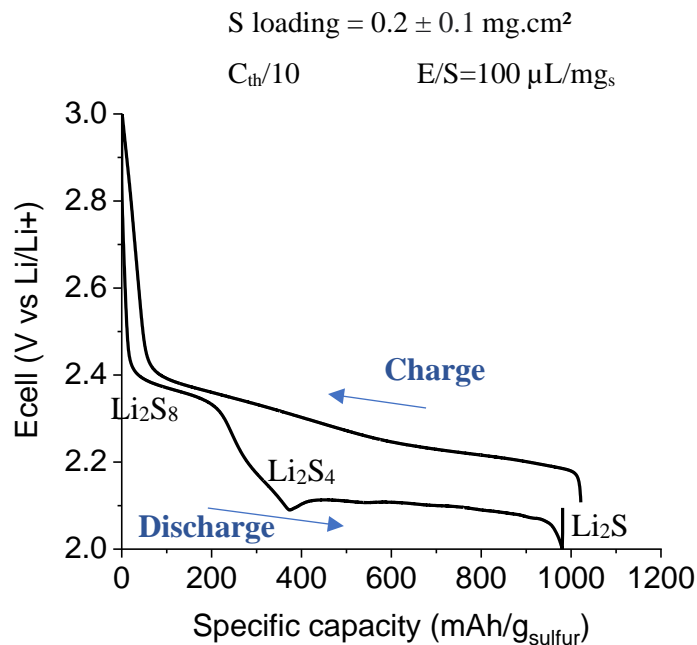


**Figure IV-14.** Typical galvanostatic discharge-charge S-0Mo curve at  $C_{th}/10$ .



Even though the galvanostatic measurements started with a discharge, the battery being assembled in a fully charged state, a cycle is defined as a charge followed by a discharge. Consequently, the Coulombic efficiency (CE) is calculated using **equation (IV-12)** considering the discharged capacity obtained after the charge.

$$CE = \frac{\text{discharged capacity}}{\text{charged capacity}} * 100 \quad \text{(IV-12)}$$

### 1.4.2 Repeatability tests

At first, repeatability tests have been made to conclude on experiment reliability. Three cells are assembled in parallel and cycled in a similar fashion. Before cycling, electrochemical impedance spectroscopy (EIS) measurements are performed, using BioLogic BCS-805 multichannel potentiostat at open circuit voltage (OCV) with a signal amplitude of 30 mV, in a frequency range from 10 kHz to 100 mHz and **Figure IV-15-a** displays the results: it shows three similar spectra with two semi-circles followed at low frequency by a straight line almost vertical. This confirms the good reproducibility of the cell. In addition, these spectra are consistent with those reported by S.Walus *et al.*<sup>155</sup> on Li || S<sub>8</sub> cells.

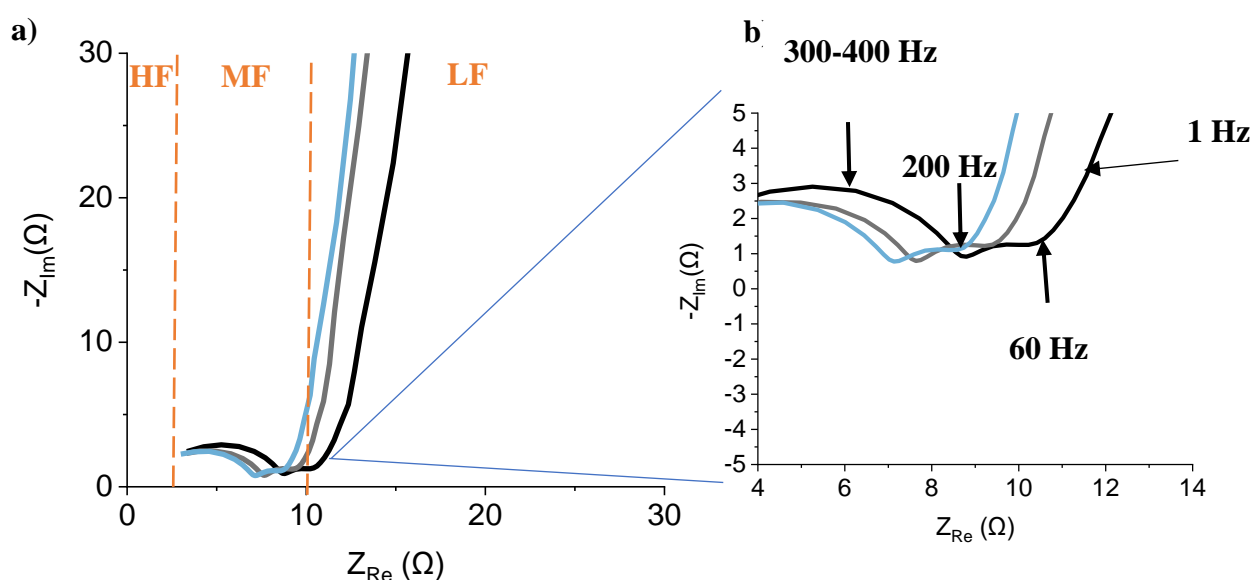


**Figure IV-15.** Repeatability tests on fresh two-electrode Li || S-0Mo coin cells (3 samples) a) Nyquist plot of EIS measurements b) Zoom on the EIS between Z<sub>Re</sub> = 4-14 Ω.

According to S. Walus *et al.*<sup>155</sup> the Nyquist plot of two-electrode Li || S<sub>8</sub> cells can be divided in three main regions : high (HF), middle (MF) and low frequency (LF) region as shown in **Figure IV-16** reproducing a Nyquist plot from this work. The HF region can be attributed to the ohmic contributions of the cell (ionic migration in the electrolyte, all the electrical connections (coin cells casing, cables, sample holder). In our case, this HF region is not visible due to the BioLogic BCS-805 battery cycler frequency limitation to 10kHz. So the beginning of the MF semi-circle is not apparent. In the work of S. Walus *et al.*<sup>155</sup>, this MF region spans approximately from 60 kHz to 60 Hz which is quite similar to the one obtained on the Li || S-0Mo coin cells in **Figure IV-15**. Then, the straight line almost vertical in the LF region below 60 Hz is attributed to the blocking electronic charge transfer of the sulfur electrode<sup>155</sup>.

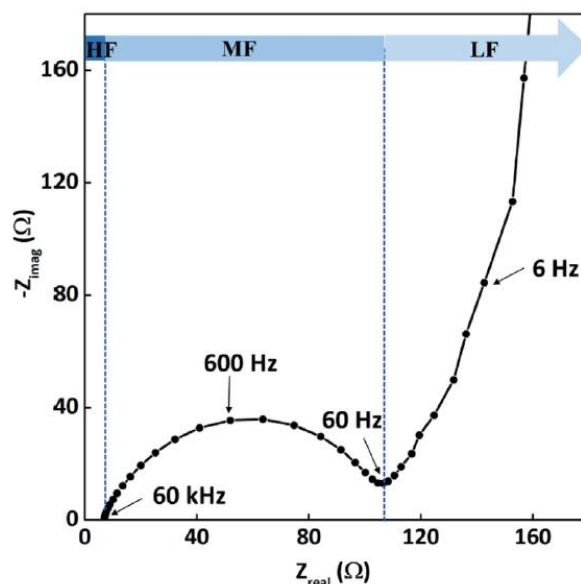


**Figure IV-16.** Characteristic Nyquist plot of a fresh Li/S coin cell at the initial state measured at 25°C (reproduced from S. Walus *et al.*<sup>155</sup>).

The MF region interpretation of the EIS spectra cannot be attributed to a single phenomenon due to the complexity of the Li–S system. Deconvolution of different parameters affecting the cell performance and contributing to the impedance of a complete Li–S cell must be accomplished through a thorough EIS study of symmetric cells with a systematic approach using model symmetric cells<sup>155,156</sup> (S<sub>8</sub> || S<sub>8</sub> and Li || Li). S. Walus *et al.*<sup>157</sup> and J. Conder *et al.*<sup>156</sup> demonstrates that the sulfur positive electrode has a marginal contribution in the overall MF regions, mainly associated to bad electronic contacts between the sulfur particles bound together by the carbon particles and the binder<sup>157</sup>. The main MF contribution in a fresh cell just after assembly is associated to lithium metal solid electrolyte interphase (SEI)<sup>155,156</sup>. In our Li

|| S<sub>8</sub> cell, another semi-circle (fc~60 Hz) can be observed at the beginning of the LF regions, as shown in the zoom of **Figure IV-15-b**. It is ascribed to LiPS electronic charge transfer<sup>155</sup>. This indicates that the LiPS had already begun to be produced even before applying the initial current to the cell (self-discharge).

Based on **Figure IV-15**, the EIS signatures are then characteristics to Li || S<sub>8</sub>. Results are repeatable meaning that coin cells are assembled correctly with a low total resistance below 15 Ω, mainly attributed to lithium metal contribution and to a lesser extent, to the LiPS charge transfer.

**Figure IV-17** exhibits the specific discharge capacity and the CE of three Li || S-0Mo cells at C<sub>th</sub>/10. The two cells have the same trend: a rapid discharge capacity degradation down to about 900 mAh.g<sup>-1</sup> over the first 5 cycles, accompanied by significant fluctuations in CE in between about 95 to 98 %, followed by system stabilization with a slower loss of capacity, down to around 800 mAh.g<sup>-1</sup> after 35 - 38 cycles. After 35 to 38 cycles, the cells fail associated with a loss in capacity of about 200 mAh.g<sup>-1</sup> after 10 more cycles. This capacity decay is preceded by a decrease in CE down to 85 % after 45 cycles in total. This is characteristic of lithium dendrites forming soft short-circuits<sup>158</sup>.

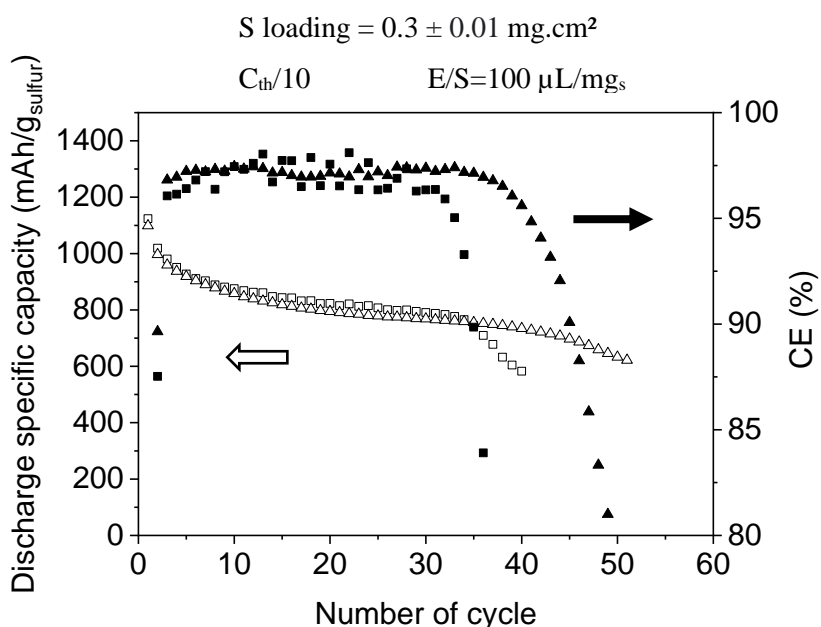


**Figure IV-17.** S-0Mo cycling stability repeatability – 2 coin-cells.  
Conditions: 25°C in 1 M LiTFSI, 1 wt% LiNO<sub>3</sub>, DOL/DME v/v 1/1.

To conclude, the assembly of Li || S-0Mo coin cells under the same conditions results in quite good repeatability in terms of battery characteristics in cycling. Electrodes based on S-32Mo-400-H<sub>2</sub>S(15) and S-48Mo-400-H<sub>2</sub>S(15) also exhibit such repeatability. Therefore, each electrochemical test involves the assembly of two coin cells for each type of active materials and the comparison is provided in the next section.

### **1.4.3 Electrochemical results**

The EIS measurements conducted during the repeatability tests are shown in **Figure IV-15**. They reveal presence of a loop at frequencies typically in between 200 and 20 Hz ascribed to the presence of polysulfides within the electrolyte in the cathode. Therefore, the appearance of polysulfide species into the electrolyte occurs during periods of rest, which is due to the solubility of elemental sulfur that can diffuse and be reduced on the lithium surface, i.e. self-discharge phenomenon. **Figure IV-18** displays the evolution of the cell voltage of Li || S<sub>8</sub> cells over 120 hours in Open Circuit Voltage (OCV) condition at 25°C. It can be observed that self-discharge occurs for the three composite materials with different self-discharge rate. The OCV voltages quickly decrease for S-0Mo and S-32Mo-400-H<sub>2</sub>S(15), while S-48Mo-400-H<sub>2</sub>S(15) exhibits slower self-discharge. For both MoS<sub>2</sub>-KB composites, the self-discharge tends to stabilize at 2.5 and 2.7 V vs. Li<sup>+</sup>/Li for S-32Mo-400-H<sub>2</sub>S(15) and S-48Mo-400-H<sub>2</sub>S(15) respectively, on contrary to S-0Mo that reaches an OCV of 2.3 V vs. Li<sup>+</sup>/Li after 120 h. At this potential, long chains S<sub>8</sub> is reduced to Li<sub>2</sub>S<sub>6</sub> and Li<sub>2</sub>S<sub>4</sub> chains (see **chapter I**). The self-discharge rate is thus slowed down by the use MoS<sub>2</sub>-KB which interacts with the polysulfides generated limit their diffusion within the electrolyte. The OCV potential of S-48Mo-400-H<sub>2</sub>S(15) reached 2.61 V vs. Li<sup>+</sup>/Li after 120h of OCV, indicating that it retains quite efficiently the Li<sub>2</sub>S<sub>8</sub> long chains. In addition, the reduction of the self-discharge rate is directly correlated to the adsorption capacity which is more efficiently with S-48Mo-400-H<sub>2</sub>S(15). This result is interesting. To go further, the battery is then cycled right after cell assembly.

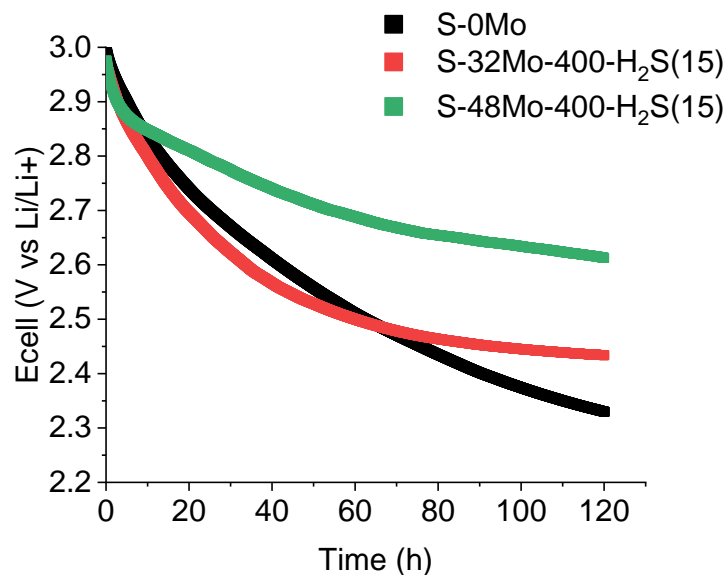


**Figure IV-18.** Self-discharge of fresh Li || S<sub>8</sub> cells during 120 hours of storage at OCV. Conditions: 25°C in 1 M LiTFSI, 1 wt% LiNO<sub>3</sub>, DOL/DME v/v 1/1.

The addition of MoS<sub>2</sub>-KB inside the electrode formulation gives similar galvanostatic curves than the S-0Mo as shown in **Figure IV-14** and are consistent with typical sulfur signature of a liquid Li/S battery<sup>31,144</sup>. The modification of mechanism related to the use of MoS<sub>2</sub>-carbon structure is still a topic of controversy in the literature and at this point it remains unclear. Nonetheless, it can be pointed out that the classical nucleation signature of Li<sub>2</sub>S clearly visible as a dip (whiplash) in the discharge curve shown in the zoom in **Figure IV-19**, tends to disappear when increasing the MoS<sub>2</sub> content in the MoS<sub>2</sub>-KB composite, which suggests an easier Li<sub>2</sub>S<sub>2</sub> or Li<sub>2</sub>S nucleation. In addition, the increase of MoS<sub>2</sub> content change the shape of the region A, with a shorter first plateau (-2.5% and -5% for 32 and 48Mo respectively), while a small plateau appears around 2,15V vs Li<sup>+</sup>/Li. In this range of state of discharge, mainly Li<sub>2</sub>S<sub>6</sub> and/or Li<sub>2</sub>S<sub>4</sub> are present, according to our UV-Vis analysis it could be the result of specific LiPS adsorption trough adsorption.

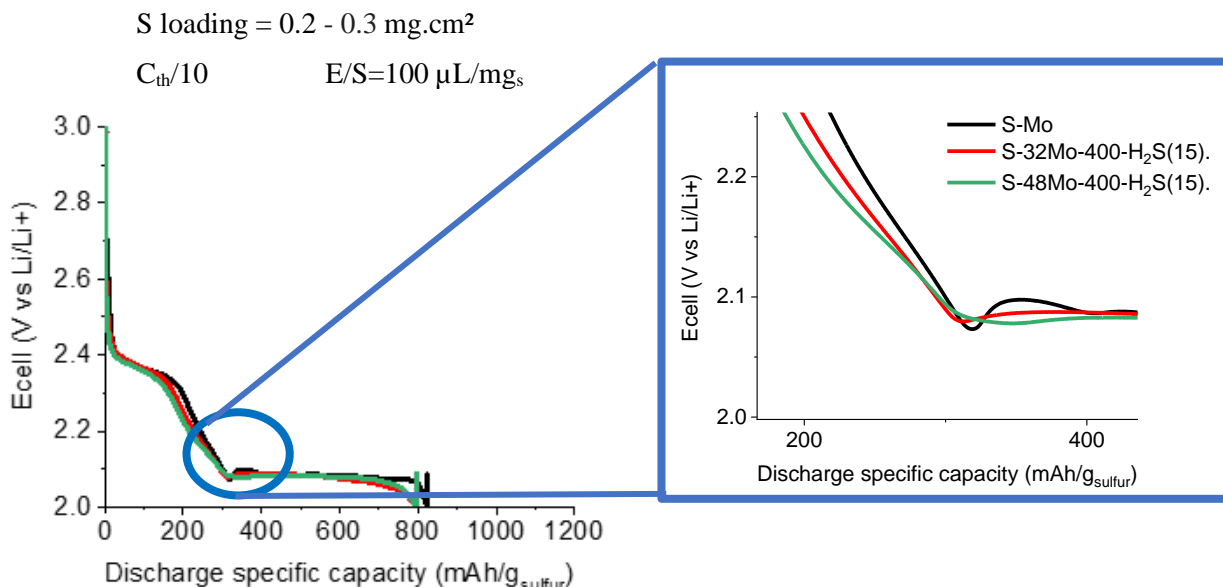


**Figure IV-19.** Comparison of the discharge for the reference and the MoS<sub>2</sub>-KB based electrodes after 20<sup>th</sup> cycles. Zoom at the beginning of the second plateau where Li<sub>2</sub>S nucleation occurs.

The cycling performances are then studied in further details to determine the influence of the use of MoS<sub>2</sub>-KB over cycling (see **Figure IV-20**). The capacity values of S-32Mo-400-H<sub>2</sub>S(15) cannot be directly compared to the other samples due to the extended cycling range between 1.8V-3V vs Li<sup>+</sup>/Li instead of 2V-3V vs Li<sup>+</sup>/Li. However, its constant capacity loss and CE can still be analyzed. The initial discharge specific capacity reached is 1123 and 1090 mAh.g<sup>-1</sup> for S-0Mo and S-48Mo-400-H<sub>2</sub>S(15) respectively. There is a significant drop in capacity over the first 5 cycles before reaching a capacity stability around 927 and 826 mAh.g<sup>-1</sup>. The retention capacity after 60 cycles is 695 mAh.g<sup>-1</sup> with a capacity retention rate of 82 % (based on the 5<sup>th</sup> cycle) which is superior to the S-0Mo cycling performances over time. The capacity decreases to 775 mAh.g<sup>-1</sup> after 33 cycles, which account for a capacity retention of 81%. After the 33<sup>th</sup> cycle a strong capacity fading is observed for S-0Mo, accompanied by a drop of CE, due to side effect such as soft short due to lithium dendrites. Even the capacity retention is high, capacity fluctuations are observed (sawtooth capacity). A constant capacity losses (based on the 5<sup>th</sup> cycle) of 5.4 mAh.g<sup>-1</sup>/cycle is observed for S-0Mo (between 5<sup>th</sup> and 33<sup>th</sup> cycles) while S-32Mo-400-H<sub>2</sub>S(15) and S-48Mo-400-H<sub>2</sub>S(15) electrode offers only a loss of 4.9 and 2.8 mAh.g<sup>-1</sup>/cycle respectively. Increasing the MoS<sub>2</sub> loading from 32 wt.% to 48 wt.% enables a reduction in capacity loss of 1.75, which is directly correlated with the 1.3-fold increase in adsorption capacity observed for 48 wt.% of MoS<sub>2</sub> on KB. The use of MoS<sub>2</sub>-KB, for both 32 wt.% and 48 wt.% of MoS<sub>2</sub>, enables to reach a better capacity stability compared to S-0Mo.

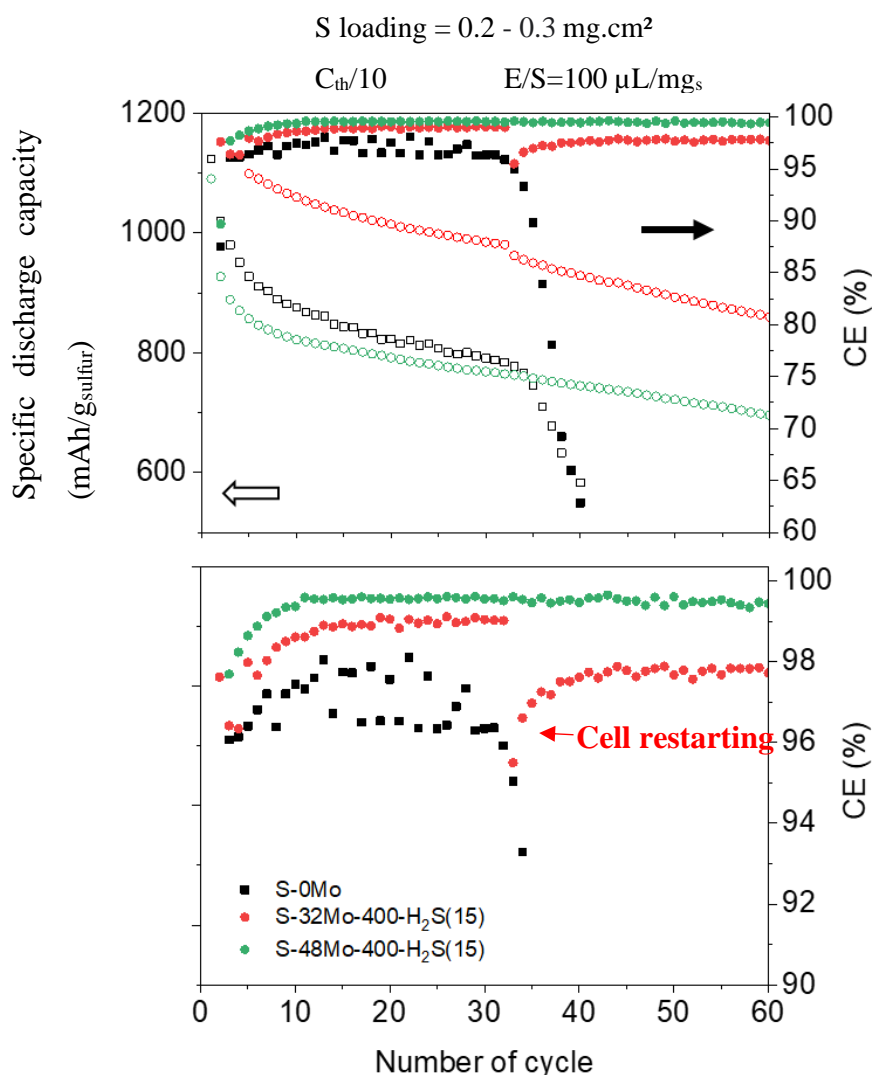


**Figure IV-20.** Cycle stability and Coulombic efficiencies of S-0Mo, S-32Mo-400-H<sub>2</sub>S(15) and S-48Mo-400-H<sub>2</sub>S(15) cells. Conditions: 25°C in 1 M LiTFSI, 1 wt% LiNO<sub>3</sub>, DOL/DME v/v 1/1, in the 2-3 V vs Li/Li<sup>+</sup> voltage range (for 0% and 48% wt. MoS<sub>2</sub> on KB) and between 1.8-3 V vs Li/Li<sup>+</sup> voltage range (for 32 wt.% MoS<sub>2</sub> on KB) at C/10 (1C= 0.2-0.6 μA.cm<sup>-2</sup>).

Looking at the evolution of the CE shown in the zoom of **Figure IV-20** gives relevant information on the impact of the MoS<sub>2</sub> absorbent on the shuttle-effect. There is a significant drop in capacity over the first 5 cycles, which corresponds to the rise of CE. For S-48Mo-400-H<sub>2</sub>S(15), the CE increase from 97 % and stabilizes after 10 cycles to 99.5+/-0,1% during the next 60 cycles. The same behavior is observed for S-32Mo-400-H<sub>2</sub>S(15) with a stabilization at to 99.0+/-0,1%. After a cycling stopped for three days, the cell has been restarted and a loss in CE is observed and tends to stabilize around 97.7 +/-0,1%. While for S-0Mo, the CE lower stabilizes at 97+/-0,5% followed by a rapid drop after 33 cycles, indicating the premature end of life of the cell.

The use of MoS<sub>2</sub>-KB, as composite material in the positive electrode is thus beneficial in Li-S application, enables to obtain very high CE, demonstrating the strong reduction of shuttling and enhances the cycle life. This behavior is correlated with the MoS<sub>2</sub> content supported on KB, in line with the better adsorption capacity calculated in chapter III. Indeed, for similar MoS<sub>2</sub> slab length and stacking, the capacity loss in mAh.g<sup>-1</sup>/cycle ( $4.9/2.8 = 1.8$ ) seems to be corroborated with the increase in available surface area (surface ratio = 1.4-1.5) (see chapter II) for the adsorption of Li<sub>2</sub>S<sub>6</sub> and Li<sub>2</sub>S<sub>4</sub>

For comparison purpose, capacities of region A and region B (see Figure IV-14 for the region definition) are compared in Figure IV-21. It is worth noting that for both samples the 419 mAh.g<sup>-1</sup> at the end of the region A is not achieved, highlighting a limitation in the conversion of S<sub>8</sub> into Li<sub>2</sub>S<sub>4</sub>. The capacity of region A tends to be rapidly reduced for S-0Mo after 40<sup>th</sup> cycle with a loss of 3.85 mAh.g<sup>-1</sup> per cycle while it remains two and half times more stable for S-48Mo-400-H<sub>2</sub>S(15) with a loss of 1.6 mAh.g<sup>-1</sup> per cycle. The same tendency is observed in the region B. From the capacities given in Figure IV-21-a, the region ratio ( $R_{ratio}$ ), defined as the capacity ratio between the region B and region A, is calculated. Its gives information on the amount of Li<sub>2</sub>S<sub>4</sub> effectively converted into Li<sub>2</sub>S. The theoretical value for full S<sub>8</sub> conversion in Li<sub>2</sub>S is  $R_{ratio} = 3$ , which means that the capacity of region B theoretically accounts for three times that of region A (419 mAh.g<sup>-1</sup>). A ratio inferior to 3 directly highlights conversion limitation in the last discharge steps Li<sub>2</sub>S<sub>4</sub> to Li<sub>2</sub>S. The evolution of the experimental  $R_{ratio}$  over cycles is displayed in Figure IV-21-b. For both samples,  $R_{ratio}$  remains stable and close to 1.6 over 40 cycles so that the rate of conversion of Li<sub>2</sub>S<sub>4</sub> into Li<sub>2</sub>S is not complete but constant.

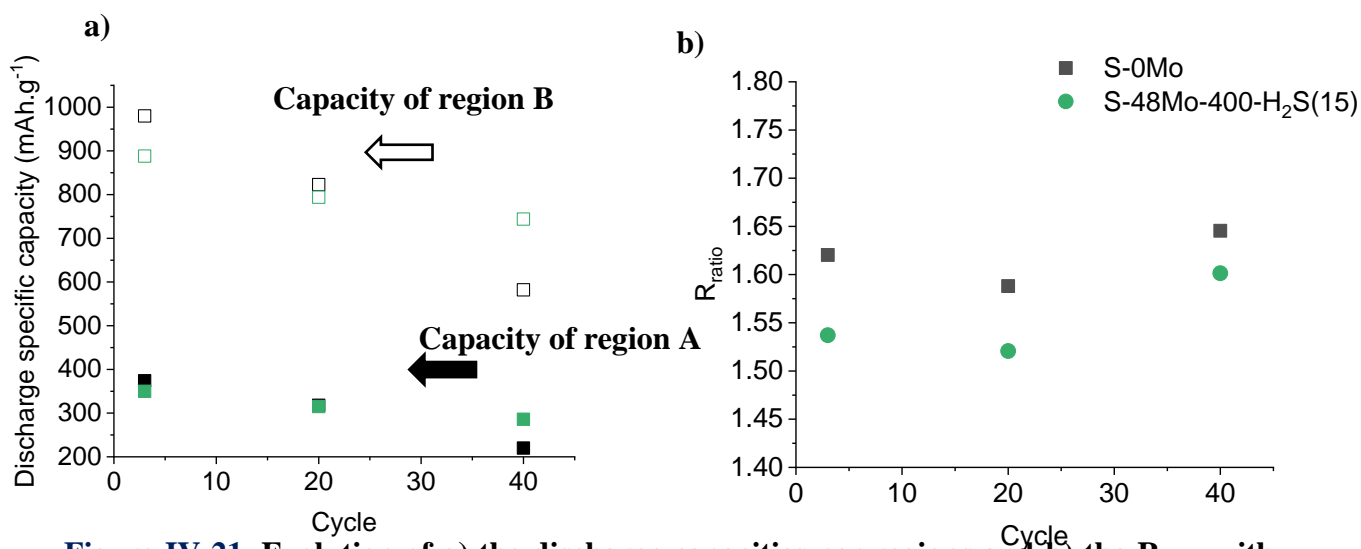
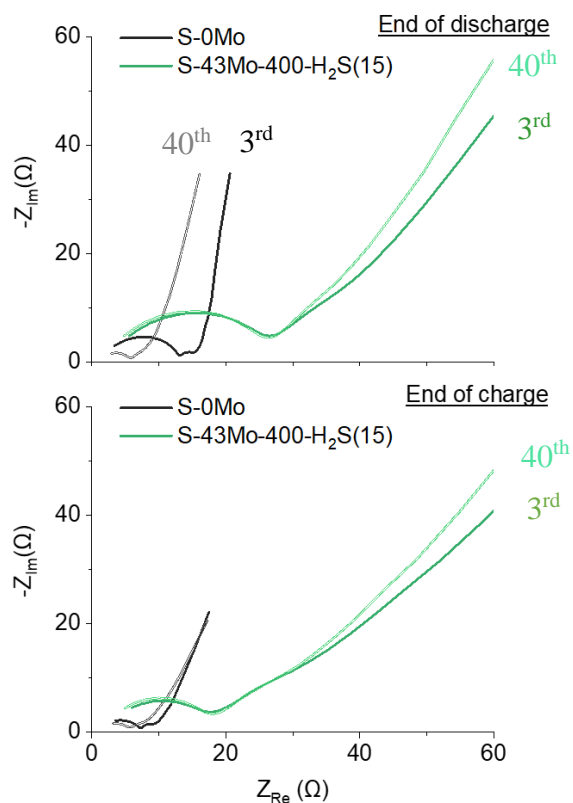


Figure IV-21. Evolution of a) the discharge capacities per regions and b) the  $R_{ratio}$  with cycle number.



The spectra plotted in **Figure IV-22** show that at the end of the charge or discharge the reference electrode is fully blocking with almost a vertical straight line at low frequency, the electrochemical reaction becomes impossible, while for 48 wt.% of supported MoS<sub>2</sub>, we observe a 45° line characteristic of diffusion process, suggesting that the reactions are kinetically hindered but seems possible.



**Figure IV-22.** The Nyquist plots of S-0Mo and S-48Mo-400-H<sub>2</sub>S(15) at the end of a) discharge and b) charge.

#### 1.4.4 Discussion with literature data

The electrochemical performance of Li-S coin cells with S-48Mo-400-H<sub>2</sub>S(15) compared with other similar research work is listed in **Table IV-8**. MoS<sub>2</sub> can be mechanically mixed with S, as demonstrated in the works by J.Luo *et al.*<sup>140</sup>. A.Abraham *et al.*<sup>159</sup> have confirmed that the addition of MoS<sub>2</sub> and the presence of defects in the layers improve the Coulombic efficiency. MoS<sub>2</sub> can also be incorporated into a carbon matrix. These studies reveal an improvement in retention capacity, Coulombic efficiency, and excellent long-term cycle stability (over 500 cycles). These findings indicate that the use of a combined MoS<sub>2</sub>-carbon host has a positive impact on reduction the shuttle effect through interactions with polysulfides. J.He *et al.*<sup>160</sup> even demonstrated that cycling a high loading electrode of 10 mg<sub>s</sub>.cm<sup>2</sup> resulted in a highly reversible

**Chapter IV – Electrochemical performances of S-MoS<sub>2</sub>-KB composite active material as positive electrode**

capacity of 1184 mAh.g<sup>-1</sup> and a capacity retention of 96.3% after 200 cycles at 1C, suggesting that scaling up for practical applications is feasible with optimizations.

**Table IV-8. Comparison of the results with other literature**

Host structure	MoS <sub>2</sub> (wt.%) in the host	S loading (mg <sub>s</sub> .cm <sup>-2</sup> )	Adsorbent/active sulfur ratio	E/S (μL.mg <sub>s</sub> )	C-rates	Cycles	Reversible capacity (mAh.g <sup>-1</sup> )	CE (%)	Reference
<b>MoS<sub>2</sub> in the host structure (MoS<sub>2</sub>-carbon)</b>									
MoS <sub>2</sub> -KB	32	0.4	2.9	100	0.1	60	700	99.4	This work
uMoS <sub>2</sub> -HCSM	-	1.1	-	-	0.5	500	940	97	<sup>52</sup>
MoS <sub>2</sub> -GA-DR-	30	-	-	-	0.2	500	820	100	<sup>161</sup>
MoS <sub>2</sub> -x-rGO	-	1.5	-	-	0.5	600	630	99.6	
1T MoS <sub>2</sub> -3DG	-	10.0	-	-	0.1	200	1180	96.3	<sup>160</sup>
MoS <sub>2</sub> @HCS	33.3	-	-	-	0.5	500	640	98	<sup>162</sup>
MoS <sub>2</sub> -MCHS	17.5	0.5	-	-	0.2	100	1040	-	<sup>163</sup>
<b>MoS<sub>2</sub> as individual material</b>									
2D MoS <sub>2-x</sub> nanosheets	-	1.5	-	-	0.5	500	820	100	<sup>159</sup>
MoS <sub>2</sub>	-	-	-	-	2	500	830	-	<sup>140</sup>

Nevertheless, it remains challenging to compare the available systems in literature because crucial data for understanding them are missing (e.g. MoS<sub>2</sub> percentage in the final material, sulfur loading, and especially the E/S and MoS<sub>2</sub>/S/ratios). Numerous papers promote MoS<sub>2</sub>-carbon based adsorbents, but none provides a systematic quantification of adsorption capacity nor the reasons to select specific formulation such as the amount of adsorbent to incorporate inside the electrodes. As demonstrated in this study, based on the adsorption capacity *Nads*, an optimum weight *adsorbent/S/ ratio*, corresponding to almost 50% of *Nads*, is crucial to observe the effect of adsorption on the system, leading unfortunately to the reduction of sulfur loading.

Furthermore, Li-S battery electrodes are complex, comprising multiple components, which complicates the distinction between polysulfide interactions originating from carbon, MoS<sub>2</sub>, and binders. Thus for further analysis, it appears mandatory to precise the formulation, and specifically the ratio E/S, Ads/S. Investigations are still needed to further understand i) the LiPS equilibria in a reference solvent such as DOL-DME-LiTFSi thanks e.g. to UV-VIS investigation such as presented in chapter III with other equivalent LiPS (Li<sub>2</sub>S<sub>8</sub>, Li<sub>2</sub>S<sub>4</sub>, etc), ii) the adsorption process, and iii) its impacts on the electrochemical characteristic to optimize the Li-S electrode thanks to the understanding of the role of each parameter in polysulfides interactions in solutions.

## **1.5 Conclusion**

Here, we successfully achieved to synthesize S-MoS<sub>2</sub>-KB with a sulfur content of 25-30% which is calculated from the adsorption capacity of MoS<sub>2</sub>-KB to work with an appropriate MoS<sub>2</sub>/active sulfur ratio that theoretically enables to adsorb 20 to 40% of the Li<sub>2</sub>S<sub>6</sub> produced. This sulfur content is also selected to accommodate the volume expansion that occurs sulfur reduction into Li<sub>2</sub>S to maintain the sufficient pore volume initial structure without electrode pulverization.

Due to the high carbon content and a remaining porous volume of 1.2 cm<sup>3</sup>.g<sup>-1</sup> in S-48Mo-400-H<sub>2</sub>S(15) (48 wt.% MoS<sub>2</sub> in MoS<sub>2</sub>-KB, equivalent to 39 wt.% in S-MoS<sub>2</sub>-KB), the conventional PVDF-NMP mixture proves unsuitable for electrode formulation. This results in four primary issues encountered during electrode preparation: (a) non-adherence on the current collector (b) electrode peeling (c) heterogeneous particle distribution and (d) cracking. A series of optimizations lead to a final formulation composition of 60/2/40 wt.% CAM/CB/CMC-SBR, with a CMC:SBR water soluble binder ratio of 10:30. A 3-step drying protocol is employed to achieve homogeneous electrodes, eliminating any issues of electrode peeling or cracking.

Coin cells are constructed using electrodes featuring a sulfur loading of 0.38 mg<sub>s</sub>.cm<sup>-2</sup> and a carefully chosen E/S ratio. This choice considers the electrode and separator volume, ensuring optimal wettability and alignment with the conditions specified for the UV-Vis measurements. Employing an E/S ratio of 100 μL.mg<sub>s</sub><sup>-1</sup>, the coin cells achieve a reversible capacity of 695 mAh.g<sup>-1</sup> with a Coulombic efficiency of 99.4% after 60 cycles.

It has been demonstrated that the use of MoS<sub>2</sub>-KB allows for (a) an improved capacity retention and (b) an increase in Coulombic efficiency, indicating a strong reduction in the LiPS shuttling thanks to adsorbent interactions with polysulfides. The enhancement of Coulombic efficiency is directly linked to the materials' adsorption capacity and the quantity of active sites available to adsorb polysulfides. Increasing the MoS<sub>2</sub> loading content effectively reduces the shuttle effect. Thus the adsorbent content must be consistent with a large adsorption of LiPS (e.g. Li<sub>2</sub>S<sub>6</sub>). Therefore, it is essential for comparison purpose and discussion to systematically quantify polysulfide adsorption to select materials that offer the best adsorption capacity before incorporating them into the electrodes, and to give the weight adsorbent/S ratios in the electrode formulation, and E/S after cell assembly.

Interestingly, we demonstrate that the use of MoS<sub>2</sub>-KB also alters the shape of the electrochemical curves, with suggests a reduction in activation energy associated with Li<sub>2</sub>S<sub>2</sub>/Li<sub>2</sub>S nucleation. At last, the presence of MoS<sub>2</sub> adsorbent modify the region A, reducing the length of the first plateau, while a pseudo plateau increases at 2,15V vs Li<sup>+</sup>/Li. However, the microscopic mechanism remains a subject of debate in the literature, and further studies are necessary.



## General conclusion

---

Nowadays, human activities are increasingly dependent on electricity supply for a wide array of transport and stationary applications, which implies to develop efficient ways to store electricity at large scale. Batteries are good candidates and are already ubiquitous in smartphones, laptops, or electric vehicles. To meet the requirements of these new applications, it is essential to increase the energy density and the durability. Unfortunately, current lithium-ion batteries are reaching their performance limits and the exploration of new chemistries is required. Among next-generations, Lithium-sulfur (Li-S) batteries are attracting increasing attention. Indeed, Li-S batteries owing to their high theoretical energy density ( $2600 \text{ Wh.kg}^{-1}$ ) have the potential to store more energy (about 3 times practically) than Li-ion batteries. The unique electrochemical mechanism of these systems involves soluble, mobile, and reactive lithium polysulfide intermediates ( $\text{Li}_2\text{S}_x$ ,  $2 \leq x \leq 8$ ) (LiPS). Their back-and-forth movement between electrodes, known as “shuttle-effect” is one of the major drawbacks/challenges that limits the commercialization of this promising technology, giving rise to self-discharge, low active sulfur utilization, poor coulombic efficiency, and rapid capacity decay.

Among the various research directions, the development of host materials takes the lead in terms of volume of paper published on this topic. The scientific community has shown interest in numerous material families capable of both limiting the shuttle effect through i) physical confinement or/and ii) entrapping polysulfides through chemisorption or electrostatic interactions. This has led to the study of various metal-based materials, such as oxides, sulfides, nitrides, carbides, and even conductive polymers. The electrochemical performance of the sulfur-positive electrode has seen significant enhancements since Nazar's pioneering work in 2013. However, certain fundamental aspects are still debated, notably the nature and the concentration of polysulfides that interact with this host materials. At certain point, this aspect is very scarcely explored in the literature. The LiPS-host material/adsorbent interactions are consistently highlighted by demonstrating the reduction of UV-Vis signal from a given polysulfides equivalent. Nevertheless, this remains predominantly a qualitative consideration. These studies do not take into account the nature of the polysulfides involved in these interactions, while some attempts have been made to identify the wavelengths associated with different types of LiPS. UV-Vis spectra are primarily recorded in the 350-700 nm range (corresponding mainly to  $\text{Li}_2\text{S}_4$ ,  $\text{Li}_2\text{S}_6$  and  $\text{S}_3^{\bullet-}$  signals), thus concealing a portion of the signal

from 250-350 nm, which reveals the presence of  $S_8$ . An analysis of the complete spectrum allows for reflection on the disproportionation equilibria (spontaneous reactions leading to  $Li_2S_x \Leftrightarrow Li_2S_y + \frac{(y-x)}{8} S_8 (x < y)$ ) that complexify the system. While quantitative studies are starting to emerge, they are currently limited in number. In this PhD work, we aimed to provide insights into the adsorption phenomenon, addressing two main questions: what is the nature and concentration of polysulfides involved? How are disproportionation and electrochemical equilibria affected by the nature of the adsorbent? We propose thus a robust methodology, by looking at the adsorption phenomenon and the alteration of polysulfide species in LiPS solution using supported  $MoS_2$  incorporated into porous Ketjenblack carbon network as a model material ( $MoS_2$ -KB).

Indeed  $MoS_2$ -Ketjenblack has been chosen because :

- KB carbonaceous support develops a substantial total pore volume of  $4.4 \text{ cm}^3\text{g}^{-1}$  of which 69%, 23% and 8% are developed by macro, meso and micropores respectively and a large specific surface area of  $1364 \text{ m}^2\text{g}^{-1}$ . These characterizations confirms that the KB texture should be suitable i) to offer a substantial surface area for optimal dispersion of the  $MoS_2$  particles, ii) to host a significant volume of sulfur active material (sulfur), iii) to store the excess of electrolyte inside KB macropores and iv) to provide residual space to accommodate volumetric variations observed upon cycling (+/- 80%). Its  $0.25 \text{ S.cm}^{-1}$  conductivity is also sufficient to ensure a fast enough transport of electrons within the positive electrode.
- $MoS_2$  is a versatile material. By using an incipient wetness impregnation gas phase sulfidation synthesis protocol, it is possible to play on the nature and the number of adsorption active sites of its structure to optimize the interactions with LiPS. This synthesis method enables to get small  $MoS_2$  slabs whose size is inferior to 5 nm, well dispersed, with stacking of 1 or 2. These small slabs are favorable to promote a high fraction of edges+corners adsorption sites while a low stacking improves the access to the basal site also supposed to adsorb LiPS. Both edges and basal planes offer adsorption sites, and the preference for adsorption on one over the other has not been demonstrated under our conditions.

A standard UV-Vis procedure using *in situ* probe used directly inside the glove box helps to minimize the artefact obtained with *ex situ* conventional quartz-cuvette. These artefacts are due to the adsorption of polysulfides at the silica cuvette surface (confirmed by Aerosil 200 adsorption investigations) and the risk of air contamination leading to polysulfides degradations. This first step aims to bring quantitative characterization of the  $\text{Li}_2\text{S}_6$  equivalent solution, as this intermediate-chain polysulfide is widely used as LiPS model. The spectral decomposition across the entire UV spectrum reveals that the  $\text{Li}_2\text{S}_6$  equivalent spectrum is composed of five contributions, with two attributed to  $\text{S}_8$  at 230 and 285 nm, and three others to  $\text{S}_4^{2-}$  and  $\text{S}_6^{2-}$ , at 325, 365, and 425 nm in line with the disproportionation reaction of  $\text{Li}_2\text{S}_6$  into  $\text{S}_4^{2-}$  and  $\text{S}_8$ . A methodology to determine the molar extinction coefficients of  $\text{S}_8$ ,  $\text{S}_4^{2-}$ , and  $\text{S}_6^{2-}$  has also been described, but needs to be consolidated. Indeed, the lack of literature on this topic restricts the scope of this approach and makes it challenging to compare our values with existing data. We highlight that the proportion of each polysulfide species remains unchanged with the initial concentration of  $\text{Li}_2\text{S}_6$ . Their respective concentrations vary in the mixture and the accurate determination is still challenging.

This initial study of the equivalent  $\text{Li}_2\text{S}_6$  solution is crucial as it serves as the basis for the study of the adsorption phenomenon. This spectral decomposition methodology allows to determine the nature of the adsorbed polysulfides on the surface of three model materials: Aerosil 200 (silica material),  $\text{MoS}_2$ -KB with  $\text{MoS}_2$  loading of 32 et 48 wt.%. For all three materials, adsorption is selective towards  $\text{S}_4^{2-}$  and  $\text{S}_6^{2-}$  species. The adsorption constants ( $k_{ads}$ ), calculated from adsorption isotherms based on Langmuir model assumptions, indicate that the adsorption strength appears to vary depending the adsorbent nature  $k_{ads}$  following the relative order 48 wt.% of  $\text{MoS}_2$  on KB # 32 wt.% of  $\text{MoS}_2$  on KB  $\gg$  Aerosil 200. To the best of our knowledge, no work in that direction has been performed yet to compare our results. Adsorption on the material surfaces and the disproportionation equilibrium are in competition. This study thus raises questions about the attribution of species in the literature. It highlights the complexities of these interactions, emphasizing the need for further research to better understand this multiphase system.

In terms of quantity of the adsorption capacity ( $N_{ads}$ ) depends on i) the nature of the adsorbent, thus establishing a maximum value of the number of moles of  $\text{Li}_2\text{S}_6$  adsorbed (surface saturation), which varies as follows : 48 wt.% of  $\text{MoS}_2$  on KB  $>$  Aerosil 200  $>$  32 wt.% of  $\text{MoS}_2$  on KB and ii) on the exposed surface. It has been demonstrated for  $\text{MoS}_2$ -KB that the adsorption capacity varies proportionally with the exposed surface of  $\text{MoS}_2$ . Therefore, an increased



number of accessible adsorption sites for similar MoS<sub>2</sub> nature (in slab length and stacking). One strategy to increase this exposed surface consist in tuning the MoS<sub>2</sub> loading supported on KB. Under another synthesis condition, the  $N_{ads}$  is also found to be improved after sulfidation under pure H<sub>2</sub>S conditions at 400°C with a post treatment under H<sub>2</sub> and N<sub>2</sub> at 300°C. By creating more truncated triangular MoS<sub>2</sub> monolayers, exhibiting more edges and corners than usual hexagonal morphology, the specific adsorption of polysulfides species is enhanced.

In addition, to the insights into the MoS<sub>2</sub> structure/LiPS adsorption, this quantitative approach enables to determine the appropriate weight adsorbent/sulfur ratio to be incorporated into electrode design to see the real impact of adsorbent on the electrochemical performances. S-MoS<sub>2</sub>-KB electrodes have been prepared with an appropriate weight adsorbent/sulfur ratio of 2-3 that theoretically enables to adsorb between 20 to 40% of the Li<sub>2</sub>S<sub>6</sub> and Li<sub>2</sub>S<sub>4</sub> produced. Electrochemical characterizations of these materials have subsequently revealed three main results: Firstly, the electrode formulation highlights the challenge of shaping an ink from a high carbon content and the remaining porous volume of S-MoS<sub>2</sub>-KB at 1.2 cm<sup>3</sup>.g<sup>-1</sup>. A series of optimizations lead to a final formulation composition of 58/2/40 wt.% composite active material/carbon black/CMC-SBR, with a CMC:SBR water soluble binder ratio of 10:30. A 3-step drying protocol is employed to achieve homogeneous electrodes, eliminating any issues of electrode peeling or cracking.

Secondly, MoS<sub>2</sub>-KB enables to enhance electrochemical capacity retention and an to increase Coulombic efficiency at C/10, reflecting a substantial reduction in LiPS shuttling due to the interactions between the adsorbent and polysulfides. This improvement in Coulombic efficiency is closely associated with the material's adsorption capacity and the number of active sites available for polysulfides adsorption. Under the following conditions, electrode with sulfur loading of 0.38 mg<sub>s</sub>.cm<sup>-2</sup> and E/S ratio of 100 μL.mg<sub>s</sub><sup>-1</sup>, the Li-S batteries were able to achieve without any failure a reversible capacity of 695 mAh.g<sup>-1</sup> with a Coulombic efficiency of 99.4 % after 60 cycles at C/10. Thirdly, it is demonstrated that the shape of the electrochemical curves is altered by the use of MoS<sub>2</sub>-KB, which suggests a reduction in the activation energy associated with Li<sub>2</sub>S<sub>2</sub>/Li<sub>2</sub>S nucleation.

The possible prospects for continuing this study can be divided into 3 key aspects: material, UV-Vis analysis and electrochemical study.

At material scale, further investigation can include the performance of temperature-programmed reduction (TPR) to assess the removal of  $H_2$  adsorbed from  $H_2S/H_2$  sulfidation gas at the surface of  $MoS_2$ , with a specific focus on the post-treatment under  $H_2$  and  $N_2$ . Additionally, new  $MoS_2$ -KB materials could be synthesized, characterized by high  $MoS_2$  loading and a greater fraction of truncated triangular  $MoS_2$ , as it has been demonstrated that the highest adsorption capacity has been associated with these two structures when considered separately.

For UV-Vis analysis, another preliminary study of  $Li_2S_8$  and  $Li_2S_4$  equivalent solutions is needed to accurately attribute the contributions of  $S_4^{2-}$ , determine the position of the  $S_8^{2-}$  contribution, and continue the work of estimating the concentrations of  $S_4^{2-}$  and  $S_8$  in solution. In addition, it will be interesting to continue the Multi Curve Resolution (MCR) study initiated (not presented in this manuscript) on the samples analyzed by UV-Vis to understand which LiPS vary collectively.

For electrochemical study, various prospects can be taken. Efforts can be made on improving the electrode formulation by reducing the binder content from 40 wt.% to less than 20 wt.%, aiming to both eliminate potential artifacts related to LiPS adsorption by polymer binders and enhance the energy density of the final electrode. New electrodes should be formulated to finalize the study, of  $MoS_2$ -Ketjenblack structure – electrochemical performance relationships with the samples obtained under the modification of sulfidation conditions. Furthermore, it is worth looking into higher sulfur loadings, around  $3 \text{ mg}\cdot\text{cm}^{-2}$ , to examine a more energy-dense system while maintaining the same  $MoS_2/S$  ratio, enabling an evaluation of cycling performance under these conditions more representative of commercial applications.



---

## References

---

1. Renewables now. Renewables 2021 - Global Status Report GLOBAL STATUS REPORT. Available at <https://www.ren21.net/reports/global-status-report/>.
2. Hannah Ritchie and Max Roser. Energy mix. Available at <https://ourworldindata.org/energy-mix>.
3. Jérôme Sabathier. A GLOBAL CAR MARKET ON A ROLLER COASTER. Available at [<https://www.ifpenergiesnouvelles.com/article/global-car-market-roller-coaster>] (2021).
4. International Energy Agency. WORLD ENERGY OUTLOOK 2019.
5. International Energy Agency. Innovation in Batteries and Electricity Storage. Technology report — September 2020.
6. Battery 2030. Battery 2030+ Roadmap, Inventing the sustainable batteries of the future.
7. Zhang, Q. *et al.* Sulfide-Based Solid-State Electrolytes: Synthesis, Stability, and Potential for All-Solid-State Batteries. *Advanced materials (Deerfield Beach, Fla.)* **31**, e1901131; 10.1002/adma.201901131 (2019).
8. Ji, X., Lee, K. T. & Nazar, L. F. A highly ordered nanostructured carbon-sulphur cathode for lithium-sulphur batteries. *Nature materials* **8**, 500–506; 10.1038/nmat2460 (2009).
9. Seh, Z. W., Sun, Y., Zhang, Q. & Cui, Y. Designing high-energy lithium-sulfur batteries. *Chemical Society reviews* **45**, 5605–5634; 10.1039/c5cs00410a (2016).
10. Wild, M. *Lithium Sulfur Batteries* (Wiley, 2019).
11. Guo, J. & Liu, J. A binder-free electrode architecture design for lithium–sulfur batteries: a review. *Nanoscale Adv.* **1**, 2104–2122; 10.1039/C9NA00040B (2019).
12. Huang, X. *et al.* Recent advances of hollow-structured sulfur cathodes for lithium–sulfur batteries. *Mater. Chem. Front.* **4**, 2517–2547; 10.1039/D0QM00303D (2020).
13. Wild, M. *et al.* Lithium sulfur batteries, a mechanistic review. *Energy Environ. Sci.* **8**, 3477–3494; 10.1039/C5EE01388G (2015).
14. Barchasz, C. *et al.* Lithium/sulfur cell discharge mechanism: an original approach for intermediate species identification. *Analytical chemistry* **84**, 3973–3980; 10.1021/ac2032244 (2012).
15. Ding, N., Li, X., Chien, S. W., Liu, Z. & Zong, Y. In situ monitoring the viscosity change of an electrolyte in a Li-S battery. *Chemical communications (Cambridge, England)* **53**, 10152–10155; 10.1039/c7cc04841f (2017).
16. Patel, M. U. M. & Dominko, R. Application of in operando UV/Vis spectroscopy in lithium-sulfur batteries. *ChemSusChem* **7**, 2167–2175; 10.1002/cssc.201402215 (2014).
17. Zhu, W. *et al.* Investigation of the reaction mechanism of lithium sulfur batteries in different electrolyte systems by in situ Raman spectroscopy and in situ X-ray diffraction. *Sustainable Energy Fuels* **1**, 737–747; 10.1039/C6SE00104A (2017).

18. Korff, D., Colclasure, A. M., Ha, Y., Smith, K. A. & DeCaluwe, S. C. Pathways Toward High-energy Li-sulfur Batteries, Identified via Multi-reaction Chemical Modeling. *J. Electrochem. Soc.* **169**, 10520; 10.1149/1945-7111/ac4541 (2022).
19. Peng, G. *et al.* New Insight into the Working Mechanism of Lithium-Sulfur Batteries under a Wide Temperature Range. *ACS applied materials & interfaces* **13**, 55007–55019; 10.1021/acsami.1c15975 (2021).
20. Zheng, D. *et al.* Investigation of the Li-S Battery Mechanism by Real-Time Monitoring of the Changes of Sulfur and Polysulfide Species during the Discharge and Charge. *ACS applied materials & interfaces* **9**, 4326–4332; 10.1021/acsami.6b08904 (2017).
21. Wang, Q. *et al.* Direct Observation of Sulfur Radicals as Reaction Media in Lithium Sulfur Batteries. *J. Electrochem. Soc.* **162**, A474-A478; 10.1149/2.0851503jes (2015).
22. Zheng, D. *et al.* The Progress of Li–S Batteries—Understanding of the Sulfur Redox Mechanism: Dissolved Polysulfide Ions in the Electrolytes. *Adv. Mater. Technol.* **3**, 1700233; 10.1002/admt.201700233 (2018).
23. Gupta, A. & Manthiram, A. Unifying the Clustering Kinetics of Lithium Polysulfides with the Nucleation Behavior of Li<sub>2</sub>S in Lithium-Sulfur Batteries. *Journal of materials chemistry. A* **9**, 13242–13251; 10.1039/D1TA02779D (2021).
24. Sadd, M. *et al.* Visualization of Dissolution-Precipitation Processes in Lithium–Sulfur Batteries. *Advanced Energy Materials*, 2103126; 10.1002/aenm.202103126 (2022).
25. Bruce, P. G., Freunberger, S. A., Hardwick, L. J. & Tarascon, J.-M. Li-O<sub>2</sub> and Li-S batteries with high energy storage. *Nature materials* **11**, 19–29; 10.1038/nmat3191 (2011).
26. Ellis, B. L., Lee, K. T. & Nazar, L. F. Positive Electrode Materials for Li-Ion and Li-Batteries. *Chem. Mater.* **22**, 691–714; 10.1021/cm902696j (2010).
27. Barghamadi, M., Kapoor, A. & Wen, C. A Review on Li-S Batteries as a High Efficiency Rechargeable Lithium Battery. *J. Electrochem. Soc.* **160**, A1256-A1263; 10.1149/2.096308jes (2013).
28. Cha, E., Patel, M., Bhoyate, S., Prasad, V. & Choi, W. Nanoengineering to achieve high efficiency practical lithium-sulfur batteries. *Nanoscale horizons* **5**, 808–831; 10.1039/c9nh00730j (2020).
29. Mammoottil Abraham, A., Kammampata, S. P., Ponnurangam, S. & Thangadurai, V. Efficient Synthesis and Characterization of Robust MoS<sub>2</sub> and S Cathode for Advanced Li-S Battery: Combined Experimental and Theoretical Studies. *ACS applied materials & interfaces* **11**, 35729–35737; 10.1021/acsami.9b11967 (2019).
30. Pang, Q., Liang, X., Kwok, C. Y. & Nazar, L. F. Advances in lithium–sulfur batteries based on multifunctional cathodes and electrolytes. *Nat Energy* **1**; 10.1038/nenergy.2016.132 (2016).
31. Ji, X., Lee, K. T. & Nazar, L. F. A highly ordered nanostructured carbon-sulphur cathode for lithium-sulphur batteries. *Nature materials* **8**, 500–506; 10.1038/nmat2460 (2009).
32. Liang, X. *et al.* Tuning Transition Metal Oxide-Sulfur Interactions for Long Life Lithium Sulfur Batteries: The “Goldilocks” Principle. *Adv. Energy Mater.* **6**, 1501636; 10.1002/aenm.201501636 (2016).

33. Xiao, L. *et al.* A soft approach to encapsulate sulfur: polyaniline nanotubes for lithium-sulfur batteries with long cycle life. *Advanced materials (Deerfield Beach, Fla.)* **24**, 1176–1181; 10.1002/adma.201103392 (2012).
34. Raulo, A. *et al.* Bio-inspired poly(3,4-ethylenedioxythiophene): Poly(styrene sulfonate)-sulfur@polyacrylonitrile electrospun nanofibers for lithium-sulfur batteries. *Journal of Power Sources* **431**, 250–258; 10.1016/j.jpowsour.2019.05.055 (2019).
35. Zheng, J. *et al.* Lewis acid-base interactions between polysulfides and metal organic framework in lithium sulfur batteries. *Nano letters* **14**, 2345–2352; 10.1021/nl404721h (2014).
36. Wang, P. *et al.* Emerging Catalysts to Promote Kinetics of Lithium–Sulfur Batteries. *Adv. Energy Mater.* **11**, 2002893; 10.1002/aenm.202002893 (2021).
37. Huang, C. *et al.* Multifunctional reaction interfaces for capture and boost conversion of polysulfide in lithium-sulfur batteries. *Electrochimica Acta* **334**, 135658; 10.1016/j.electacta.2020.135658 (2020).
38. Yuan, Z. *et al.* Powering Lithium-Sulfur Battery Performance by Propelling Polysulfide Redox at Sulfiphilic Hosts. *Nano letters* **16**, 519–527; 10.1021/acs.nanolett.5b04166 (2016).
39. Liu, Y., Cui, C., Liu, Y., Liu, W. & Wei, J. Application of MoS<sub>2</sub> in the cathode of lithium sulfur batteries. *RSC Adv.* **10**, 7384–7395; 10.1039/C9RA09769D (2020).
40. Chen, Z., Lv, W., Kang, F. & Li, J. Theoretical Investigation of the Electrochemical Performance of Transition Metal Nitrides for Lithium–Sulfur Batteries. *J. Phys. Chem. C* **123**, 25025–25030; 10.1021/acs.jpcc.9b04670 (2019).
41. Wu, F. *et al.* Boosting High-Performance in Lithium-Sulfur Batteries via Dilute Electrolyte. *Nano letters* **20**, 5391–5399; 10.1021/acs.nanolett.0c01778 (2020).
42. Liang, X., Rangom, Y., Kwok, C. Y., Pang, Q. & Nazar, L. F. Interwoven MXene Nanosheet/Carbon-Nanotube Composites as Li-S Cathode Hosts. *Advanced materials (Deerfield Beach, Fla.)* **29**; 10.1002/adma.201603040 (2017).
43. Rao, D. *et al.* Mechanism on the Improved Performance of Lithium Sulfur Batteries with MXene-Based Additives. *J. Phys. Chem. C* **121**, 11047–11054; 10.1021/acs.jpcc.7b00492 (2017).
44. Wei Seh, Z. *et al.* Sulphur-TiO<sub>2</sub> yolk-shell nanoarchitecture with internal void space for long-cycle lithium-sulphur batteries. *Nature communications* **4**, 1331; 10.1038/ncomms2327 (2013).
45. Holoubek, J. *et al.* Low-Cost Li||SPAN Batteries Enabled by Sustained Additive Release. *ACS Appl. Energy Mater.* **4**, 6422–6429; 10.1021/acsaem.1c00257 (2021).
46. Chen, Y. *et al.* Advances in Lithium-Sulfur Batteries: From Academic Research to Commercial Viability. *Advanced materials (Deerfield Beach, Fla.)*, e2003666; 10.1002/adma.202003666 (2021).
47. Li, C., Liu, R., Xiao, Y., Cao, F. & Zhang, H. Recent progress of separators in lithium-sulfur batteries. *Energy Storage Materials* **40**, 439–460; 10.1016/j.ensm.2021.05.034 (2021).

48. Rezan Demir-Cakan. *Li-S Batteries The Challenges, Chemistry, Materials, and Future Perspectives by Rezan Demir-Cakan* ,
49. Bonnicksen, P. & Muldoon, J. The Dr Jekyll and Mr Hyde of lithium sulfur batteries. *Energy Environ. Sci.* **13**, 4808–4833; 10.1039/D0EE02797A (2020).
50. Kim, J., Elabd, A., Chung, S.-Y., Coskun, A. & Choi, J. W. Covalent Triazine Frameworks Incorporating Charged Polypyrrole Channels for High-Performance Lithium–Sulfur Batteries. *Chem. Mater.* **32**, 4185–4193; 10.1021/acs.chemmater.0c00246 (2020).
51. Wu, D. S. *et al.* Quantitative investigation of polysulfide adsorption capability of candidate materials for Li-S batteries. *Energy Storage Materials* **13**, 241–246; 10.1016/j.ensm.2018.01.020 (2018).
52. Hu, X. *et al.* Uniform loading of ultrathin MoS<sub>2</sub> nanosheets on hollow carbon spheres with mesoporous walls as efficient sulfur hosts for promising lithium-sulfur batteries. *Journal of Alloys and Compounds* **965**, 171427; 10.1016/j.jallcom.2023.171427 (2023).
53. Tonin, G. *et al.* Operando investigation of the lithium/sulfur battery system by coupled X-ray absorption tomography and X-ray diffraction computed tomography. *Journal of Power Sources* **468**, 228287; 10.1016/j.jpowsour.2020.228287 (2020).
54. Wang, D. R. *et al.* Rate Constants of Electrochemical Reactions in a Lithium-Sulfur Cell Determined by Operando X-ray Absorption Spectroscopy. *J. Electrochem. Soc.* **165**, A3487-A3495; 10.1149/2.0981814jes (2018).
55. Quilty, C. D. *et al.* Ex Situ and Operando XRD and XAS Analysis of MoS<sub>2</sub> : A Lithiation Study of Bulk and Nanosheet Materials. *ACS Appl. Energy Mater.* **2**, 7635–7646; 10.1021/acsaem.9b01538 (2019).
56. Guo, Q., Lau, K. C. & Pandey, R. A XANES study of lithium polysulfide solids: a first-principles study. *Mater. Adv.* **2**, 6403–6410; 10.1039/D1MA00450F (2021).
57. Wang, H. *et al.* In Situ NMR Observation of the Temporal Speciation of Lithium Sulfur Batteries during Electrochemical Cycling. *J. Phys. Chem. C* **121**, 6011–6017; 10.1021/acs.jpcc.7b01922 (2017).
58. Hannauer, J. *et al.* The Quest for Polysulfides in Lithium-Sulfur Battery Electrolytes: An Operando Confocal Raman Spectroscopy Study. *Chemphyschem : a European journal of chemical physics and physical chemistry* **16**, 2755–2759; 10.1002/cphc.201500448 (2015).
59. Hagen, M. *et al.* In-Situ Raman Investigation of Polysulfide Formation in Li-S Cells. *J. Electrochem. Soc.* **160**, A1205-A1214; 10.1149/2.045308jes (2013).
60. Conder, J. *et al.* Direct observation of lithium polysulfides in lithium–sulfur batteries using operando X-ray diffraction. *Nat Energy* **2**; 10.1038/nenergy.2017.69 (2017).
61. Zhou, G., Zhao, Y. & Manthiram, A. Dual-Confined Flexible Sulfur Cathodes Encapsulated in Nitrogen-Doped Double-Shelled Hollow Carbon Spheres and Wrapped with Graphene for Li-S Batteries. *Adv. Energy Mater.* **5**, 1402263; 10.1002/aenm.201402263 (2015).

62. Zou, Q. & Lu, Y.-C. Solvent-Dictated Lithium Sulfur Redox Reactions: An Operando UV-vis Spectroscopic Study. *The journal of physical chemistry letters* **7**, 1518–1525; 10.1021/acs.jpcclett.6b00228 (2016).
63. He, Q., Freiberg, A. T. S., Patel, M. U. M., Qian, S. & Gasteiger, H. A. Operando Identification of Liquid Intermediates in Lithium–Sulfur Batteries via Transmission UV–vis Spectroscopy. *J. Electrochem. Soc.* **167**, 80508; 10.1149/1945-7111/ab8645 (2020).
64. Chianelli, R. R., Berhault, G. & Torres, B. Unsupported transition metal sulfide catalysts: 100 years of science and application. *Catalysis Today* **147**, 275–286; 10.1016/j.cattod.2008.09.041 (2009).
65. Mao, J., Wang, Y., Zheng, Z. & Deng, D. The rise of two-dimensional MoS<sub>2</sub> for catalysis. *Front. Phys.* **13**; 10.1007/s11467-018-0812-0 (2018).
66. Zhang, W., Zhang, P., Su, Z. & Wei, G. Synthesis and sensor applications of MoS<sub>2</sub>-based nanocomposites. *Nanoscale* **7**, 18364–18378; 10.1039/c5nr06121k (2015).
67. Vazirisereshk, M. R., Martini, A., Strubbe, D. A. & Baykara, M. Z. Solid Lubrication with MoS<sub>2</sub>: A Review. *Lubricants* **7**, 57; 10.3390/lubricants7070057 (2019).
68. Stephenson, T., Li, Z., Olsen, B. & Mitlin, D. Lithium ion battery applications of molybdenum disulfide (MoS<sub>2</sub>) nanocomposites. *Energy Environ. Sci.* **7**, 209–231; 10.1039/C3EE42591F (2014).
69. Dai, H., Tang, M., Huang, J. & Wang, Z. A Series of Molecule-Intercalated MoS<sub>2</sub> as Anode Materials for Sodium Ion Batteries. *ACS applied materials & interfaces* **13**, 10870–10877; 10.1021/acsami.0c21106 (2021).
70. Bara, C. *et al.* Surface-dependent sulfidation and orientation of MoS<sub>2</sub> slabs on alumina-supported model hydrodesulfurization catalysts. *Journal of Catalysis* **344**, 591–605; 10.1016/j.jcat.2016.10.001 (2016).
71. Chen, J., Dominguez Garcia, E., Oliviero, E., Oliviero, L. & Maugé, F. Effect of high pressure sulfidation on the morphology and reactivity of MoS<sub>2</sub> slabs on MoS<sub>2</sub>/Al<sub>2</sub>O<sub>3</sub> catalyst prepared with citric acid. *Journal of Catalysis* **339**, 153–162; 10.1016/j.jcat.2016.04.010 (2016).
72. Oliviero, L., Travert, A., Dominguez Garcia, E., Chen, J. & Maugé, F. Catalysis by sulfides: Advanced IR/CO spectroscopy for the identification of the most active sites in hydrodesulfurization reactions. *Journal of Catalysis* **403**, 87–97; 10.1016/j.jcat.2021.02.018 (2021).
73. Ossila. Molybdenum Disulfide (MoS<sub>2</sub>): Theory & Applications. Available at <https://www.ossila.com/pages/molybdenum-disulfide-mos2>.
74. Merki, D., Vrabel, H., Rovelli, L., Fierro, S. & Hu, X. Fe, Co, and Ni ions promote the catalytic activity of amorphous molybdenum sulfide films for hydrogen evolution. *Chem. Sci.* **3**, 2515; 10.1039/c2sc20539d (2012).
75. Hakala, M., Kronberg, R. & Laasonen, K. Hydrogen adsorption on doped MoS<sub>2</sub> nanostructures. *Scientific reports* **7**, 15243; 10.1038/s41598-017-15622-z (2017).



76. Samy, O., Zeng, S., Birowosuto, M. D. & El Moutaouakil, A. A Review on MoS<sub>2</sub> Properties, Synthesis, Sensing Applications and Challenges. *Crystals* **11**, 355; 10.3390/cryst11040355 (2021).
77. Xu, W., Yan, S. & Qiao, W. Magnetism in monolayer 1T-MoS<sub>2</sub> and 1T-MoS<sub>2</sub> H tuned by strain. *RSC Adv.* **8**, 8435–8441; 10.1039/C7RA10304B (2018).
78. Jayabal, S. *et al.* Understanding the high-electrocatalytic performance of two-dimensional MoS<sub>2</sub> nanosheets and their composite materials. *J. Mater. Chem. A* **5**, 24540–24563; 10.1039/C7TA08327K (2017).
79. Bolar, S., Shit, S., Murmu, N. C., Samanta, P. & Kuila, T. Activation Strategy of MoS<sub>2</sub> as HER Electrocatalyst through Doping-Induced Lattice Strain, Band Gap Engineering, and Active Crystal Plane Design. *ACS applied materials & interfaces* **13**, 765–780; 10.1021/acsami.0c20500 (2021).
80. Joyner, J. *et al.* Graphene Supported MoS<sub>2</sub> Structures with High Defect Density for an Efficient HER Electrocatalysts. *ACS applied materials & interfaces* **12**, 12629–12638; 10.1021/acsami.9b17713 (2020).
81. Hernandez Ruiz, K. *et al.* Effect of microstructure on HER catalytic properties of MoS<sub>2</sub> vertically standing nanosheets. *Journal of Alloys and Compounds* **747**, 100–108; 10.1016/j.jallcom.2018.02.347 (2018).
82. Sun, Y., Alimohammadi, F., Zhang, D. & Guo, G. Enabling Colloidal Synthesis of Edge-Oriented MoS<sub>2</sub> with Expanded Interlayer Spacing for Enhanced HER Catalysis. *Nano letters* **17**, 1963–1969; 10.1021/acs.nanolett.6b05346 (2017).
83. Palencia-Ruiz, S., Uzio, D., Legens, C., Laurenti, D. & Afanasiev, P. Stability and catalytic properties of 1T-MoS<sub>2</sub> obtained via solvothermal synthesis. *Applied Catalysis A: General* **626**, 118355; 10.1016/j.apcata.2021.118355 (2021).
84. H. Tributsch. Layer-Type Transition Metal Dichalcogenides — a New Class of Electrodes for Electrochemical Solar Cells. *Berich. Bunsen Gesell* **81** (1977).
85. van Deelen, T. W., Hernández Mejía, C. & Jong, K. P. de. Control of metal-support interactions in heterogeneous catalysts to enhance activity and selectivity. *Nat Catal* **2**, 955–970; 10.1038/s41929-019-0364-x (2019).
86. Bara. Catalyseurs d'hydrotraitement à base de Mo supporté sur alumine : genèse de la phase active et effet de support par une approche science des surfaces, 14 octobre 2015.
87. Araki, Y., Honna, K. & Shimada, H. Formation and Catalytic Properties of Edge-Bonded Molybdenum Sulfide Catalysts on TiO<sub>2</sub>. *Journal of Catalysis* **207**, 361–370; 10.1006/jcat.2002.3534 (2002).
88. Wang, H. *et al.* MoSe<sub>2</sub> and WSe<sub>2</sub> nanofilms with vertically aligned molecular layers on curved and rough surfaces. *Nano letters* **13**, 3426–3433; 10.1021/nl401944f (2013).
89. Wang, H. *et al.* High electrochemical selectivity of edge versus terrace sites in two-dimensional layered MoS<sub>2</sub> materials. *Nano letters* **14**, 7138–7144; 10.1021/nl503730c (2014).

90. Zhang, C. *et al.* Morphology-performance relation of (Co)MoS<sub>2</sub> catalysts in the hydrodesulfurization of FCC gasoline. *Applied Catalysis A: General* **556**, 20–28; 10.1016/j.apcata.2018.02.026 (2018).
91. Li, M., Li, H., Jiang, F., Chu, Y. & Nie, H. The relation between morphology of (Co)MoS<sub>2</sub> phases and selective hydrodesulfurization for CoMo catalysts. *Catalysis Today* **149**, 35–39; 10.1016/j.cattod.2009.03.017 (2010).
92. Rasamani, K. D., Alimohammadi, F. & Sun, Y. Interlayer-expanded MoS<sub>2</sub>. *Materials Today* **20**, 83–91; 10.1016/j.mattod.2016.10.004 (2017).
93. Li, L. *et al.* Role of Sulfur Vacancies and Undercoordinated Mo Regions in MoS<sub>2</sub> Nanosheets toward the Evolution of Hydrogen. *ACS nano* **13**, 6824–6834; 10.1021/acsnano.9b01583 (2019).
94. Paul, J.-F. & Payen, E. Vacancy Formation on MoS<sub>2</sub> Hydrodesulfurization Catalyst: DFT Study of the Mechanism. *J. Phys. Chem. B* **107**, 4057–4064; 10.1021/jp027668f (2003).
95. Baubet, B., Devers, E., Hugon, A., Leclerc, E. & Afanasiev, P. The influence of MoS<sub>2</sub> slab 2D morphology and edge state on the properties of alumina-supported molybdenum sulfide catalysts. *Applied Catalysis A: General* **487**, 72–81; 10.1016/j.apcata.2014.09.010 (2014).
96. Li, Y. *et al.* Selective Preparation of 1T- and 2H-Phase MoS<sub>2</sub> Nanosheets with Abundant Monolayer Structure and Their Applications in Energy Storage Devices. *ACS Appl. Energy Mater.* **3**, 998–1009; 10.1021/acsaem.9b02043 (2020).
97. Dominguez Garcia, E., Chen, J., Oliviero, E., Oliviero, L. & Maugé, F. New insight into the support effect on HDS catalysts: evidence for the role of Mo-support interaction on the MoS<sub>2</sub> slab morphology. *Applied Catalysis B: Environmental* **260**, 117975; 10.1016/j.apcatb.2019.117975 (2020).
98. Xu, Z.-L., Kim, J.-K. & Kang, K. Carbon nanomaterials for advanced lithium sulfur batteries. *Nano Today* **19**, 84–107; 10.1016/j.nantod.2018.02.006 (2018).
99. MSE Suppliers. Lithium Ion Battery Supplies, Equipment, & Materials - Carbone C. Available at <https://www.msесupplies.com/collections/lithium-ion-battery-materials/carbon-c>.
100. Jozwiuk, A., Sommer, H., Janek, J. & Brezesinski, T. Fair performance comparison of different carbon blacks in lithium–sulfur batteries with practical mass loadings – Simple design competes with complex cathode architecture. *Journal of Power Sources* **296**, 454–461; 10.1016/j.jpowsour.2015.07.070 (2015).
101. Tengen, B. *et al.* Immobilizing Poly(vinylphenothiazine) in Ketjenblack-Based Electrodes to Access its Full Specific Capacity as Battery Electrode Material. *Adv Funct Materials* **33**; 10.1002/adfm.202210512 (2023).
102. Fuelcell store. Carbon Black - Ketjenblack EC-600JD. Available at <https://www.fuelcellstore.com/ketjenblack-carbon-black-ec600jd>.
103. Denis Uzio. caracterisation texturale cata.

104. Neffati, R. & Brokken-Zijp, J. Structure and porosity of conductive carbon blacks. *Materials Chemistry and Physics* **260**, 124177; 10.1016/j.matchemphys.2020.124177 (2021).
105. Lion Specialty Chemicals Co. *Ketjenblack - Product Datasheet* ,
106. Häcker, J. *et al.* Operando UV/vis Spectroscopy Providing Insights into the Sulfur and Polysulfide Dissolution in Magnesium–Sulfur Batteries. *ACS Energy Lett.* **7**, 1–9; 10.1021/acseenergylett.1c02152 (2022).
107. Cui, B., Cai, X., Wang, W., Saha, P. & Wang, G. Nano storage-boxes constructed by the vertical growth of MoS<sub>2</sub> on graphene for high-performance Li-S batteries. *Journal of Energy Chemistry* **66**, 91–99; 10.1016/j.jechem.2021.06.035 (2022).
108. Maslova, O. A., Ammar, M. R., Guimbretière, G., Rouzaud, J.-N. & Simon, P. Determination of crystallite size in polished graphitized carbon by Raman spectroscopy. *Phys. Rev. B* **86**; 10.1103/PhysRevB.86.134205 (2012).
109. J. Robertson. Diamond-like amorphous carbon. *Material Science and Engineering R* **37** (2002).
110. Metzger, M. *et al.* Evaluating the High-Voltage Stability of Conductive Carbon and Ethylene Carbonate with Various Lithium Salts. *J. Electrochem. Soc.* **167**, 160522; 10.1149/1945-7111/abcabd (2020).
111. Moon, K. *et al.* A New Synthesis of Highly Dispersed MoS<sub>2</sub> Nanoparticles on Ketjenblack Carbon for Sustainable Oxygen Reduction Reaction. *Catal Lett*; 10.1007/s10562-021-03641-5 (2021).
112. Ahn, S. *et al.* Facile fabrication of sulfur/Ketjenblack-PEDOT:PSS composite as a cathode with improved cycling performance for lithium sulfur batteries. *Chemical Physics Letters* **749**, 137426; 10.1016/j.cplett.2020.137426 (2020).
113. Wang, Y. *et al.* Gadolinium oxide nanorods decorated Ketjen black@sulfur composites as functional catalyzing polysulfides conversion in lithium/sulfur batteries. *Intl J of Energy Research*; 10.1002/er.8262 (2022).
114. Zhao, X., Ahn, H.-J., Kim, K.-W., Cho, K.-K. & Ahn, J.-H. Polyaniline-Coated Mesoporous Carbon/Sulfur Composites for Advanced Lithium Sulfur Batteries. *J. Phys. Chem. C* **119**, 7996–8003; 10.1021/jp511846z (2015).
115. Gandubert, A. D., Legens, C., Guillaume, D. & Payen, E. X-ray photoelectron spectroscopy surface quantification of sulfided CoMoP catalysts. Relation between activity and promoted sites. Part II: Influence of the sulfidation temperature. *Surface & Interface Analysis* **38**, 206–209; 10.1002/sia.2249 (2006).
116. Zhang, C. *et al.* MoS<sub>2</sub> Decorated Carbon Nanofibers as Efficient and Durable Electrocatalyst for Hydrogen Evolution Reaction. *C* **3**, 33; 10.3390/c3040033 (2017).
117. Xue, N. & Diao, P. Composite of Few-Layered MoS<sub>2</sub> Grown on Carbon Black: Tuning the Ratio of Terminal to Total Sulfur in MoS<sub>2</sub> for Hydrogen Evolution Reaction. *J. Phys. Chem. C* **121**, 14413–14425; 10.1021/acs.jpcc.7b02522 (2017).

118. Afanasiev, P. & Lorentz, C. Oxidation of Nanodispersed MoS<sub>2</sub> in Ambient Air: The Products and the Mechanistic Steps. *J. Phys. Chem. C* **123**, 7486–7494; 10.1021/acs.jpcc.9b01682 (2019).
119. Wang, B., Xia, Y., Wang, G., Zhou, Y. & Wang, H. Core shell MoS<sub>2</sub>/C nanospheres embedded in foam-like carbon sheets composite with an interconnected macroporous structure as stable and high-capacity anodes for sodium ion batteries. *Chemical Engineering Journal* **309**, 417–425; 10.1016/j.cej.2016.10.073 (2017).
120. Lee, C. *et al.* Anomalous lattice vibrations of single- and few-layer MoS<sub>2</sub>. *ACS nano* **4**, 2695–2700; 10.1021/nn1003937 (2010).
121. Jiang, S. *et al.* MoS<sub>2</sub>-Coated N-doped Mesoporous Carbon Spherical Composite Cathode and CNT/Chitosan Modified Separator for Advanced Lithium Sulfur Batteries. *ACS Sustainable Chem. Eng.* **6**, 16828–16837; 10.1021/acssuschemeng.8b04157 (2018).
122. O'Brien, M., Scheuschner, N., Maultzsch, J., Duesberg, G. S. & McEvoy, N. Raman Spectroscopy of Suspended MoS<sub>2</sub>. *Physica Status Solidi (b)* **254**; 10.1002/pssb.201700218 (2017).
123. Zhang, X. *et al.* Phonon and Raman scattering of two-dimensional transition metal dichalcogenides from monolayer, multilayer to bulk material. *Chemical Society reviews* **44**, 2757–2785; 10.1039/c4cs00282b (2015).
124. Blanco, É., Afanasiev, P., Berhault, G., Uzio, D. & Loridant, S. Resonance Raman spectroscopy as a probe of the crystallite size of MoS<sub>2</sub> nanoparticles. *Comptes Rendus Chimie* **19**, 1310–1314; 10.1016/j.crci.2015.08.014 (2016).
125. Baubet, B. *et al.* Quantitative Two-Dimensional (2D) Morphology–Selectivity Relationship of CoMoS Nanolayers: A Combined High-Resolution High-Angle Annular Dark Field Scanning Transmission Electron Microscopy (HR HAADF-STEM) and Density Functional Theory (DFT) Study. *ACS Catal.* **6**, 1081–1092; 10.1021/acscatal.5b02628 (2016).
126. S. KASZTELAN, H. TOULHOAT, J. GRIMBLLOT, J.P. BONNELLE. A GEOMETRICAL MODEL OF THE ACTIVE PHASE OF HYDROTREATING CATALYSTS. *Applied Catalysis* **13** (1984).
127. Kim, K.-D. & Lee, Y.-K. Active phase of dispersed MoS<sub>2</sub> catalysts for slurry phase hydrocracking of vacuum residue. *Journal of Catalysis* **369**, 111–121; 10.1016/j.jcat.2018.10.013 (2019).
128. Afanasiev, P. The influence of reducing and sulfiding conditions on the properties of unsupported MoS<sub>2</sub>-based catalysts. *Journal of Catalysis* **269**, 269–280; 10.1016/j.jcat.2009.11.004 (2010).
129. Kim, J. W., Seo, G., Bong, S. & Lee, J. Improved Redox Reaction of Lithium Polysulfides on the Interfacial Boundary of Polar CoC<sub>2</sub>O<sub>4</sub> as a Polysulfide Catenator for a High-Capacity Lithium-Sulfur Battery. *ChemSusChem* **14**, 876–883; 10.1002/cssc.202002140 (2021).
130. Huang, Y. *et al.* A saccharide-based binder for efficient polysulfide regulations in Li-S batteries. *Nature communications* **12**, 5375; 10.1038/s41467-021-25612-5 (2021).

131. Liu, Y. *et al.* Electrolyte solutions design for lithium-sulfur batteries. *Joule* **5**, 2323–2364; 10.1016/j.joule.2021.06.009 (2021).
132. Andrei, P., Shen, C. & Zheng, J. P. Theoretical and experimental analysis of precipitation and solubility effects in lithium-sulfur batteries. *Electrochimica Acta* **284**, 469–484; 10.1016/j.electacta.2018.07.045 (2018).
133. Zheng, D., Zhang, X. & Qu, D. Quantitative Chromatographic Determination of Dissolved Elemental Sulfur in the Non-Aqueous Electrolyte for Lithium-Sulfur Batteries. *Journal of The Electrochemical Society* **Volume 162**.
134. ROBBA Alice. Développement et compréhension des mécanismes électrochimiques des accumulateurs Lithium-ion/Soufre, 2016.
135. Bieker, G. *et al.* Influence of cations in lithium and magnesium polysulphide solutions: dependence of the solvent chemistry. *Physical chemistry chemical physics : PCCP* **19**, 11152–11162; 10.1039/c7cp01238a (2017).
136. J.Badoz-Lambling, R.Bonnaterre, G.Cauquis, M.Delamar, G.Demange. La reduction du soufre en milieu organique. *Electrochemical Acta* **Volume 21, Issue 2** (1976).
137. Johann Mathias and Gerhard Wannemachier. Basic Characteristics and Applications of Aerosil. *Journal of colloid and interface science* **125** (1988).
138. Wujcik, K. H. *et al.* Lithium Polysulfide Radical Anions in Ether-Based Solvents. *J. Phys. Chem. C* **120**, 18403–18410; 10.1021/acs.jpcc.6b04264 (2016).
139. Françoise Rouquerol, Jean Rouquerol, Kenneth Sing. *Adsorption by Powders and Porous Solids. Principles, Methodology and Applications* (1999).
140. Luo, J. & Zheng, J. Metal sulfide MoS<sub>2</sub> as efficient polysulfide adsorber for high electrochemical performance lithium-sulfur batteries. *Ionics* **26**, 3809–3814; 10.1007/s11581-020-03571-z (2020).
141. Zhang, Q. *et al.* Molybdenum trisulfide based anionic redox driven chemistry enabling high-performance all-solid-state lithium metal batteries. *Energy Storage Materials* **23**, 168–180; 10.1016/j.ensm.2019.05.015 (2019).
142. Zhang, Y., He, T., Liu, G., Zu, L. & Yang, J. One-pot mass preparation of MoS<sub>2</sub>/C aerogels for high-performance supercapacitors and lithium-ion batteries. *Nanoscale* **9**, 10059–10066; 10.1039/c7nr03187d (2017).
143. Li, L., Ma, Z. & Li, Y. Accurate determination of optimal sulfur content in mesoporous carbon hosts for high-capacity stable lithium-sulfur batteries. *Carbon* **197**, 200–208; 10.1016/j.carbon.2022.06.036 (2022).
144. Lin, H. *et al.* Electrocatalysis of polysulfide conversion by sulfur-deficient MoS<sub>2</sub> nanoflakes for lithium–sulfur batteries. *Energy Environ. Sci.* **10**, 1476–1486; 10.1039/C7EE01047H (2017).
145. Ko, Y.-C. *et al.* Interconnected Microporous and Mesoporous Carbon Derived from Pitch for Lithium–Sulfur Batteries. *ACS Sustainable Chem. Eng.* **10**, 4462–4472; 10.1021/acssuschemeng.1c08196 (2022).

146. Hong, Y. *et al.* A high performance Li/S cell cathode with hierarchical architecture composed of ketjenblack@mesoporous carbon/sulfur hybrid. *Ionics* **26**, 1119–1127; 10.1007/s11581-019-03285-x (2020).
147. Park, J. H., Kim, S. H. & Ahn, K. H. Role of carboxymethyl cellulose binder and its effect on the preparation process of anode slurries for Li-ion batteries. *Colloids and Surfaces A: Physicochemical and Engineering Aspects* **664**, 131130; 10.1016/j.colsurfa.2023.131130 (2023).
148. Wang, R. *et al.* Effect of Different Binders on the Electrochemical Performance of Metal Oxide Anode for Lithium-Ion Batteries. *Nanoscale research letters* **12**, 575; 10.1186/s11671-017-2348-6 (2017).
149. Zeng, J., Fu, N., Wang, X., Zhou, A. & Yang, Z. Multipath conduction and large capacity silicon-based anodes for high stabilizing lithium-ion batteries. *Applied Surface Science* **557**, 149860; 10.1016/j.apsusc.2021.149860 (2021).
150. Cuisinier, M. *et al.* Sulfur Speciation in Li–S Batteries Determined by Operando X-ray Absorption Spectroscopy. *J. Phys. Chem. Lett.* **4**, 3227–3232; 10.1021/jz401763d (2013).
151. Robba, A. *et al.* Fingerprinting Mean Composition of Lithium Polysulfide Standard Solutions by Applying High-Energy Resolution Fluorescence Detected X-ray Absorption Spectroscopy. *The journal of physical chemistry letters* **11**, 5446–5450; 10.1021/acs.jpcclett.0c01120 (2020).
152. Fan, F. Y. & Chiang, Y.-M. Electrodeposition Kinetics in Li-S Batteries: Effects of Low Electrolyte/Sulfur Ratios and Deposition Surface Composition. *J. Electrochem. Soc.* **164**, A917-A922; 10.1149/2.0051706jes (2017).
153. Chen, Z.-X. *et al.* Cathode Kinetics Evaluation in Lean-Electrolyte Lithium-Sulfur Batteries. *Journal of the American Chemical Society* **145**, 16449–16457; 10.1021/jacs.3c02786 (2023).
154. Talaie, E. *et al.* Methods and Protocols for Electrochemical Energy Storage Materials Research. *Chem. Mater.* **29**, 90–105; 10.1021/acs.chemmater.6b02726 (2017).
155. Waluś, S., Barchasz, C., Bouchet, R. & Alloin, F. Electrochemical impedance spectroscopy study of lithium–sulfur batteries: Useful technique to reveal the Li/S electrochemical mechanism. *Electrochimica Acta* **359**, 136944; 10.1016/j.electacta.2020.136944 (2020).
156. Conder, J. *et al.* Electrochemical impedance spectroscopy of a Li–S battery: Part 1. Influence of the electrode and electrolyte compositions on the impedance of symmetric cells. *Electrochimica Acta* **244**, 61–68; 10.1016/j.electacta.2017.05.041 (2017).
157. Waluś, S., Robba, A., Bouchet, R., Barchasz, C. & Alloin, F. Influence of the binder and preparation process on the positive electrode electrochemical response and Li/S system performances. *Electrochimica Acta* **210**, 492–501; 10.1016/j.electacta.2016.05.130 (2016).
158. Rosso, M. *et al.* Dendrite short-circuit and fuse effect on Li/polymer/Li cells. *Electrochimica Acta* **51**, 5334–5340; 10.1016/j.electacta.2006.02.004 (2006).

159. Abraham, A. *et al.* Defect Control in the Synthesis of 2 D MoS<sub>2</sub> Nanosheets: Polysulfide Trapping in Composite Sulfur Cathodes for Li-S Batteries. *ChemSusChem* **13**, 1517–1528; 10.1002/cssc.201903028 (2020).
160. He, J. *et al.* Freestanding 1T MoS<sub>2</sub>/graphene heterostructures as a highly efficient electrocatalyst for lithium polysulfides in Li–S batteries. *Energy Environ. Sci.* **12**, 344–350; 10.1039/C8EE03252A (2019).
161. Liu, M. *et al.* Propelling Polysulfide Conversion by Defect-Rich MoS<sub>2</sub> Nanosheets for High-Performance Lithium-Sulfur Batteries. *ACS applied materials & interfaces* **11**, 20788–20795; 10.1021/acsami.9b03011 (2019).
162. Hu, L. *et al.* A highly efficient double-hierarchical sulfur host for advanced lithium-sulfur batteries. *Chemical science* **9**, 666–675; 10.1039/c7sc03960c (2018).
163. Zhao, Y. *et al.* Encapsulation of Few-Layer MoS<sub>2</sub> in the Pores of Mesoporous Carbon Hollow Spheres for Lithium-Sulfur Batteries. *Nanomaterials (Basel, Switzerland)* **9**; 10.3390/nano9091247 (2019).
164. Rouquerol, F., Rouquerol, J. & Sing, K. S. *Adsorption by powders and porous solids. Principles, methodology and applications* (Academic Press, San Diego, London, Boston etc., 1999).

**Appendices—**

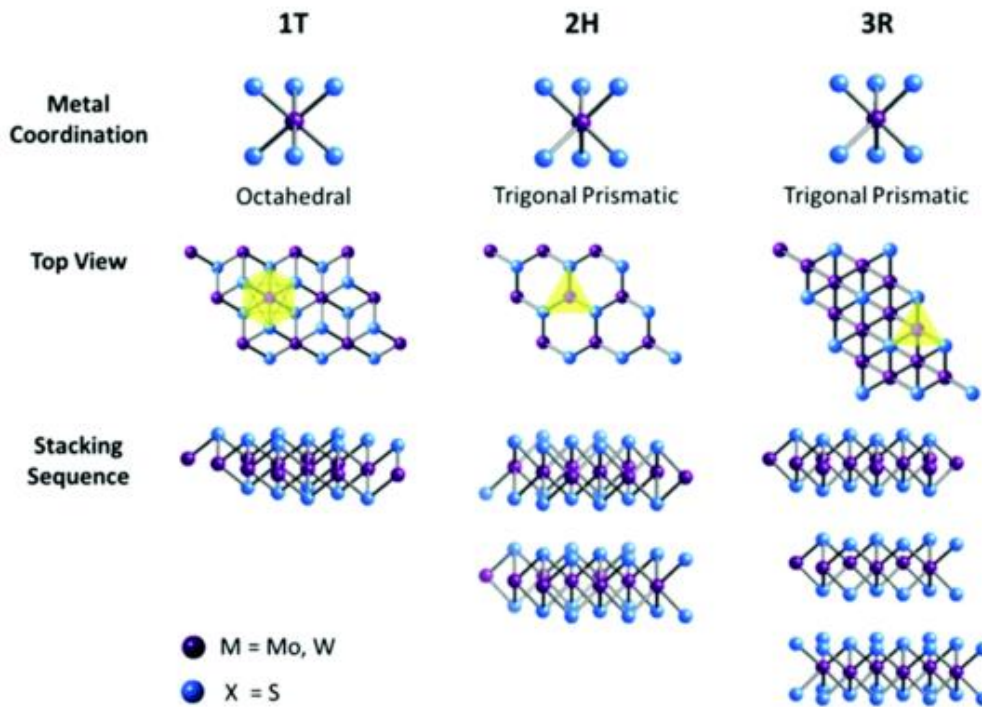
---





## Appendix A - Comparison between different MoS<sub>2</sub> polytypes

a



b

	1T	2H	3R
<b>Structure Coordination</b>	Octahedral	Trigonal Prismatic	Trigonal Prismatic
Lattice parameters	a = 3.17 Å, c = 5.99 Å and an edge sharing octahedral [34]	a = 3.15 Å, c = 12.30 Å [34]	a = 3.17 Å, c = 18.38 Å [34]
property	paramagnetic and metallic	Semiconducting	
Electrical conductivity	10 <sup>5</sup> times higher than 2H phase	Low (~0.1 S/m)	

**Figure A-1. MoS<sub>2</sub> 1T, 2H, 3R polytypes a) Coordination and stacking b) Lattice parameters and properties <sup>76</sup>**



## Appendix B - Experimental part

---

This appendix describes the techniques used to characterize the samples. Each paragraph is structured to describe the analytical method's principle and the conditions for its implementation during the study in order to provide sufficient information for the procedures to be replicated. The last part of this experimental appendix is dedicated to the synthesis protocol used to obtain unsupported MoS<sub>2</sub> used as reference in the chapter III to conduct the UV-Vis study.

### 1.1 Material characterization

#### 1.1.1 Elemental analysis

##### *CHNS*

CHNS analysis is used to measure carbon, hydrogen, nitrogen and sulfur elemental concentrations in a given sample. Samples are burned at 920°C to release gases under oxygen atmosphere. The gas mixture then passes through a chromatography column, which separates the gaseous products obtained during combustion: CO<sub>2</sub>, H<sub>2</sub>O, N<sub>2</sub> and SO<sub>2</sub>.

The elemental composition is performed using Thermo scientific Flash 2000 CHNS Analyzer. Powders (~ 1-2 mg) are previously crushed and sieved < 60 μm. Two acquisitions are made for each sample in an aluminum holder.

##### *X-ray fluorescence*

X-ray fluorescence (XRF) analysis is a method based on the interactions of matter with X-ray radiation. When matter is bombarded with X-rays, it re-emits energy X-ray fluorescence. The X-ray spectrum emitted by the material holds unique characteristics tied to the sample's composition. By analyzing this spectrum, it becomes possible to determine the elemental composition, specifically the mass concentrations of elements. The percentage of molybdenum, sulfur and phosphorus are determined by semi-quantitative X-ray fluorescence using Thermo Perform'X.

Powders (~ 1g) are previously crushed and sieved < 60 μm before acquisition performed under air.

### *Thermogravimetric analysis*

Thermogravimetric analysis (TGA) is a quantitative analysis based on the measurement of alterations in a substance's mass as it undergoes continuous heating to elevated temperatures and controlled atmosphere.

It is performed to determine the content of sulfur inside S@Mo@KB as an alternative of CHNS when needed and to quantify sulfur electrode content.

Measurements are carried out in the temperature range of 30–500°C at a heating rate of 10°C min<sup>-1</sup> under N<sub>2</sub> atmosphere. Samples are prepared inside argon-filled glove box and are exposed to air only few seconds before launching TGA instrument.

#### **1.1.2 Morphology analysis**

##### *Scanning electron microscopy*

Scanning electron microscopes (SEM) is a technique that use an electron beam (from a probe) to image samples with a resolution. The electrons are emitted from a filament and collimated into a beam in the electron source. The beam is then focused on the sample surface by a set of lenses in the electron column. The interaction of this probe with the sample generates various types of electrons and radiation, which are detected by the microscope (secondary electrons, backscattered electrons, X-ray).

SEM images and the energy-dispersive X-ray spectroscopy (EDS) are achieved to characterize the size, morphology, and chemical composition of the sample using MEB ZEISS Supra 40 (equipped with EDS Quantax Bruker detector) and FEI Nova Nona SEM 450 (equipped with EDS Oxford X-Max detector) microscopes. Two configurations (settings, type of detector) are used to obtain information on i) topographic contrast et ii) chemical contrast.

- i) Topographic contrast: secondary electron (SE) imaging at an accelerating voltage of 2 kV (SE2 detector - MEB ZEISS Supra 40)
- ii) Chemical contrast: backscattered electron (BSE) imaging at an accelerating voltage of 15 kV (HDAsB detector for MEB ZEISS Supra 40 and CBS detector for FEI Nova Nona SEM 450)

For direct observation, sieved powders are deposited on a carbon tap.

For backscattered electron (BSE) imaging, sample is prepared by “encapsulating cross-section” method which consists of sample encapsulation inside a resin, heating at 50°C overnight, polishing (silicon carbide abrasive papers + colloidal solution of water/silicon or heptane/diamond) and metallization (carbon graphite) to end up with a flat and conductive surface.

### *Transmission electron microscopy*

Transmission Electron Microscopy (TEM) operates on a similar principle than SEM. The main difference between SEM and TEM is that SEM forms images by detecting reflected or knocked-off electrons whereas TEM employs transmitted electrons (electrons passing through the sample) for image formation.

SEM is operated to determine the average length and stacking of the MoS<sub>2</sub> particles. TEM image is taken using JEOL JEM-200F operating at 200 kV. Images are recorded in bright field (BF) TEM mode as well as in scanning transmission electron microscope (STEM) mode (High-angle annular dark-field imaging (HAADF) and BF simultaneously). The image contrast mainly depends on the atomic number. Hence,  $Z_{\text{MoS}_2} \gg Z_{\text{Ketjenblack}}$ , these materials can be distinguished from each other. In bright field mode, MoS<sub>2</sub> is darker than carbon support and the opposite is observed for dark field configuration. The BF mode is useful to highlight the morphology of the support (Ketjenblack) while STEM images (especially HAADF) strengthen the metallic phase (MoS<sub>2</sub>). This is due to an increase of image contrast intensity (proportional to  $Z^{1.7}$ )<sup>125</sup> which is favorable for observing particles with high atomic number (Mo) deposited on support with lower Z (carbon).

The MoS<sub>2</sub> sheet size and stacking histograms are obtained from High Resolution HAADF-STEM mode at a magnification of 5Mx by direct analysis of microscopy images using Logrami IFPEN software.

The MoS<sub>2</sub> morphology (hexagonal or triangular-type) is determined applying a statistical method based on principal component analysis (PCA)<sup>125</sup> on high resolution HR-HAADF-STEM images which provide a “shape index” enabling to quantifying different morphology of metallic-sheet type compound on the support (e.g. carbon, alumina, silica).

For the acquisition, sieved powders are dispersed between two glass sides to avoid particles agglomeration and deposited on a copper grid covered with a holey carbon membrane.

### 1.1.3 Textural analysis

#### *Hg porosimetry*

Hg porosimetry is a technique based on the phenomenon of wettability. It relies on the non-wetting nature of mercury with respect to solids, requiring the application of pressure to force the liquid mercury metal to enter the pores of a solid.

Hg porosimetry is conducted to measure the macro+meso pore volume and the mean pore size distribution of these two pore families. Prior to the acquisition on Micromeritics AutoPore IV equipment, a pre-treatment under air for 2h at 120°C is applied to sample to remove the remaining adsorbed species at the surface (e.g. H<sub>2</sub>O, CO<sub>2</sub>).

#### *N<sub>2</sub> adsorption-desorption isotherm*

Unlike the mercury porosimetry, N<sub>2</sub> physisorption is based on physical adsorption of nitrogen inside mesopores (2 nm < pore size < 50 nm). Its implementation involves working with liquid nitrogen and introducing known quantities of gas into the solid to probe its pores. N<sub>2</sub> adsorption by the solid, the desorption is induced by purging the system to access the adsorption and desorption curves, which exhibit characteristic features related to the texture of the solid.

This is a complementary method to Hg porosimetry, performed using Micromeritics Instrument Asap 2420. The N<sub>2</sub> sorption phenomena inside micropores cannot be accurately described with theoretical hypotheses behind N<sub>2</sub> adsorption-desorption (i.e. N<sub>2</sub> adsorbed gas showing a liquid phase behavior well described by thermodynamics models). Nevertheless, microporous volume can be approximated with that technique.

Before analysis, samples are degassed for 3h at 110°C under vacuum in a glass holder and further few hours in the analysis port until reaching 1 mm Hg for leak test.

### 1.1.4 Laser Diffraction granulometry

Laser diffraction granulometry is an indirect measurement technique used to quantify particle size distribution (micron to millimeter scale). This analytical method relies on the principles of light scattering (Mie theory) and/or light diffraction (Fraunhofer theory and Mie theory). Particles illuminated by the laser light deflect it from its main axis. The amount of scattered light and the angle of deflection precisely measure the particle size.

Laser diffraction granulometry is acquired with Mastersizer 3000 Malvern T562 at dry state or liquid one (powders dissolved in ethanol prior to ultrasonic treatment).

### 1.1.5 Helium pycnometry

Helium pycnometry measures the skeletal density, which corresponds to the ratio of the mass of solid material to the sum of the solid matter volume (without pore volume) and closed pore volume within the material. Inert gas displacement is achieved by applying Boyle's Law, utilizing the relationship between volume and pressure.

Measurement is performed using Micrometrics Accupyc 1340 in a 1 cc sample holder.

### 1.1.6 Spectroscopic analysis

#### *RAMAN*

RAMAN spectroscopy is an analytical technique used to measure the vibrational energies of bonds. It specifically assesses changes in polarizability through the Raman scattering phenomenon.

RAMAN spectroscopy is selected to identify the metal-support interactions (i.e. molybdenum-Ketjenblack) due to its extremely sensitivity to Mo-O vibration modes and to characterize Ketjenblack graphitization state.

Raman measurements are made with Renishaw inVia Raman Microscope, 532 nm green laser of 75 mW combined with 50x objective. The working distance is fixed at 8 mm for a direct



powder analysis under air. Unfortunately, working with a glass-holder filled with argon did not allow to record MoS<sub>2</sub> signal for low concentration samples.

A study of the maximal laser power that can be applied to MoS<sub>2</sub> and Ketjenblack without degradations is achieved prior to the final acquisition by focusing on both MoS<sub>2</sub> (150-550 cm<sup>-1</sup>) and Ketjenblack (1100-1800 cm<sup>-1</sup>) raman windows. The use of 1% of the laser power maintained the sample integrity. Hence, spectrum is recorded with one acquisition at 1% of the laser power for 500 seconds exposure-time, between 100-1800 cm<sup>-1</sup> window. Calibration is made using silicon wafer (520.7 cm<sup>-1</sup>).

### *X-ray photoelectron spectroscopy*

X-ray photoelectron spectroscopy (XPS) is a quantitative and non-destructive extreme surface analysis technique. The principle involves irradiating the surface of a material with X-rays, leading to the ejection of a photoelectron from a specific orbital, allowing the probing of up to 10 atomic layers.

XPS is selected to evaluate the oxidative degree of molybdenum supported on Ketjenblack at the extreme sample surface. It is also a useful tool to investigate the chemical interactions between MoS<sub>2</sub>-KB and lithium polysulfides species after adsorption. Samples are examined using ESCA KRATOS Axis Supra, Al K $\alpha$  radiation, 1486 eV excitation energy, 15 kV x 10 mA, with pass energy of 20 eV. All binding energies are corrected according to the shift of the C 1s contamination peak at 284.6 eV for silica sample and for 284.1 eV for carbon samples.

### *UV-Visible spectroscopy*

UV-Vis spectroscopy is a qualitative and quantitative technique based on interaction of light with matter. The incident light UV (200-400 nm) or visible (400-800 nm) interacts with a sample. When a chemical compound absorbs discrete wavelengths from the light, some excitation and de-excitation (from excited state back to ground state) processes of electrons occur in atoms which result in the production of the absorption spectrum. The absorbance is directly influenced by the number of excited electrons transitioning from the ground state, which varies with the nature and concentration of the sample. This approach is grounded in Beer Lambert's law.

To evaluate the adsorption capacity of adsorbent materials, a series of UV-Visible (UV-Vis) spectra are performed using:

- i) a conventional configuration: 1 mm thick quartz cell and Agilent Cary 4000 UV-Vis spectrophotometer (double beam, 1 mm optical path, 100 ms integration, 3 acquisitions, 200-800 nm window) leading to sample preparation inside a glove box and analysis of < 1 mL solution outside the argon glove box in the sealed quartz cell. The spectra are processed using Cary WinUV software.
  
- ii) an optimized configuration: an optical probe fiber with a 1 mm optical path and covering the UV-Vis range (300 - 1100 nm), is directly connected to the glove box. It is coupled with Ocean Optics SR6 UV-VIS-NIR Spectrometers, which are paired with a DH-2000-BAL light source (Ocean Insight). This light source combines the continuous spectrum of a deuterium lamp in the range of 215–400 nm and a halogen lamp in the range of 360–2000 nm, respectively. The parameters used are : 100 ms integration, 100 scans to average, boxcar width value of 1, 3 acquisitions, 200-1000 nm windows. The latest configuration enables to work directly from the glove box and to analyze a bigger volume of solution (~8 mL). Data are processed using Ocean View software and the spectral deconvolution using Wire 3.3 (Renishaw).

### **1.1.7 Conductivity**

Measurement of conductivity is done using impedance spectroscopy. This technique is used for measuring the response of a system to a perturbation in a steady state by means of perturbing the electrode by a small amplitude voltage as a function of the frequency in order to get a current response (in case of impedance spectroscopy performed under potentiostatic control: PEIS). The Nyquist plot is used to visualize the impedance data obtained from a PEIS) experiment. The sample resistance ( $R_{sample}$ ) is read directly from Nyquist plot.

The conductivity is deduced from :

$$\sigma = \frac{1}{\rho} = \frac{1}{R_{sample} - R_{setup}} * \frac{L}{A} = \frac{1}{R_{sample} - R_{setup}} * \frac{L}{\pi * r^2}$$

With

$\sigma$  : conductivity (S.cm)

$\rho$  : resistivity ( $\Omega$ .cm)

R : resistance ( $\Omega$ )

L = length of conductor = pellet thickness (cm)

A = cross-sectional area of a disc (cm<sup>2</sup>)

r = disc radius (cm)

Conductivity measurements are made using the Sphere® setup from Sphere Energy, directly inside an argon glove box. Prior to measurement, the setup resistance is assessed by connecting the Sphere ® with the appropriate connectors in an open-circuit condition. The impedance measurement of the empty system allows to subtract the value of  $R_{\text{setup}}$  from the measurement with the sample ( $R_{\text{sample}}$ ).

To conduct the PEIS of the sample, few milligrams of powder are placed between two stainless steel pistons that are used as electrodes and on which a pressure of 1t/cm<sup>2</sup> and 2t/cm<sup>2</sup> is applying to sinter powder into pellet in order to increase the contact. PEIS are conducted from 1 MHz and 1 Hz with an ac amplitude of 5 mV on a BioLogic VMP3. After measurement, the Sphere ® is carefully opened to determine the pellet thickness with a micrometer caliper.

### 1.2 Synthesis of unsupported MoS<sub>2</sub>

A mixture of 4 mmol of (NH<sub>4</sub>)<sub>6</sub>Mo<sub>7</sub>O<sub>24</sub>·4H<sub>2</sub>O (4.943 g) and 56 mmol of thiourea (4.263 g) are combined in 140 mL of distilled water in a 250 mL bottle. The solution is thoroughly hand-mixed until all solids are completely dissolved. Subsequently, this solution is transferred to a 500 mL autoclave with a Teflon liner and sealed hermetically. The sealed autoclave is then placed into a preheated oven at 200°C. After 22 hours and cooling in the oven, the autoclave's contents are moved to a round-bottom flask and degassed for 5 minutes. The resulting mixture is filtered through a fritted filter and filter paper (0.2µm), yielding a black powder that underwent multiple washes with distilled water and ethanol. The solid is then dried in a vacuum oven at 60°C overnight, resulting in 2.98 g of product, which was finally stored in a sealed bag, achieving a yield of 67%.

### References

1. Baubet, B. et al. Quantitative Two-Dimensional (2D) Morphology–Selectivity Relationship of CoMoS Nanolayers: A Combined High-Resolution High-Angle Annular Dark Field Scanning Transmission Electron Microscopy (HR HAADF-STEM) and Density Functional Theory (DFT) Study. *ACS Catal.* 6, 1081–1092; 10.1021/acscatal.5b02628 (2016).
2. Rouquerol, F., Rouquerol, J. & Sing, K. S. Adsorption by powders and porous solids. Principles, methodology and applications (Academic Press, San Diego, London, Boston etc., 1999).



Appendix C – UV-Vis

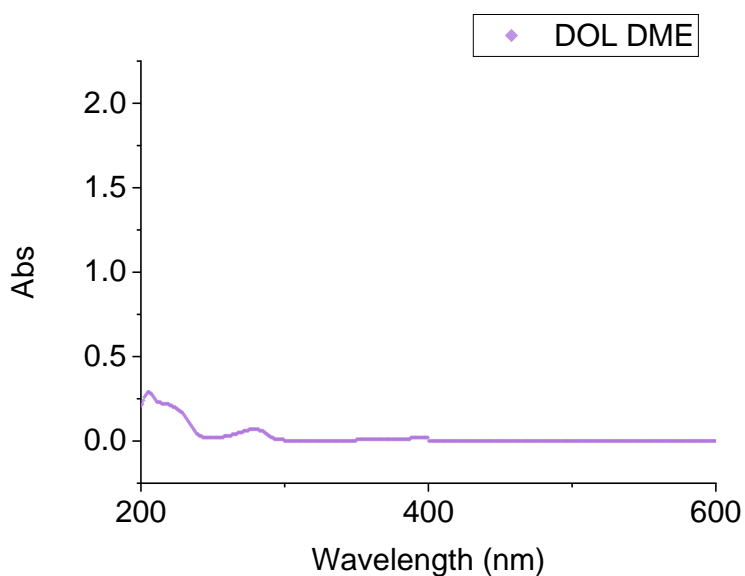


Figure C-1. UV-VIS signal of the DOL/DME solvent.

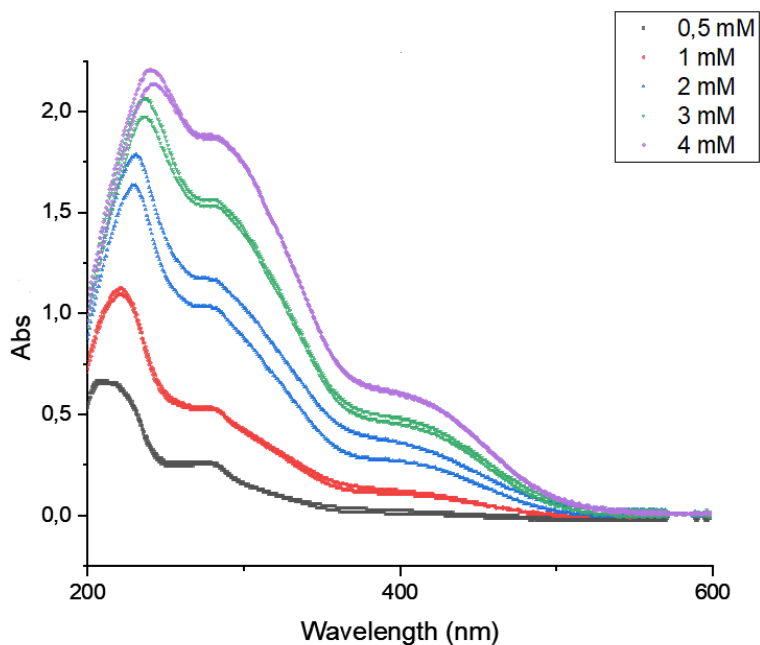


Figure C-2. Repeatability results of various standard  $\text{Li}_2\text{S}_6$  solutions prepared the 17/11/22 and the 29/11/22.



## Appendix D – Calculation instructions

### Equations used to calculate the MoS<sub>2</sub> surface

Example given for 48Mo-400-H<sub>2</sub>S(15) containing 48 wt.% of MoS<sub>2</sub>.

- The MoS<sub>2</sub> slab length ( $L_{max}$  in nm) is determined by TEM characterization
- $n_{edge}$ ,  $n_{lateral}$  and  $n_{total}$  are calculated using *K-D Kim, Y-K Lee*<sup>127</sup> reference introduced in **Figure II-12**.

$$n_{edge(\text{perslab})} = \frac{\frac{L_{max}}{d} + 1}{2} = \frac{\frac{4.4}{0.316} + 1}{2} = 7.5$$

$$n_{lateral(\text{perslab})} = 6(n_{edge} - 1) = 6 * (7.5 - 1) = 39$$

$$n_{total(\text{perslab})} = 3n_{edge}^2 - 3n_{edge} + 1 = 3 * (7.5^2) - 3 * 7.5 + 1 = 147$$

$$n_{Stotal(\text{perslab})} = 2n_{total} = 2 * 147 = 295$$

$$Slabmass(g) = \frac{n_{total} * M_w Mo + n_{Stotal} * M_w S}{Avogadro\ constant\ N_A} = \frac{147 * 96 + 295 * 32}{6,02214076 * 10^{23}} = 3,91 * 10^{23}$$

$$Number\ of\ slabs = \frac{slab\ mass}{sample\ mass} = \frac{3,91 * 10^{23}}{0.48} = 1.23 * 10^{19}$$

$$Slab\ surface\ (nm^2) = \left(3 * \frac{\sqrt{3}}{2} * d * n_{edge}\right)^2 = \left(3 * \frac{\sqrt{3}}{2} * 0,316 * 7.5\right)^2$$

$$= 14.59$$

$$Surface\ of\ all\ the\ slabs\ (m^2) = \frac{slab\ surface * 10^{-18}}{number\ of\ slab} = \frac{14.59 * 10^{-18}}{1.23 * 10^{19}} = 179$$



### Equations used to the ratio $V_{host}/V_{Li2S}$

Example given for 48Mo-400-H<sub>2</sub>S(15) containing 48 wt.% of MoS<sub>2</sub>.

- The porous volume ( $V_p$  in  $\text{cm}^3 \cdot \text{g}^{-1}$ ) is determined by Hg porosimetry;
- $V_{host}$  refers to the volume of MoS<sub>2</sub>-KB developed to confine S<sub>8</sub> or Li<sub>2</sub>S;
- $m_{host (MoS_2-KB)}$  and  $m_{S_8}$  are experimental values.

$$V_{host}(\text{cm}^3) = m_{host (MoS_2-KB)}(\text{g}) * V_p(\text{cm}^3 \cdot \text{g}^{-1}) = 1.60 * 1.2 = 1.79$$

$$V_{S_8}(\text{cm}^3) = m_{S_8} * \rho_{S_8} = 0.38 * 2 = 0.19$$

$$V_{Li_2S}(\text{cm}^3) = \text{expansion factor} * V_{S_8} = 1.8 * 1.9 = 0.34$$

$$\frac{V_{host}}{V_{Li_2S}} = \frac{1.79}{0.34} = 9.4$$

$$\frac{V_{host}}{V_{S_8}} = \frac{1.79}{0.19} = 5.3$$

## Appendix E - Figures captions

Figure 0-1. Global primary energy consumption by source <sup>2</sup> .....	1
Figure 0-2. Global EV market growth a) worldwide b) in Europe <sup>3</sup> .....	2
Figure 0-3. Comparison of the gravimetric performance of different battery technologies for automotive applications and performances expected up to 2035. <sup>6</sup> .....	3
Figure 0-4. Ragone plot for different types of electrochemical energy storage devices <sup>7</sup> .....	4
Figure I-1. Schematic diagram of a Li-S battery. ....	7
Figure I-2. a) Typical two-plateau cycling curve of Li-S <sup>11</sup> and the corresponding b) CV profile <sup>12</sup> .....	9
Figure I-3. Proposition of Li-S mechanism a) discharge mechanism in TEGDME <sup>14</sup> b) discharge/charge mechanism in 0.5 M LiClO <sub>4</sub> /DME solution <sup>20</sup> .....	10
Figure I-4. (a) Summary of degradation mechanism inside a Li-S battery (b) scheme of the shuttle effect upon cycling <sup>10</sup> .....	12
Figure I-5. Crystal structure of a) sulfur b) lithium sulfide <sup>28</sup> .....	14
Figure I-6. Ab-initio binding energies of LiS and Li <sub>2</sub> S calculation <sup>9</sup> .....	15
Figure I-7. : Lewis acid-base interactions to coordinate lithium polysulfides <sup>30</sup> .....	16
Figure I-8. Overview of Li-S strategies developed to improve the performance of Li-S batteries <sup>46</sup> .....	18
Figure I-9. Example of usual UV-Vis signal obtained after new material designed to trap LiPS and Li <sub>2</sub> S <sub>6</sub> equivalent solution. (Reproduced from <sup>61</sup> ). ....	20
Figure I-10. MoS <sub>2</sub> applications <sup>65</sup> .....	22
Figure I-11. MoS <sub>2</sub> structure a) Single slab of S-Mo-S <sup>73</sup> b) with different morphologies <sup>74</sup> c) stacking <sup>73</sup> d) distinct atomic planes/positions and e) with different sulfur coverages <sup>75</sup> .....	24
Figure I-12. Occupation of electrons in Mo 4d orbits under the crystal fields of (a) 2H phase and (b) 1T phase <sup>77</sup> .....	25
Figure I-13. Scheme of different possible orientations of MoS <sub>2</sub> clusters on supports <sup>86</sup> .....	27
Figure I-14. Binding energies for the interaction between Li <sub>2</sub> S molecules and different MoS <sub>2</sub> atomic position <sup>89</sup> .....	28
Figure I-15. Design approaches to modify MoS <sub>2</sub> structure. ....	29
Figure I-16. Carbon nanomaterials used for Li-S batteries applications <sup>98</sup> .....	30
Figure I-17. Variation of adsorption capacity with the MoS <sub>2</sub> loading for a) edges/corners adsorption only and for b) edges/corners + basal plane adsorption. ....	33
Figure I-18. Schematic organization of the overall strategy to develop S-MoS <sub>2</sub> -KB material for Li-S battery application. Green, blue, grey, orange corresponds to synthesis, characterization, adsorption characterization and electrode/battery making respectively.....	35
Figure II-1. KB morphology characterizations a) SEM image before ultrasound treatment, b and c) Bright Field TEM images of KB d) schematic structures of the three scales <sup>102</sup> .....	41
Figure II-2. Ketjenblack particles size distribution a) in volume b) in number. ....	42
Figure II-3. Textural analysis of KB a) Hg porosimetry d) N <sub>2</sub> adsorption-desorption isotherm. ....	43
Figure II-4. Raman spectrum of KB.....	45

Figure II-5. Overview of the parameters chosen to modify the MoS <sub>2</sub> -KB structure and the related synthesis settings. ....	46
Figure II-6. MoS <sub>2</sub> -KB synthesis a) Sulfidation reactor containing molecular MoS <sub>2</sub> -KB b) MoS <sub>2</sub> -KB material obtained after sulfidation.....	47
Figure II-7. 32Mo-400-H <sub>2</sub> S(15) XPS spectral decomposition. ....	50
Figure II-8. MoS <sub>2</sub> -KB compared to pure KB particles size distribution a) weighted in volume b) weighted in number. ....	51
<b>Figure II-9. SEM images of 32Mo-400-H<sub>2</sub>S(15) and 48Mo-400-H<sub>2</sub>S(15) a) direct observation of a particles b) cross section.....</b>	<b>52</b>
Figure II-10. Raman spectra of 32Mo-400-H <sub>2</sub> S(15). ....	54
Figure II-11. TEM images of 32Mo-400-H <sub>2</sub> S(15) and 48Mo-400-H <sub>2</sub> S(15) using a) BF TEM b) and c) HR HAADF-STEM. ....	55
Figure II-12. MoS <sub>2</sub> a) stacking and b) slab length distributions of 32Mo-400-H <sub>2</sub> S(15) and 48Mo-400-H <sub>2</sub> S(15)..	56
Figure II-13. Correlation of dispersion [(edges+corners)/(edges+corners+basal plan)] total with MoS <sub>2</sub> slab size and scheme of hexagonal MoS <sub>2</sub> slab. Reproduced from K-D Kim, Y-K Lee <sup>127</sup> . ....	57
Figure II-14. Hg porosimetry of MoS <sub>2</sub> -KB with different MoS <sub>2</sub> loading.....	59
Figure II-15. N <sub>2</sub> adsorption-desorption isotherm MoS <sub>2</sub> -KB with different MoS <sub>2</sub> loading. ....	59
Figure II-16. Evolution of the porous volume per pore family after Mo impregnation a) in volume b) in percentage.....	60
Figure II-17. Sulfidation program .....	64
Figure II-18. Evolution of the MoS <sub>2</sub> -KB N <sub>2</sub> isotherms with different post-treatments. ....	66
Figure II-19. MoS <sub>2</sub> a) slab length and b) stacking distributions on MoS <sub>2</sub> -KB with different sulfidation conditions. (Histograms obtained from the analysis of 22 and 28 HR HAADF-STEM images and 223 and 362 measurements) .....	68
Figure II-20. SEM images of MoS <sub>2</sub> -KB sulfided under pure H <sub>2</sub> S and 15%H <sub>2</sub> S/H <sub>2</sub> a) BF TEM, b) HR HAADF-STEM and c) at higher magnification (MoS <sub>2</sub> slabs are marked by the red circles and KB by the red arrow). ....	69
Figure II-21. Theoretical relation between shape factor and % edges+corners using the PCA method for different shape models. Reproduced from PKS01-002 internal IFPEN document. ....	70
Figure II-22. Shape index distribution with sulfidation gas nature .....	71
Figure II-23. MoS <sub>2</sub> a) slab length and b) stacking on MoS <sub>2</sub> -KB with sulfidation temperature. (Histograms obtained from the analysis of 28 and 19 HR HAADF-STEM images and 362 and 264 measurements).....	72
Figure III-1. Images of 0.4 mM S <sub>8</sub> in DOL:DME and 32 mM Li <sub>2</sub> S in different solvents.....	79
Figure III-2. Color evolution of 60 mM initial Li <sub>2</sub> S <sub>6</sub> polysulfides solution over reaction time. ....	80
Figure III-3. Standard equivalent polysulfides solutions Li <sub>2</sub> S <sub>6</sub> . ....	81
Figure III-4. Li <sub>2</sub> S <sub>6</sub> (3 mM in DOL-DME) UV-Vis signal using a quartz cuvette. ....	82
Figure III-5. Li <sub>2</sub> S <sub>6</sub> (3mM) UV-Vis signal evolution after 72h when using quartz cuvette. ....	84
Figure III-6. In situ UV-Vis probe setup connected to the glove box.....	85
<b>Figure III-7. Superposition of Li<sub>2</sub>S<sub>6</sub> (3mM) UV-Vis signals at time=1h and 72h using an in situ probe. ....</b>	<b>85</b>
Figure III-8. Li <sub>2</sub> S <sub>6</sub> UV-Vis signal comparison between ex situ cuvette quartz (dash) and in situ probe (line). ....	86
Figure III-9. UV-Vis spectrum of Li <sub>2</sub> S <sub>6</sub> solutions in DOL/DME (v/v 50/50).....	87

Figure III-10. Calibration curve: Area of the $\text{Li}_2\text{S}_6$ solutions spectra integration as a function of concentration.	87
Figure III-11. Spectral decomposition and fitting of 0.8 mM $\text{S}_8$ (red curve refers to experimental curve, green curves to the individual peaks and blue curve to simulated Gaussian curve).	89
Figure III-12. Spectral decomposition and fitting of 4 mM $\text{Li}_2\text{S}_6$ (red curve refers to experimental curve, green curves to the individual peaks and blue curve to simulated Gaussian curve).	90
Figure III-13. Evolution of area of each contribution/peak as a function of initial $\text{Li}_2\text{S}_6$ concentration in a) 200-325 nm b) 325-600 nm regions.	92
Figure III-14. UV-Vis signals of $\text{S}_8$ at different concentrations in DOL-DME.	93
Figure III-15. Evolution of the massif area as a function of $\text{S}_8$ concentration.	93
Figure III-16. Evolution of $230 \pm 10$ and $285 \pm 5$ nm peak area as a function of $\text{S}_8$ concentration.	94
Figure III-17. Superposition of the evolution of $230 \pm 10$ nm $\text{S}_8$ contribution in $\text{S}_8$ and $\text{Li}_2\text{S}_6$ solutions. In blue, evolution $\text{S}_8$ in elemental $\text{S}_8$ solution from Figure III-16 and in red evolution in $\text{Li}_2\text{S}_6$ from Figure III-13.	96
Figure III-18. Evolution of several contributions as a function of $\text{Li}_2\text{S}_6$ equivalent concentrations.	97
Figure III-19. Evolution of 48Mo-400- $\text{H}_2\text{S}$ adsorption capacity in ( $\mu\text{mol/g}$ ) over time after addition of 0.57 mL of $\text{Li}_2\text{S}_6$ solution (corresponding to 3.2 mM).	101
Figure III-20. Example of fitting obtained after the adsorption of 4.1 mM $\text{Li}_2\text{S}_6$ on 48Mo-400- $\text{H}_2\text{S}$ (15) adsorbent (red curve refers to experimental curve, green curves to the individual peaks and blue curve to simulated Gaussian curve).	102
Figure III-21. Equilibrium UV-Vis spectra obtained on the supernatant of the a) 32Mo-400- $\text{H}_2\text{S}$ (15) b) 48Mo-400- $\text{H}_2\text{S}$ (15) and c) Aerosil 200 after (15) successive $\text{Li}_2\text{S}_6$ equivalent additions.	105
Figure III-22. Evolution of peak area of each specie contribution with the initial $\text{Li}_2\text{S}_6$ concentration for a) 32Mo-400- $\text{H}_2\text{S}$ (15) b) 48Mo-400- $\text{H}_2\text{S}$ (15) c) Aerosil 200.	106
<b>Figure III-23. Evolution of the area of the different contributions after adsorbent saturation at a) 325 b) 365 and c) 425 nm compared to <math>\text{Li}_2\text{S}_6</math>.</b>	<b>107</b>
Figure III-24. Comparison of the adsorption isotherms per contribution at a) 325 nm b) 365 nm c) 425 nm for Aerosil 200, 32Mo-400- $\text{H}_2\text{S}$ (15) and 48Mo-400- $\text{H}_2\text{S}$ (15). Points represents experimental data and lines the Langmuir adsorption isotherm.	108
Figure III-25. 32Mo-400- $\text{H}_2\text{S}$ (15) XPS spectra centered on a) molybdenum Mo 3d b) sulfur S 2p c) lithium Li 1s.	111
Figure III-26. Images of the 3 mM $\text{Li}_2\text{S}_6$ color solution evolution after addition of 32Mo-400- $\text{H}_2\text{S}$ (15), 48Mo-400- $\text{H}_2\text{S}$ (15), Ketjenblack and $\text{MoS}_2$ .	113
Figure III-27. UV-Vis spectra of $\text{Li}_2\text{S}_6$ solution before and after the addition of KB, $\text{MoS}_2$ , 32Mo-400- $\text{H}_2\text{S}$ (15) and 48Mo-400- $\text{H}_2\text{S}$ (15).	114
Figure III-28. Comparison of the evolution of a) $N_{\text{ads}}$ and b) the $\text{MoS}_2$ surface ratio.	115
Figure III-29. Images of the 3 mM $\text{Li}_2\text{S}_6$ color solution evolution after addition of $\text{MoS}_2$ -KB synthesized under varying sulfidation conditions.	116
Figure III-30. UV-Vis spectra of $\text{Li}_2\text{S}_6$ solution before and after the addition of adsorbent synthesized with various of sulfidation conditions.	117
Figure III-31. Effect of $\text{MoS}_2$ nanoparticles engineering (comparison in terms of $N_{\text{ads}}$ per gram of $\text{MoS}_2$ ).	119

Figure III-32. Images of the 3 mM  $\text{Li}_2\text{S}_6$  color solution evolution after addition of Aerosil 200 and  $\text{MoS}_2$ .....120

Figure IV-1. Comparison of experimental and theoretical electroactive sulfur content  $S_8$  .....129

Figure IV-2. Adsorbent/S ratio obtained from S-MoS<sub>2</sub>-KB.....129

**Figure IV-3. Ratio of  $V_{\text{host}}/V_{\text{Li}_2\text{S}}$  from S-MoS<sub>2</sub>-KB samples .....130**

Figure IV-4. From material synthesis to battery assembly, the processing chart.....131

Figure IV-5. Formulation issues a) non-adherence on the current collector b) electrode peeling, c) heterogeneous particle distribution and d) cracking. ....132

Figure IV-6. Slurry viscosity when using a) 10 wt.% of CMC-SBR (5-5) and b) 40 wt.% of CMC-SBR (10-30). .....133

Figure IV-7. a) Doctor blade device b) S-0Mo typic wet electrode film deposited on aluminum foil.....135

Figure IV-8. S-0Mo electrode after optimization.....136

Figure IV-9. Schematic representation of a two-electrodes coin cell (CR2032) .....138

Figure IV-10. Percentage of polysulfides ( $\text{Li}_2\text{S}_6$  or  $\text{Li}_2\text{S}_4$ ) trapped depending on the adsorbent nature.....140

Figure IV-11. Evolution of sulfur species upon electrochemical discharge of sulfur electrode by XANES (reproduced from M. Cuisiner et al.<sup>150</sup>). .....141

Figure IV-12. Evolution of the  $\text{Li}_2\text{S}_6$  and  $\text{Li}_2\text{S}_4$  concentrations in the electrolyte with E/S ratio, calculated for a sulfur mass of 0.3 mg. ....143

Figure IV-13. Galvanostatic discharge curves of S-0Mo before and after normalization –conditioning step . Conditions: 25°C in 1 M LiTFSI, 1 wt%  $\text{LiNO}_3$ , DOL/DME v/v 1/1. ....145

Figure IV-14. Typical galvanostatic discharge-charge S-0Mo curve at  $C_{10}/10$ . ....145

Figure IV-15. Repeatability tests on fresh two-electrode Li || S-0Mo coin cells (3 samples) a) Nyquist plot of EIS measurements b) Zoom on the EIS between  $Z_{\text{Re}} = 4-14 \Omega$ . ....146

Figure IV-16. Characteristic Nyquist plot of a fresh Li/S coin cell at the initial state measured at 25°C (reproduced from S. Walus et al.<sup>155</sup>). .....147

Figure IV-17. S-0Mo cycling stability repeatability – 2 coin-cells. ....148

**Figure IV-18. Self-discharge of fresh Li ||  $S_8$  cells during 120 hours of storage at OCV. Conditions: 25°C in 1 M LiTFSI, 1 wt%  $\text{LiNO}_3$ , DOL/DME v/v 1/1. ....150**

Figure IV-19. Comparison of the discharge for the reference and the MoS<sub>2</sub>-KB based electrodes after 20<sup>th</sup> cycles. Zoom at the beginning of the second plateau where  $\text{Li}_2\text{S}$  nucleation occurs. ....151

**Figure IV-20. Cycle stability and Coulombic efficiencies of S-0Mo, S-32Mo-400- $\text{H}_2\text{S}(15)$  and S-48Mo-400- $\text{H}_2\text{S}(15)$  cells. Conditions: 25°C in 1 M LiTFSI, 1 wt%  $\text{LiNO}_3$ , DOL/DME v/v 1/1, in the 2-3 V vs Li/Li<sup>+</sup> voltage range (for 0% and 48% wt. MoS<sub>2</sub> on KB) and between 1.8-3 V vs Li/Li<sup>+</sup> voltage range (for 32 wt.% MoS<sub>2</sub> on KB) at  $C/10$  ( $1C = 0.2-0.6 \mu\text{A}\cdot\text{cm}^{-2}$ ). ....152**

Figure IV-21. Evolution of a) the discharge capacities per regions and b) the  $R_{\text{ratio}}$  with cycle number. ....153

Figure IV-22. The Nyquist plots of S-0Mo and S-48Mo-400- $\text{H}_2\text{S}(15)$  at the end of a) discharge and b) charge.154

## Appendix F - Tables captions

Table I-1. Principal electrochemical reactions occurring at the positive electrode during discharge <sup>13</sup> .....	9
Table I-2. Characteristics of carbon additives used in battery electrode formulation.....	31
Table II-1. KB elemental analysis using CHNS.....	40
<b>Table II-2. KB textural characteristics. Results are obtained from <sup>a</sup> Hg porosimetry, <sup>b</sup> N<sub>2</sub> adsorption-desorption isotherm.</b> .....	44
Table II-3. Mass of PMA used in the impregnation solution for a targeted percentage of supported MoS <sub>2</sub> . ....	47
Table II-4. Sample nomenclature according to their MoS <sub>2</sub> loading obtained using XRF.....	48
Table II-5. Elemental analysis of MoS <sub>2</sub> -KB with Mo loading.....	48
Table II-6. Decomposition of Mo 3d XPS spectra for 32Mo-400-H <sub>2</sub> S(15). The data express the relative percentage of atoms according to their oxidation state. ....	50
Table II-7. Semi quantitative study of C, O, P, Mo contents grains by grains for SEM cross section of a) 32Mo-400-H <sub>2</sub> S(15) and b) 48Mo-400-H <sub>2</sub> S(15).....	53
Table II-8. Slabs characteristics with MoS <sub>2</sub> loading.....	58
Table II-9. Evolution of MoS <sub>2</sub> -KB textural characteristics with MoS <sub>2</sub> loading. Results are obtained from <sup>a</sup> Hg porosimetry, <sup>b</sup> N <sub>2</sub> adsorption-desorption isotherm.....	61
Table II-10. Targeted modification of the MoS <sub>2</sub> structure with variations of the standard incipient wetness impregnation-sulfidation protocol. ....	63
Table II-11. Sample nomenclature according to their sulfidation conditions.....	63
Table II-12. MoS <sub>2</sub> -KB elemental analyses with post-treatment.....	65
<b>Table II-13. MoS<sub>2</sub>-KB XRF elemental analysis with sulfidation gas nature.</b> .....	67
Table II-14. Experimental shape index calculated.....	71
Table II-15. Average slab length, stacking with sulfidation temperature.....	72
Table II-16. MoS <sub>2</sub> slab nature for 21-28 wt.% of MoS <sub>2</sub> on KB calculated by extrapolation of the results obtained for 14 wt.%.....	73
<b>Table III-1. Attribution of absorption peak of polysulfides according to literature.</b> .....	83
Table III-2. Wavelengths of polysulfides species obtained from the spectral curve fitting.....	91
Table III-3. Reaction stoichiometry table.....	95
Table III-4. Calculated concentration of S <sub>8</sub> and S <sub>4</sub> <sup>2-</sup> in Li <sub>2</sub> S <sub>6</sub> equivalent (first estimation).....	96
Table III-5. Calculated concentration of S <sub>8</sub> , S <sub>4</sub> <sup>2-</sup> and S <sub>6</sub> <sup>2-</sup> in Li <sub>2</sub> S <sub>6</sub> equivalent (second estimation).....	98
Table III-6. Experimental Li <sub>2</sub> S <sub>6</sub> volume addition protocol to get adsorption isotherms. ....	100
Table III-7. Adsorption equilibrium constant <i>k<sub>ads</sub></i> and <i>n<sub>ads sat.</sub></i> .....	109
Table III-8. Semi-quantitative analysis of XPS spectra before and after polysulfides adsorption.....	111
Table III-9. Adsorption capacity with MoS <sub>2</sub> loading.....	114
Table III-10. Adsorption capacity with sulfidation conditions variations.....	117
Table III-11. Ratio comparison of the different adsorption value calculated with the exposed surface area.....	118
Table III-12. Nads comparison of the experimental data and the literature.....	121
Table IV-1. Mass of sulfur and MoS <sub>2</sub> -KB calculated from equation IV-1.....	127

<i>Table IV-2. Elemental analysis of S- MoS<sub>2</sub>-KB samples obtained from CHNS.....</i>	<i>127</i>
<i>Table IV-3. Experimental MoS<sub>2</sub>, MoS<sub>2</sub>-KB and S<sub>active</sub> content in S- MoS<sub>2</sub>-KB and the corresponding adsorbent/S ratio.....</i>	<i>128</i>
<i>Table IV-4. Electrode thickness and sulfur loading obtained for different doctor blade gaps. ....</i>	<i>135</i>
<i>Table IV-5. S-MoS<sub>2</sub>-KB electrode properties (average values obtained from 6 samples on the same electrode)</i>	<i>137</i>
<i>Table IV-6. Comparison of theoretical and experimental weight adsorbent/S ratios.....</i>	<i>139</i>
<i>Table IV-7. Porous volume of the electrode, separator and electrode+ separator.....</i>	<i>142</i>
<i>Table IV-8. Comparison of the results with other literature .....</i>	<i>155</i>

## Abstract

---

### **Comprehensive study of the MoS<sub>2</sub>-Ketjenblack structure – electrochemical performance relationships in lithium sulfur batteries**

Lithium-sulfur (Li-S) batteries are promising candidates for energy storage. Due to their high theoretical gravimetric and volumetric energy density of 2500 Wh.kg<sup>-1</sup> and 2800 Wh.L<sup>-1</sup> [9], they have the potential to practically store about 3 times more energy than Li-ion batteries. However, several challenges hinder their commercial development. Among those, the “shuttle-effect” is one of the major drawbacks and consists of a back-and-forth movement between electrodes of the dissolved intermediates polysulfides (Li<sub>2</sub>S<sub>x</sub>, 2 ≤ x ≤ 8) giving rise to low active sulfur utilization, poor coulombic efficiency, and rapid capacity decay.

In literature, many strategies have been proposed ranging from protective lithium metal (Li) passive layers to electrolyte separator functionalization, and new positive electrode design using efficient polysulfides trapping materials (e.g. porous carbon, metal-organic frameworks, metal-based material such as oxides or hydroxides or even sulfides materials)<sup>46</sup>. Among them, MoS<sub>2</sub> has proven to be a good adsorbent candidate to interact with polysulfide species<sup>39</sup>. This PhD project is dedicated to the design of supported MoS<sub>2</sub>-Ketjenblack (MoS<sub>2</sub>-KB) for Li-S positive electrode to tackle the “shuttle effect” phenomenon. We aimed to better understand the parameter playing a role on the polysulfide trapping mechanism to design an optimized MoS<sub>2</sub>-KB electrode to i) mitigate polysulfide shuttling, and ii) favor their reduction into Li<sub>2</sub>S.

Samples with MoS<sub>2</sub> loading, slab length variations and MoS<sub>2</sub> morphology modifications are synthesized to modify the type and number of active sites to study the impact on polysulfides interactions, and the resulting impact on the Li-S battery performances.

To do so, we setup a new UV-Vis methodology using *in situ* probe to systematically quantify the polysulfides adsorption onto the developed materials. Indeed, this methodology limits the artefacts due to the setup compared to usual UV-Vis setup using a quartz cuvette and helps to understand the true effect of adsorbents nature (MoS<sub>2</sub>, MoS<sub>2</sub>-Ketjenblack, silica) on the



adsorption phenomena and how it may modify the chemistry in solution of polysulfides (disproportionation and speciation). Finally, the sulfur impregnated porous MoS<sub>2</sub>-KB powders are subsequently integrated into the formulation of sulfur-positive electrodes within a coin cell battery environment to assess their effectiveness as both polysulfides trap and catalytic surface to convert polysulfides. The electrochemical measurements performed aim to quantitatively determine whether it would enhance the electrochemical performance (capacity, faradic efficiency, power, cycle life) over time.

### References

1. Seh, Z. W., Sun, Y., Zhang, Q. & Cui, Y. Designing high-energy lithium-sulfur batteries. *Chemical Society reviews* **45**, 5605–5634; 10.1039/c5cs00410a (2016).
2. Chen, Y. *et al.* Advances in Lithium-Sulfur Batteries: From Academic Research to Commercial Viability. *Advanced materials (Deerfield Beach, Fla.)*, e2003666; 10.1002/adma.202003666 (2021).
3. Liu, Y., Cui, C., Liu, Y., Liu, W. & Wei, J. Application of MoS<sub>2</sub> in the cathode of lithium sulfur batteries. *RSC Adv.* **10**, 7384–7395; 10.1039/C9RA09769D (2020).

## Résumé

---

### **Etude des relations entre la structure et les performances électrochimiques de matériaux MoS<sub>2</sub>-Ketjenblack pour les batteries lithium-soufre.**

Les batteries lithium-soufre (Li-S) sont des technologies de batterie prometteuses pour répondre à la demande croissante de stockage d'énergie. En raison de leur densité d'énergie théorique élevée de 2500 Wh.kg<sup>-1</sup> en poids et de 2800 Wh.L<sup>-1</sup> en volume [1], elles ont le potentiel de stocker pratiquement 3 fois plus d'énergie que les batteries Li-ion. Cependant, plusieurs défis entravent leur développement commercial. Parmi eux, l'effet de « navette redox » est l'un des principaux inconvénients de la technologie. Cette navette redox consiste en un mouvement d'aller-retour des polysulfures (Li<sub>2</sub>S<sub>x</sub>, 2 < x < 8), composés intermédiaires générés lors de la dissolution du soufre entre les électrodes, entraînant une faible utilisation de soufre actif, une perte d'efficacité coulombique et une rapide dégradation de la capacité électrochimique au cours du temps.

Dans la littérature, de nombreuses stratégies ont été proposées pour réduire ce phénomène, allant de l'utilisation de couches passives protectrices du lithium métal (Li), à la fonctionnalisation des séparateurs d'électrolyte, en passant par la conception de nouvelles électrodes positives utilisant des matériaux dont la fonction principale est de capturer efficacement les polysulfures (carbone poreux, structures métallo-organiques, matériaux à base de métaux tels que des oxydes ou des hydroxydes, voire des matériaux sulfures par exemple) [2]. Parmi les solutions proposées, le MoS<sub>2</sub> s'est révélé être un bon candidat pour interagir spécifiquement avec les polysulfures [3].

Ce projet de thèse est dédié à la conception d'électrodes positives de batteries Li-S, à base de MoS<sub>2</sub>-Ketjenblack (MoS<sub>2</sub>-KB), pour résoudre le phénomène de « navette redox ». Il vise à mieux comprendre les paramètres jouant un rôle dans le mécanisme de capture des polysulfures afin de concevoir des électrodes positive de MoS<sub>2</sub>-KB optimisées pour i) réduire la diffusion des polysulfures et ii) favoriser leur réduction en Li<sub>2</sub>S.

Différents échantillons de MoS<sub>2</sub>-KB ont été synthétisés en veillant à varier la morphologie, la teneur, et la longueur des feuillets de MoS<sub>2</sub> afin de modifier, à la fois, le type et le nombre de

sites actifs disponibles et d'étudier l'impact sur les interactions avec les polysulfures et les performances des batteries Li-S qui en résulte.

Pour ce faire, une nouvelle méthodologie UV-Vis, utilisant une sonde *in situ* pour quantifier systématiquement l'adsorption des polysulfures par les matériaux synthétisés, a été développée. En effet, cette méthodologie limite les artefacts générés lors de l'utilisation d'une configuration plus répandue : mesure UV-Vis avec cuvette en quartz. La méthodologie *in situ* contribue ainsi à comprendre l'effet réel de la nature des adsorbants ( $\text{MoS}_2$ ,  $\text{MoS}_2$ -Ketjenblack, silice) sur les phénomènes d'adsorption et comment cela peut modifier la chimie des polysulfures en solution (réactions de dismutation et spéciation). Enfin, les échantillons poreux de  $\text{MoS}_2$ -KB, préalablement imprégnés de soufre, ont été intégrés dans la formulation d'électrodes positives Li-S afin d'évaluer leur efficacité d'adsorption et de conversion des polysulfures dans un système réel, au sein de pile-bouton. Des mesures électrochimiques ont été menées afin d'évaluer quantitativement l'impact de ces matériaux sur les performances électrochimiques (capacité, efficacité faradique, puissance, durée de vie du cycle) au fil du temps.